
Smartphone-readable physically- unclonable anti-counterfeiting labels based on microlens array and microphosphor particles

Zur Erlangung des akademischen Grades eines

Doktors der Ingenieurwissenschaften

(Dr.-Ing.)

von der KIT-Fakultät für Elektrotechnik und Informationstechnik
des Karlsruhe Institute für Technologie (KIT)

angenommene

Dissertation

von

Vinay Kumar, M.Sc.

geboren am 10.08.1994 in Telo, Indien

Tag der mündlichen Prüfung:

25.02.2025

Hauptreferent:

Prof. Dr. Bryce Sydney Richards

Korreferent:

Prof. Dr. Thomas J. Soerensen

Kurzfassung

Gefälschte Produkte stellen weltweit ein erhebliches Risiko für die öffentliche Gesundheit, die Sicherheit und das geistige Eigentum dar, was sie zu einem kritischen Problem macht, das dringend der Aufmerksamkeit und innovativer Lösungen bedarf. Physikalisch nicht klonbare Etiketten (engl. PULs) bieten eine vielversprechende Möglichkeit, Fälschungen zu bekämpfen, erfordern aber oft spezielle Geräte zur Authentifizierung. In meiner Doktorarbeit stelle ich ein neuartiges PUL-Konzept vor, das ein Mikrolinsen-array (ML) und Phosphorpartikel verwendet und speziell für die Authentifizierung mit Smartphones entwickelt wurde.

Der ursprüngliche PUL-Entwurf meiner Doktorarbeit besteht aus einem ML-Array, das auf eine lumineszierende Polymerfolie laminiert ist und, die mit Mikropartikeln durchsetzt ist. Mikroskopische Partikelverteilungen können somit auf makroskopischer Ebene sichtbar gemacht werden. Gadoliniumoxysulfid, das mit Ytterbium- und Erbium-Ionen dotiert ist, wird als UC-Dotierungspartikel im PUL-Design verwendet. Die zufällige Verteilung dieser Partikel in der Polymermatrix in Verbindung mit dem Fokussierungseffekt des ML-Arrays erzeugt einzigartige und nicht klonierbare Lumineszenzmuster. Zur Untersuchung dieser PUL-Merkmale wird ein Anregungslaser von 980nm verwendet, der nicht klonierbare Muster im sichtbaren Emissionsbereich erzeugt. Der Einfallswinkel (engl. AOI) beeinflusst das beobachtete Muster und macht die Etiketten somit unklonierbar. Für diese ersten PULs beträgt die AOI-Toleranz - die zulässige Abweichung des AOI für eine genaue Musterauthentifizierung - $0,2^\circ$, mit einer geschätzten Falsch-Positiv-Wahrscheinlichkeit von 10^{-15} . Während die Authentifizierungsrobustheit stark genug ist, um Fälschungsversuchen zu widerstehen, stellte die Empfindlichkeit dieses ersten PUL-Designs gegenüber der AOI eine Herausforderung für praktische Anwendungen dar.

Um dieser Einschränkung zu begegnen, wird in einer Folgestudie der Einfluss der Partikelgröße und der Brennweite des ML auf die Toleranz der Etiketten gegenüber AOI-Schwankungen untersucht. In dieser Studie werden mit Cerium (Ce^{3+}) dotierte abwärtskonvertierende Yttrium-aluminium-granat (YAG)-Partikel als Dotierstoffe im PUL verwendet. Durch die Erhöhung der durchschnittlichen Partikelgröße von (9 ± 1)

μm auf $(32,5 \pm 2) \mu\text{m}$ und die Verwendung von ML mit einer Brennweite von $550\mu\text{m}$ wird die AOI-Toleranz miteinander Steigerung deutlich von $0,8^\circ$ auf $3,6^\circ$ gegenüber dem ursprünglichen PUL-Design 18-fache verbessert. Diese Verbesserung erhöht die Robustheit und Anwendbarkeit der Etiketten erheblich, ohne die Sicherheitsstandards zu beeinträchtigen. Darüber hinaus ermöglicht das verbesserte PUL-Design die Verwendung einer inkohärenten Lichtquelle (eine 450nm -licht-emittierende Diode, LED) und die Authentifizierung mit einer Smartphone-Kamera auf die Rückseite des Etiketts gerichtet. Dadurch werden auch die Hardware-Anforderungen für die PUL-Validierung deutlich vereinfacht.

Aufbauend auf diesen Ergebnissen konzentriert sich die letzte Phase meiner Doktorarbeit auf die Entwicklung eines benutzerfreundlichen Authentifizierungsprotokolls, das speziell für Smartphones entwickelt wurde. Der Schwerpunkt liegt auf der Optimierung der einfachen Platzierung des Smartphones während der musterbasierten Authentifizierung, um eine nahtlose und effiziente Benutzererfahrung zu gewährleisten. Dies beinhaltet die Entwicklung eines einschichtigen Etiketts, das vollständig aus Polydimethylsiloxan (PDMS) besteht und mit abwärtskonvertierenden DS Partikeln, in seinem gesamten Volumen verteilt und eine ML-Anordnung umgeben von Mikrostrukturen auf seiner Oberseite integriert. Der Authentifizierungsprozess nutzt die Taschenlampe des Smartphones als Anregungsquelle und die Kamera zur Bildaufnahme, wobei optische Filter sicherstellen, dass nur die Emission der Phosphorpartikel erfasst wird. Für den effizienten Vergleich und die Authentifizierung der einzigartigen Leuchtmuster wird ein vereinfachtes binäres Zeichenkettenkodierungsverfahren eingesetzt. Mit einer Positionierungstoleranz des Smartphones von 1cm wird eine hohe Authentifizierungsgenauigkeit von $>99\%$ erreicht. Darüber hinaus wird die Authentifizierung des PUL bei unterschiedlichen Abständen zwischen Blitz und Kamera von bis zu 3cm erfolgreich durchgeführt - ein Bereich, der von allen Smartphones eingehalten wird und, wodurch die universelle Kompatibilität der Etiketten gewährleistet ist. Die biegsame Oberfläche des einlagigen Voll-PDMS-Etiketts passt sich auch gekrümmten Produktoberflächen an, was eine einfache Validierung seiner nicht klonbaren Eigenschaften mit einem Smartphone ermöglicht. Darüber hinaus ist das Etikett auch bei hohen Temperaturen und nach einer Langzeitlagerung von sechs Monaten stabil.

Diese Ergebnisse belegen, dass PULs auf der Grundlage von ML-Arrays und Phosphorpartikeln eine vielversprechende Lösung für den Kampf gegen Fälschungen sind. Die Vorteile der Etiketten, einschließlich ihrer einfachen Anwendung und ihrer robusten Sicherheitsmerkmale, machen sie zu einer attraktiven Wahl für den Schutz von Produkten vor Fälschungen. Diese Forschungsarbeit bildet die Grundlage für die Weiterentwicklung der nächsten Generation von Fälschungsschutzetiketten, die eine verbesserte optische Leistung, eine einfache Anwendung und eine kosteneffiziente Produktion für den Einsatz in großem Maßstab bieten.

Abstract

Counterfeit products pose significant risks to public health, safety, and intellectual property on a global scale, making them a critical issue that requires urgent attention and innovative solutions. Physical unclonable labels (PULs) offer a promising solution for combating counterfeiting, although they often require specialized equipment for authentication. My PhD thesis presents a novel PUL concept utilizing a microlens (ML) array and phosphor particles, designed for smartphone-based authentication.

The initial PUL design in my PhD work features a ML array laminated onto a luminescent-microparticle-doped polymer film, facilitating microscopic particle distributions to be made visible on a macroscopic scale. Gadolinium oxysulfide doped with ytterbium and erbium trivalent ions is used as UC dopant particles in the PUL design. The random distribution of these particles within the polymer matrix, combined with the focusing effect of the ML array having focal length, $f = 1900\mu\text{m}$, generates unique and unclonable luminescent patterns. To examine these PUL features, a 980nm excitation laser is used, generating unclonable patterns in the visible emission range. The angle of incidence (AOI) affects the observed pattern, making the labels unclonable. For these initial PUL, an AOI tolerance – reflecting the allowable deviation in AOI for accurate pattern authentication – is 0.2° , with an estimated probability of false positive at 10^{-15} . While the authentication robustness is sufficiently strong to resist counterfeiting, the sensitivity of this initial PUL design to AOI posed a challenge for real-world applications.

To address this limitation, a subsequent study explores the impact of particle size and ML focal length on the label's tolerance to AOI variations. In this study, Cerium (Ce^{3+})-doped yttrium aluminum garnet (YAG) downshifting (DS) particles are used as dopant in the PUL. By increasing the average particle size from $(9 \pm 1) \mu\text{m}$ to $(32.5 \pm 2) \mu\text{m}$ and utilizing ML with $f = 550\mu\text{m}$, the AOI tolerance improves significantly from 0.8° to 3.6° , resulting in an 18-fold enhancement compared to the initial PUL design. This improvement substantially increases the label's robustness and practical applicability while preserving its security standard. Additionally, the engineered PUL design utilizes an incoherent light source (a 450nm light emitting diode, LED) and enabled authentication using a smartphone camera directed at the back surface of the label, thus simplifying the hardware requirement for PUL validation.

Building upon these findings, the final phase of my PhD research focuses on developing a user-friendly authentication protocol specifically designed for smartphones. The focus is on optimizing the ease of smartphone placement during pattern-based authentication, ensuring a seamless and efficient user experience. This involves developing a single-layer all-polydimethylsiloxane (PDMS) label consisting of DS particles dispersed throughout its volume, with a ML array surrounded by micro-scattering texture forming a scattering surface on its top surface. The authentication process involves using a smartphone's flashlight as an excitation source and its camera for image capture, with optical filters ensuring that only the emission from the phosphor particles is detected. A simplified binary string encoding scheme is implemented to represent the unique luminescent patterns, enabling efficient comparison and authentication. High authentication accuracy >99% is achieved with a smartphone positioning tolerance of 1cm. Additionally, PUL authentication is successfully achieved with varied distances between the flash and camera, up to 3cm, a range within which all smartphones operate, ensuring universal compatibility with our labels. Moreover, the flexible surface of single-layer all-PDMS label enables conformal application to curved product surfaces, facilitating easy validation of its unclonable features with a smartphone, and has shown stability under elevated temperatures and long-term storage conditions over a six-month period.

These findings establish that the ML array and phosphor based PUL represents a promising anti-counterfeiting solution. The label's advantages, including ease of use and robust security features, position it as an attractive choice for protecting products from counterfeiting. This research lays the groundwork for the advancement of next-generation anti-counterfeiting labels that offer enhanced optical performance, user accessibility and cost-effective production for large-scale implementation.

Table of contents

1	Introduction	1
1.1	Motivation	1
1.2	Anti-counterfeiting	3
1.3	Research objective	6
1.4	Layout of the thesis	7
2	Background	10
2.1	Physical unclonable labels	10
2.1.1	Properties of PULs	10
2.1.2	Different applications	11
2.2	State of the art.....	12
2.2.1	Speckle-based PULs	14
2.2.2	Luminescence-based PULs	15
2.2.3	Surface features based PULs	16
2.3	Smartphone as a transformative tool in the laboratory	18
2.3.1	CMOS-based camera sensor of a smartphone.....	18
2.3.2	Comparative study of smartphone-based authentication of existing unclonable anti-counterfeiting labels	21
2.4	Choice of luminescent materials for unclonable security	23
2.5	Luminescence mechanism in lanthanides-doped phosphor materials	25
2.6	Optics of ML arrays	30
2.6.1	ML as an illumination element.....	30
2.6.2	ML as a collection element.....	33
2.7	A review of ML arrays fabrication methods	33
2.8	Fundamental study of the TPL	36
2.8.1	Fundamental theory of 2PP	36
2.9	Summary	37
3	Methodology	38
3.1	Modelling a ML in COMSOL.....	38
3.2	ML fabrication using the TPL.....	39
3.2.1	Sample preparation steps	39
3.2.2	Print parameters selection	40

3.3	Two layered PUL using a ML array and phosphor doped PDMS layer	44
3.4	Fabrication procedure of DS phosphor doped unclonable labels	46
3.5	Manufacture of single-layered all-PDMS unclonable label	48
3.6	Characterization techniques	49
3.6.1	Scanning electron microscopy (SEM)	50
3.6.2	Morphology analysis of luminescent phosphors	50
3.6.3	Morphology Analysis of ML arrays	51
3.7	Diffuse reflectance	53
3.8	Steady-state PL spectroscopy	56
3.8.1	PL excitation and emission spectra	56
3.9	Experimental protocol	58
3.9.1	Coherent source	59
3.9.2	Non-coherent source	60
3.10	CMOS-based camera sensors and calibration procedure	62
3.10.1	Smartphones camera calibration: Exploring the exposure triangle	63
3.10.2	Optimizing smartphone camera settings for enhanced image quality	64
3.11	Schematic: Design understanding of an unclonable label for front-side illumination and front side detection	65
3.12	Schematic of single smartphone authentication setup for verifying the unclonable label	67
3.13	Summary	68

4 ML arrays and luminescent phosphor based physical unclonable anti-counterfeiting labels 69

4.1	Introduction	69
4.2	Label design and working principle	70
4.3	Consistency of the PUL's point-patterns across camera placements	73
4.4	Overview of Perspective and affine transformation	74
4.5	Qualitative characterization of the labels	77
4.5.1	Reproducibility of a bright point-pattern	79
4.5.2	Multiple Patterns from a Single Unclonable Label	79
4.5.3	Uniqueness of each Label	80
4.6	Quantitative analysis of the labels	80
4.6.1	Image processing algorithm	80
4.6.2	Steps for generating a threshold number of votes	83

4.7	Label authentication as a function of AOI	87
4.8	Design assessment of the unclonable label	89
4.8.1	Figure of merits	89
4.8.2	Challenges	90
4.9	Summary	93

5 Expanding the AOI tolerance of the unclonable anti-counterfeiting label's design 94

5.1	Introduction	95
5.2	Design and working principle of the unclonable label.....	97
5.3	Experiment using an LED excitation and CMOS-based camera detector ..	98
5.4	Qualitative analysis: AOI tolerance of PUL against phosphor particle size	99
5.5	Statistical interpretation of the randomness of the point-patterns.....	102
5.6	Quantitative analysis of the labels with different size phosphor particles .	104
5.6.1	Generating a threshold number of votes for label authentication	104
5.6.2	Quantitative analysis of the AOI tolerance with phosphor particle size	107
5.7	Understanding the particle size range for validating a linear relation of AOI tolerance	108
5.8	Label demonstration using an LED and smartphone camera.....	111
5.9	Labels with widely spaced ML arrays and scattering surface.....	113
5.9.1	Qualitative analysis of labels including widely spaced ML arrays and scattering surface.....	116
5.9.2	Quantitative analysis of labels including widely spaced ML arrays and scattering surface.....	117
5.9.3	Label authentication using a single smartphone	120
5.10	Merits of the label design	122
5.10.1	High AOI tolerance for label authentication	122
5.10.2	Low-cost authentication setup	122
5.10.3	Application in anti-counterfeiting.....	123
5.10.4	Smartphone-based authentication	124
5.11	Challenges of the label design	124
5.11.1	Application-oriented challenge.....	124
5.11.2	Authentication oriented challenges	126
5.11.3	Label stability with aging	127
5.12	Summary	129

6 Designing an unclonable label for authentication using a smartphone.....130

6.1	Introduction	130
6.2	Label design and working principle	131
6.2.1	Experiment using a smartphone	132
6.2.2	Simulation theory for the 2D distribution of emission profile from a bright particle over a ML.....	135
6.3	Label authentication algorithm.....	137
6.3.1	Transforming the bright pattern into an artificial binary pattern	138
6.3.2	Logic for the similarity comparison of a test-reference image pair	138
6.4	Qualitative Analysis: AOI Tolerance of the labels	140
6.4.1	Two layered PUL	140
6.4.2	Single layered all PDMS PUL	142
6.5	Statistical interpretation of randomness of the labels	143
6.6	Quantitative comparison of the labels	144
6.7	Classifying the tolerance of point-pattern robustness against smartphone position.....	148
6.8	Classifying the tolerance behavior of pattern robustness under variable LED – camera distance	152
6.9	Analyzing the vertical placement tolerance of a single smartphone for authentication of a given label.....	155
6.10	Label's optical performance analysis under constant solar illumination at elevated temperature	157
6.11	Conformal application of flexible label to curved surface.....	159
6.12	Summary	160

7 Conclusion.....162

7.1	Prototype design of PULs using ML arrays and a UC phosphor doped PDMS layer	162
7.2	Optimizing the PUL design for enhanced AOI tolerance	163
7.3	Advanced PUL design for smartphone-compatible authentication	164
7.4	Outlook.....	165

8 References168

Acknowledgments

I would like to express my sincere gratitude to Professor Bryce S. Richards for providing me with the opportunity to pursue my PhD in the 'Nanophotonics for Energy (N4E)' group at the Institute of Microstructure Technology (IMT), at KIT through a DAAD scholarship. I am deeply grateful for his mentorship, which has included insightful feedback, constructive criticism, and unwavering support throughout my research. I am sincerely thankful to my immediate supervisor, Dr. Ian Howard (advanced materials and optical spectroscopy group), for his continuous support, guidance, and invaluable supervision. His expertise, creativity, and understanding, along with his encouragement to explore new ideas, have refined my thinking and greatly improved the quality of my research.

A special thanks to Dr. Stephan Dottermusch, whose creative problem-solving and calm character provided me with multi-faceted solutions. I gained significant visions from his creativity and practical experience with optics and various characterization skills. Sharing my office space with him and Dr. Deski Beri at IMT was both educational and enjoyable.

I also express my gratitude to my colleagues Dr. Ngei Katumo and Mr. Fabrizio Gota, at IMT for their creative contributions to my PhD project, and for sharing cheerful moments outside the labs. Thanks to Dr. Dmitry Busko and Dr. Damien Hudry for ensuring the smooth operation of optics and chemistry labs as well as for providing insightful training on different instruments and laboratory setups. Special thanks to Dr. Arun Jaiswal and Mr. Ashutosh Singh, KIT for the wonderful time we spent together in Karlsruhe city during my PhD work.

This work was made possible by the financial support of the German Academic Exchange Service (DAAD) through their Ph.D. scholarship program. Additionally, I am grateful to the KIT International affairs office for awarding me the DAAD STIBET Scholarships during my doctoral studies. These scholarships not only provided essential financial support but also facilitated opportunities to extend my knowledge and visibility in optics and photonics beyond my core research.

I am also thankful for the support and guidance from new colleagues who welcomed me and aided my adaptation to the PhD environment, including initial training on

instruments and introduction to research life. My gratitude extends to Dr. Andrey Tushartov, Dr. Guojun Gao, Dr. Reetu Elza Joseph, Dr. Roman Lyubimenko, Dr. Aditya Chauhan, Dr. Gan Huang, Dr. Ida Humbert, Dr. Tuhin Samanta, Dr. Bharat Sharma, Dr. Stephan Hengsbach, Dr. Milian Kaiser, Dr. Ritzer David, Natalia Kiseleva, Jan Fischer, Julie Roger, Roja Singh, Fernando Arteaga-Cardona, Dr. Aiman Roslizer, Dr. Nils Rosemann, Dr. Eduard Madirov, Achim Voigt, Smile Kataria and all N4E group colleagues. Your encouragement, insights and companionship were invaluable. Special appreciation to Ngei and Jan for their help in proofreading my thesis.

I extend my gratitude to the entire IMT staff for fostering a productive research environment and providing assistance as needed. My sincere thanks to Alexandra Moritz and Dr. Markus Guttman for their valuable contributions to the design and fabrication of my anti-counterfeiting label's metallic molds. I also appreciate the support from the International Student Office (IStO) at KIT during my stay. Additionally, I am grateful to Siegfried Roth, Hartmut Speck and Oliver Kaas (International affairs office, KIT) for their valuable advice and guidance on administrative matters.

Above all, my deepest gratitude goes to my family, especially my parents and brothers Dr. Subhash Kumar, Vikash, Vikram and Vimal Kumar, for their constant encouragement and support. I am forever grateful and dedicate this work to you. I am also eternally grateful to my beloved wife, Divya Barnwal (BiwiMeri), and my son, Divyan Shresth (Shivu). Your unwavering love, support and sacrifices have been the driving force behind the final phase of my academic journey while writing my PhD thesis.

List of publications

Patent:

1. Howard, I.A., Dottermusch, S., Richards, B. S., **Kumar V.** (2024). Label and system for verifying the authenticity of items and method for verifying authenticity of items, US patent application publication, Pub. No. US2024/0386447 A1, Appl. No. 18/569,761, Pub. Date: Nov. 21, 2024.

First author publications:

2. **Kumar, V.**, Dottermusch, S., Katumo, N., Chauhan, A., Richards, B. S. & Howard, I. A. (2022). Unclonable anti-counterfeiting labels based on microlens arrays and luminescent microparticles. *Advanced Optical Materials*, 10, 2102402.
3. **Kumar, V.**, Dottermusch, S., Chauhan, A., Richards, B. S. & Howard, I. A. (2022). Expanding the angle of incidence tolerance of unclonable anticounterfeiting labels based on microlens arrays and luminescent microparticles. *Advanced Photonics Research*, 3, 2100202.
4. **Kumar, V.**, Gota, F., Neyret, J., Katumo, N., Chauhan, A., Dottermusch, S., Richards, B. S. & Howard, I. A (2023). Smartphone authentication of unclonable anticounterfeiting labels based on a microlens array atop a microphosphor-doped layer. *Advanced Materials Technologies*, 2201311.

Co-authored publications:

5. Katumo, N., Ruiz-Preciado, L. A., **Kumar, V.**, Hernandez-Sosa, G., Richards, B. S. & Howard, I. A. (2021). Anticounterfeiting labels with smartphone-readable dynamic luminescent patterns based on tailored persistent lifetimes in $\text{Gd}_2\text{O}_3\text{:Eu}^{3+}/\text{Ti}^{4+}$. *Advanced Materials Technologies*, 6(7), 2100047.
6. Woidasky, J., Sander, I., Schau, A., Moesslein, J., Wendler, P., Wacker, D., Gao, G., Kirchenbauer, D., **Kumar, V.**, Busko, D., Howard, I. A., Richards, B. S., Turshatov, A., Wiethoff, S., Lang-Koetz, C. (2020). Inorganic fluorescent

marker materials for identification of post-consumer plastic recycling. *Resources, Conservation and Recycling*, 161, 104976.

Conference contribution:

7. **Kumar, V.**, Dottermusch, S., Chauhan, A., Katumo, N., Richards, B. S. & Howard, I. A. Unclonable anti-counterfeiting based on randomly distributed microphosphor particles under a microlens arrays, *Conferences Internationales Materiaux Et Technologies (CIMTEC)*, 9th forum on new materials, 25 – 29 June 2022, Perugia, Italy (Oral presentation).

1 Introduction

1.1 Motivation

In an era characterized by rapid technological advancements and increasing global interconnectedness, the issue of authenticity assumes significant importance across various industries. The growth of counterfeit products and unauthorized duplications has become a substantial challenge.^{1,10} According to the organisation for economic co-operation and development (OECD) and the European union intellectual property office (EUIPO), the estimated value of counterfeit goods traded globally reached approximately USD 464 billion in 2023, a staggering figure compared to the total value of international trade, which was around USD 17.9 trillion.¹¹ Approximately 5% of the merchandise imported into the European union consists of counterfeit items.¹¹ In 2020, the clothing industry experienced a significant financial setback, with annual sales losses due to counterfeiting activities reaching 26.3 billion euros.¹² The monetary value allocated to counterfeit cosmetics and personal care goods amounted to 4.7 billion euros.¹³ Counterfeiting not only imposes substantial financial losses on industries, but also jeopardizes consumer safety and breaches trust.¹⁴ To tackle this problem, robust and fool-proof strategies must be introduced, encouraging the development of new solutions that transcend conventional methods.

The underlying motivation for this research stems from the necessity to address the issue of counterfeiting, which poses a significant threat across various domains. Counterfeit products endanger both brand integrity and public health, encompassing a wide range of items, including luxury goods and crucial drugs.¹⁵ Traditional authentication methods, such as holograms and barcodes were once considered secure.^{16,17} However, they are now vulnerable to advanced counterfeiting techniques that exploit technological progress.¹⁸ In this context, there is an urgent demand for innovative and highly secure anti-counterfeiting systems that can effectively counter the ingenuity of modern counterfeiters.

The conventional methods of authentication for anti-counterfeiting, such as holographic labels¹⁹, security inks²⁰ and barcodes¹⁷ depend on physical attributes and security measures.²¹ While these methods have demonstrated a certain level of effectiveness, they are becoming more susceptible to duplication by highly skilled

counterfeiters using advanced technologies. Recently, there has been a notable shift in the field of authentication towards the integration of cutting-edge technologies, including blockchain, RFID (radio-frequency identification), and NFC (near-field communication).²²⁻²⁴ These technologies enable real-time tracking and verification of products, allowing customers and authorities to authenticate product legitimacy instantaneously using mobile applications or internet databases. The use of machine learning algorithms and artificial intelligence (AI)-based image recognition techniques has provided corporations with enhanced capabilities to identify counterfeit products with greater precision and effectiveness.²⁵ In a rapidly evolving landscape, the integration of digital and physical authentication methodologies presents itself as a potentially valuable strategy to mitigate the global distribution of counterfeit products. This convergence promises to provide customers and businesses with enhanced security measures and a renewed sense of confidence in product integrity.

However, counterfeiters continually adapt to new technologies, and even covert solutions can be replicated if they become visible with the right tools. This necessitates a shift towards solutions that are inherently unique, difficult to replicate, and fundamentally rooted in the principles of physics. Physical unclonable labels (PULs) have emerged as a cutting-edge strategy to combat counterfeiting. PULs harness the complexity inherent in physical systems to generate unique identifiers that are virtually impossible to duplicate.^{26,27} Unlike digital encryption, which relies on secret keys, PULs exploit physical variations that naturally occur during manufacturing processes. These variations manifest as minute discrepancies in physical components that, when probed, yield distinct responses. The resulting distinctive and unpredictable response serves as an unclonable identifier. PULs have attracted significant attention due to their inherent security features, as they do not require storage of secret keys, making them resistant to traditional attacks such as hacking and reverse engineering. Additionally, PULs are particularly appealing for resource-constrained applications due to their lack of reliance on additional hardware components. Consequently, PULs represent a robust, scalable, and cost-effective solution to the growing counterfeiting problem.

These unique identification solutions leverage the inherent complexity of physical systems to create virtually unreplicable identifiers. Security labels based on physically unclonable challenges often comprise a physical form of labelling, such as a microchip integrated into either the product itself or its packaging.²⁸ These labels provide

essential capabilities to generate a unique digital fingerprint for individual label, which can be securely maintained within a database. The verification of this fingerprint can be conveniently conducted through the utilization of specialized readers or smartphone applications, offering instantaneous validation of product genuineness.²⁹ PULs have found widespread application in various industries, particularly in pharmaceutical and electronics sectors.^{30,31} The electronics industry utilizes PULs to mitigate the risks associated with counterfeit electronic components, safeguarding the integrity of critical systems and preventing potential hazards. Moreover, the deployment of PULs is increasingly observed in high-end consumer goods, luxury items, and even food products, where maintaining brand authenticity and ensuring consumer safety are paramount. These labels provide a robust defence against counterfeit products, playing a vital role in safeguarding brand reputation and promoting customer trust in today's dynamic marketplace. By exploring the principles of quantum mechanics, nanotechnology, and micro-optics, PULs offer a formidable defence against counterfeiting and unauthorized duplication. Researchers have utilized various optical materials for anti-counterfeiting applications, including metal-organic frameworks (MOFs)³², carbon dots (CDs)³³, quantum dots (QDs)³⁴, perovskite nanocrystals³⁵, plasmonic nanoparticles³⁶, self-wrinkling materials and polymer dots^{37,38}.

My Ph.D. research work explores a novel approach that integrates microlens array (ML arrays) and photoluminescent (PL) materials to create PULs.² ML arrays, composed of an array of miniature lenses, manipulate incident light in intricate ways onto the particles layer. This results in the creation of bright point-patterns that are inherently difficult to reproduce.² This combination of factors presents a unique strategy for developing anti-counterfeiting labels, enhancing their effectiveness and posing unclonable challenges for counterfeiters attempting to mimic or replicate these security measures.

1.2 Anti-counterfeiting

Counterfeiting is the act of making copycat items with the goal of tricking buyers into believing they are acquiring genuine goods and has emerged as a global threat.³⁹ Counterfeiters exploits technological advancements to create increasingly convincing replicas of authentic products. During the COVID-19 pandemic, the proliferation of counterfeit drugs and medical supplies posed a significant threat with serious implications for human health and well-being.⁴⁰ Fake medicines often lack essential

ingredients necessary for efficacy, rendering them not only ineffective but also potentially harmful. Consequently, the use of counterfeit pharmaceuticals can lead to negative consequences such as the worsening of clinical symptoms, increased transmission rates of the virus, and, tragically, mortality due to delayed or inappropriate medical interventions. Similarly, counterfeit masks, while purported to offer protection, fail to provide the requisite filtering efficiency, thereby increasing the risk of virus transmission.⁴¹ These complex issues underscore the urgent need for stringent measures to combat counterfeiting and maintain the integrity of medicinal supplies, thereby safeguarding public health and welfare in the context of the COVID-19 pandemic.

Counterfeit products span a diverse range of industries, including consumer goods, electronics, luxury items, automotive parts, pharmaceuticals, and even critical aerospace components.^{42,43} These illicit replicas pose not only economic challenges but also serious risks to public health, national security, and intellectual property rights. Counterfeiters continuously adapt and refine their techniques, making their imitation products increasingly difficult to distinguish from genuine ones. Therefore, the demand for novel and robust solutions is urgent, driving the exploration of cutting-edge technologies grounded in the physical properties of materials.

PULs present an innovative approach to tackling counterfeiting by exploiting the natural variability in physical systems. These responses serve as cryptographic keys or identifiers, forming the basis of robust authentication systems. Even the smallest differences in manufacturing conditions, imperfections, and intrinsic material properties result in unique PUL responses. Consequently, attempts to clone or replicate these responses become ineffective. This intrinsic uniqueness sets PULs apart from traditional security strategies, making them ideal for protecting goods from the risks of counterfeiting.

One promising application of PULs technology is the creation of anti-counterfeiting labels, which serve as a physical fingerprint for products.¹ These labels, integrated directly onto products or their packaging, are designed to possess distinctive and unpredictable features that are exceptionally difficult to reproduce. Unclonable labels offer a practical and effective means of authentication, enabling consumers, manufacturers, and regulatory authorities to verify the authenticity of a product with absolute assurance. Figure 1.1 illustrates a comprehensive anti-counterfeiting strategy

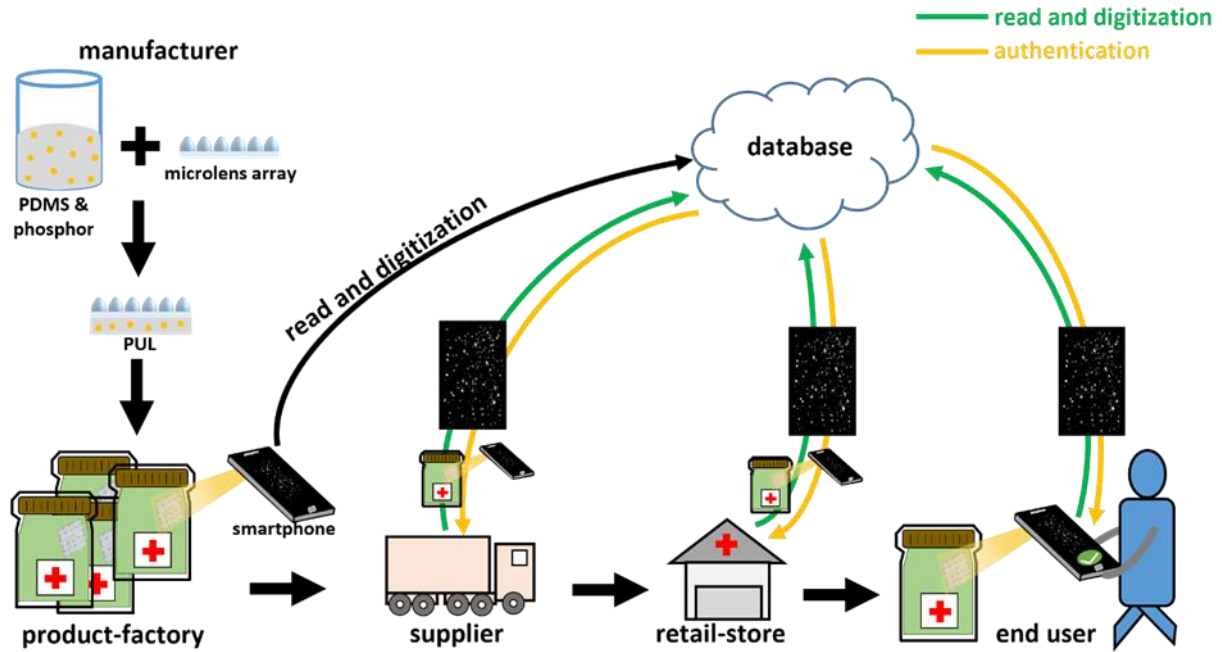


Figure 1.1 Illustration of the process for creating and applying physical unclonable labels (PULs) for the verification of products within a supply chain. This diagram demonstrates the straightforward and rapid authentication method using a smartphone's flashlight and camera across various stages of product distribution. This approach mirrors the anti-counterfeiting strategy described by Gu et al.¹⁻³

within a supply-chain system, revolving around the integration of PULs to safeguard products.² In Figure 1.1, a schematic example of PUL is presented using the union form of ML arrays and phosphor layer, demonstrated at different stages of the supply-chain. This method provides a robust and efficient method for safeguarding products against counterfeiting, ensuring product authenticity and traceability throughout the supply chain. The labels possess distinctive physical properties that make them extraordinarily challenging to replicate. The diagram shows the application of these labels at different stages of the supply chain, emphasizing their role in product authentication. It demonstrates how a smartphone with a flashlight and camera can be used for authentication: the flashlight illuminates the PULs, and the camera captures their reflection-based patterns. This approach eliminates the need for additional equipment like excitation sources or detectors. Additionally, a digital database is utilized to store encoded product information. Two authentication schemes are presented: in the first, test images (recorded by end-users) are compared against all reference images in the database, in the second, a unique identification code accompanies each label, simplifying the comparison process.²

The development of unclonable label technologies showcases their versatility and transformative potential. Leveraging a diverse array of physical phenomena, including

optical, electrical, and chemical characteristics, these labels exhibit a high degree of adaptability.^{26,28,44} However, the transition of PULs technology from laboratory to market presents formidable challenges. To achieve commercial viability, unclonable labels must reconcile the competing demands of uniqueness, efficient manufacturing, and straightforward verification. Moreover, ensuring cost-effectiveness, scalability, and seamless integration into existing supply chains is crucial. Ultimately, the successful implementation of such labels requires a meticulous approach to design, mitigating the risks of false positives and negatives in authentication processes.

1.3 Research objective

The primary objective of my PhD research is to conceive, fabricate, and comprehensively analyse unclonable labels based on ML arrays and PL materials. These labels exploit the delicate interplay between micro-optics and luminescence, along with a random distribution of phosphor particles in polydimethylsiloxane (PDMS), to produce visually complex and fundamentally distinctive patterns that can be serve as potential verification features. This study aims to enhance the arsenal of anti-counterfeiting technologies by utilizing the specific features of ML arrays and the PL mechanism. The research is guided by the following objectives:

- Design and fabricate unclonable labels that combine the capabilities of ML arrays and phosphor particles.
- Characterize the performance of the unclonable labels under various conditions, including different angles of incidence (AOI), phosphor particles sizes and illumination sources.
- Develop algorithms and methodologies for the authentication of unclonable labels using conventional devices such as digital cameras and smartphones.
- Investigate the scalability and practicality of the proposed unclonable label technology for real-world applications.
- Demonstrate the application of PULs to various products, such as medicine boxes and blister packs, considering the conformal contact with product surface.

This work addresses the critical problem of counterfeiting within supply chain systems by proposing novel concepts for anti-counterfeiting labels. Building on previous investigations, the primary goals are to enhance the security and traceability of products using PULs. The labels integrate ML arrays and phosphor-loaded polymer layer to generate distinct and non-reproducible PL emission patterns. This unique

methodology has practical benefits, including the use of ordinary light-emitting diodes (LEDs) for excitation and the capability to verify labels using a smartphone. The study also examines the tolerance for fluctuations in AOIs and explores the potential applications of these labels in various contexts, such as blister packs and currency authentication. The objective is to make a valuable contribution to the advancement of effective and efficient methods for preventing counterfeiting, ultimately leading to improvements in the reliability and security of supply chain systems and protection against the proliferation of counterfeit goods.

1.4 Layout of the thesis

My PhD thesis is divided into seven chapters, each chapter supports in the investigation, fabrication, and validation of PULs based on the interaction of ML arrays and phosphor particles.

Chapter 2 provides a comprehensive overview of the foundation concepts and technologies underpinning this research. It starts with an overview of PULs, including their properties and applications. The chapter then reviews the state of the art, focusing on speckle-based, luminescence-based, and surface features-based PULs. It also explores the impact of smartphones in laboratories, particularly their complementary metal-oxide semiconductor (CMOS) sensors for authenticating unclonable anti-counterfeiting labels. The discussion continues with the selection of luminescent materials, highlighting lanthanide-based phosphors and their PL properties. Additionally, the chapter covers ML arrays, their optical roles, and fabrication methods, before introducing the fundamentals of two-photon lithography (TPL).

Chapter 3 outlines the experimental methodologies employed in this research. The chapter commences with a computational approach, modelling ML in COMSOL, followed by a detailed description of the fabrication process for ML arrays using direct laser writing (DLW). Subsequently, the fabrication of two distinct types of unclonable labels is presented: a two-layered structure incorporating a ML arrays and micron size phosphor particle, and a single-layered all-PDMS label. The chapter then delves into the characterization techniques used to assess the fabricated structures, including scanning electron microscopy for morphological analysis and steady-state PL spectroscopy for optical properties. To evaluate the performance of the developed labels, experimental protocols using both coherent and non-coherent light sources are

described. Finally, the chapter concludes with a comprehensive explanation of the smartphone-based authentication setup, including camera calibration procedures and the design of the unclonable label for optimal performance. These methodologies form the backbone of the experimental work conducted in this thesis.

Chapter 4 delves into the characterization and assessment of the preliminary design of the unclonable labels based on a ML array and upconversion (UC) phosphor particle doped layer, focusing on their design and working principles. It presents qualitative and quantitative evaluations of PULs, including image processing algorithm. The chapter concludes with a summary of key findings and a thorough assessment of the preliminary design of the label.

Chapter 5 explores the practical implementation and evaluation of the proposed unclonable labels, particularly their use with LEDs and smartphone cameras for authentication. The chapter begins with the tuning of label parameters, e.g. focal length of ML arrays, incorporating the Ce^{3+} -doped yttrium aluminum garnet (YAG) downshift (DS) phosphor particle size, label's thickness etc. Furthermore, the work introduces a simplified experimental setup using a smartphone. Both qualitative and quantitative analysis demonstrate the resilience of the design-tuned labels to variations in the AOI of excitation light, while statistical analysis confirms their randomness and uniqueness. Further, the chapter demonstrates the feasibility of label authentication using a single smartphone for both transmission and reflection-based authentication setups. Finally, it summarizes the pros and cons of the label design, highlighting its low cost, potential anti-counterfeiting applications, durability, and challenges that need addressing for broader adoption.

Chapter 6 delves into the design and implementation of a user-friendly unclonable label authenticated using a smartphone. The label is developed in a single-layer geometry incorporating sparsely distributed ML arrays and scattering microtexture on top, with DS particles are randomly dispersed in bulk volume. This PUL entity generates unique patterns enabling reliable authentication even under variable smartphone placement and LED-camera distance. The chapter presents a robust label authentication algorithm that transforms captured images into binary string IDs for efficient pattern matching. Qualitative and quantitative analyses of the two-layered and single-layered labels demonstrate their exceptional robustness and uniqueness. The label's optical performance under harsh environmental conditions is thoroughly examined, confirming

its stability and resilience. The chapter concludes by demonstrating the application of the novel label for anti-counterfeiting purposes and showcasing the conformal application of flexible labels to curved surfaces, emphasizing the label's versatility.

Chapter 7 presents a summary of my PhD research, which explored innovative approaches to anti-counterfeiting labels using ML arrays and phosphor particles. This chapter combines the key findings, tracing the progression from the initial prototype designs to advanced PUL configurations optimized for smartphone-based authentication. The research demonstrated significant advancements, including improved angular tolerance, enhanced robustness in real-world applications, and practical integration with consumer devices like smartphones. Furthermore, the chapter identifies several promising directions for future work, such as developing multi-phosphor systems to enable diverse authentication signatures, incorporating fiducial markers for faster and more reliable validation, and refining ML arrays designs to improve compatibility with off-axis illumination. These recommendations aim to build upon the foundation established in this work, advancing the technology toward practical, scalable, and secure anti-counterfeiting solutions accessible to a wide range of users.

2 Background

2.1 Physical unclonable labels

PULs have emerged as a revolutionary method for protecting digital and physical systems against counterfeiting and unauthorized access within the realm of security and authentication. The goal of designing and authenticating a PUL should be a label that is easy to read, but nearly impossible to model or physically reproduce. PULs-based anti-counterfeiting labels provide a non-algorithmic one-way function composed of unclonable elements/features.⁴⁵ Each PUL results from a random and stochastic process and poses unique features; therefore, it is even impossible for the manufacturer to reproduce the existing PUL.⁴⁶ The following section outlines the fundamental characteristics of a PUL and provides an exposition on various cutting-edge developments associated with it.

2.1.1 Properties of PULs

PULs represent a deviation from traditional cryptographic methodologies that heavily depend on the use of confidential keys.⁴⁷ Instead, manufacturers utilize the inherent variability and unpredictability present in physical systems during the production process.⁴⁶ The underlying concept of PULs is remarkably straightforward: the uniqueness of physical systems arises from small discrepancies in materials, fabrication processes, or flaws. PULs leverage inherent variations found in natural systems to generate unique and non-reproducible digital fingerprints or identifiers. When subjected to a probe, PULs generate responses that are distinct to the physical system, and this response forms the foundation for ensuring secure authentication. Significantly, PULs exhibit the advantageous characteristic of not being dependent on the storage of secret keys, thereby rendering them resistant to a range of attacks including hacking, reverse engineering, and brute-force attacks.⁴⁶ The key properties that distinguish PULs from conventional security measures are their inherent variability, unpredictability, and resistance to replication.^{45,46,48,49} PULs leverage microscopic differences in physical systems, which can result from:

- Variations in manufacturing conditions
- Material properties
- Minor imperfections

The key properties of the PUL includes:

Unique variability in physical systems:

Each physical system exhibits a unique and inherent variability that cannot be accurately replicated. This uniqueness is intrinsic to the system, making it impossible to reproduce an identical counterpart.

Unpredictable responses:

The responses of PULs are highly unpredictable. Even minor changes in the physical system can lead to significantly dissimilar outcomes, making it challenging to predict how the system will respond under different conditions. The inherent unpredictability of PULs is crucial in preventing counterfeiters from reproducing PUL-based security.

Unclonable nature of PULs:

PULs are unclonable, meaning they pose a significant challenge to replication. Counterfeiters are unable to precisely duplicate the physical characteristics responsible for PUL's responses. The unique and complex nature of these physical attributes makes it impossible to create an exact clone of a PUL, ensuring that the original system remains secure.

Difficulty in counterfeiting the PULs:

Counterfeiters face extreme difficulty in creating fake PULs. This difficulty arises from the inability to replicate the unique and complex nature of the physical attributes underlying PULs.

2.1.2 Different applications

The versatility of PUL-based technology extends across a wide range of applications, with unclonable labelling being one of the most promising in the following areas:

- Authentication and anti-counterfeiting: PULs provide a practical and efficient means of authenticating products, documents, or digital systems. These labels serve as unique, physical fingerprints that can be verified with confidence, making them highly effective in countering counterfeit products and ensuring the integrity of supply chains.⁵⁰

- Secure key generation: PULs are also used for secure key generation in cryptographic applications. The unique responses generated by PULs can be transformed into cryptographic keys, enhancing the security of digital communication and data protection.⁵⁰
- Hardware security: PULs are integrated into hardware components, such as microchips and sensors, to ensure their authenticity and protect against hardware-level attacks.⁵¹
- Identity and access control: PUL-based authentication is employed in access control systems, ensuring that only authorized individuals or devices gain access to secure areas or networks.⁵²
- Secure transactions: PULs play a crucial role in securing financial transactions, preventing fraud, and ensuring the privacy and integrity of digital payments.⁵²

2.2 State of the art

Although early works from the 1980s already discussed random patterns for authentication purposes,⁵³ Pappu *et al.* in 2002 first introduced the term ‘physical one-way function’, which they later defined as an unclonable label. They also presented the initial concept for a physical structure that generates an image-based PUL.⁵⁴ This PUL utilized a plastic film doped with randomly distributed light scatters. When illuminated with a laser beam, the film produces a speckle pattern. The resulting speckle pattern acts as a one-way function of the incident laser properties, the configuration of silica scatters, and the detector position.⁵⁴ Furthermore, the study investigated the connection between physical systems and cryptography; and proposed protocols and applications using the physical one-way function. While the unclonable features of the silica-doped label are impossible to predict, the complexity of the physical system and the authentication setup limited its frequent implementation on small scales. Babu *et al.* (2010) proposed a four-component PUL system for product authentication.⁵⁵ The system used a secure optical tag made of epoxy resin microparticles with a high refractive index coating and stochastically distributed on the product surface. A registration module captured an image of the tag to generate a key-value pair. A verification module utilized a smartphone with add-on optics, while a client-server application facilitates communication with a key database.⁵⁵

The utilization of PUL has received considerable interest due to its capacity to offer unforgeable and distinctive identifiers for products, thereby augmenting security and

traceability in diverse domains.⁴⁸ Recent studies have been primarily directed towards the advancement of novel varieties of PULs as well as enhancing the operational efficacy of pre-existing PULs. Arppe and Sørensen present a comprehensive analysis of chemical methodologies employed in the creation of PULs.⁴⁶ PULs, which are intrinsically present in various materials and devices, exhibit resistance to cloning, rendering them highly suitable for deployment in security-related scenarios. Chemical techniques, such as colloid self-assembly, precipitation, and polymerization, facilitate the formation of distinct patterns in polyurethane foams, thereby providing advantages in terms of adaptability, scalability, and resistance to environmental factors.⁴⁶ Chemical-based PULs exhibit a wide range of potential applications, encompassing product authentication as well as document and data security.⁵⁶ The following section explores different PULs employing engineered nano/microstructures and chemical methodologies to elucidate the underlying stochastic mechanism governing the formation of unclonable anti-counterfeiting labels.

Following this review, an overview of existing PUL contenders is provided in Table 2.1, comparing the unclonability, performance parameters and challenges for anti-counterfeiting applications.

Table 2.1 Comparative study of PUL in anti-counterfeiting applications highlighting unclonability, performance and challenges.

PUL contenders in anti-counterfeiting	Unclonable aspects	PUL performance quantification	Challenges
Silica microparticles in epoxy matrix ⁵⁴	Macroscopic speckle pattern from microparticles scattering	Encoding capacity = 2^{228} ($\sim 10^{69}$). False-positive authentication rate = 10^{-69}	Light source and detector sensitivity (placement & properties) in the PUL validation.
Disordered TiO ₂ hetero nanostructures ⁵⁷	Stochastic TiO ₂ aggregation on MoS ₂ nanoflakes	Encoding capacity = 2^{437} ($\sim 3.55 \times 10^{131}$). False-positive and false negative rate of 7.6×10^{-46} and 3.7×10^{-45} .	Fabrication complexity and dependence on SEM, AFM & Raman Spectroscopy.
Gold (Au) core-shell structured NPs with Raman tags ¹	Disordered Au NPs pattern on a silica/scotch substrate	Encoding capacity = 2^{2500} ($\sim 3.8 \times 10^{752}$) in a (50×50) scan area.	Need for complex setup: Motorized mounting, laser excitation & confocal Raman system.

PUL contenders in anti-counterfeiting	Unclonable aspects	PUL performance quantification	Challenges
Perovskite fluorescent crystals ³⁵	Randomly generated perovskite fingerprint patterns	Encoding capacity = 2^{900000} in a (8×8) pixels scan.	Requires complex setup for PUL validation: fluorescence microscopy and spectrophotometry.
Disordered phosphorescent patterns from organic crystals ⁵⁸	Macroscopic pattern formation via stochastic nucleation of (MoS ₂ +TiO ₂) NPs on PUL's surface.	Encoding capacity = 10^{17} (on a 25µm-scale PUL). False positive & negative rate $\sim 10^{-50}$.	Necessity of a UV excitation and confocal microscopy for PUL's pattern validation.
Nanofracture-enabled Au Nanodisks ⁵⁹	Randomly distributed Au nanodisks grown by 'sketch and peel' lithography on SiO ₂ .	Encoding capacity = 2^{2500} ($\sim 10^{750}$). Inter hamming distance = 0.497 (std. dev. < 0.02). Intra hamming distance ≈ 0 (std dev. < 0.00098).	Requires high magnification (50×) microscopy for the features observation in PUL.

The domain of anti-counterfeiting and secure authentication has witnessed significant progress and expansion in recent years, particularly with the development of PULs. The following section provides a comprehensive review of the current advancements in PULs – based technology, emphasizing three main methodologies and implementations: speckle-based, luminescence-based PULs and surface-features-based PULs. These approaches exploit the intrinsic physical characteristics of materials to enhance security and facilitate product authentication.

2.2.1 Speckle-based PULs

Speckle patterns, generated by the scattering of coherent light, offer high sensitivity to a medium's structure. This property allows for unique and unpredictable responses to challenges, making them ideal for PULs realization.⁵⁴ Speckle-based PULs offer a robust solution for anti-counterfeit applications by leveraging unique, unclonable speckle patterns for verification. Table 2.2 provides a comparative analysis of various speckle based PUL contenders for their potential use as anti-counterfeit labels.

Table 2.2 Comparative study of speckle based PULs in anti-counterfeiting applications highlighting unclonability, performance and challenges.

Speckle-based PULs	Unclonable aspects	PUL performance quantification	Challenges
Bionic PULs on plant tissues ⁶⁰	Stochastic speckle response from molded PDMS/PVA bionic film.	Encoding capacity = 2^{5000} ($\sim 1.41 \times 10^{1505}$). Inter & intra-HD = 0.49 (std. dev. $< 5 \times 10^{-5}$) & 0.02, with false-positive/negative rate $< 10^{-200}$.	Requires coherent source as excitation. Sensitivity of PUL authentication to light source and detector alignment.
PULs based on optical waveguiding and diffusion through a silica fiber ⁶¹	Random speckle generated by scattering and waveguiding due to fiber's structural irregularities.	Encoding capacity = 17^{255} . Inter & intra-HD = 0.49 and 0.09 respectively, with mean variance of 3.7×10^{-4} & 2.3×10^{-4} .	Requires specialized instrumentation for PUL validation (e.g. optical microscope, CCD camera, spectrometer, magnifying lens).
Chaotic metasurface & perovskite QDs based PULs ⁶²	Unique fluorescence-based speckle patterns from perovskite QDs on Aluminum-coated PMMA metasurface.	Encoding capacity = $2^{156,250}$. Inter and intra HD = 0.49 and 0.086, with std. dev. $< 1.6 \times 10^{-6}$ and 1.74×10^{-6} .	

2.2.2 Luminescence-based PULs

Luminescence-based PULs represent a promising security technology that utilizes the distinctive luminescent characteristics of specific materials to generate unclonable identifiers. These materials, such as phosphors², quantum dots⁶², and organic luminophore⁶³ exhibit unique emission properties that make them difficult to replicate. Due to their inherent ability to produce distinct luminescent signatures, luminescence-based PULs have gained significant attention in various security applications, including product anti-counterfeiting¹⁰, secure document authentication⁶⁴ and tamper-evident labeling²¹. Table 2.3 provides a comparative analysis of luminescence based PUL candidates for anti-counterfeit labelling, evaluating their performance and challenges.

Table 2.3 Comparative study of luminescence based PULs in anti-counterfeiting applications highlighting unclonability, performance and challenges.

Luminescence-based PUL	Unclonable aspects	PUL performance quantification	Challenges
Lanthanides (III) doped zeolite taggants in polyvinyl alcohol (PVA) film ⁶⁵	Unique PL patterns from random loading of Ln ³⁺ ions in the zeolite crystal.	Encoding capacity = 6×10^{104} . false-positive rate = 3.6×10^{-96} .	Dependence on specialized optical detectors (confocal microscope, CCD spectrometers) for the PUL validation.
Protein fused silk luminescent microparticles as an edible PUL ⁶⁶	Unique fluorescent images from stochastic distribution of silk microparticles in a white silk film.	Encoding capacity = 2^{120} . Probability of false-positive & negative rate = 9.64×10^{-13} and 3.1×10^{-12} .	Increased forgery risk due to single PL pattern per PUL. Requires specific optical setup for PUL validation (filter-based CCD, wavelength-selective LEDs).
PUL based on multicolour light mixing using microscale concave interface ⁶⁷	Colourful patterns generation dependent on dye dispersion in inkjet-printed microcavities.	High authentication accuracy (> 90%) of the PUL. Zero false-positive rate (under threshold 0.9).	Dependence on specific optical setup: UV radiation, inverted microscopy with a 20× magnifying lens and a CCD camera.

2.2.3 Surface features based PULs

Surface features based PULs rely on the physical characteristics of a surface, such as microscale or nanoscale features, for security and authentication purposes. These features may include irregularities, texture patterns, or surface imperfections which are inherently difficult to replicate accurately. Due to their unique natures, surface features based PULs find applications in diverse areas such as product authentication, secure packaging, and access control. However, successful implementation necessitates careful consideration of the manufacturing processes employed and their potential to introduce variations in the surface characteristics. Surface features based PUL contenders are comparatively assessed in Table 2.4 for anti-counterfeit application, with quantitative performance parameters and associated challenges presented.

Table 2.4 Comparative study of surface features based PULs in anti-counterfeiting applications highlighting unclonability, performance and challenges.

Surface-features based PUL	Unclonable aspects	PUL performance quantification	Challenges
PUL based on unique surface roughness ⁶⁸	Diffuse scattering pattern resulting from intrinsic surface roughness of a non-reflective sample.	Angular (2-6%), linear (10-15%) deviation in diffuse intensity pattern with 10^{-20} false-positive rate using matt-finish plastic cards.	Dependency on specialized laser illumination and read-out equipment for the PUL validation. Necessitates careful maintenance to ensure PUL functionality.
PUL based on surface wrinkle micropattern of silica-coated alkoxy silane particles co-doped with rhodamine-B ⁶⁹	Drying-induced stochastic wrinkles on silane microparticles coated with inelastic silica film.	Encoding capacity = 10^{135} . Intra and inter HD = 0.16 and 0.66, with std. deviation of 3.9×10^{-2} and 9.2×10^{-2} .	Necessity of confocal or portable microscopy for the PUL feature validation.
PUL based on dewetting instabilities in polymer thin film ⁷⁰	Unique surface topologies created by random assembly of gold NPs via stochastic dewetting.	Encoding capacity = 2^{256} . high inter-PUL heterogeneity (HD= 0.47) & negligible intra-PUL variation (HD \approx 0).	Requires complex instrumentation (SEM, AFM and Raman spectrometer) for PUL feature authentication.

While PUL-based security offers unprecedented counterfeit resistance, their practical application is hindered by complex fabrication and verification processes. Most PULs necessitate sophisticated equipment, including wavelength-selective filters, microscopy, specialized light sources, spectrometers, and motorized mechanical mounts for PULs authentication. These stringent requirements pose significant challenges for widespread adoption within supply chains, where end-consumers need to easily verify product authenticity.¹ To address the limitations of current PUL-based label authentication processes, my PhD research emphasizes a paradigm shift towards simplified verification method. Leveraging the widespread adoption of

smartphones, a practical and accessible authentication system can be developed.⁷¹ By integrating smartphone capabilities, the commercial viability of unclonable labels can be enhanced while ensuring robust security against counterfeiting.^{72,73} The following section explores the transformative role of smartphones in laboratory settings, specifically focusing on the capabilities of their CMOS-based camera sensors. A comprehensive review of existing smartphone-based unclonable label systems is presented, encompassing the underlying unclonable aspects, quantitative metric for PUL security assessment, and authentication methodologies leveraging smartphone camera technology.

2.3 Smartphone as a transformative tool in the laboratory

Smartphones, ubiquitous gadgets in contemporary society, have emerged as transformative tools in scientific research.^{74,75} Their powerful hardware and software capabilities have empowered researchers to undertake innovative studies previously deemed unattainable.^{76,77} The convergence of advanced sensors, high-performance processors and connectivity options within smartphones has boosted advancements across a broad spectrum of scientific disciplines. From climate monitoring to biomedical diagnostics, precision thermometry, anti-counterfeiting measures, radiation detection, and data-intensive analysis, smartphones have demonstrated their potential to revolutionize research practices.⁷⁸⁻⁸³ These advancements demonstrate the smartphone's potential to democratize scientific research, making it more accessible to a wider audience. By replacing bulky equipment with a compact smartphone, researchers can streamline laboratory processes, reduce costs and accelerate timelines while ensuring global reach to cutting-edge research.^{84,85}

2.3.1 CMOS-based camera sensor of a smartphone

The smartphone camera, which is based on a CMOS sensor, is utilized in this thesis to detect the emissions-based point pattern from the unclonable labels. This process is utilized for customized applications in the field of anti-counterfeiting. An incoming photon is captured by the CMOS sensor of the smartphone camera, which then uses the photoelectric effect to transform the photons into electrons.⁸⁶⁻⁸⁸ In the subsequent step, the electrons are transformed into a voltage, which is then used to derive a pixel value.⁸⁶

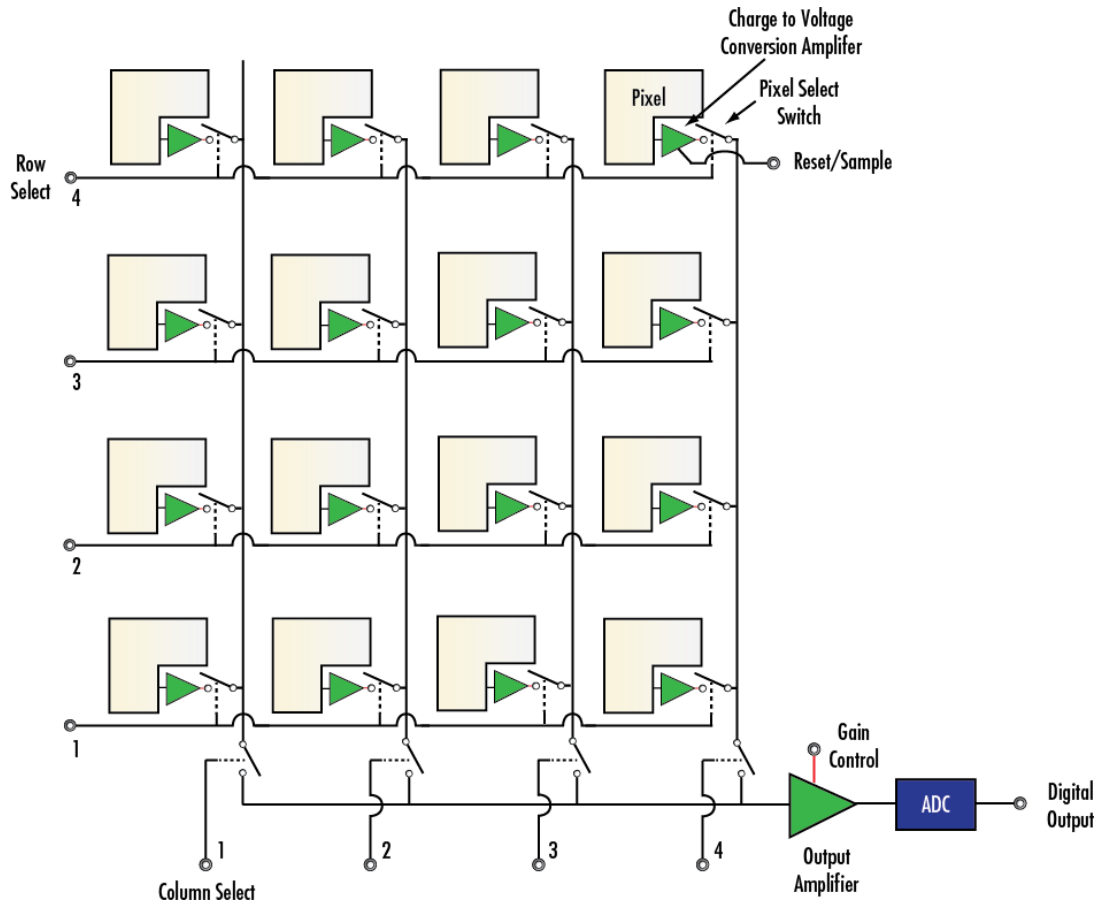


Figure 2.1 Schematic representation of a complementary metal oxide semiconductor (CMOS) based camera sensor. The Figure is adapted from Edmund optics.⁴

Figure 2.1 presents a schematic representation of a standard CMOS sensor that is used in smartphone cameras.^{4,89} A CMOS sensor incorporates an array of photosensitive elements, referred to as pixels. Each pixel includes a ML designed to focus incident light onto an underlying photodiode pair.^{86,89} These photodiodes serve as light detectors, converting incoming photons into electrical charge carriers.

Following the generation of photocarriers, the accumulated charge is converted into a voltage signal through specialized circuitry.⁸⁹ This voltage signal, which encodes the captured image information, is subsequently amplified to enhance its detectability. The amplified signal is then discretized into a digital format using analog-to-digital converters (ADCs), enabling further computational processing.⁸⁹ The CMOS sensor architecture integrates the functions of ML, photodiodes, amplification stages and ADCs, facilitating the conversion of optical input into a digital image representation.^{4,89} To synchronize image acquisition, a global or rolling shutter mechanism may be employed, operating in conjunction with pixel-level multiplexing.

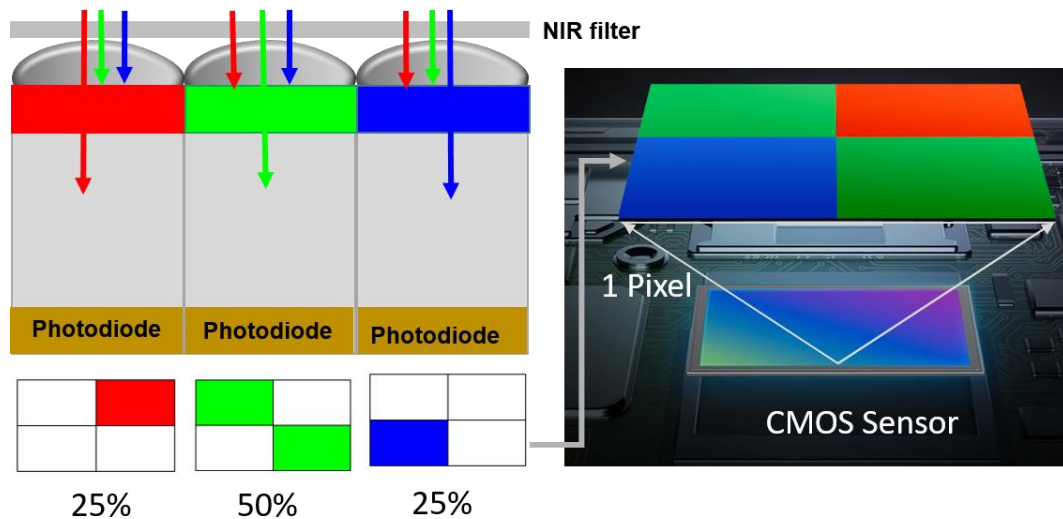


Figure 2.2. A simplified arrangement of the Bayer filter array placed on the photosites of a CMOS camera sensor, enabling the device to capture colour information. The array thoroughly distributes green (50%), blue (25%), and red (25%) photosites, ensuring comprehensive colour representation. To exclude unwanted NIR radiation, a NIR filter is strategically placed in front of the ML. This simplified representation omits the optical focusing effect of the ML.⁹

The CMOS image sensor, a core of smartphone cameras, excels in capturing vibrant and lifelike imagery.^{86,89} This capability is a result from an optimized design that integrates layered filters atop the CMOS photosites.^{9,88,89} Figure 2.2 presents a schematic representation of the Bayer filter array, which is positioned on the photosites of a CMOS camera sensor to capture colour information. An initial NIR (near-infrared) filter blocks wavelengths beyond the visible spectrum to each photosite. This prevents the capture of light imperceptible to the human eye and minimize image noise.⁹ While standard smartphone cameras are optimized for visible light through NIR filtering, modifications can enable NIR detection. This functionality is crucial for authenticating security labels embedded with NIR-emitting PL materials, which remain invisible to the naked eye.^{9,89} By harnessing the modified camera's NIR sensitivity, covert authentication becomes feasible without compromising the security of the label.

The next filtering layer in the CMOS sensor utilizes a Bayer filter array superimposed on the photosites. This array assigns each photosite sensitivity to one of the three colour: red, green or blue.^{4,9} The combination of NIR filtering and colour-dedicated photosites enables the CMOS camera sensor to capture realistic and visually appealing images that closely resemble human vision.^{4,9} To mimic human visual perception, green photosites are doubled relative to red and blue counterparts, enhancing green light sensitivity and resolution.^{4,9} Subsequent to colour capture, an algorithm combines the three colour channels into a single pixel, albeit at the cost of

reduced spatial resolution. To optimize data transmission, the RGB value are interpolated using the YUV 4:2:2 sampling technique, which controls neighbouring pixel information. In this format, the Y component represents luminance (intensity), ranging from black to white, while U and V components correspond to chrominance, representing blue and red colour differences, respectively.^{4,9}

2.3.2 Comparative study of smartphone-based authentication of existing unclonable anti-counterfeiting labels

The widespread availability of smartphones, combined with their advanced capabilities, offers significant potential to use them as authentication devices for validating PULs by accessing their unclonable characteristics. Table 2.5 provides a comprehensive overview of smartphone authenticable PULs systems, highlighting their unclonable aspects as security features. It also presents a quantitative metric for assessing the security performance of existing PULs. Furthermore, the table highlights the authentication methodologies employed in these systems, with a particular focus on the role of smartphone cameras in capturing and analysing unique characteristics of PULs.

Table 2.5 Comparative study of smartphone authenticable PULs in anti-counterfeiting applications highlighting unclonability, performance quantification and smartphone integration in validation process.

Smartphone-authenticable PULs	Unclonable aspects of PUL	PUL performance quantification	Smartphone's role in PUL authentication
PUL based on QR-code embedded PVA film doped with scattering, absorbing and PL microparticles ⁹⁰	Stochastic arrangement of microparticles on top of a printed QR code sheet	Encoding capacity = 2.5×10^{120} . Validation accuracy = 99.63%, with zero false-positive rate.	Random scattering pattern captured using a macrolens-equipped smartphone for PUL authentication.
Grain boundary-based PULs with patterned porous structures ⁹¹	Self-assembled honeycomb grain boundaries from polystyrene-based polymer.	Encoding capacity = 10^{225} . High intra-correlation (~ 0.95) & low inter-correlation value (~ 0.2).	Image acquisition of honeycomb film using a smartphone equipped with a portable lens.

Smartphone-authenticable PULs	Unclonable aspects of PUL	PUL performance parameters	Smartphone's role in PUL authentication
PUL based on unclonable micro-textured perovskite film with clonable micro-profile ³⁸	Random crystallization of perovskites on a pre-defined laser-etched surface.	Encoding capacity = 2.1×10^{623} . Validation accuracies = 97.9% and ~ 100% for true & false images.	Smartphone-integrated portable microscope enabling analysis of the shape and texture features from the PULs.
Polyester NPs-embedded polymer film as recyclable PULs ⁹²	Random agglomeration based micropatterns, formed by drop-casting polyester NPs solution on polymer film atop QR code.	Low variability in PUL pattern results in limited encoding capacity, affecting algorithmic discrimination. Validation accuracy >99% with false positive rate < 5%.	Capture of PUL pattern by smartphone camera and validation through server-based digital matching comparison.
Total internal reflection (TIR)-based PUL with PMMA microspheres on a transparent substrate ⁹³	TIR-based bright-dark patterns formed by randomly dispersed PMMA microspheres.	Encoding capacity = 2^{370} . Intra and inter HD = 0.068 & 0.5, with an error rate 1.6×10^{-23} .	Smartphone integration with handheld microscope for image capture, key extraction, and analysis.
Smart Nano-based PUL by drop-casting platinum (Pt) NPs solutions on silicon substrate ⁷³	Colorimetric switching of Pt NPs induced by stochastic deposition and chemical environment variation.	Encoding capacity = 3×10^{135} . Pattern validation accuracy = 98.22%.	Colour switching patterns from Pt catalysts recorded by smartphone camera.
Random micro-fractal gold (Au) film on SiO ₂ substrate as an unclonable security ⁹⁴	Thermal stress-induced void formation and fractal micro-network developed in gold film.	Encoding capacity = 10^{348} . High Inter-correlation (0.42) and high intra-correlation coefficient (1.0).	Smartphone with clip-lens imaged the random Au surface features.

2.4 Choice of luminescent materials for unclonable security

Luminescent materials with distinct spectral and temporal emission characteristics are essential for developing robust anti-counterfeiting measures.⁹⁵ Material selection requires careful consideration of factors such as environmental stability, compatibility with substrates, particle size distribution, and manufacturing processes. Table 2.6 provides a tabular overview of different luminescent materials employed in the realization of unclonable labels, highlighting their key attributes and limitations for anti-counterfeiting application.

Table 2.6: Choice of luminescent materials for security application in PUL, highlighting their key features and limitations towards anti-counterfeiting.

Luminescent material contenders	Key features	Limitations towards anti-counterfeiting application
Transition metal dopants ⁹⁶	Sharp emission spectra, long lifetime, potential for narrow emission bands, high photostability, resistance to photobleaching	Low quantum yield, susceptibility to quenching, complex synthesis, limited colour tunability, host matrix dependency
Organic dyes ^{97,98}	Broad emission spectra, high quantum yields, solution processability, colour tunability	Photobleaching, low photostability, environmental sensitivity, spectral overlap, potential for counterfeiting through spectral manipulation
Quantum dots (QDs) ^{97,99}	Size-tunable emission spectra, high quantum yields & brightness, narrow emission lines, exceptional brightness, resistance to photobleaching	Toxicity, batch-to-batch variability, surface related quenching, potential for spectral manipulation through surface engineering
Carbon dots (CDs) ¹⁰⁰	Tunable emission, Water solubility, biocompatibility, low toxicity, cost-effective synthesis	Low quantum yields, broad emission spectra, unclear luminescence mechanism
Nanocrystals ¹⁰¹	Tunable anti-stokes emission, high luminescence efficiency	Size distribution, low quantum yield, surface defects, toxicity, complex synthesis
Lanthanide-doped phosphors ^{102,103}	Sharp emission spectra, long luminescence lifetimes, high stability, energy transfer up-conversion, large stokes shift	Synthesis complexity, relatively low quantum yields for certain ions, sensitivity to quenching, material cost

Transition metal dopants are potentially utilized in realizing high-security labels due to their distinctive characteristic features, including sharp emission spectra and long luminescence lifetimes.⁹⁶ However, their practical implementation is hindered by the complex synthesis and limited colour tunability options. Organic dyes, while offering colour tunability and ease of processing, are susceptible to counterfeiting due to their relatively low stability.⁹⁷ Quantum dots, renowned for their exceptional brightness and narrow emission, are suitable for covert and machine-readable labels, though toxicity concerns and batch-to-batch variations must be considered.⁹⁹ Carbon dots present a low-cost, biocompatible option for disposable labels, but their lower quantum yields and broad emission spectra limit their application.¹⁰⁰ Nanocrystals, particularly up-conversion NPs, offer enhanced security through their unique anti-Stokes emission, but complex synthesis and potential low efficiency are challenges.¹⁰¹

Lanthanide-doped phosphors emerge as a strong contender for anti-counterfeiting applications due to their inherent advantages. Their characteristic sharp emission spectra, long luminescence lifetimes, and high stability offer a robust foundation for creating highly secure and counterfeit-resistant labels.¹⁰⁴ The shielded f-electron configuration of lanthanide ions contributes to their inherent stability against quenching and environmental factors, enhancing the label's security. Furthermore, energy transfer processes between different lanthanide ions within a host matrix facilitate the creation of complex, multi-spectral emission patterns, significantly augmenting the label's security features.¹⁰⁵ While challenges such as synthesis complexity, cost and low quantum yield exist, these can be mitigated through innovative approaches. For instance, the integration of ML arrays can significantly enhance the PL brightness of lanthanide-doped phosphor by focusing incident light onto individual particles within the phosphor layer.²

Moreover, the utilization of micron-sized lanthanide phosphor particles in anti-counterfeiting labels is driven by several factors that collectively enhance security features and label performance. Firstly, the micron-scale dimensions significantly improve luminescence efficiency through enhanced light scattering and absorption.^{106,107} The increased surface area facilitates efficient light interaction, leading to a higher probability of lanthanide ion excitation and minimized self-absorption effects, thereby boosting luminescence intensity.¹⁰⁷ Secondly, micron-sized phosphor particles play a crucial role in improving the smartphone camera's ability to

capture, process, and analyse luminescent patterns, making them vital for advanced anti-counterfeiting technologies.¹⁰⁸ Their fine-grained structure enables the creation of intricate and high-resolution luminescent patterns, increasing the information density and reducing pixelation for sharper images.¹⁰⁹ The increased surface area of these particles boosts light scattering and absorption, directing more emitted light towards the camera sensor and improving the signal-to-noise ratio, resulting in clearer and more distinct patterns.¹⁰⁹ Additionally, these particles align well with the optical resolution and pixel size of smartphone cameras, ensuring precise capture of the luminescent details. The high-resolution patterns also facilitate effective image processing, aiding in accurate authentication and verification. Lastly, the compatibility of micron-sized phosphor particles with various printing and coating processes allows for their homogeneous dispersion, facilitating integration into diverse substrates like paper, plastic, and metal.⁴ This ensures consistent luminescence properties across the label area, contributing to overall security and reliability. In summary, micron-sized lanthanide phosphor particles enhance anti-counterfeiting labels through improved light interaction, spatial resolution, controlled emission properties, and manufacturing compatibility. These factors position them as a leading luminescent material for realising unclonable anti-counterfeiting labels.

2.5 Luminescence mechanism in lanthanides-doped phosphor materials

Lanthanides, also known as rare earth elements, exhibit unique electronic configurations and transitions due to their partially filled 4f orbitals.¹⁰⁵ This section provides a foundation overview of lanthanide electronic configurations, oxidation states and associated transitions. Subsequent discussion explores the PL mechanism underpinning luminescence in lanthanide-based inorganic phosphors, encompassing both UC and DS processes.

The lanthanide series encompasses a group of 15 elements, extending from lanthanum (La, with an atomic number $Z = 57$ and an electronic configuration of $[\text{Xe}] 5d^1 6s^2$) to lutetium (Lu, $Z = 71$, featuring an electronic configuration of $[\text{Xe}] 4f^7 5d^1 6s^2$) within the periodic table.¹¹⁰ Here, the symbol Z is used to represent the atomic number of each element. The arrangement of elements is determined by their atomic number, and the filling pattern of the 4f is not sequential.^{4,104} Predominantly, lanthanides adopts a +3-oxidation state, characterized by the electronic configuration

[Xe] $4f_n$, where n varies from 0 to 14 corresponding to the ions of La^{3+} through Lu^{3+} respectively.¹⁰⁴ However, exceptions include divalent ions (Eu^{2+} , Sm^{2+} , Yb^{2+}) and tetravalent ions (Ce^{4+} and Tb^{4+}). These deviations are attributed to the stability associated with half-filled or fully-filled 4f orbitals.¹¹¹ Lanthanide ions possess distinctive spectroscopic and magnetic properties due to their 4f electrons, whereas their chemical and optical behaviour is mostly determined by the 5d and 6s valence electrons.^{103,104,111,112} Their optical behaviour primarily involves three transition types: intra-4f transitions, 4f-5d transitions, and charge transfer transitions. Intra-4f transitions, governed by strict selection rules, yield sharp emission lines, while 4f-5d transitions, facilitated by parity changes, contribute to broader emission bands.^{103,104,111,112} Building upon the fundamental understanding of lanthanide electronic configurations, the subsequent section delves into the PL mechanisms governing luminescence in lanthanide-based inorganic phosphors.

The investigation of the PL mechanism in lanthanides based inorganic phosphors has garnered significant attention in numerous studies.^{112,113} Eliseeva *et al.* in 2010 conducted a study that offers a comprehensive examination of the fundamental mechanisms underlying PL processes. The study elucidates the nature of phosphors, which are luminescent substances capable of emitting light upon exposure to radiation. In general, lanthanide luminescence may be divided into three types, which are determined by the energy transfer process that occurs upon excitation. These categories include DS, quantum cutting (QC), and UC process.^{111,112}

UC is a non-linear optical process, whereas DS and QC are generally considered linear optical processes that are independent of the excitation intensity.¹¹⁴⁻¹¹⁶ However, it is worth noting that QC, while ideally linear under standard conditions, may exhibit deviations from linearity in certain contexts, such as under high excitation intensities or in materials with complex energy transfer dynamics.^{117,118} UC process sequentially stimulate electrons from low energy states into an excited state at upper energy level via a real, lower-lying metastable excited state.^{119,120} In Ln^{3+} based phosphors, the UC process is caused by well-defined ladder-like energy states that make it easier for energy to combine and relax radiatively.^{119,120} Initial absorption is the first step in the UC process, which results in the formation of an intermediate excited state. From this intermediate state, the neighbouring ions transmit their energy to one another by a

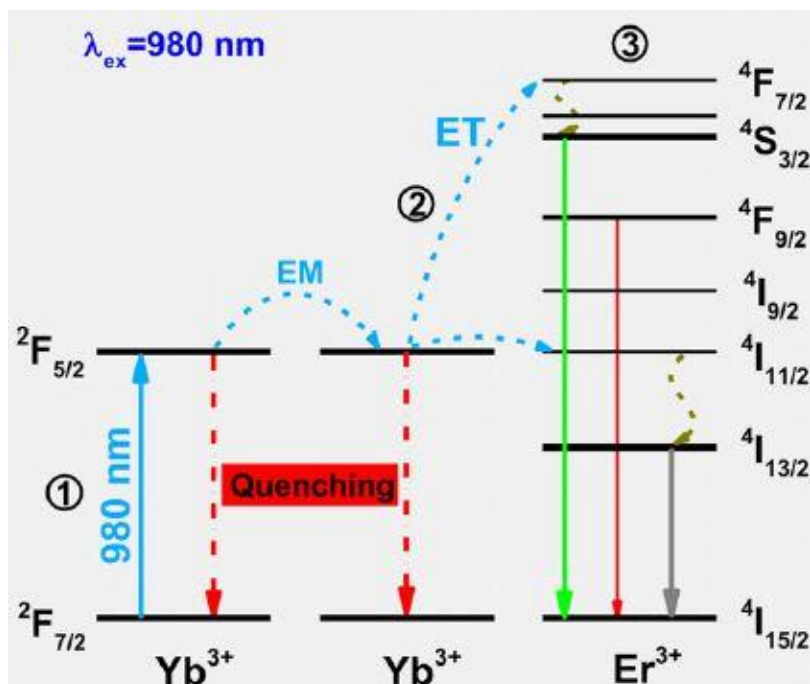


Figure 2.3 ETU based up-conversion (UC) mechanism from the duo-pair of activator and emitter ions, $\text{Er}^{3+}/\text{Yb}^{3+}$ upon excitation at 980nm.⁷

variety of mechanisms until one of the ions accomplishes a metastable state. 'Sensitizers' and 'activators' are key components in UC processes.¹⁰⁴ Sensitizers efficiently absorb incident radiation and transfer this energy to activator ions. Activators subsequently emit upconverted photons, typically at higher energies than the absorbed radiation. Energy transfer mechanisms, such as energy transfer up-conversion (ETU) redistribute energy among ions. ETU involves energy transfer from a sensitizer ion to an activator ion, promoting the latter to a higher energy state. It is a non-linear process in which two or more low-energy photons are absorbed and combined to emit a single higher-energy photon. The excited ion then relaxes to its ground state by emitting a photon with higher energy than the absorbed photons.⁷

The trivalent ytterbium (Yb^{3+}) and erbium (Er^{3+}) ions, which serves as a sensitizer-emitter pair in the $\text{Gd}_2\text{O}_2\text{S}$ host lattice, are integral to the one of the most frequently reported UC process. it produces a red emission peaked at 655nm, along with green emissions at 525nm and 543nm.⁷ Yb^{3+} , with its energy level ($^2\text{F}_{5/2}$) around 980nm, acts as the sensitizer ion, absorbing NIR photons and transferring the energy to Er^{3+} .^{121,122} The UC mechanism, schematically shown in Figure 2.3, highlights the energy transfer between the sensitizer Yb^{3+} and the emitter Er^{3+} ions under 980 nm excitation. Yb^{3+} Is An efficient sensitizer due to its simple energy-level structure which minimizes non-radiative decay losses, and its large absorption cross-section enables efficient absorption of NIR photons.^{121,122} Furthermore, the spectral overlap between the energy

levels of Yb^{3+} and Er^{3+} enhances the energy transfer efficiency.^{121,122} Er^{3+} acts as the activator ion, with its energy levels, particularly the transitions between $^2\text{H}_{11/2}/^4\text{S}_{3/2} \rightarrow ^4\text{I}_{15/2}$ and $^4\text{F}_{9/2} \rightarrow ^4\text{I}_{15/2}$, resulting in distinct green and red UC emission bands respectively.¹²¹ It is also necessary for the host lattice to have a low phonon energy for an efficient UC process.^{120,123-125} Low phonon energy reduces the likelihood of non-radiative losses, ensuring that the energy absorbed and transferred by the ions is utilized effectively. In my PhD research, the $\text{Gd}_2\text{O}_2\text{S}$ host matrix is implemented as an UC phosphor due to its low phonon energy, which minimizes the likelihood of non-radiative losses.^{121,125} It ensures efficient energy transfer between the Yb^{3+} sensitizer and the Er^{3+} emitter, a critical aspect of achieving the UC process. By reducing multi-phonon relaxation, the low phonon energy of $\text{Gd}_2\text{O}_2\text{S}$ enables more efficient utilization of the absorbed energy.

DS, a process that transforms a high-energy photon into lower-energy photon, has been captivating researchers for decades.^{116,126,127} DS involves the absorption of a single high-energy photon followed by the emission of a single lower-energy photon. The energy difference between the absorbed and emitted photons is typically lost as heat or through non-radiative relaxation. This process limits the photoluminescence quantum yield (PLQY) to a maximum of 100% since each absorbed photon results in the emission of at most one photon. This distinguishes DS from multi-photon processes like down-conversion, which can lead to higher quantum yields.¹²⁰ The mechanism behind the DS process has a rich history, dating back to the early work of Weber and Hovel in the mid-1970s.¹²⁸ Initially, the primary focus of DS research was to improve the efficiency of solar cells by converting UV radiation into visible light.¹²⁹⁻¹³² However, DS technology has evolved significantly since then, expanding its applications to encompass a wide range of materials, including dyes, phosphors and QDs. These materials are utilized in various fields, such as enhancing surface lighting and display technology as well as in biomedical imaging.¹³³⁻¹³⁵ For example, The application of $\text{Eu}^{3+}/\text{Eu}^{2+}$ DS phosphor extends beyond lighting technologies, and it plays significant utility in security labelling and anti-counterfeiting.^{108,136-139} Katumo *et. al.* demonstrated dual-colour dynamic anti-counterfeiting labels using Eu^{2+} -doped DS phosphors, where a smartphone flashlight excited the samples and the smartphone camera recorded the persistent emission from the DS phosphor particles.¹⁰⁸

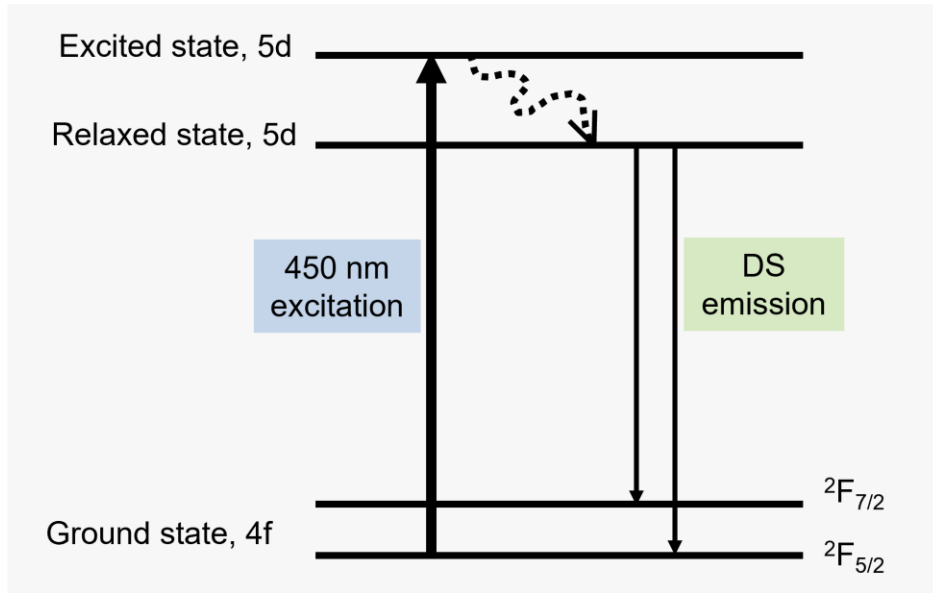


Figure 2.4 Schematic energy level diagram showing the downshifting (DS) mechanism in Ce³⁺ doped YAG phosphor, under a 450nm excitation.⁶

In my PhD research, Ce³⁺-doped YAG phosphor is utilized as DS particles for realizing unclonable labels. This material is chosen due to their efficient luminescent properties under a 450nm excitation. The Ce³⁺ ions in YAG exhibit a 4f₁ electronic configuration, resulting in specific energy levels, including the ground state split into $^2F_{5/2}$ and $^2F_{7/2}$ due to spin-orbit coupling, and the excited state arising from the 5d configuration, split by the crystal field of the YAG host into several sublevels.^{6,140} Moreover, the YAG:Ce³⁺ phosphor exhibits a significant Stokes shift, which minimizes reabsorption losses and ensures high energy conversion efficiency.^{6,140} This makes them highly suitable for integration into devices such as lighting systems, displays, and security labels.⁶

Figure 2.4 shows a schematic energy level diagram representing the transitions involved in Ce³⁺ doped YAG phosphor under a 450nm excitation. Upon excitation, electrons are promoted from the 4f ground state levels $^2F_{5/2}$ and $^2F_{7/2}$ to the higher 5d state, specifically to one of the lowest 5d sublevels. Subsequently, the excited electrons undergo non-radiative relaxation to the lowest 5d sublevel, transferring energy through lattice vibrations (phonons).¹⁴⁰ Radiative transitions then occur from the 5d state back to the 4f ground state, with emissions to both $^2F_{5/2}$ and $^2F_{7/2}$ levels, producing photons in the visible range, particularly between 500-650 nm.¹⁴⁰ The emission wavelengths, around 550nm and 600nm, correspond to the visible wavelength region. These transitions, involving excitation to the 5d state, non-radiative relaxation, and subsequent radiative emission from (5d → 4f) electronic transition, underpin the

functionality of Ce³⁺ doped YAG phosphors in converting blue light (450nm excitation) into a broad spectrum of visible light, thus making them integral to white LED applications.^{6,140}

2.6 Optics of ML arrays

ML arrays is a two-dimensional arrangement of miniature lenses with diameters typically ranging from μm to mm. These lenses are often arranged in regular patterns, such as square or hexagonal grids. ML arrays manipulate light by focusing, collimating, or diffusing incident radiation, enabling a wide range of applications in optics and imaging systems. ML arrays are important in the proposed unclonable label technology, as they fulfil essential functions in both the illumination and collection of PL responses.^{141,142} This section provides an in-depth analysis of the optical properties of ML arrays, explaining their fundamental mechanisms of operation and their crucial roles in the development of unclonable labels.

2.6.1 ML as an illumination element

ML possess the ability to manipulate incident light with a high degree of accuracy and control, resulting in focused and precisely regulated illumination.^{141,142} In the following section, the theory of focus generation is presented, considering Rayleigh and Abbe's diffraction limitation.

2.6.1.1 Theory of focus formation of incident light

The concept of focus formation through ML is centred on their capacity to manipulate light. When light traverses a ML, it undergoes refraction, resulting in the convergence or divergence of light rays. ML, also referred to as minuscule optical components are capable of focusing light rays to generate a small concentrated focal spot. This unique ability to concentrate light makes ML extremely valuable, in applications such as imaging, sensing and spectroscopy.¹⁴²⁻¹⁴⁴ In the present section, the mechanism behind the creation of a focal volume from a ML is discussed considering the principles of geometrical optics. When light encounters a ML it undergoes refraction and bends towards the axis. The degree to which light rays bend is determined by the focal length of the ML, which represents the distance from the lens itself to its focal point. This focal point serves as the convergence point, for all refracted rays resulting in a tiny, intensified spot of light. The size of this spot or focal volume is dictated by another

parameter known as numerical aperture (NA) associated with the ML.^{142,145} NA quantifies the lens's ability to gather light without any unit of measurement.^{142,145} Higher NA lenses possess numerical apertures consequently leading to focal spots.

Considering a scenario, when a visible wavelength light is incident at normal incidence on the ML surface. The focal volume generated by the ML arrays is expressed using the following formula¹⁶²:

$$V_f = \frac{k * \lambda^2 * NA^2}{\pi} \quad (2.1)$$

Wherein, V_f is the focal volume of the ML arrays, λ is the wavelength of light, k is the constant approximately equal to 0.5 and NA is the numerical aperture of the ML.^{142,145} The formula shows that the focal volume (V_f) decreases as the wavelength of the incident light increases. In terms of shorter wavelengths, like blue light create smaller focal spots compared to longer wavelengths, e.g. red light.^{142,145}

2.6.1.2 Rayleigh criterion

The Rayleigh criterion and the Abbe diffraction limit are important concepts in the optics of ML. The Rayleigh criterion defines the minimum resolvable detail and sets limits on the ability to distinguish between closely spaced features in the illumination pattern.^{146,147} The criterion is crucial for ensuring the precision of the illumination provided by a ML.

The Rayleigh criterion, also known as Rayleigh's resolution criterion, is a fundamental principle utilized in optics to ascertain the level of detail that can be resolved in an optical system, such as a telescope or microscope.¹⁴⁷ The criterion is named after Lord Rayleigh who was responsible for its development. As per the Rayleigh criterion, two sources of light are considered resolved when the central point of the diffraction pattern, also known as the Airy disc, created by one source aligns with the fringe, or minimum, of the diffraction pattern produced by the other source.^{146,147} Two objects are resolved when the central bright spot of one object aligns with the dark ring of the other object in their respective diffraction patterns. The Rayleigh criterion can be mathematically expressed as follows¹⁴⁷:

$$\theta = 1.22 * \frac{\lambda}{D} \quad (2.2)$$

Where, θ represents the angular resolution, measured in radians, λ denotes the wavelength of light employed, and D signifies the diameter of the aperture, such as that of a lens or a telescope.^{146,147} The Rayleigh limit is a critical threshold used to determine the resolution of systems and is commonly utilized in the design and assessment of optical instruments.^{146,147} Obtaining a resolution that surpasses the Rayleigh limit presents difficulties because of the wave properties of light and the occurrence of diffraction.^{146,148} Once exceeding this threshold, the intricate particulars become indiscernible, resulting in the merging of two distinct sources. It is important to mention that although the Rayleigh criterion offers guidance, the actual performance of instruments can be affected by factors such as the quality of optical components, aberrations, and other relevant considerations within the system.^{146,148}

2.6.1.3 The Abbe diffraction limit

The resolution of ML-based illumination systems is additionally limited by the Abbe diffraction limit. This statement establishes a relationship between the wavelength of light and the dimensions of a ML, as well as its numerical aperture (NA).^{149,150} A comprehensive study of the Abbe diffraction limit is imperative to effectively optimize the performance of ML arrays.

In the field of microscopy, the concept of the Abbe diffraction limit, which is also known as the Abbe resolution limit, is a principle that defines the minimum distance that can be resolved between two distinct points in a specimen.^{149,151} Ernst Abbe, a German physicist of the 19th century, initially introduced it.¹⁵¹ This limit is crucial in determining the measurable distance between two separate points within a specimen. This phenomenon is linked to the diffraction of light as it traverses a lens, which ultimately restricts a system's ability to distinguish the positions of objects.^{150,151} The Abbe diffraction limit is mathematically defined by the following equation¹⁶⁸:

$$\theta = \frac{\lambda}{2 * NA} \quad (2.3)$$

In equation 2.3, λ denotes the wavelength of the light, and NA refers to the numerical aperture of the optical system.¹⁵¹ Based on this principle, the resolution of a system is directly correlated with the wavelength of light and inversely correlated with the numerical aperture. Enhanced resolution is achieved by reducing the wavelength and increasing the numerical aperture.^{150,151} The numerical aperture as briefed in the

previous section, quantifies the light gathering capacity of an optical system. It is linked to both incoming and outgoing angles of light through the lens. Essentially smaller values for the minimum resolvable distance indicate a better resolution capability, for a given optical system. It should be noted that the idea of the Abbe diffraction limit stands for the limitations imposed by the wave characteristics of light.¹⁴⁹⁻¹⁵¹ Surpassing this threshold to attain higher resolutions is challenging due to the influence of diffraction. Scientists have developed advanced techniques, such as super-resolution microscopy, to surpass the Abbe limit, thus allowing us to visualize structures at lower resolutions.^{148,150}

2.6.2 ML as a collection element

In addition to their role as illumination elements, ML can also function as efficient collection elements.^{152,153} They capture and direct emission light towards detectors or cameras, enabling the retrieval of unique luminescent patterns from the PUL utilized in this work. The field of view (FOV) of an ML refers to the range of area from which it can collect light, specially from the point of illumination overhead the ML surface.¹⁵³ When a tiny light source is positioned at the ML focal volume, all outgoing rays emits from the point source in a collimated manner from ML surface. However, if the light source is located off the plane the light rays coming from a point light source (underneath the ML) form an illumination cone, in a cone shape. A detailed study of the role of ML as a collection element is presented in the methodology chapter (section 3.11), where a schematic experimental design from my PhD work is used. The FOV of the ML depends on this angle of the cone, which is determined by how close the light source is from its focal plane.^{153,154} The angle of the illumination cone can be mathematically defined utilizing a formula as follows:

$$\theta = 2 * \sin^{-1} \frac{NA}{2} \quad (2.4)$$

Here, θ is the angle of the illumination cone. NA is a parameter that measures the ability of the ML to gather light. Lenses, with a higher NA have larger numerical apertures, which leads to smaller cones of illumination.^{154,155}

2.7 A review of ML arrays fabrication methods

ML arrays are integral components in numerous optical applications, ranging from imaging systems¹⁴², LEDs¹⁵⁶, displays¹⁵⁷ to anti-counterfeiting⁸. The fabrication

techniques for ML arrays have evolved significantly, driven by the need for precision, scalability, and adaptability to diverse applications. This literature review explores different established optical methods used in the fabrication of ML arrays, referencing pivotal scientific studies that have significantly contributed to this field.

UV curing and soft lithography with inkjet printing: UV curing, combined with soft lithography and inkjet printing offers a direct and efficient method for fabricating ML arrays structure, leveraging the controlled deposition capabilities of inkjet technology alongside the rapid solidification of UV-curable polymers. Zhang *et al.* demonstrated that ML arrays can be printed directly on ultra-thin substrates using a drop-on-demand inkjet printer, where surface tension shapes the droplets into spherical lenses, cured via UV exposure.¹⁵⁸ Nam *et al.* fabricated ML arrays using a soft lithography process.¹⁵⁹ They created a PDMS mold from a photolithography master and then replicated the lens pattern into a photosensitive polymer via UV curing. Similarly, Shen *et al.* developed a UV roll-to-roll nanoimprinting method to fabricate ML arrays films, enhancing organic LED (OLED) out-coupling efficiency.¹⁶⁰ This method enabled ML arrays film fabrication with high print resolution, allowing for scalable and cost-effective production.

Two photon lithography: TPL, also known as DLW, offers exceptional precision and design flexibility for fabricating ML arrays.¹⁶¹ This technique employs a focused laser beam to directly pattern the desired lens structure onto a photosensitive substrate. Malinauskas *et al.* developed a femtosecond laser-induced two-photon polymerization (2PP) technique for creating high-resolution ML.¹⁶² This method uses femtosecond pulses for precise, 3D structuring, enabling accurate and flexible fabrication of customized ML arrays for diverse optical applications. My PhD work involved the creation of ML arrays master mold through TPL, followed by replica molding using UV curing and soft lithography to generate a batch of samples.

Nanoimprinting lithography: Nanoimprinting lithography (NIL) is a high-throughput, cost-effective technique for fabricating ML arrays.¹⁶³ This process involves transferring ML patterns from a master mold into a resist layer through mechanical pressure. Dutta *et al.* developed a method for replicating polymer ML using nanoimprint lithography with a Ni-stamp created via proton beam irradiation.¹⁶⁴ This technique ensures high-fidelity imprinting of ML patterns onto polymer films, combining advanced proton beam

and nanoimprint technologies for precise ML replication in optics and photonics. NIL is particularly suitable for large-area and mass production of ML arrays.

Thermal reflow method: This method involves coating a substrate with a photoresist layer, which is then patterned using UV light through a mask with circular array designs. After developing the photoresist, cylindrical features are left on the substrate. Heating these features causes them to reflow and reshape into spherical ML due to surface tension, resulting in uniform and precise ML arrays.¹⁶⁵ Qiu *et al.* developed a novel thermal reflow technique to produce ML arrays with high packing density. By carefully controlling the polymer melting process, they achieved precise lens geometries and improved optical performance.¹⁶⁶

Photolithography and etching: Photolithography, coupled with etching processes, constitutes a high-precision method for fabricating ML arrays. This technique involves using a photomask to transfer a pattern onto a photoresist-coated substrate, followed by etching to form the desired lens profile.¹⁶⁷ Lim *et al.* developed a method to fabricate concave ML arrays by first using laser patterning to define shapes on a substrate, followed by isotropic etching to form concave profiles.¹⁶⁸ This approach allows for high-resolution and precise ML fabrication.

The reviewed fabrication techniques highlight the diversity of approaches available for ML arrays fabrication, each with its advantages and limitations. UV curing with soft lithography provide simpler and cost-effective alternatives but may have limitations in achieving complex lens shapes.¹⁴³ DLW offer high flexibility and customization but may require sophisticated equipment. Nanoimprinting lithography stands out for its suitability in large-scale production.¹⁴³ Thermal reflow is limited by poor uniformity, dimensional control, and difficulty in producing complex lens patterns.¹⁴³ Photolithography and etching offer high precision but can be costly and time-consuming.¹⁴³ Future research in ML arrays fabrication is likely to focus on combining these techniques to leverage their respective strengths. Additionally, advancements in materials science, such as developing new polymers and nanocomposites, will further enhance the performance and functionality of ML arrays.

2.8 Fundamental study of the TPL

TPL offers a powerful means of constructing ML arrays with unparalleled intricacy and design flexibility.⁵ This section provides a fundamental overview of the theoretical principles of TPL, emphasizing its suitability for fabricating complex microstructures.

2.8.1 Fundamental theory of 2PP

2PP forms the foundation of TPL, utilizing its superior resolution to trigger polymerization reactions on a microscale.^{5,169,170} This sophisticated approach facilitates the crafting of complex three-dimensional architectures with unprecedented accuracy, underscoring its significance in the realm of microfabrication. 2PP is a nonlinear optical process, fundamentally based on the two-photon absorption (TPA) theory and has gained importance as a highly useful fabrication technique.⁵ It is also referred as DLW, femtosecond laser writing, and dip-in laser lithography. Göppert-Mayer first proposed this idea in 1931.⁵ It involves simultaneously absorbing two photons of equal or different frequencies to excite a molecule from its ground state to a higher energy level.⁵

The absorption of a single UV photon (compared to that of two near IR (NIR) photons) exemplifies the TPA process. In the Jablonski diagram shown in Figure 2.5 (on left), the TPA cycle includes the excitation of a particle by two photons of equivalent energy, all in all summarizing to the energy difference between the upper and lower states.⁵ In

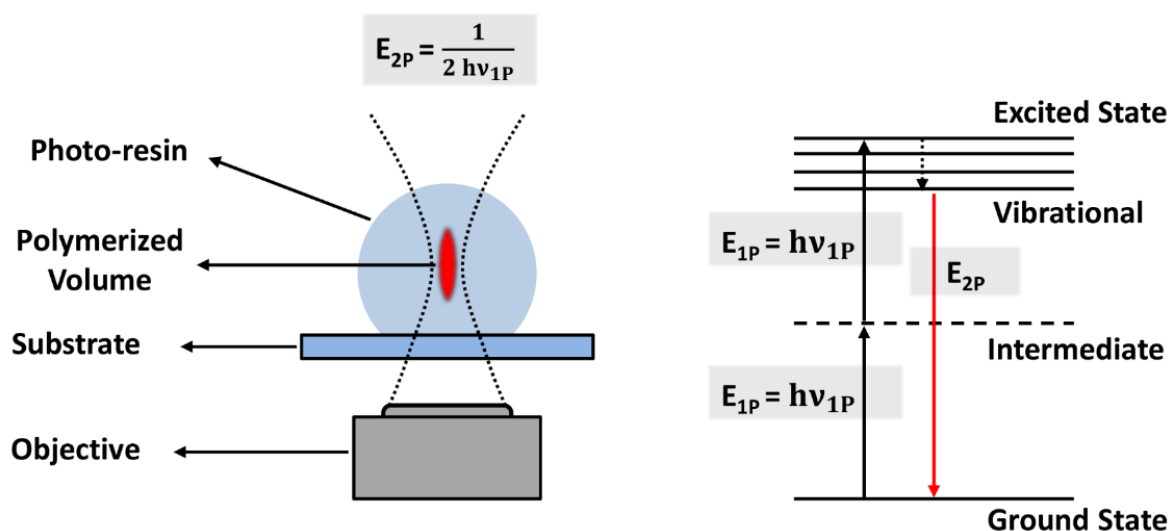


Figure 2.5 Direct-laser writing (DLW) a) Schematic setup showing the two-photon polymerization (2PP) process, where the photoresist is polymerized only in a small volume called a voxel. An inverted objective guides a laser beam into the photoresist. b) The process is based on the absorption of two low-energy photons ($E_{1P} = h\nu_{1P}$) by the photoresist, which results in the emission of a high-energy photon ($E_{2P} = h\nu_{2P}$) that triggers polymerization.⁵

contrast to one-photon absorption (OPA), a direct system where energy retention is proportional to light intensity of a single photon; TPA is nonlinear, described by retention relative to the square of the photon intensity (I^2).⁵ When compared to OPA, the two times exponential fall-off of absorbed intensity from the center of a focused laser beam shows that TPA has a greater resolution due to its nonlinear nature.⁵ Figure 2.5 (on right) describes the exposure mechanism of the photoresist, illustrating a transition from an excited photon-induced intermediate state to a vibrational state. This transition subsequently leads to the breaking of polymer bonds in the case of a positive-tone resist, or the establishment of cross-linking bonds when dealing with a negative-tone resist. In the context of TPP, the construction of three-dimensional objects transcends the conventional layer-by-layer approach.⁵ Microstructures are realized through DLW on a transparent photoresist, which, while highly absorptive at UV wavelengths, remains typically transparent in the infrared (IR) spectrum.^{171,172} This enables the fabrication of complex 3D microstructures utilizing high-intensity, ultrashort NIR laser pulses, provided the combined energy of the two photons surpasses the material's photosensitive absorption energy threshold.^{5,171} This approach offers unmatched flexibility and accuracy in the creation of micron-scale fine-layered objects.^{171,172}

2.9 Summary

This chapter provided a comprehensive overview of PULs and the underlying technologies relevant to this research. The unique properties and diverse applications of PULs were discussed, highlighting their potential in various fields. A detailed analysis of existing PUL technologies, including speckle-based, luminescence-based, and surface feature-based approaches, was presented. The chapter further explored the role of smartphones as a platform for PUL authentication, emphasizing the capabilities of CMOS-based camera sensors. A comparative study of smartphone-based authentication for existing PULs was conducted to identify potential challenges and opportunities. To develop novel PULs, the chapter delved into the properties of lanthanide-based inorganic phosphors, their PL mechanisms, and the optics of ML arrays. These components are essential for creating highly secure and robust PULs. Finally, the chapter provided an overview of existing fabrication methods of ML arrays, with a particular focus on TPL, a key technique for fabricating micro-optical components.

3 Methodology

This chapter outlines the methodologies employed in this research, detailing the processes involved in modelling ML, fabricating PULs and characterizing phosphor materials. The chapter begins with a description of ML modelling using COMSOL Multiphysics, addressing geometry selection, design consideration, mesh quality and export procedures. Following this, the fabrication of ML through DLW is discussed, including sample preparation steps, print parameter selection and the use of the Nanophotonic Profession GT2 machine (Nanoscribe GmbH, Germany).

The chapter then shifts to the fabrication methods for unclonable labels, with a focus on two-layered design incorporating ML array glass substrate and UC phosphor particles. This section also covers the procedure for developing a single-layer all-PDMS label, which integrates DS phosphor particles, ML arrays and a scattering surface on top.

Characterization techniques are discussed in detail, including scanning electron microscopy for morphological analysis and steady-state PL spectroscopy for evaluating optical properties, such as excitation, emission and diffuse reflectance spectra. The experimental setup is described, detailing different excitation sources, camera detectors, calibration settings for the smartphone camera and exposure settings.

3.1 Modelling a ML in COMSOL

Figure 3.1 shows the steps implemented in COMSOL Multiphysics software to create a computer-aided design (CAD) of a ML.^{173,174} To design a ML in COMSOL Multiphysics, the process begins with defining a solid microsphere with a given radius of curvature (ROC, denoted as R_{sphere}), as depicted in step 1 of Figure 3.1. In step 2, a solid cube is positioned to cut out a specific portion of the sphere's geometry (normal cut-out), to achieve the ML with the desired parameters. The edge dimension of the solid cube must be greater than the diameter of the solid sphere. The geometry workplane, axis type selection and rotation type value for solid sphere and cube are same throughout the design procedure. In making the sphere and cube design, an appropriate meshing algorithm, such as the tetrahedral mesh along with an extra-fine mesh quantity, is used to discretize the microsphere and substrate. This step is

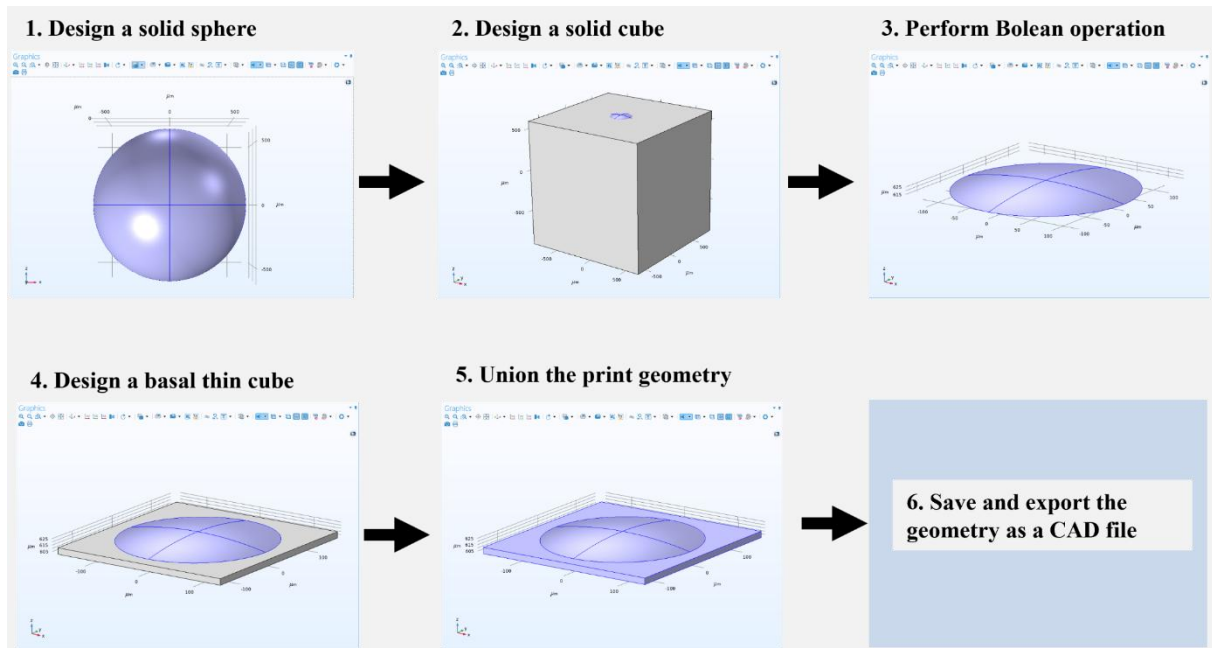


Figure 3.1 Design steps involved in COMSOL Multiphysics software for building a CAD geometry of a ML using a solid sphere.

essential to perform as it ensures that the mesh is sufficiently fine to accurately capture the curvature of the ML.¹⁷⁵ In step 3, a Boolean subtraction operation is performed between the two solids, resulting in a ML with the desired base diameter and height.¹⁷⁶ In step 4, a thin planar surface is created directly underneath the ML, with its top surface in contact with the base of the ML. Step 4 is necessary for the printing step for obtaining a smooth and even-distribution of the base surface of the ML. In step 5, a union operation is carried out between the ML and the thin cube, to consolidate them into a single geometrical file.¹⁷³ In step 6, the union geometry is saved as a CAD file.

3.2 ML fabrication using the TPL

TPL offers precise control over ML fabrication. This section outlines the essential steps involved in the TPL process, commencing with sample preparation steps and progressing to the optimization of print parameters utilizing the 2PP based 3D printer.

3.2.1 Sample preparation steps

The CAD designs of ML arrays are created in COMSOL multiphysics.¹⁷³ The files are exported as STL (Stereolithography) versions. The STL model is opened in the 3D printing software called 'DeScribe'. 'DeScribe' processes the CAD design and assigns the geometry as a set of collective points to the 3D printer. A detailed step-by-step process followed by the printer is presented as follows:

Design configuration: Initiate the sample preparation by configuring the 3D CAD model of desired ML geometry using the printer software. Specify parameters such as lens dimensions, arrangement, and any specific design requirements.

Material selection: Choose an appropriate photosensitive material compatible with TPL. Consider factors like polymerization properties, curing characteristics, and transparency to ensure optimal results during the printing process.

Substrate setup: Prepare the substrate, ensuring it is clean and suitable for the intended ML application. Proper substrate preparation contributes to the adhesion and overall quality of the printed ML arrays.

Calibration checks: Perform calibration checks on the 3D printer to ensure accurate printing. Verify alignment, laser power, and other critical parameters to maintain precision throughout the fabrication process.

Loading material: Load the selected photosensitive material into the printing chamber. Implementing proper loading of photoresist is crucial to ensure the material consistency and avoid discrepancies during the printing process.

Printing parameters configuration: Set the printing parameters such as exposure time, layer thickness, and scanning speed according to the material specifications and ML design. Adjust these parameters to achieve the desired resolution and accuracy.

Initiate printing: Start the printer to initiate the TPL process. Monitor the printing progress and ensure that environmental conditions are optimal for the polymerization of the photosensitive material, which results in a precise and well-defined ML arrays.

3.2.2 Print parameters selection

The DeScribe software offers advanced features that streamline data entry and manage the printing process with precision. Its primary objective is to provide detailed control over the meso-scale 3D printing workflow, ensuring an accurate translation of CAD designs into physical structures. It includes a print-job editor with a data-import wizard, an interactive 3D preview and a print simulation feature, allowing users to interactively enter and edit data.

Figure 3.2 shows the logical flow-chart of the DLW-based 3D printing. By slicing and hatching the CAD model in DeScribe software, the printer recognizes the designed

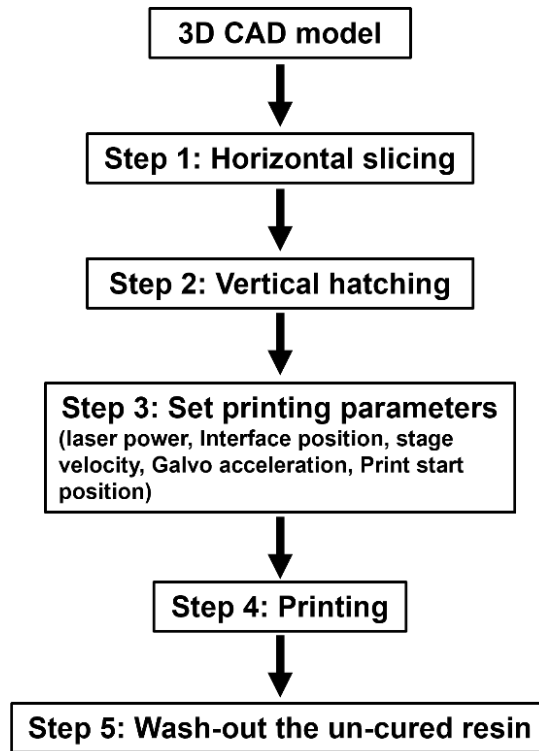


Figure 3.2 Logical flow-chart of printing procedure of the 2PP-based 3D printer.⁵

CAD model as a set of collective points. It scans every single point of the CAD model using an orientation-controlled focused laser beam, called a 'voxel'.⁵ In this way, the voxel of the laser beam polymerizes the liquid resin placed on the glass substrate, and the CAD model is printed in a layer-by-layer fashion in a solid form.⁵ The principle of printer is based on a TPA process, where the liquid resin polymerizes only in the high-intensity voxel region. A 25× objective with an NA of 0.8 is positioned in direct contact (in an inverted geometry facing upwards) with the Nanoscribe IP-S photoresist. This objective is chosen because of its potential of large scanning range for printing mesoscale structures up to a few mm range in the XY-plane. While the use of an objective with an NA of 0.8 involves a trade-off – achieving a larger FOV at the cost of reduced resolution and limiting the smallest achievable feature size – this reduction in resolution is not a limiting factor for the current ML arrays design.¹⁷⁷ The ML array is developed on a scale of greater than 10µm, which is sufficient to achieve the desired smooth optical quality of the ML. The print job begins with system initialization, which includes setting the inversion of the z-axis and configuring the writing process to use a galvanometer (Galvo) in continuous mode. This involves setting the piezo settling time, Galvo acceleration, stage velocity, and enabling parameter monitoring. Offsets for the scan fields in the x, y, and z-axes, are then defined, followed by the writing parameters, including power scaling. Specific parameters for different writing phases (shell writing,

solid writing, and base writing) are set, including laser power and scan speed for each phase. The printing instructions include a base laser power and scan speed based on the shell writing parameters and establish an initial interface position. The process positions the stage at a starting point e.g. (5000, -5000) and enters a nested loop to perform operations across the set number of grid. Within each iteration of the loop, the script identifies an interface at a predefined position, resets the Z-offset to zero, and sets the laser power and scan speed for solid writing. It includes commands from external files to execute specific writing patterns, adjusting Z-offset and stage position as necessary for each inclusion.

After processing each point on the grid, the stage moves to prepare for the next set of operations, ensuring comprehensive coverage across the target material surface. The program is structured to automate the fabrication of complex structures with precision, layer by layer, using different laser parameters and speeds for various sections (base, contour and solid interior) of the material. The inclusion of external files suggests that the program is modular, allowing for the integration of complex geometries or patterns predefined in those files, making it highly adaptable for different fabrication tasks. The DeScribe software supports various input formats, including STL for 3D import, DXF, BMP, PNG and TIFF formats for 2D imports.

The printer software is configured to control a laser-based fabrication process, likely for creating or engraving precise features on a material, with specific reference to a mesh source file for a glass object. The script begins with metadata including the creation time and source file information, indicating it works with a mesh from the source STL file. The transformation command in the software specifies that the object is not scaled or rotated but is translated along the z-axis, likely for alignment purposes within the machine's coordinate system. The slicing parameters indicate that the object will be sliced in fixed intervals of $1\mu\text{m}$, with a simplification tolerance of $0.05\mu\text{m}$ and self-intersections fixed, ensuring the sliced model is optimized for the laser writing process without losing significant details. In the hatching section, the program sets the configuration for contouring and filling the sliced sections of the object. It specifies a single contour per slice and a hatching distance of $0.5\mu\text{m}$. The hatching angle is set to auto, allowing the system to determine the optimal angle for hatching lines within each slice, and the hatch lines are configured to be one-way, indicating the directionality of the laser's path. The output options detail the operational parameters for the laser

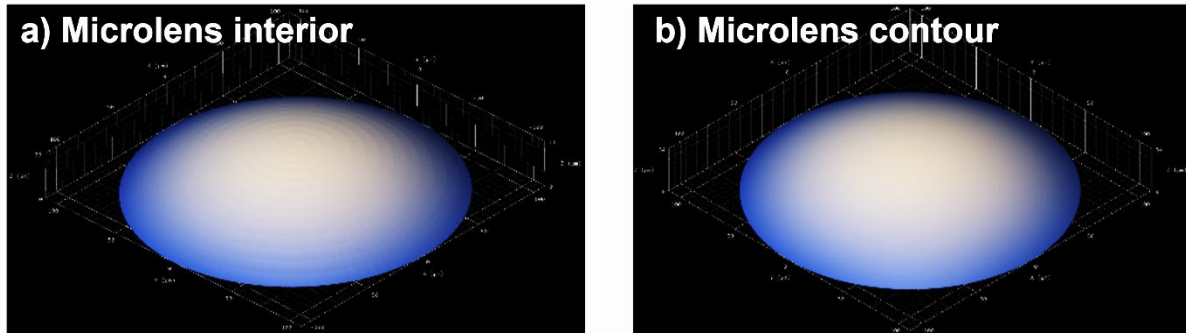


Figure 3.3 CAD model of single ML interior (solid) and ML contour (surface only), designed in DeScribe software.

writing, including using a piezo for z-axis control, constant exposure settings, and specifying the writing direction as upward. At this stage, the scan mode is set to use a galvanometer, indicating a system designed for rapid and precise laser positioning.

The program then moves to operational commands, starting with setting the interface position, adjusting the z-position to a very fine increment ($1\mu\text{m}$), and positioning the stage to begin writing at the user's coordinates. It then includes commands from an external source file which likely contains specific instructions for laser engraving or fabricating one section of the glass object based on the defined parameters and the mesh model. Thus, the machine software's configured printing commands facilitate a sophisticated process of precise laser fabrication, utilizing detailed mesh models and customized laser writing parameters to achieve high-precision creation or modification of glass objects. In the 3D printing process, the resolution in the X-Y plane is primarily determined by the laser spot size, which depends on the NA of the focusing objective lens.⁵ In the current 3D printing setup for fabricating the ML arrays, the $25\times$ objective lens with an NA of 0.8 is employed, achieving a lateral resolution in X-Y plane of $0.5\mu\text{m}$. This enables a precise fabrication of features at the micron scale, making it suitable for realizing the ML arrays with the desired lens dimensions and optical quality. The resolution in the Z-direction is governed by the axial confinement of the laser focal volume and controlled by the fine adjustments in Z-offsets during the printing process. In the current configuration, the Z-resolution is set to $1\mu\text{m}$, ensuring accurate vertical layer stacking and precise control over the height of each printed ML. Together, these chosen X, Y and Z resolutions enable reliable layer-by-layer polymerization, ensuring the ML array is fabricated with optimal structural resolution and functional properties.

To develop rigid and solid ML, a solid interior with a base diameter $220\mu\text{m}$ and a height of $33\mu\text{m}$ is enclosed above the ML contour. Figure 3.3 shows a single unit of combined

ML interior and corresponding surface contour. The designed ROC of ML interior and contour is 200 μm and 200.5 μm , with base diameters of 220 μm and 222 μm respectively. A finer mesh is applied to the contour compared to the interior solid to achieve a smooth outer surface of high optical quality. While this difference in mesh density is imperceptible in Figure 3.3 due to the micro-scale variation in the applied mesh on the surface of the two geometries, it significantly reduces both the amount of printing material and the time to develop the complete structure. The height of the ML contour is 33.5 μm . This example model includes a printed 14 \times 14 ML arrays system in a square lattice, with an inter-lens spacing of 750 μm . The numerical values of design parameters of the ML are chosen to develop a prototype ML arrays sample, resulting in a focal length of focal length (f) of 1900 μm calculated using the formula:

$$f = R * \frac{n}{(n-1)} \quad (3.1)$$

3.3 Two layered PUL using a ML array and phosphor doped PDMS layer

The fabrication process for ML arrays through the TPL process is detailed in the previous section. The preliminary design of the PUL integrates a ML array fabricated on an indium tin oxide (ITO)-coated glass slide and a PDMS layer embedded with micron-sized UC phosphor particles. PDMS was selected due to its unique combination of flexibility, ease of fabrication and transparency.¹⁷⁸ These properties are essential for ensuring optimal optical performance and reliable embedding of phosphor particles. Furthermore, PDMS exhibits excellent biocompatibility, chemical inertness, and durability, which are critical for the long-term stability and functionality of the

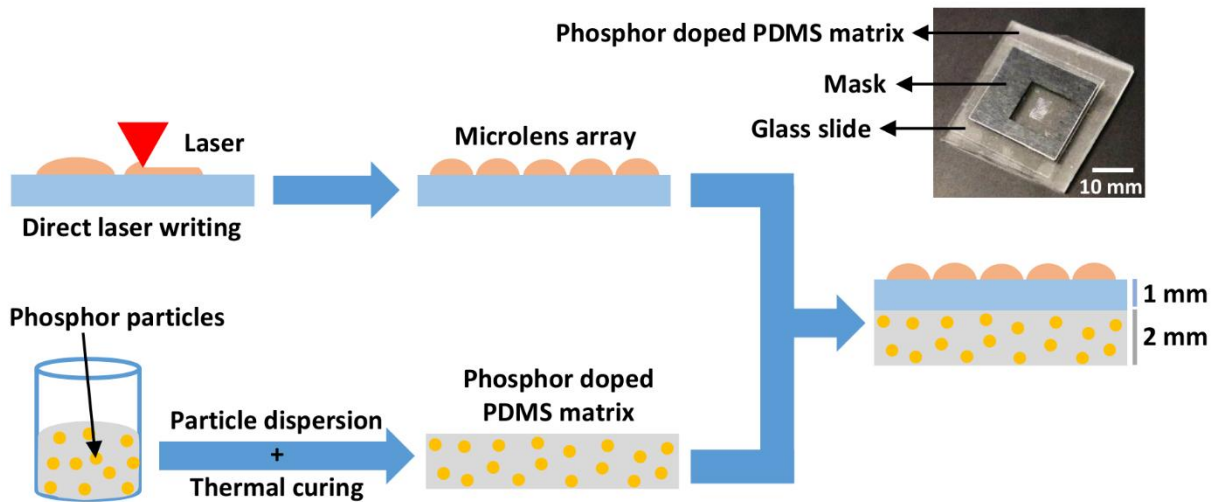


Figure 3.4 Schematic illustration of fabrication steps involved in fabricating two-layer UC phosphor doped unclonable label, wherein a polymer-based ML array is laminated onto a glass substrate, and is attached with UC doped PDMS matrix. Reproduced with permission from Kumar *et al.*²

unclonable label.¹⁷⁸ The balance of optical and mechanical properties makes PDMS particularly suited to this application. In the fabrication process of ML arrays via TPL, the near-identical refractive indices of the glass substrate and the liquid photoresin (Nanoscribe IP-S photoresist) hinder the accurate detection of the interface by the fabrication system. The application of an ITO-coated glass substrate addresses this challenge by introducing a refractive index mismatch, thereby facilitating precise identification of the interface between the glass substrate and the liquid photoresin. The ML array glass substrate is placed on top of the phosphor doped PDMS layer. The manufacturing process of the ML array is schematically detailed in Figure 3.4. In this case, the ML are designed with a sphere featuring a ROC of 625 μm , resulting in a focal length (f) of 1900 μm , calculated by equation 3.1. This design ensures effective encapsulation of the central volume from ML within the 2000 μm thick PDMS layer while ML array is developed on a 1000 μm thick glass slide. The ML, with a base diameter of 250 μm , exhibits a concavity of approximately 13 μm . Each ML array consists of 240 ML arranged in a hexagonal cluster measuring 5 \times 3 mm², with a pitch of 250 μm .

The elastic nature of the cured PDMS network allows for optical contact between the substrate and the PDMS layer through pressure.¹⁷⁸ Initially, three distinctive labels are created for optical characterization, utilizing the micron size Gadolinium oxysulfide, Gd₂O₂S: 18% Yb³⁺, 2% Er³⁺ (GOSYE) UC phosphor, enhancing the contrast in emission intensity between particles located within the focal volume. The GOSYE phosphor particles are on size scale of <10 μm and are integrated into the PDMS at a concentration of 0.1 weight%, equivalent to 1000 parts per million, (ppm) by mass ratio.

The fabrication of the microparticle layer involves dispersing the optimal weight of the UC phosphor particles in the silicone elastomer base (SYLGARD 184, Dowsil, RTV-A) using a high-speed dispersion device (CAT M. Zipper GmbH). The curing agent (RTV-B) is then introduced to the RTV-A solution in a 10:1 ratio. The mixture is placed in a vacuum desiccator (0.2Pa, 15 minutes) to eliminate air bubbles. Subsequently, the mixture is poured into a 2mm thick polished metal mold and cured at 150°C for 30 minutes in open-air. The elevated temperature ensures the curing of the PDMS layer without compromising the optical and chemical properties of the phosphor particles.¹⁷⁹

3.4 Fabrication procedure of DS phosphor doped unclonable labels

This section outlines the fabrication procedure for an unclonable label, which integrates a Ce^{3+} -doped YAG ($\text{Y}_3\text{Al}_5\text{O}_{12}:\text{Ce}^{3+}$) DS phosphor embedded in a PDMS layer and a ML array featuring a relatively short focal length, $f = 550\mu\text{m}$, in contrast to the UC phosphor-based prototype PULs. Firstly, a master substrate of ML array is designed using the COMSOL Multiphysics software and then printed on a 1mm thick ITO-coated glass substrate through TPL using the Nanoscribe IP-S photoresist. A 256-element ML array is created in a hexagonally close-packed manner over approximately thirty hours. The lenses, with an ROC of $200\mu\text{m}$ and a base width of $250\mu\text{m}$, form a square grid of 16×16 lenses. A subsequent step involves depositing a thin layer of PDMS mixed with DS phosphor particles. The PDMS base is blended with the DS phosphor particles, labelled as S (D50 particle size $9.0 \pm 1 \mu\text{m}$), M (D50 particle size $20.5 \pm 1 \mu\text{m}$) or L (D50 particle size $32.5 \pm 2 \mu\text{m}$), using the high-speed dispersion device to achieve a phosphor concentration of 0.5 wt.% in the PDMS layer. The resulting solution is vacuumed for 12-15 minutes. The solution is poured onto a 1mm-thick glass substrate with $200\mu\text{m}$ spacers, covered with a $400\mu\text{m}$ -thick glass substrate, and cured on a hot plate at 120°C for 15-20 minutes. Replicating ML features onto this thinner coverslip allows for a reduction in label thickness compared to the previous design. A detailed optical characterization of the three DS phosphor is discussed in the following section. Following the curing of PDMS, a ML array is replicated onto the front side of the $400\mu\text{m}$ -thick glass coverslip.

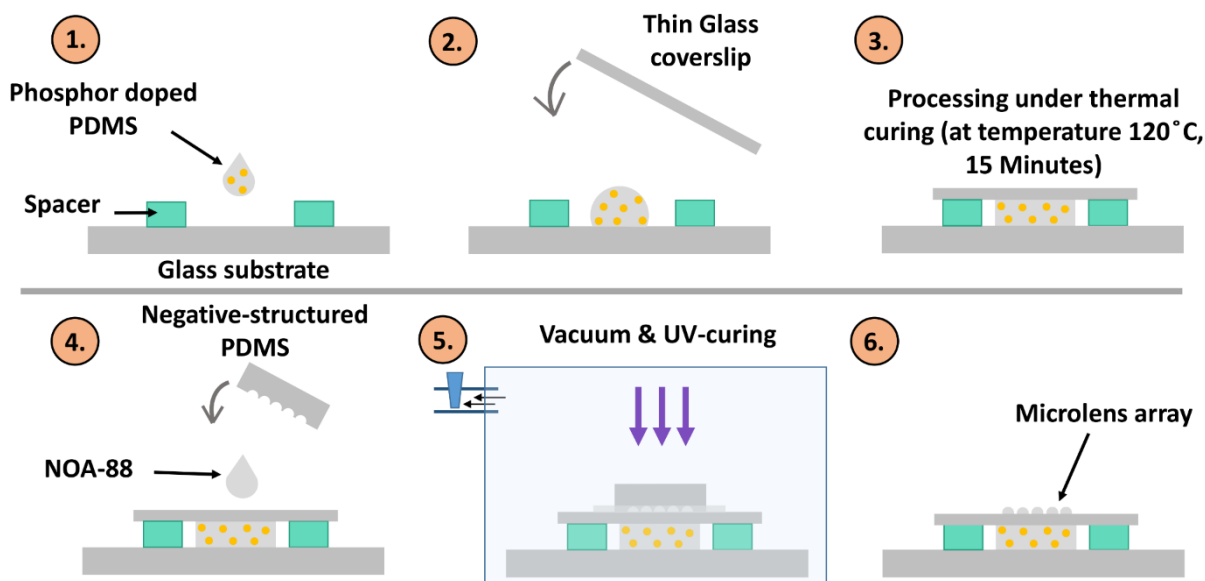


Figure 3.5 A schematic showing the unclonable label fabrication process, featuring ML arrays and commercialized DS phosphor layer. Reproduced with permission from Kumar *et al.*³

Figure 3.5 schematically represents the label fabrication process, with a slight modification to achieve lenses with a reduced label thickness. Initially, a negative structure of the ML is developed on a PDMS stamp. A 10:1 mass ratio of RTV component A and B is used to realise an inverse ML arrays replica on a PDMS, from a master substrate of the ML arrays. This PDMS stamp of negatively replication ML array is processed through pulse-laser deposition (PLD). This technique is chosen for its ability to produce high-quality uniform coating and its suitability for depositing thin layers, particularly in the nm range. While alternative techniques such as sputtering, chemical vapor deposition (CVD) and atomic layer deposition (ALD) are commonly used for thin-film fabrication, PLD stands out due to its precise control over film composition and thickness, as well as its capacity to deposit a wide range of materials.¹⁸⁰ Furthermore, PLD minimizes the risk of contamination and allows for the deposition of materials that may not easily adhere to substrate using other methods.¹⁸¹ Consequently, a (30-50) nm thick aluminium oxide (Al_2O_3) layer is deposited on the ML array substrate. PLD is performed by Dr. Dirk Fuchs at the Institute of Quantum Material & Technology (IQMT) at KIT.

A plasma-etching process followed by vapor treatment with PFOTS silane (trichloro-1H,1H,2H,2H-perfluorooctyl-silane, Sigma-Aldrich) is applied to the oxide-coated negative PDMS stamp.^{182,183} The PFOTS vapor treatment is carried out in a closed desiccator for nearly 10 minutes, creating an anti-adhesive layer that ensures easy removal of the negative PDMS stamp from the UV-cured ML arrays structure.¹⁸² The silane treated PDMS stamp is then pressed onto a glass substrate coated with a commercialized UV-treatable resin, Norland optical adhesive NOA-88, and is exposed to UV light (365nm, 10^3mWcm^{-2}) for 2 minutes. After UV exposure, the PDMS stamp is carefully peeled away. To facilitate removal of the PDMS stamp from the UV-cured ML arrays after each imprint, it is recommended to apply the vapor deposition of the anti-adhesive layer before each imprint. In this section, the discussion is limited to the fabrication procedure; and the scanning electron microscope (SEM) images of the ML arrays produced in the NOA-88 is presented in the following section of this chapter. Considering the refractive index (n) of the cured NOA-88 as 1.57, the focal length (f) of the ML is determined to be $550\mu\text{m}$, using equation 3.1.

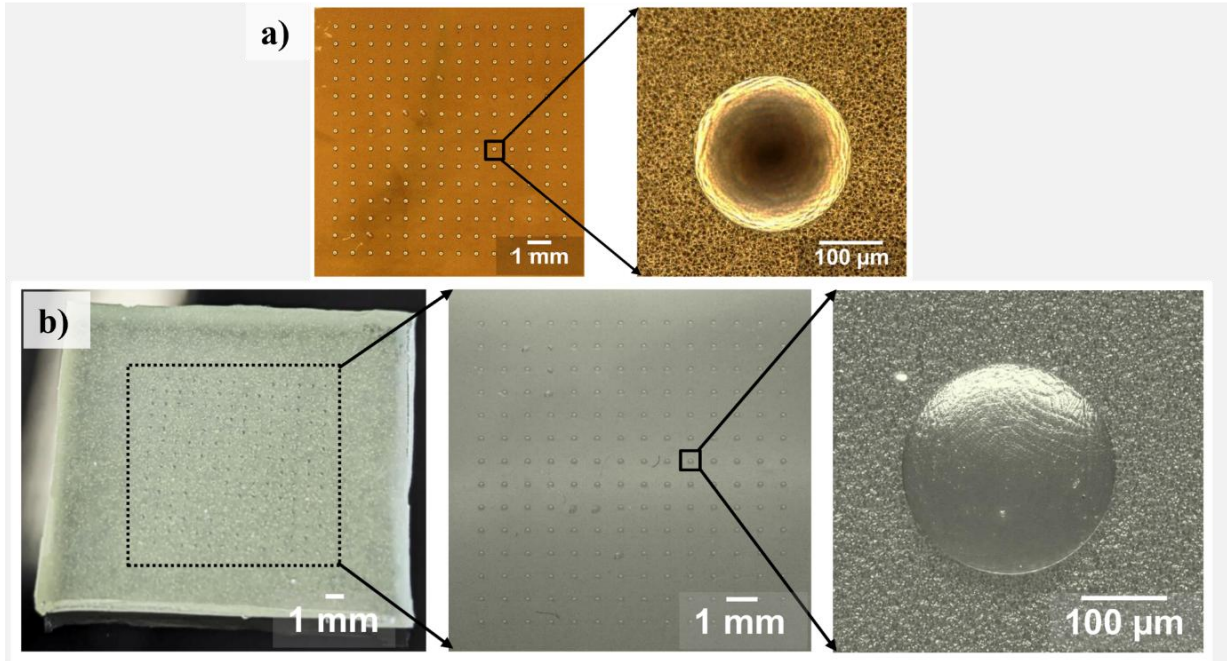


Figure 3.6. a) Image showing the replication of negative microstructure of the ML and silicon micro-cones onto a nickel shim. b) Image of the single layer all PDMS unclonable label. Formation of the unclonable PDMS label is realised by pouring the DS phosphor doped PDMS uncured solution onto the negative master. Reproduced with permission from Kumar *et al.*⁸

3.5 Manufacture of single-layered all-PDMS unclonable label

The manufacture of a single-layered, all-PDMS unclonable label begins with the creation of a master substrate, shown in Figure 3.6. This involves using the DLW technique to produce a master substrate containing a 14×14 ML arrays on a <100>-oriented silicon wafer. The master substrate of ML array is fabricated using the Nanoscribe IP-S photoresist through the 2PP-based 3D printer. This printer develops the ML array structures on the silicon surface over a duration of 36-hours.

After the master substrate is created, surface treatment is conducted to prepare it for replication processes. First, a nanolayer of Al_2O_3 is deposited using PLD to enhance structural resilience. Following this, plasma etching is applied on the master substrate for approximately two minutes, which introduces scratches to the Al_2O_3 surface and therefore activates the surface for subsequent deposition.¹⁸² The plasma-activated oxide layer is then treated with PFOTS silane coating in a closed desiccator for nearly 15-20 minutes, functioning as an anti-adhesive layer facilitating easy release for the subsequent replication steps.^{182,183} To create negative microstructure in PDMS, uncured and degassed PDMS is poured onto the silane-coated master substrate. It then undergoes an additional degassing step to remove any remaining air pockets

between PDMS and micro-structured surface of the master substrate. The degassing ensures complete surface contact, as any trapped air that could disrupt the molding process is eliminated.¹⁸²

Finally, the PDMS is subjected to a thermal curing process to solidify the replicated microstructures. These negative microstructures on PDMS are subsequently transferred onto a silicon wafer using NOA-88 photoresist, resulting in positively microstructured features on the silicon surface. Next, a nickel shim is prepared to serve as a robust negative template for replication. This process involves replicating the ML array structures and silicon microtextures, onto the nickel shim. A series of steps, including chromium deposition, gold deposition, masking and electroplating in a galvanic bath, are employed to achieve this.¹⁸² By carefully controlling the current density, a slow and uniform growth of the nickel layer is achieved, as shown in Figure 3.6 a. The completed nickel shim is subsequently treated with oxygen plasma at 22°C for approximately two hours, further enhancing its surface characteristics for PDMS molding. Dr. Markus Guttman at IMT provided the nickel shim using his in-lab facilities that has negatively replication of silicon texture and the ML arrays. The PDMS solution is prepared by thoroughly mixing RTV-B into phosphor-doped RTV-A at a 1:10 ratio. This mixture is then degassed for 20 minutes to eliminate trapped air. The degassed PDMS solution is poured onto the negative nickel shim, which is contained within a 1mm PMMA frame to define the shape. To ensure optimal surface contact between the uncured PDMS and the nickel's microstructures, the solution undergoes a second degassing phase for an additional 10 minutes. In subsequent step, the PDMS sample is placed on a hot plate at a stable temperature of 100°C for 15 minutes, allowing the phosphor doped PDMS to get cured. Afterwards, the PDMS layer is carefully separated from the nickel shim using a sharp-edged blade. The resulting product is a single-layered, all-PDMS unclonable label with a thickness of less than 2mm. The top surface of this label has positively replicated ML arrays which are surrounded by a silicon-textured surface, while the bulk volume contains randomly dispersed DS particles. This single-layered PDMS label is depicted in Figure 3.6 b.

3.6 Characterization techniques

Lanthanides-based inorganic phosphors are implemented as luminescent particles to realize the unclonable labels. For the UC based prototype PULs, GOSYE UC particles are used. GOSYE phosphor is chosen as the initial UC phosphor due to its efficient in-

house synthesis using a flux-assisted solid-state method.¹⁸⁴ Dr. Ngei Katumo at IMT, KIT synthesized the GOSYE particles via the in-house solid-state reaction method.¹⁸⁴ For the DS-doped unclonable label, commercialized DS particles, ‘YYG isiphor’ are utilized. ‘YYG isiphor’ consists of Ce³⁺-doped YAG phosphor, commercialized by Sigma Aldrich. The choice of YAG-based DS phosphor is driven by the desire to enable excitation with low-cost light sources, such as smartphone flashlight or a 450 nm LED, and to facilitate detection in visible emission, which can be easily captured using a standard smartphone camera. This section presents the SEM characterization of inorganic phosphors and the ML arrays. Furthermore, the steady-state PL spectroscopy analysis of the UC and DS phosphor is conducted.

3.6.1 Scanning electron microscopy (SEM)

SEM serves as a critical analytical tool for examining sample size and their morphological characteristics.¹⁸⁵⁻¹⁸⁷ It operates by directing a finely focused beam of electrons at the sample, utilizing the shorter wavelengths of electrons to achieve nm-scale resolutions.¹⁸⁵ This allows for detailed observation of minute surface features.^{185,187} The SEM accelerates a primary electron beam to high kinetic energy (typically 1-30 keV) using high voltage.¹⁸⁵ When the electron beam interacts with the sample, it induces various signals, including low-energy secondary electrons (SE) from surface interaction and high-energy backscattered electrons (BSE) from deeper layers.¹⁸⁵ Additionally, interactions can generate photons through cathodoluminescence and emit characteristic x-rays.¹⁸⁵ For imaging, SEM primarily collects secondary electrons due to their sensitivity to the surface topography, thereby providing highly detailed images that reveal the sample’s morphology and texture.^{185,187} The morphological analyses reported in this dissertation are conducted using a Zeiss supra 60 VP.

3.6.2 Morphology analysis of luminescent phosphors

A SEM examination provides useful information about the UC and DS phosphors physical properties, opening the door to a deeper comprehension of their properties and potential applications in a variety of technological fields. The UC particles predominantly exhibit a rod-like morphology. Volumetric measurements indicate an average UC particles size of approximately 10µm (shown in Figure 3.7 a).

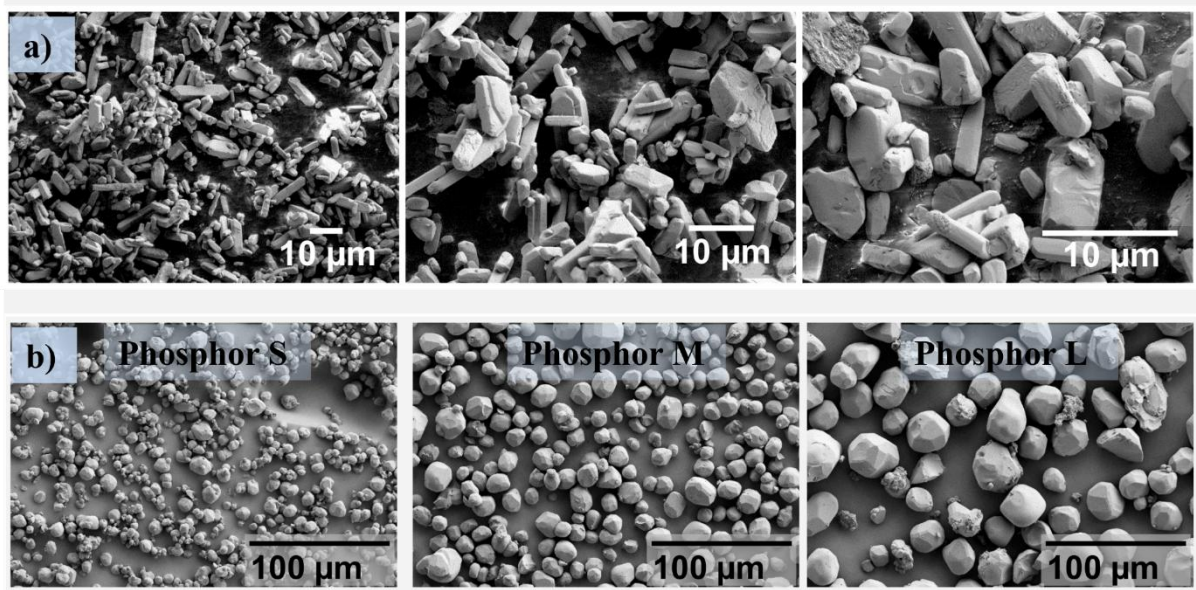


Figure 3.7 SEM images of a) GOSYE UC phosphor particles exhibiting rod-like shape that are well dispersed to each other. b) YAG isophor, with notation S (small), M (medium) and L (large) showing an increasing trend of the size of particles (trend from left to right direction). The particles in each cases are separated to each other. Reproduced with permission from Kumar *et al.*^{2,3}

Figure 3.7 b) provides an extensive representation of the size and morphologies of the three DS phosphor particles – YAG-547-210 (Phosphor S), YAG-560-200 (Phosphor M), and YAG-557-230 (Phosphor L) – purchased from Sigma-Aldrich. These Ce^{3+} -doped YAG phosphors exhibit a spherical structure with distinct particle sizes, as described in section 3.4. The size variation among the phosphor is a key feature highlighted in Figure 3.7 b). Notably, the DS particles demonstrate excellent dispersion without any agglomeration, which is crucial for achieving a uniform distribution within the PDMS matrix. This uniformity ensures that each DS phosphor doped PUL contains an equivalent number of luminescent particles, thereby maintaining a consistent number of bright emission particles over varying the AOIs across different unclonable labels.

3.6.3 Morphology Analysis of ML arrays

Using a SEM, size, structure, and surface morphology of the master substrate for the ML arrays created through the intricate process of DLW, are examined. The SEM image confirms the presence of a smooth and print defect-free surface profile for the ML. In Figure 3.8 a), SEM images confirm that the ML arrays are part of a spherical surface with a base diameter of 250µm. Considering the ROC = 625µm, this leads to a 13µm height for each printed lens. The ML arrays, referred to in Figure 3.8 a), consists of 240 ML organized in a hexagonal pattern of 5mm×3mm and spaced 250µm

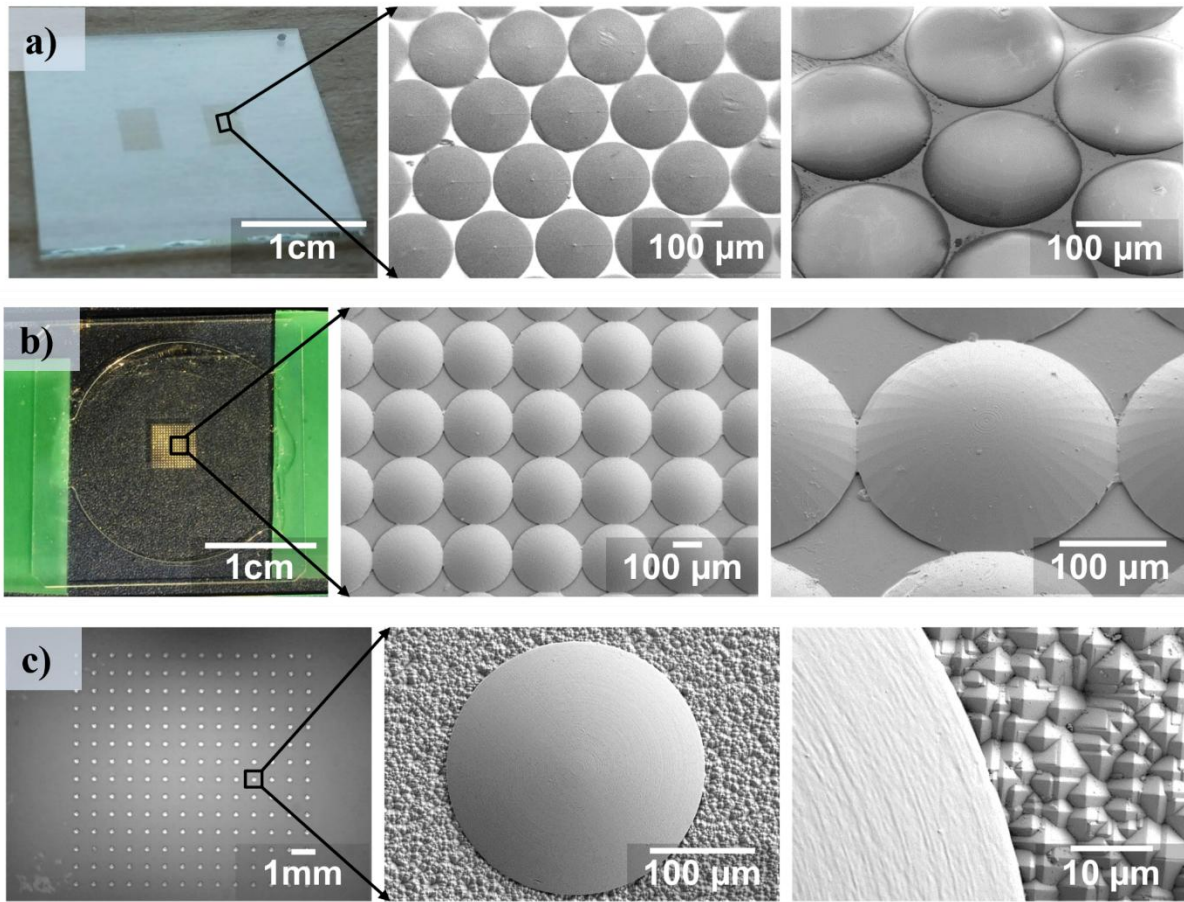


Figure 3.8 Scanning electron microscope (SEM) of a) Printed ML arrays on the top surface of the glass substrate, featuring SEM images of hexagonally packed ML arrays. b) Top view optical and SEM images of square close packed ML array c) Optical image of 14×14 ML arrays distributed in square packing, is captured by a smartphone, and accompanied by SEM images revealing the printed lens structure on the silicon micro-cones. Reproduced with permission from Kumar *et al.*^{2 3 8}

apart (considering the centre-to-centre distance of two neighbour ML). SEM images of the ML arrays reproduced in the NOA-88 validate the precise profile of individual ML, which are arranged in a square close-packing pattern (Figure 3.8 b). In this design, each lens has a base diameter of 250μm. With an ROC of 200μm and base diameter of the designed ML, the height of each ML is approximately 4μm. Moreover, the ML arrays are arranged in a 16×16 square lattice with inter-lens distance of 250μm, considering the centre-to-centre distance. Fundamentally, the SEM investigation gives a visual demonstration of the nature of the ML exhibit improvement process, showcasing the ideal surface qualities and the viability of the bonding instrument. This assessment highlights the accuracy and excellence achieved in the creation of the ML arrays utilizing DLW on a silicon substrate, opening avenues for further investigation and applications in cutting edge optical innovations. Figure 3.8 c) shows a 14×14 ML

arrays that are arranged in square distribution with a centre-to-centre distance of 750µm. Each ML in Figure 3.8 c) has a base diameter of 250µm and an ROC of 200µm.

3.7 Diffuse reflectance

This section outlines the procedure for measuring diffuse reflectance to characterize luminescent phosphors, with specific examples including GOSYE UC particles and the commercially available Ce³⁺-doped YAG DS phosphor.

Utilizing a ultraviolet-visible-infrared (UV-Vis-IR) spectrophotometer for diffuse reflectance spectroscopy (DRS) offers an approach to analyse the optical properties of materials by focusing on the interaction of light with samples that scatter, rather than transmit radiation.¹⁸⁸⁻¹⁹⁰ This method is particularly appropriate for examining solid samples and powders, which are not suitable for traditional transmission spectroscopy.^{4,189,190} The technique relies on the principle that light, upon striking a material, can be absorbed, transmitted, or reflected, with DRS concentrating on the light diffusely reflected after undergoing multiple internal reflections. This reflection is influenced by the sample's intrinsic properties, such as colour, molecular structure, and particle size.^{188,189} Theoretical foundations, such as the Kubelka-Munk theory, further enhance the method's utility by correlating diffuse reflectance with absorption and scattering coefficients, assuming an idealized condition of infinite thickness and uniform illumination.¹⁸⁹

The practical application of DRS involves a spectrophotometer setup equipped with an integrating sphere to efficiently capture scattered light.¹⁹⁰ The setup utilises the PerkinElmer LAMBDA 950 UV-Vis-IR spectrophotometer for acquiring diffuse reflection data from the phosphor samples. This instrument is equipped with a 150mm diameter integrating sphere, the inner surface of which is coated with Spectralon – a highly porous polytetrafluoroethylene (PTFE) material known for its broadband diffuse reflecting properties, manufactured by Labsphere, Inc.⁴ This choice of coating is crucial, as Spectralon is renowned for its high reflectivity across the UV to NIR spectrum, ensuring minimal loss of light within the sphere. The spectrophotometer employs a dual light source configuration: a deuterium lamp for the UV region (wavelengths greater than 319nm) and a tungsten halogen lamp for the extended UV to NIR range.⁴ For deeper UV analysis, down to approximately 250nm, the deuterium lamp is utilized due to its capability to cover this lower wavelength range. This

combination ensures comprehensive spectral coverage for the analysis. The integration of these light sources with a double monochromator enables precise selection of wavelengths for scanning, a critical feature for targeted analysis.

A rotating reflective chopper wheel plays a pivotal role in the setup by splitting the incident beam into two paths: one for sample probing and the other serving as a reference. The sample-probing beam is aligned to pass through the beam opening of the integrating sphere, striking the sample positioned diametrically across. Since the integrating sphere captures and diffuses both specular and diffuse reflected light, careful positioning of the sample and adjustment of the optical setup ensure that light reflecting at sharp angles from the sample has minimal impact on the detector's measurement of diffuse reflectance.⁴ The alignment process involves optimising the angle at which the light beam hits the sample (i.e. AOI) and positioning the sample correctly within the integrating sphere to avoid direct reflections that could distort the measurement, ensuring accurate capture of diffusely scattered light from the sample. As the reference beam is positioned off-centre in the spectrophotometer, it does not impinge directly on the sample. Instead, it interacts only with light scattered from the integrating sphere's surface, minimizing direct reflectance interference and capturing an accurate representation of diffuse reflectance.⁴ Within the integrating sphere, two detectors are used: a PMT (photomultiplier tube) detector, responsive to wavelengths between 200-860nm, and an indium gallium arsenide (InGaAs) detector, responsive to the 860-2500 nm range. The combined data acquisition capabilities of these detectors

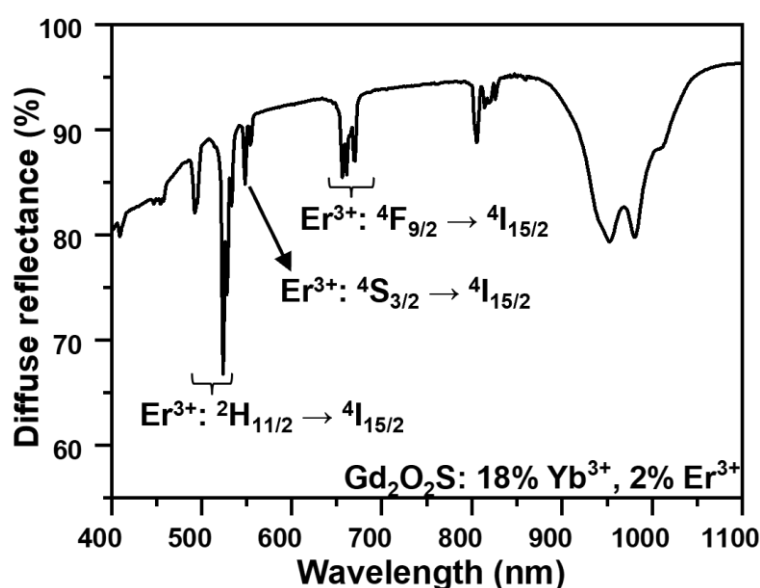


Figure 3.9 Spectral based diffuse reflectance of the UC phosphor $\text{Gd}_2\text{O}_2\text{S}: 18\% \text{Yb}^{3+}, 2\% \text{Er}^{3+}$. Reproduced with permission from Kumar *et al.*²

span the entire UV to NIR spectrum, offering comprehensive coverage for detailed spectral analysis.⁴

Figure 3.9 presents the diffuse reflectance spectra of the GOSYE UC phosphor measured over a wavelength range of 400 to 1100nm using the UV-vis-NIR spectrophotometer. The diffuse reflectance spectrum of the phosphor exhibits distinct absorption features attributed to both Yb³⁺ and Er³⁺ ions. For Yb³⁺, a broad absorption band centred around 980nm is observed, corresponding to the $^2F_{7/2} \rightarrow ^2F_{5/2}$ transition. This absorption is crucial for the energy transfer process to Er³⁺ ions. For Er³⁺, multiple absorption bands are evident: a strong band around 980 nm associated with the $^4I_{15/2} \rightarrow ^4I_{13/2}$ transition overlaps with the Yb³⁺ absorption, facilitating efficient energy transfer. Additionally, weaker absorption bands are observed near 520nm and 650nm, corresponding to the $^4I_{15/2} \rightarrow ^4F_{9/2}$ and $^4I_{15/2} \rightarrow ^4S_{3/2}$ transitions of Er³⁺, respectively. These absorption bands play a vital role in the subsequent UC emission processes of Er³⁺ ions, leading to the characteristic green and red emissions under 980nm excitation.

Figure 3.10 shows the diffuse reflectance spectra of commercially available Ce³⁺ doped YAG DS phosphor, measured using the UV-vis-NIR spectrophotometer. The diffuse reflectance spectrum of Ce³⁺ doped YAG phosphor exhibits two prominent absorption bands. A broad and intense absorption band is centred around 250-300 nm, while a secondary less pronounced band is observed in the 400-500 nm region. These absorption bands correspond to the $4f \rightarrow 5d$ electronic transitions of Ce³⁺ ions, which

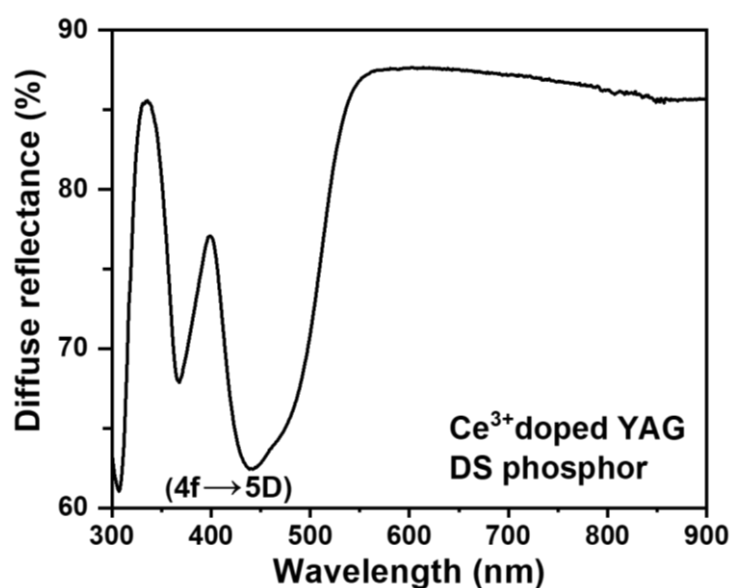


Figure 3.10 Spectral based diffuse reflectance of Ce³⁺ doped YAG DS phosphor. Reproduced with permission from Kumar *et al.*²

are significant for the DS process. In this process, high-energy UV photons are absorbed and subsequently re-emitted as lower-energy visible photons, facilitated by the radiative $5d \rightarrow 4f$ transition of Ce^{3+} ions.

3.8 Steady-state PL spectroscopy

Steady-state PL spectroscopy is an optical analytical technique used to measure the emission intensity of a material as a function of the excitation wavelength. This method provides valuable information on the emission characteristics of materials, aiding in the differentiation of materials with distinct optical properties, even when chemical similarities exist.¹⁹¹⁻¹⁹³ This section outlines the acquisition process of PL excitation and emission spectra using a spectrofluorometer. Additionally, PL emission spectra of the UC phosphor is presented, acquired using a 980nm laser diode (LD) as the excitation source, with UC emission detected via an optical fibre-coupled spectrometer.

3.8.1 PL excitation and emission spectra

The acquisition of PL excitation and emission spectra is conducted using a Varian Cary 50 eclipse spectrofluorometer.⁴ Powdered phosphor samples are positioned within quartz cuvettes, situated in the optical path between two monochromators embedded in the spectrofluorometer.⁴ The first monochromator is linked to a xenon flash lamp, functioning as the dynamic excitation source. This monochromator continuously calibrates the xenon flash lamp, coordinating a thorough scan across the desired excitation range. The second monochromator, connected to the photomultiplier tube (PMT), acts as the signal detector. This monochromator is fixed at the PL emission wavelength of interest during the excitation spectra measurements. The cuvettes are fixed using a specialized sample holder that ensures precise alignment, allowing for accurate and reproducible measurements. One cuvette contains the phosphor sample, while the second cuvette contains is left empty to serve as a control. This arrangement allows for the correction of background signals, ensuring that the observed PL is solely attributed to the phosphor sample. The use of two cuvettes helps to eliminate experimental errors and provide a more accurate representation of the phosphor's optical properties. Throughout the measurement process, the PL of the sample is precisely monitored at a designated wavelength while varying the excitation wavelength.⁴ The dynamic calibration of the excitation monochromator facilitates continuous tracking of PL at different excitation wavelengths.

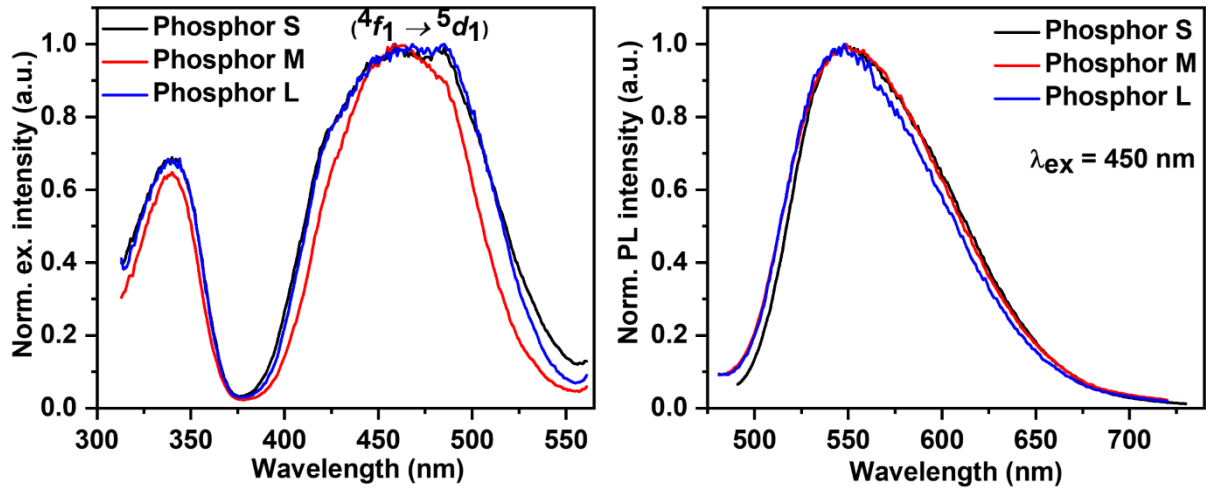


Figure 3.12 Steady-state PL spectra analysis of Ce^{3+} doped YAG DS phosphor. Left and right Figure represent the excitation and emission spectra of the DS phosphor, respectively. The three notation S, M and L refers to three different size range of the DS particles. Reproduced with permission from Kumar *et al.*³

PL excitation and emission spectra of Ce^{3+} -doped YAG DS phosphor is gathered using the Varian Cary 50 Eclipse spectrofluorometer, using the following steps performed: First, the phosphor sample is prepared and securely mounted. For the excitation spectrum, the emission monochromator is set to 450nm to detect emission at this wavelength. The excitation wavelength is then gradually varied from 300 to 560 nm using the integrated xenon lamp, while the emission intensity at 450nm is continuously monitored and recorded. This reveals the wavelengths at which the phosphor absorbs light and emits at 450nm, shown in Figure 3.12 (left-side). For the emission spectrum, the excitation monochromator is set to 450nm, and the emission monochromator is scanned across 480nm to 730nm while maintaining excitation at 450nm. The emission

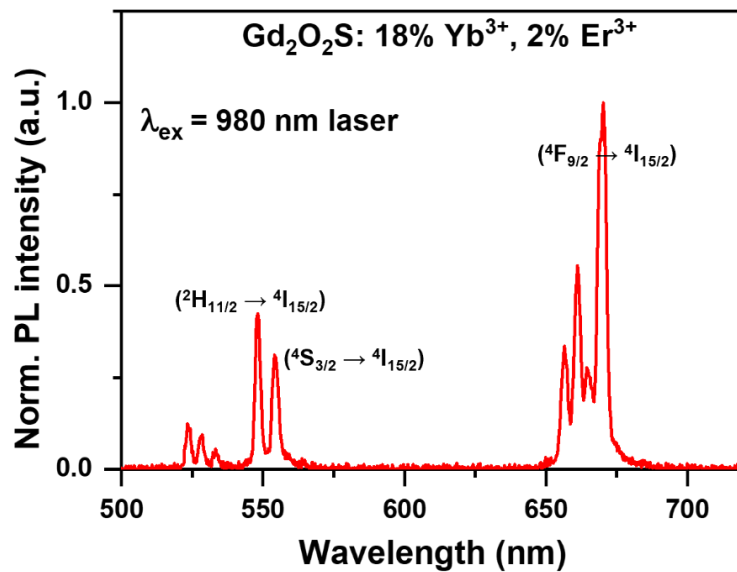


Figure 3.11 UC emission spectra of $\text{Gd}_2\text{O}_2\text{S}: 18\% \text{Yb}^{3+}, 2\% \text{Er}^{3+}$ under 980nm laser excitation. Reproduced with permission from Kumar *et al.*²

intensity is recorded as a function of the emission wavelength, displaying the wavelengths at which the phosphor emits light when excited at 450nm, shown in Figure 3.12 (right-side).

PL emission spectra of UC phosphor is acquired by exciting the samples with an external light source, a 980 nm LD and subsequently collecting the emitted light using a fiber-coupled spectrometer (CCS100/M, Thorlabs). This methodology is preferred over utilizing excitation light from the spectrofluorometer due to several advantages. External sources, such as LEDs or LD, provide a stable excitation wavelength that can be tailored to the precise needs of the experiment, often with higher intensity and better control over the excitation conditions. This approach allows for more accurate excitation-emission profiling and is particularly useful for samples requiring high-intensity or narrowly focused excitation. In this experimental setup, a specific excitation source, a 980nm LD (L980P010, Thorlabs), is directed through lenses to achieve a power density of 1Wcm^{-2} at the sample surface. The excitation light is focused into an integrating sphere where the UC sample is placed. The emitted spectral light is then collected through the sphere's exit port, shown in Figure 3.11. A 950nm short-pass filter (FES0950, Thorlabs) is used to ensure selective wavelength transmission, allowing only the desired UC emission wavelengths to pass through. The collected emission is directed via an integrated fibre optic cable (FP1000URT, Thorlabs) into a compact spectrometer for detection and analysis.

3.9 Experimental protocol

In this section, the excitation sources are meticulously outlined, encompassing both coherent and non-coherent options. The calibration of camera detectors is addressed, ensuring precision in data collection. The calibration of smartphone cameras, specifically focusing on the exposure triangle, is thoroughly discussed for accurate imaging. Further, specific smartphone camera acquisition settings are detailed, providing standardized parameters for experimentation. Schematic representations are provided for various experimental setups, including front illumination-back detection, front illumination-front and back detection, and the design of an unclonable label for front side illumination and detection. Additionally, a schematic illustrates the setup for single smartphone authentication, emphasizing the verification process for the unclonable label. These details offer a comprehensive insight into the experimental framework, laying the groundwork for subsequent procedures and analysis.

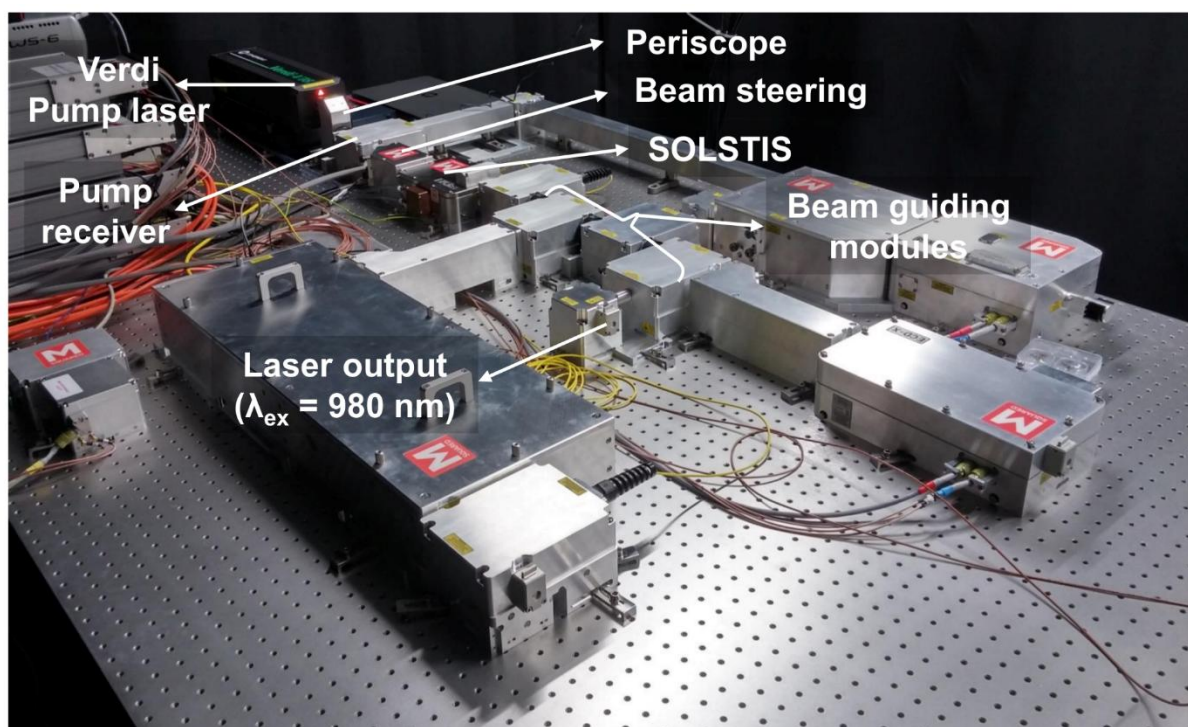


Figure 3.13 Coherent laser source Verdi V-8/V-10 (commercialized from Coherent Inc.) providing the tuned excitation at 980 nm wavelength.

3.9.1 Coherent source

To investigate the UC phosphor-loaded PULs, a class IV Verdi V-8/V-10 laser (commercialized from Coherent Inc.) is employed. The high power of this laser system is essential for achieving a uniform, expanded, and collimated laser beam profile across the entire ML array surface of the UC-doped unclonable label, regardless of the AOI. A 980nm laser diode was found to be insufficient for generating such a consistent illumination profile covering the entire ML arrays area of $\sim 1\text{cm}^2$.

The laser system, shown in Figure 3.13, is a solid-state, diode-pumped system based on the frequency-doubled technology, utilizing neodymium-doped yttrium vanadate crystal (Nd: YVO₄) to achieve a monochromatic green output at 532nm. The system consists of a laser head and a power supply unit connected by a dedicated cable, which houses both optical fibres for light transmission and electrical conductors for control and monitoring, forming an integrated advanced system. The fibre optical cables play a crucial role in efficiently delivering light from the diode arrays within the power supply to the laser head, ensuring the proper excitation of the Nd: YVO₄ crystal to produce the desired laser output. While the Verdi V-8/V-10 is typically used for generating 532nm light through frequency-doubling of 1064nm, it can be configured to

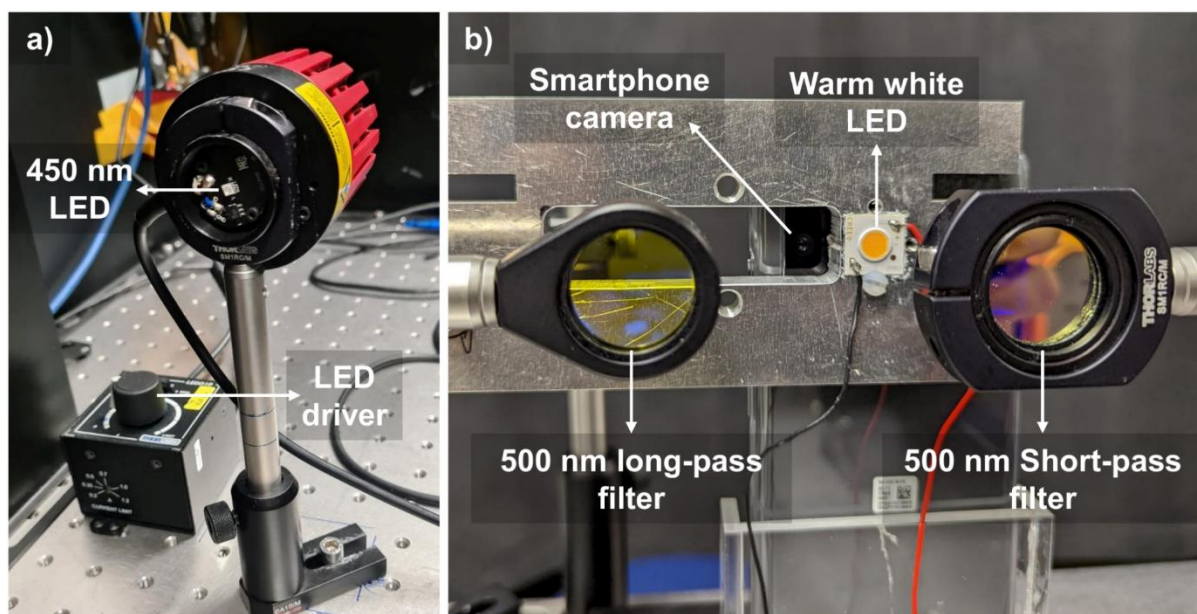


Figure 3.14 Non-coherent excitation light source a) A 450 nm blue LED (M450LP1), commercialized from Thorlabs that is operated with a power control driver (LEDD1B, Thorlabs) b) A commercialized warm light LED source (XLamp, CXA1304) providing the emission in yellow region (dominantly in 450 – 750 nm region).

produce 980nm lasing by optimizing the Nd: YVO₄ crystal and the pump system. This configuration involves pumping the Nd: YVO₄ crystal with 808nm diode laser, exciting the Nd³⁺ ions to the ³F₃ energy level. Lasing at 980nm is achieved through the ³F₃ → ⁴I_{9/2} transition, distinct from the 1064nm lasing transition. The laser cavity is tailored with wavelength-selective mirrors to favour 980nm output, while suppressing competing wavelengths like 1064nm, and may include adjustments to Nd³⁺ doping concentrations or quenching elements. The output coupler is designed to efficiently extract the 980nm light, while thermal management facilitated by an integrated chiller ensures stable operation at high power levels.

3.9.2 Non-coherent source

450nm LED

In this study, a 450nm wavelength LED (M450LP1, Thorlabs) and a warm white LED (CXA1304 XLamp) is used as excitation source for illuminating the DS-doped phosphor labels, shown in Figure 3.14 a) and b). The 450nm LED emits light in an uncollimated fashion at its nominal wavelength of 450nm. It features a singular LED element, which is securely affixed to a heat sink's terminus, the entirety of which is encased within a structure that boasts SM1 internal threading. One of the notable attributes of this mounted LED system is its exceptional thermal stability. This

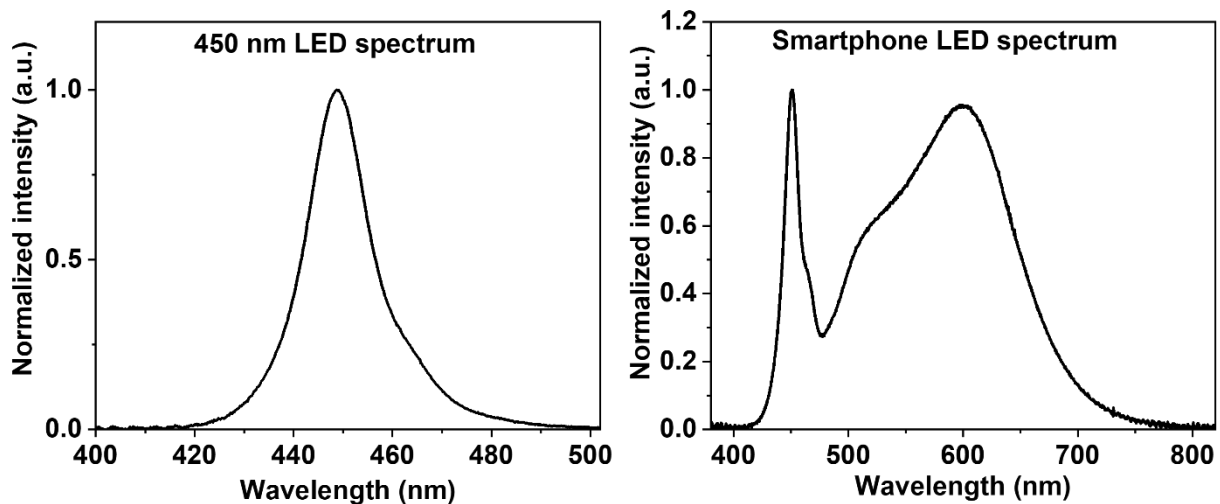


Figure 3.15 Normalized illumination intensity profile against wavelength for a) a 450nm LED (M450LP1, Thorlabs) b) smartphone LED illumination (Samsung galaxy S20).

characteristic is important as it effectively mitigates the potential degradation of the LED's optical output power. To ensure the optimal performance of the LED, it is imperative that it is powered by a constant current, with an upper limit set at 2000mA.¹⁹⁴ Furthermore, the requisite current source must be capable of delivering this specified current at a forward voltage of 3.5V to accommodate the LED's electrical requirements.

To controlling the current supplied to such high-power LEDs, an LED driver (LEDD1B, Thorlabs) has been implemented. This driver functions as a current controller, engineered to serve to high-power LEDs by supplying a current range from 200mA to 1200mA. A distinctive feature of this driver is its adjustable current limit, which serves as a safeguard for the connected LED, ensuring its protection from potential overcurrent damage.¹⁹⁴ The adjustability of the output current limit is a critical functionality, permitting continuous variation from 0.2A to 1.2A. This adjustment is facilitated through the manipulation of a key slot located on the driver unit's frontage interface. This feature guarantees that the output current remains within the predefined safety limit, thereby ensuring the longevity and stability of the LED's performance, irrespective of variations in other operational settings or the modulation of input voltage.¹⁹⁴

Figure 3.15 a) and b) presents the normalized intensity profile plotted against wavelength for a 450nm LED and a smartphone flashlight LED (Samsung galaxy S20) respectively. The measurements were conducted using the compact CCD spectrometer coupled with an optical fibre, with illumination intensity is recorded for an integration time of 0.2 seconds. The spectral output of the 450nm LED is characterized

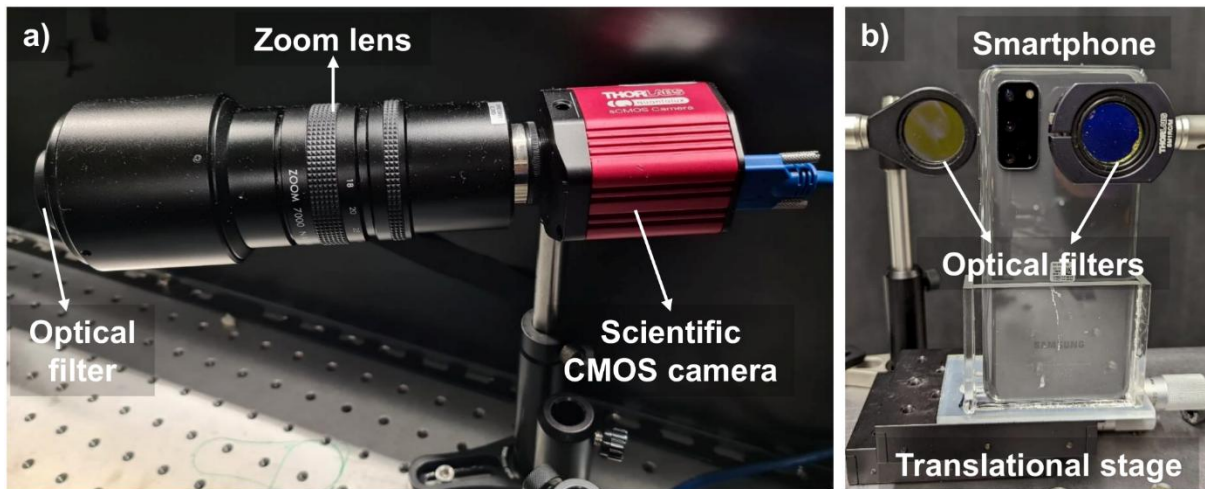


Figure 3.16 CMOS-based camera detector a) A scientific CMOS camera (CS2100M-USB, Thorlabs) camera equipped with a zoom lens (MVL7000, Thorlabs). b) Smartphone camera (Samsung galaxy S20).

by a bell-shaped curve centred at approximately 450nm (i.e. blue-coloured emission), exhibiting a full width half maximum (FWHM) value of 30nm. In contrast, the smartphone LED emits white light, encompassing a broad wavelength range across the visible spectrum, from approximately 400nm (violet) to 700nm (red). This spectrum displays peak emissions around 450nm and 600nm. The peak emission at 600nm originates from a phosphor coating that converts a portion of the blue light into other colours, predominantly yellow.¹⁹⁵

3.10 CMOS-based camera sensors and calibration procedure

This section dives into the point-by-point qualities of the scientific (s)-CMOS based camera (CS2100M-USB, Thorlabs), unravelling its capacities for imaging applications, shown in Figure 3.16 a). The camera sensor, which is categorized as s-CMOS monochrome, has a resolution of 2.07 megapixels, or 1920 (H) × 1080 (V), with a pixel size of 5.04μm. Notably, the sensor exhibits a quantum efficiency of 61% at 600nm, enhancing light sensitivity within the relevant spectral range. The camera system provides a versatile range of imaging parameters. E.g. the exposure time can be adjusted from (2.9×10^{-5} to 7.77) sec in 3×10^{-5} sec increments, enabling optimization for various imaging conditions. A 16-bit analog-to-digital converter (ADC) ensures high-resolution image acquisition. Additionally, the camera supports digital binning from (1×1) to (16×16) pixels, enhancing image signal-to-noise ratio and frame rate, particularly in low-light or high-speed imaging scenarios. The region of interest (ROI) can be flexibly defined, ranging from a minimum of (8×2) pixels to the full sensor resolution of (1920×1080) pixels, accommodating various imaging requirements.

Figure 3.16 b) shows the main camera, centrally positioned in the Samsung galaxy S20 smartphone. This main camera of the smartphone is equipped with a 12 MP Sony IMX555 sensor, which has a size of 1/1.76 inches and a pixel size of 1.8 μ m and features dual pixel phase detection autofocus (PDAF). Additionally, the camera utilizes pixel binning technology to improve performance in low-light conditions.

Zoom lens for optical image enlargement

The s-CMOS camera system, coupled with a Thorlabs MVL7000 zoom lens, provides a flexible imaging platform, referred in Figure 3.16 a). This lens offers a 6 \times optical zoom capability through a variable focal length range of (18-108) mm. The system is designed for working distances between 130mm and 305mm, which can be extended to 610mm by removing the close-up lens. Precise focal length adjustment is essential to optimize image quality across this operational range. The zoom lens offers a maximum aperture of f/2.5, facilitating optimal light gathering for high-quality image acquisition under various lighting conditions. Compatible with both 1/3-inch and 2/3-inch image sensors, the lens provides FOV flexibility ranging from 3.18° to 34.0°, enabling diverse imaging perspectives. Additionally, a maximum magnification of 1.1 \times at a working distance of 130mm can be achieved, suitable for capturing detailed close-up images without compromising image quality.

3.10.1 Smartphones camera calibration: Exploring the exposure triangle

The concept of the exposure triangle in photography and videography relies on the intricate balance between three pivotal elements: ISO sensitivity (as defined by the International organization for standardization), shutter speed, and aperture.¹⁹⁶⁻¹⁹⁸ These elements function collaboratively to capture moments with optimal resolution.

ISO sensitivity: ISO measures the camera sensor's sensitivity to light, influencing the amplification of the signal generated by the sensor's photosites upon capturing light.¹⁹⁶ Generally, ISO sensitivity is kept as low as possible to maintain image quality, as higher ISO settings can introduce noise, thereby degrading the resolution and image clarity.¹⁹⁶

Shutter speed: It determines the duration for which the sensor is exposed to light, measured in seconds or fractions of a second. A faster shutter speed means the sensor is exposed to light for a shorter period, which is beneficial for freezing motion but may require adjustments in ISO sensitivity or aperture to ensure sufficient light exposure.¹⁹⁷

Conversely, a slower shutter speed allows more light to reach but may require a lower ISO sensitivity or smaller aperture to avoid overexposure.¹⁹⁷

Aperture: It refers to the size of the lens opening through which light passes to reach the camera sensor.¹⁹⁸ It is denoted by a f-number (f-stop), where a lower f-number signifies a larger aperture, allowing more light to enter. Aperture not only affects exposure but also influences the depth of field, determining the extent to which different areas of the image appear in focus.¹⁹⁸

Achieving the optimal balance among shutter speed, ISO sensitivity, and aperture is crucial for capturing high-quality photographs and videos under varied lighting conditions. Each setting influences the others, and understanding their relationship is key to mastering photography.¹⁹⁸ For instance, in low light conditions, one might choose a wider aperture (lower f-number) to allow more light into the camera sensor or increase the ISO sensitivity, although this can reduce image sharpness and introduce digital noise. Similarly, to capture the dynamic motion without blur, a photographer might opt for a faster shutter speed, adjusting ISO sensitivity and aperture to maintain correct exposure.¹⁹⁶⁻¹⁹⁸ This delicate balancing act is fundamental to achieving desired photographic outcomes, whether capturing the stillness of a landscape or the dynamic motion.

3.10.2 Optimizing smartphone camera settings for enhanced image quality

The initial step towards achieving professional-level image capture using a smartphone involves comprehensive manipulation of camera functionalities, which is possible through the activation of the Camera2 API (Application Programming Interface).^{199,200} Enabling the Camera2 API facilitates enhanced manual control over fundamental aspects of photographic exposure, specifically the exposure triangle settings.²⁰⁰ This feature can be activated on a variety of smartphones operating on the Android platform, particularly those running versions from Lollipop, Marshmallow, or any subsequent releases up to the year 2021. This includes models from manufacturers such as Samsung, Google (Pixel series), Lenovo, and Xiaomi. To determine device compatibility with the Camera2 API, users can utilize the 'Camera2 probe' application available on the Google Play Store.

Upon enabling the Camera2 API, users may opt for an open-source application developed by Mark Harman, known as 'Camera HD' in the Galaxy store and "Open

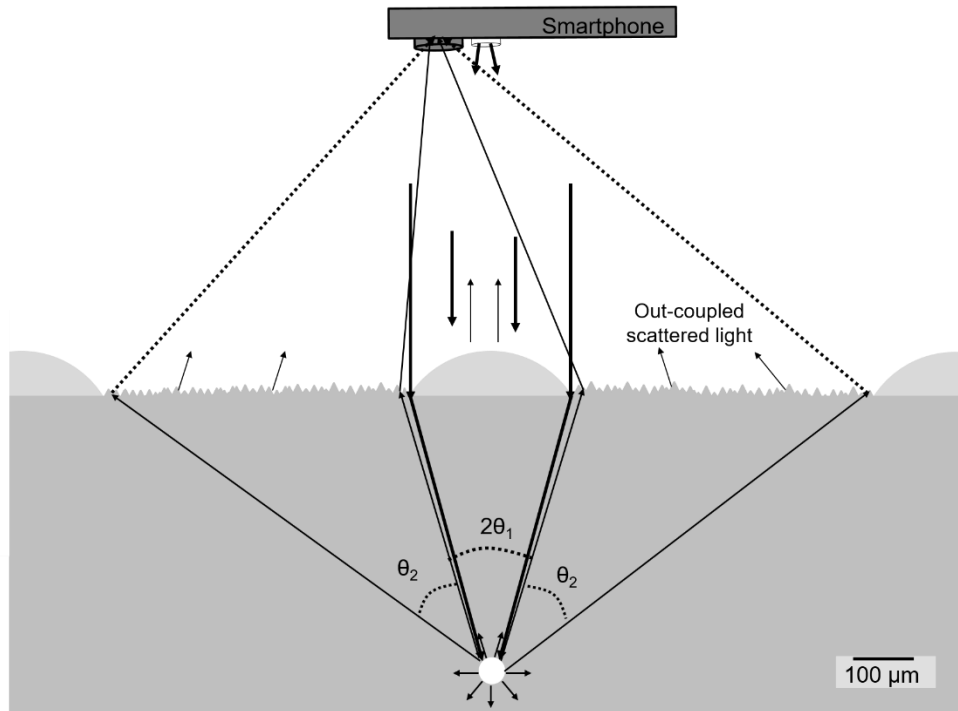


Figure 3.17 Schematic illustration of the PUL illumination using a smartphone flashlight and emission out-coupling towards the front side of the label from a bright particle underneath a ML. Although the emission from the bright particle is isotropic, it exhibits a collimated emission from the overhead ML surface, whereas a scattered emission from the textured surface.

Camera" (version 1.48.1, Code: 77) in the Google play store. To standardizing the testing environment, the application's settings are adjusted to achieve a spatial resolution of 4032×3024 pixels, with a frame rate of 30 frames per second (corresponding to a shutter speed of 1/33 seconds). The white balance is specifically set to 7000K, the colour effect parameter is left unaltered (none), and the auto-level feature is deactivated. The sensitivity of the camera's sensor is manually set to ISO 450, a value that can be varied in accordance with the chosen shutter speed, and the exposure time is fixed at 1/50 seconds and locked. These configurations are preserved within the application's settings manager, allowing for their retrieval and reuse in the image acquisition from the labels under illumination conditions. This experimental is conducted using a Samsung Galaxy S20 smartphone, as the primary imaging device.

3.11 Schematic: Design understanding of an unclonable label for front-side illumination and front side detection

In this section, the ratio of emission light that out-couples from the surface of a single top-head ML and the surrounding scattering surface from an underneath bright particle is mathematically estimated. Figure 3.17 shows a schematic illustration of a smartphone flashlight interaction with the ML and phosphor embedded PUL. As

$$\Phi = 360^\circ$$

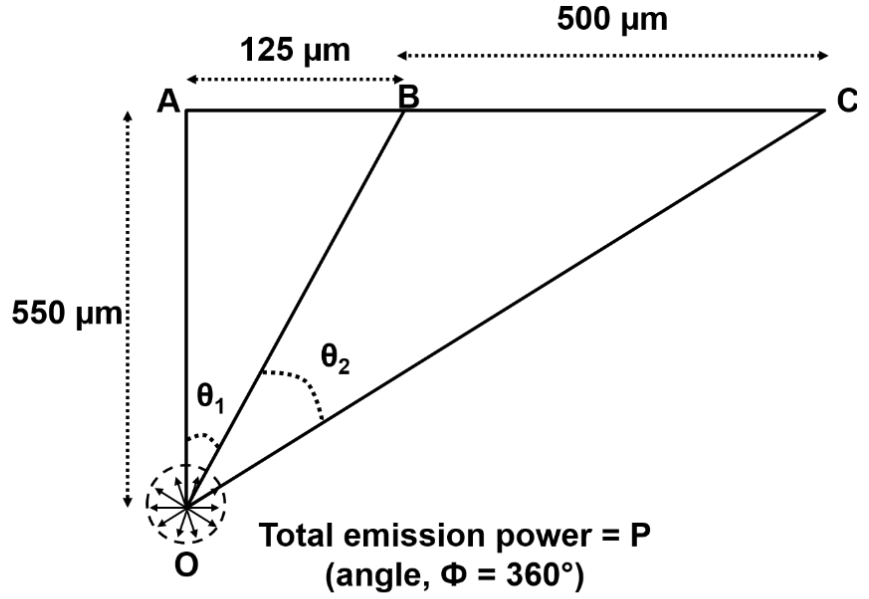
$$\theta_1 = 12^\circ 8'$$

$$\theta_2 = 35^\circ 7'$$

$$P_{\text{collimated}} = \frac{P}{\Phi} * \theta_1$$

$$P_{\text{scattering}} = \frac{P}{\Phi} * \theta_2$$

$$\frac{(I)_{\text{collimated}}}{(I)_{\text{scattering}}} = \frac{\frac{P_{\text{collimated}}}{AB}}{\frac{P_{\text{scattering}}}{BC}}$$



$$(I)_{\text{collimated}} = 1.43 * (I)_{\text{scattering}}$$

Figure 3.18 A mathematical 1-D model of the PUL, wherein a bright particle underneath a ML exhibits an isotropic emission. The model finds that the out-coupled emission intensity from the ML surface is 1.43 times the out-coupled scattering emission from the surrounding textured surface.

mentioned in the design section, the focal length (f) of the ML is 550μm, with a base diameter of 250μm. The center-to-center distance of two non-diagonal ML is 750μm. In the design, a DS phosphor with a mean size (D50 diameter) of ~ 35μm is considered. As shown in Figure 3.17, the smartphone flashlight illuminates the top surface of the label, generating a focal volume underneath the ML.

A mathematical model of the PUL has been hypothesized in a 2D plane (along a single axis), though this model is equally applicable to a 3D representation of the PUL. The interaction between a phosphor particle and the excitation light within the focal volume generates isotropic emission. This emission results in two distinct types of out-coupling towards the front side of the label: the emission light from a bright particle out-couples in a collimation manner through the top-head ML surface, while the emission light from the surrounding rough surface scatters in a non-collimation manner towards the front side of the label. The roughness outside the ML arrays plays a significant role in enhancing the detection of emission light from a bright particle. Specifically, the rough surface promotes diffuse scattering, which increases the amount of scattered light directed towards the front side of the label. Without this rough surface, the emission light from a bright phosphor particle under a ML would predominantly be collimated towards the front side, leading to less efficient detection of emitted light for off-axis

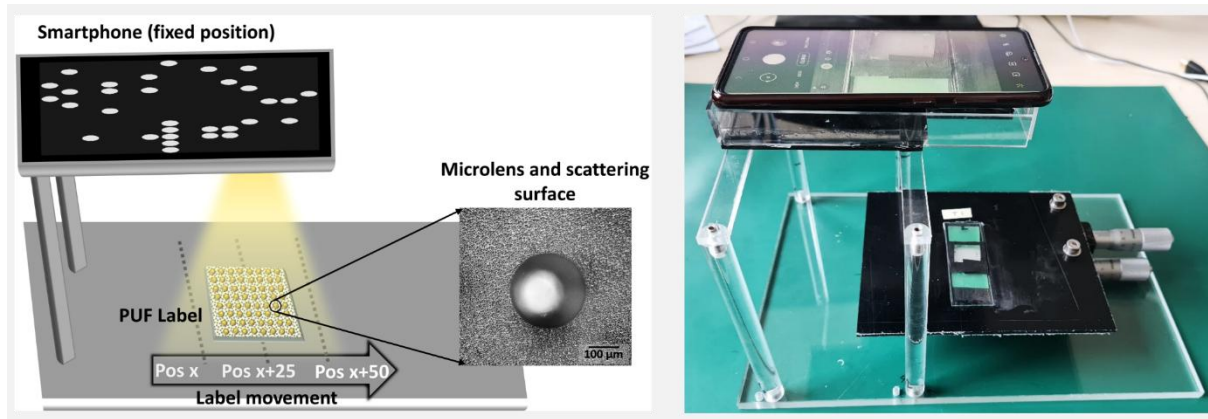


Figure 3.19 Schematic of the experimental setup including a smartphone as excitation and detection source; the setup includes excitation rejection filters (un-seen) glued on smartphone flashlight and camera. The label is placed on a horizontal plane on a movable uniaxial stage, whereas the smartphone is fixed in its position lying in a plane parallel to the label, at a height of 10cm. The label is translated along the axial direction, by 25mm and 50mm to record different point patterns from a single label.

detection in the front. The rough surface, however, scatters emission light in a more diffusive manner, enabling the emission to spread in all directions, including towards the front-side direction of the label.

As illustrated in Figure 3.18, the current design parameters of the label show that the intensity ratio of the collimated output to the scattering output from a bright particle towards the front side of the label is 1.43:1. This implies that a greater amount of emission light from a bright particle is out-coupled from the ML surface towards the front side of the label, primarily due to the combined effect of the collimated emission through the lens and enhanced scattering from the rough surface. Therefore, the roughness outside the ML arrays plays a critical role in enhancing the emission detection by improving the scattering of light, thereby increasing the overall sensitivity of the PUL.

3.12 Schematic of single smartphone authentication setup for verifying the unclonable label

In this section, the experimental method to investigate the unique and unclonable characteristics of the PUL is detailed. Figure 3.19 illustrates the setup, wherein a smartphone serves dual purposes: it provides illumination via its flashlight to excite the label and captures the resulting point-pattern through its camera. The smartphone is positioned at a fixed height of 10cm above the label, ensuring direct illumination on the label's front surface. The label itself is mounted on a uniaxial stage that allows for

precise lateral movements. To filter the light in the experiment, the smartphone is equipped with two wavelength-selective filters: a 500nm short-pass filter (FES0500, Thorlabs) attached to the flashlight, and a 500nm long-pass filter (FEL0500, Thorlabs) in front of the camera lens.

This setup enables the observation of the pattern emitted by the label under illumination. When the smartphone's flashlight is turned on, the ML on the label's surface focus the light into tiny volumes within the phosphor layer beneath. The random distribution of phosphor particles within these focal volumes results in the emission of bright spots, which are captured by the smartphone's camera. Furthermore, the label incorporates silicon scattering textures on its front surface, which enhances the out-coupling of light emitted by particles at angles beyond the critical angle for a flat surface, thereby improving the visibility of the bright spots. The point-pattern recorded by the smartphone camera varies as the label is moved by the uniaxial stage, due to a lateral shift in the focal volumes and consequently, the illumination of a new subset of phosphor particles. This shift results in the generation of a novel pattern, a phenomenon that has been thoroughly analysed with respect to the AOI and the size of the phosphor particles.

3.13 Summary

This chapter discussed the design, fabrication, characterization, and experimentation of unclonable labels using ML arrays and luminescent phosphors. It began with an overview of the ML arrays, including its modelling in COMSOL and fabrication using DLW. Subsequently, the chapter covered the two-layered label and single-layered all-PDMS label, followed by descriptions of the fabrication procedures for each label. Characterization techniques used to assess the quality of the labels were also covered, including SEM and steady-state PL spectroscopy. The experimental protocols involving both coherent and non-coherent light sources were outlined. The chapter delved into the use of CMOS-based camera sensors, detailing the calibration procedure and optimization of smartphone camera settings to enhance image quality. Finally, schematics were presented for understanding the design of unclonable labels under front-side illumination and detection, as well as for a single smartphone authentication setup to verify the unclonable labels.

4 ML arrays and luminescent phosphor based physical unclonable anti-counterfeiting labels

4.1 Introduction

This chapter presents the prototype design and fundamental proof-of-principle study of a PUL consisting of a ML arrays and a phosphor-doped PDMS layer. The ML arrays are printed on an ITO-coated 1mm-thick glass substrate using the DLW method. The PUL is realized by pressing the phosphor-doped PDMS layer to the plane surface side of the ITO-coated glass substrate. GOSYE UC particles, and a commercialized DS phosphor (Ce^{3+} -based YAG) are employed separately to study the operation of the prototype label design. The UC phosphor doped labels involve use of a 980nm laser as an excitation source while DS phosphor-doped labels require the use of 450nm LED as an excitation source. The luminescence patterns from the labels are recorded using a scientific CMOS camera equipped with an excitation rejection filter. The results presented in this chapter are based on the following first-author publication and a submitted patent:

Kumar, V., Dottermusch, S., Katumo, N., Chauhan, A., Richards, B. S., & Howard, I. A. (2022). Unclonable anti-counterfeiting labels based on microlens arrays and luminescent microparticles. *Advanced Optical Materials*, 2022, 10, 2102402.

Howard, I.A., Dottermusch, S., Richards, B. S., **Kumar V.** (2024). Label and system for verifying the authenticity of items and method for verifying authenticity of items, US patent application publication, Pub. No. US2024/0386447 A1, Appl. No. 18/569,761, Pub. Date: Nov. 21, 2024.

.The ideas for the above publications were conceived by the author, Stephan Dottermusch, Ian. A. Howard and Bryce S. Richards after the first author realized that a luminescence-based bright point pattern could be generated from a ML arrays and phosphor doped PDMS unclonable label. Multiple unique point patterns can be obtained from a single label as a function of the AOI of an excitation source, i.e. when

varying the AOI through rotating the label (with respect to the incidence laser beam), different point patterns are observed by a detector from the same label.

During the development of this work, Ngei Katumo, together with the author, prepared the UC phosphor at the Institute of Microstructure Technology (IMT). Subsequently, the author used the phosphor particles (as a dopant) to fabricate a 2mm thick PDMS layer containing randomly dispersed phosphor particles. The ML arrays were designed by the author in COMSOL Multiphysics and printed using the 2PP-based 3D printer with the assistance of Stephan Dottermusch at IMT. The author assembled an optical experiment setup using a periscope system inclusive of a pair of mirrors/lenses, a motorized rotational stage, a 3D-printed sample holder, and a CMOS camera to provide an excitation and detection platform for the unclonable label. Luminescence-based bright and unique point patterns were recorded from different labels using this measurement setup by the author. Stephan Dottermusch and Ian A. Howard, along with the first author participated in developing the algorithm, image processing (in Matlab), interpreting the results, and developing the text for the publications.

This chapter presents a comprehensive study of the unclonable aspects of ML arrays and phosphor based PULs. The study starts with a proof-of-concept study and a prototype authentication system that are presented to demonstrate the working principle of ML array-based labels utilizing a UC phosphor, under a 980nm laser excitation. Next, a detailed qualitative analysis of the bright point patterns from the PULs is presented, highlighting their reproducibility, AOI influence, and uniqueness of patterns. Finally, a quantitative analysis is performed using an image processing algorithm to compare test-reference image pairs and determine the label's authentication probability as a function of AOI offset. These results demonstrate the strong unclonable characteristics of ML array based PULs.

4.2 Label design and working principle

The unclonable label consists of a ML array glass substrate and a PDMS layer containing randomly dispersed UC microparticles. The doping concentration of the UC phosphor in the PDMS is 0.1 wt. %; and the thickness of the PDMS layer is 2mm. To design a ML, a spherical surface of $ROC(R) = 625\mu\text{m}$ is selected, which leads to the formation of a focal point at focal length $f = \frac{R.n}{n-1} = 1900\mu\text{m}$, $n = 1.5$ is the refractive index of the lens material. With a base diameter of $250\mu\text{m}$, the designed ML has a

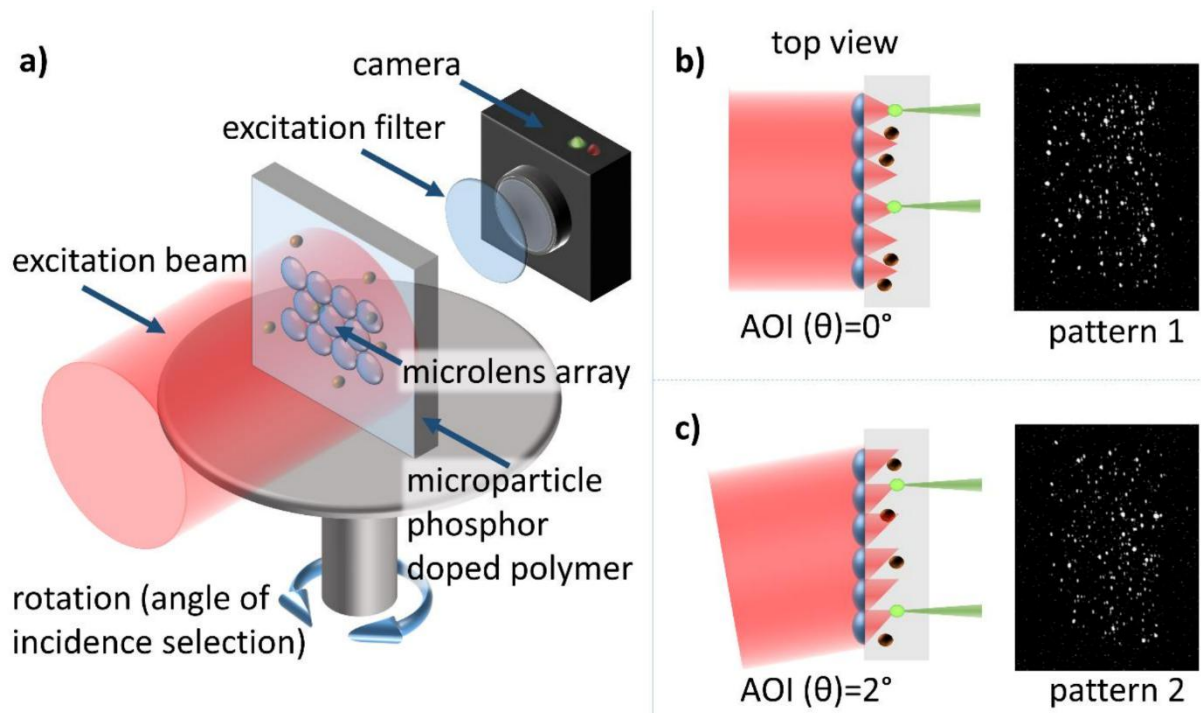


Figure 4.1 Schematic Overview of a PUL utilizing a ML array coupled with phosphor doped PDMS. (a) the mechanism by which a collimated light source illuminates the surface of a ML array, focusing light into the phosphor doped PDMS layer beneath, resulting in the emission of light from specific points. These emissions are captured as distinct bright points by a camera equipped with an excitation filter. The label is mounted on a rotating stage to demonstrate the effect of varying the AOI of the excitation beam. Emission patterns at (b) an AOI of 0° , indicating normal incidence, and (c) an AOI of 2° , showing the shift in the pattern with a slight AOI adjustment. These images exemplify the label's response to changes in excitation angle, serving as a basis for its use in authentication systems. Adapted with permission from Kumar *et al.*²

height of $13\mu\text{m}$. The ML arrays consisted of 240 ML, arranged in a hexagonal pattern of $5\text{mm} \times 3\text{mm}$ with a $250\mu\text{m}$ pitch. Because the cured PDMS matrix is elastomeric, an optical contact is established directly between the glass substrate and the matrix by pressing them together. In this way, when the PUL is illuminated from the ML surface side, a focal volume is generated in $1900\mu\text{m}$. Given the thickness of the glass substrate of $1000\mu\text{m}$, and the thickness of the PDMS matrix (of $2000\mu\text{m}$), the designed geometry of the label ensures that the ML forms the focal volume within the phosphor doped PDMS region. Figure 4.1 a) illustrates a prototypic implementation of the unclonable label design and an authentication system. In its generic form, the label is composed of a ML array and luminescent microparticles randomly distributed on the focal plane. The authentication system requires an illumination source that excites the microparticles and has sufficiently low divergence so that tight focal spots are achieved under the ML. A degree of control over the AOI is required. Furthermore, a camera is needed to image the emission pattern from the label. Herein, the illumination source is

fixed in position and is either an expanded 980nm laser beam (for the UC phosphor), a 450nm light-emitting diode, or a smartphone flash (for the DS phosphor). The laser beam is expanded and collimated by a pair of lenses (focal lengths – 25mm and + 125mm) that are placed in the path of the beam, therefore providing uniform illumination to each ML of the label. The label is placed in a holder on a rotational stage (CR1-Z7/M, Thorlabs) with one degree of rotational freedom. Upon illumination, each ML in the array focuses the incident light to a specific focal volume within the label that may or may not be coincident with a phosphor particle. In the case where a phosphor microparticle is occupying the focus, the emission from that microparticle will be much brighter than the emission from other phosphor particles that are not occupying the focal volume. Because of the random locations of phosphor microparticles (created from the stochastic fabrication procedure), a random subset of foci coincides with microparticles. Thus, a pattern of bright emission points is observed, which resembles a night sky constellation, corresponding to the bright stars. UC phosphors are known for their ability to convert invisible NIR light into visible light in a non-linear manner in a highly efficient manner.^{7,121} It is for this reason that such UC phosphor are initially selected for this application, given that this nonlinearity increases the ratio of the emission brightness of a particle within a focus to one outside of it. As an alternative, a standard DS phosphor (that exhibits linear emission response with an excitation intensity¹²⁶) can also be implemented as bead doping particles within an unclonable label and it is found to generate sufficient contrast to realize a point pattern under a 450nm LED excitation. Finally, the emission from bright particles is captured from the back side of the label using the s-CMOS camera after a 950nm short-pass optical filter, to block the illumination light.

Figure 4.1 b) and c) show the microscopic principle of operation and macroscopically observed emission point patterns from the label. In Figure 4.1 b), excitation light hits the ML side of the label at normal incidence, which leads to the formation of foci directly under their centres, and if a particle happens to lie in such a focal volume, a point of bright emission occurs from that ML. An example image of a UC-based pattern from the label is also shown (Pattern 1), recorded at AOI = 0°. It demonstrates that distinct bright emission point pattern from lenses whose foci coincide with a particle is easy to differentiate from the background. Although emission from a bright particle occurs in an isotropic fashion, a certain amount of the emission will escape the substrate and be captured by the camera, as schematically illustrated in Figure 4.1 b) by the green

cones. A non-normal incidence of the excitation light leads to a shifting of the foci positions, as shown in Figure 4.1 c). Considering a collimated light illumination, the lateral shift (x) of the foci due to a change in the AOI (θ) can be calculated as $x = f \cdot \tan(\theta)$ where f is the focal length of the ML. When there is a change in the AOI, the foci position also changes and this change in position is given by the function $\frac{dx}{d\theta} = f \cdot \sec^2 \theta$. For AOIs close to normal incidence (under small angle approximation), $\sec^2 \theta \approx 1$, so $dx \approx f d\theta$. For the initial demonstration with the designed ML of $f = 1900\mu\text{m}$, a lateral shift (x) of foci is $33\mu\text{m}/^\circ$. Therefore, with $f = 1900\mu\text{m}$, a 2° shift in the AOI causes the foci to move by $66\mu\text{m}$. As a result of this, an entirely unrelated constellation appears at AOI = 2° because the focus volumes overlap with a completely different set of randomly dispersed microparticles, which is far larger than the average size of UC microparticles of $10\mu\text{m}$. This results in the creation of the new point pattern, as shown in Figure 4.1 c).

In summary, the label design exploits the simplicity of observing the overlap of micron-scale focal volumes under ML arrays with random microparticles on the macroscopic dimension (in terms of bright points). Because the position of the focal volumes is affected by the AOI of the light, the bright point pattern will also vary as a function of the AOI. Emission patterns are dependent on AOI, which makes these labels more secure but also impacts the accuracy with which labels and sources should be positioned. It is to be highlighted that the authentication system does not require precision in camera positioning to verify a pattern recorded from a label at a fixed AOI. It is possible to verify the similarity of a point pattern of a given unclonable label that is recorded at different camera positions, by implementing proper image transformation. In the next section, a study is made to understand the effect of camera positions that record different projections of the same pattern under fixed AOI. However, by implementing an appropriate transformation (affine transformation) to different projection images (as test images), it is possible to verify the similarity of the patterns from a reference image.

4.3 Consistency of the PUL's point-patterns across camera placements

The AOI change of excitation light influences the pattern seen as it changes the foci position of ML arrays underneath, which leads to a random overlapping of foci to a different set of particles in the phosphor layer. Under a fixed AOI to the label, when

the camera is placed in different locations behind the label, it observes different projections of a single pattern. This leads to a difference in the perspective views of the pattern. In the following section, the change in perspective is demonstrated through various test images recorded from different camera positions, which are then compared with a reference image. However, a feature-based affine transformation is applied to the different perspective images of a single pattern, which compares the similarities of point pattern images, allowing the different perspectives to be authenticated.^{201,202}

4.4 Overview of Perspective and affine transformation

Before presenting the feature-based similarity comparison of the patterns, an overview of image transformation under perspective and affine transformation is presented with a simple example of a set of 5 lines drawn in a 2D plane.²⁰²⁻²⁰⁴ The human eye (or a camera system) perceives nearby objects as being larger than those that are far away.²⁰⁵ In a general sense, this is called ‘perspective’.^{203,206} While transformation is the transfer of an object from one state to another. As a definition, ‘perspective transformation’ involves the transformation of the coordinates of a given object by forming converging lines that then connect to a point of view that is commonly referred to as a centre of projection.^{203,206} As a result, it is not able to provide an accurate view of various sides of an object. It could be said that after the transformation, the size of the object varies depending on its distance or position from the view plane.^{203,206} Furthermore, it does not maintain the relative proportion of objects in a given space.

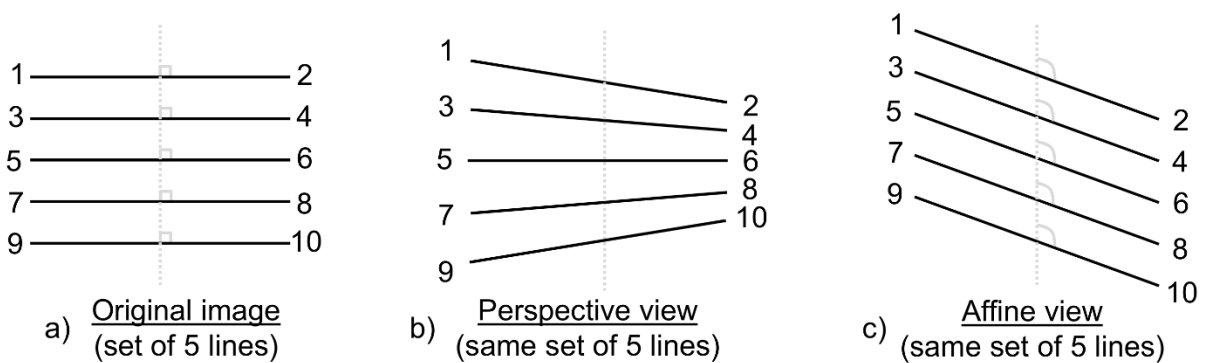


Figure 4.2 Image of 10 point-set that are joined by five different straight line in a 2D plane. a) shows the original image wherein the lines remain parallel at right angle to an axis of symmetry. b) represents the perspective view of the original lines from a different view, wherein they lie on concurrent lines intersecting in a single point some distance away (towards right) of the image. c) shows affine transformation of original image wherein the lines remain parallel, and the mid-point of each line lies on the axis of symmetry, but the angle between the lines and the axis is different to the original image.

Whereas an ‘affine transformation’ is defined as any transformation that is able to maintain both co-linearity (e.g., all points that lie on a line initially remain on that line after transformation) and distance ratios (e.g., the midpoint of a line segment remains the midpoint after the transformation).^{202,204,207} Figure 4.2 a) shows a simple demonstration of perspective and affine transformation of an original image that consists of 5 parallel lines that intersect at a right angle to the axis of symmetry. In Figure 4.2 b), the same set of lines is shown after a perspective transformation, that loses its symmetry and has different angles of intersection with the centre (dotted) line. Figure 4.2 c) shows the affine transformation of the original image that preserves its parallelism, co-linearity, and distance ratio of points with respect to the symmetry axis.²⁰⁷ A brief introduction to image transformation in perspective and affine observation is followed by a discussion of how the appearance of a single point pattern under different conditions of camera position results in different perspectives of the single point pattern image. An affine transformation-based image processing is applied to different test images, which verifies the same patterns based on a similar comparison of bright points of the test and reference images.

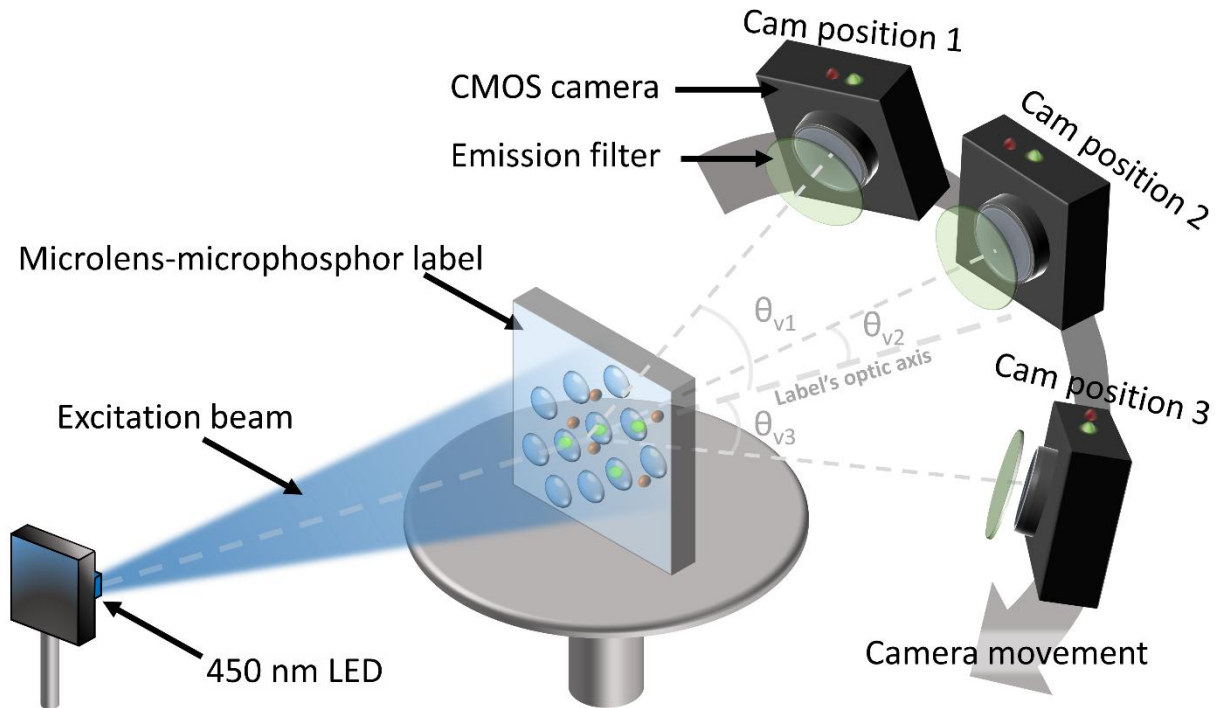


Figure 4.3 Schematic of the Authentication setup with the PUL label illuminated with 450nm LED (at AOI = 0°), and a CMOS camera as a detector for recording the transmission-based PL point-patterns from the labels. Three different camera viewing angles are considered with respect to the label optic axis: at $\theta_{v1} = 25^\circ$, $\theta_{v2} = 10^\circ$, and $\theta_{v3} = -10^\circ$. An arrow indicates how the camera moves behind the label to observe the transmission-based point patterns. Adapted with permission from Kumar *et al.*²

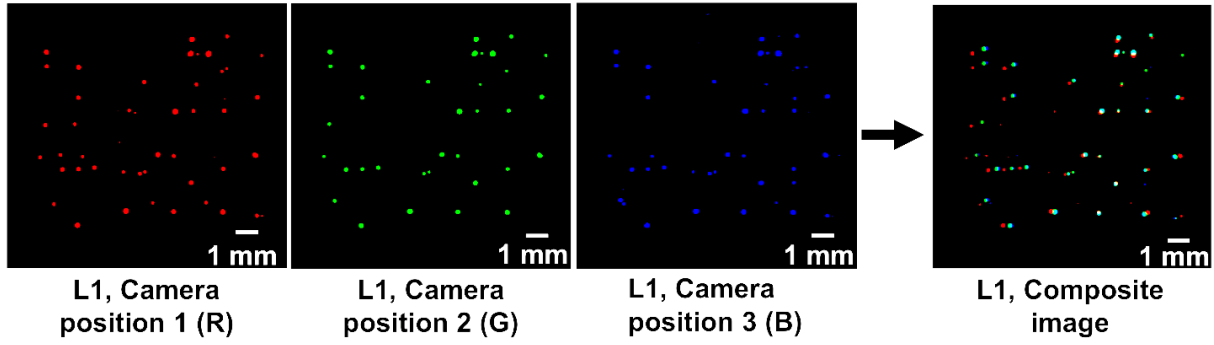


Figure 4.4 Comparison of the point-pattern obtained from a given label (L1) at three different camera positions ($\theta_{v1} = 25^\circ$, $\theta_{v2} = 10^\circ$ and $\theta_{v3} = -10^\circ$ respectively) without affine transformation. In false colours, red (R), green (G) and blue (B) represent the point-pattern images obtained from the three camera positions. The three images are composited into a single frame after non-reflective similarity transformation. The point patterns are simply shifted to their most similar locations. Although they are somewhat in agreement (the same points of the 3D spacer are being emitted), a change in perspective of the camera viewing causes systematic differences to appear. The affine transformation is able to account for this difference. Reproduced with permission from Kumar *et al.*²

Figure 4.3 shows the schematic representation of the authentication setup that is used to investigate the role of different camera placements in recording different projections of a single pattern from a given label. A label with $f = 550\mu\text{m}$ ML arrays (with an inter-lens spacing of $750\mu\text{m}$, centre-to-centre distance) and consisting of 0.5 wt. % of the DS phosphor-doped PDMS layer is placed on the sample stage. The ML surface of the label is illuminated by the 450nm LED, and the luminescence-based pattern is captured by the CMOS camera equipped with a zoom lens and a 500nm long-pass filter. The AOI between the LED and the label is fixed at $\text{AOI} = 0^\circ$, and the intensity of the light from the LED to the label is specified as 10 mWcm^{-2} . To record a single pattern from different perspective views, the CMOS camera is placed in three different positions behind the label recording the same pattern at three different viewing angles. These viewing angles are at $\theta_{v1} = +25^\circ$, $\theta_{v2} = +10^\circ$, and $\theta_{v3} = -10^\circ$ respectively, concerning the label's optic axis. The dotted lines in Figure 2 are meant to help the reader understand the different angular positioning of the camera. For each position of viewing, the distance between the CMOS camera and the label is 32cm.

The grayscale images of a single pattern are captured from the label (L1) at the three different camera viewing angles and processed into MATLAB to represent them in a binary image with a false-colour representation of red (R), green (G), and blue (B) respectively, shown in Figure 4.4. The three images are shifted in a way that maximizes the number of overlapping points between them (For this, a non-reflective similarity transformation-based function is used from the MATLAB image registration toolbox). In the composite image produced by combining the three images R, G, and B, it is

found that the point patterns do not overlap, as shown in Figure 4.4. While the same points emit on the sample regardless of where the camera is positioned, the change in perspective caused by the change in camera positions, causes those same points on the sample plane to be mapped to different pixel locations on the camera. Therefore, a distorted similarity matching is achieved in the composite image for the three different perspective images.

As a part of the authentication procedure, the first step is always to perform an affine transformation on the test image to ensure that it matches the reference image in the most accurate manner possible. (This is discussed in greater detail in the following section of the algorithm development). The method for demonstrating how this is going to eliminate the dependence on the camera position is to select the three brightest points in the red channel image as reference points, then select the same three points in the green and blue channel images to define the affine transformation that will be applied to the green and blue channels. Figure 4.4 illustrates the superposition of the R, G, and B channels after they have been transformed by an affine transform. After performing the affine transformation, the point patterns are equivalent in this case since they consist of the same points. This is shown in the composite image, wherein the test images overlap with a reference image in a single frame, thereby generating a white (W) colour pattern image by overlapping $R + G + B \rightarrow W$ bright luminescent points. Affine transformation in the test images with respect to the reference image eliminates the image distortion due to scaling, rotation, or translation shift of the camera.²⁰⁷ It is therefore possible to implement authentication systems that are not affected by precise camera location.

4.5 Qualitative characterization of the labels

The prototype labels consisting of ML arrays of $f = 1900\mu\text{m}$ and the UC particles doped PDMS layer are used to make qualitative comparisons of the patterns. The bright points in the luminescence-based patterns that are obtained from the prototype UC labels are used as key features. Figure 4.1 shows the experimental setup used for the characterization of the prototype UC-phosphor labels. A 980nm CW laser is employed to illuminate the ML. The excitation beam is expanded to a diameter of 10mm using a pair of lenses. This experiment is carried out with the excitation beam having a power density of 100mWcm^{-2} . An s-CMOS camera together with a zoom lens is used to capture the phosphor emission (seen as bright points). There is a 32cm distance

between the camera and the label, giving a viewing angle of 10° relative to the normal of the label. As a part of the image capture process, a short-pass filter of 900nm wavelength (FES0900, Thorlabs) is inserted before the camera, and this suppressed the presence of excitation light in the image. In Figure 4.5, a qualitative analysis of the similarity between the images creates for the three different cases is presented:

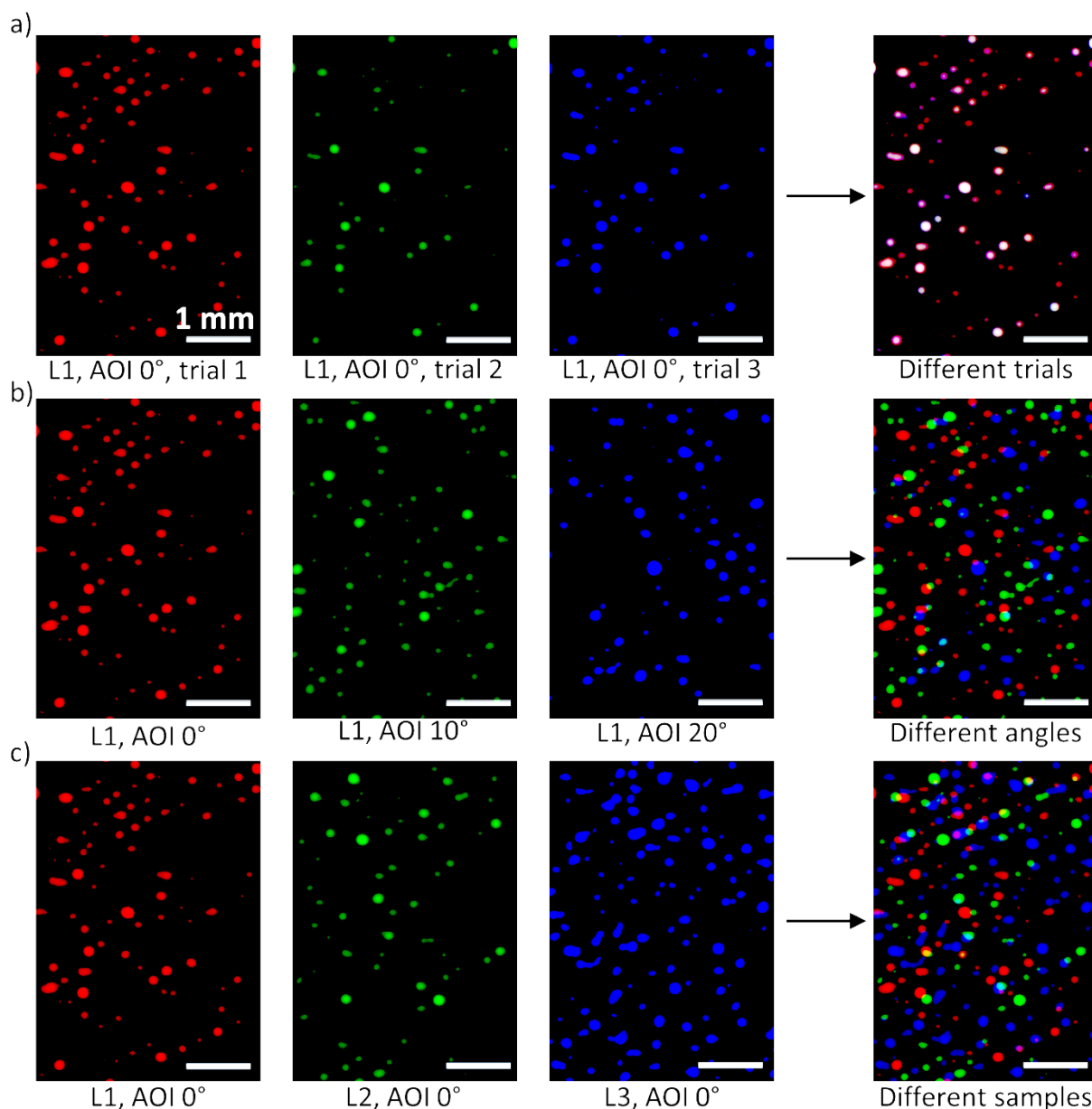


Figure 4.5 Qualitative Analysis of Luminescent Point Patterns Across three different conditions. Each set of conditions is represented through images in red, green, and blue channels, alongside a merged composite image for detailed comparison: a) Demonstrates the consistency of point patterns for the same label (L1) across multiple trials with identical AOI, confirming reproducibility as the images align closely. b) Exhibits the variability in patterns from the same label (L1) when subjected to different AOIs, highlighting the distinct patterns that emerge with angle variation. c) Illustrates the unique patterns produced by different labels under the same AOI, underscoring the individuality of each label. Reproduced with permission from Kumar *et al.*²

4.5.1 Reproducibility of a bright point-pattern

The objective of this study is to validate the consistency of the patterns produced by a single label (designated as L1) when subjected to the same lighting conditions on multiple occasions. To achieve this, the label is illuminated at a perpendicular angle, and its pattern is captured using the s-CMOS camera, this process is repeated three times. Between each capture, the label is removed, and the stage is arbitrarily rotated before being reset to its original perpendicular orientation and the label is repositioned for imaging.

The results of these trials are depicted in Figure 4.5 a), where each of the three images representing the luminescent patterns from the trials is shown. Furthermore, these images are then processed into red, green, and blue channels to create a composite RGB image, effectively overlaying the patterns from the three distinct trials. This composite visualization demonstrates the high degree of pattern reproducibility across the trials, with most of the luminescent points aligning perfectly to form white points in the RGB image, indicating only minimal deviations among the trials.²⁰⁸ This evidence supports the premise that the luminescence-based pattern generation by the label under consistent illumination conditions is highly reliable and reproducible.

4.5.2 Multiple Patterns from a Single Unclonable Label

The capability of a single PUL (label L1) to produce a number of distinct and unpredictable patterns by altering the AOIs is explored. For this purpose, label L1 is secured in the holder and PL-based patterns are captured at three distinct AOIs: 0°, 10°, and 20°. The adjustments to the AOIs led to the ML's focal points shifting by 330µm and 660µm for the 10° and 20° angles, respectively. These shifts are substantially greater than the size of the UC particles within the label, resulting in noticeably different patterns of bright points for each AOI.

As illustrated in Figure 4.5 b), these patterns are merged into a single image frame, creating a final RGB composite where each pattern is represented in a separate channel. Unlike the results shown in Figure 4.4, the RGB composite here displays a variety of pure-coloured spots instead of white spots, clearly demonstrating the unique pattern generation capabilities of the same label when subjected to varying AOIs.

4.5.3 Uniqueness of each Label

The aim of this study is to underline the distinctiveness of individual labels (designated as L1, L2, L3) by sequentially placing each into the sample holder and capturing images at same AOI (in this case, AOI = 0°).

The experiment yields three images, one for each label, alongside an RGB composite image created by merging the three images, each assigned to a different colour channel. This procedure is mirrored in the analysis presented in Figure 4.5 c). The presence of single-coloured bright spots within the composite image serves as evidence of the distinct patterns generated by each label, highlighting their unique characteristics. This observation aligns with the findings from Figure 4.5 c), further emphasizing the lack of overlap between the patterns of the different labels and affirming their uniqueness.

4.6 Quantitative analysis of the labels

The above analysis provides a feature-based qualitative overview of luminescence patterns that are used to compare the prototype design of the UC based PULs. The ability of these labels to manage secured information (using different point patterns) is a key consideration, and therefore, it is important to apply an authentication algorithm to evaluate these labels on a quantitative basis. The following section is a detailed description of the authentication algorithm, along with a flowchart showing how it works, illustrated in Figure 4.6. The algorithm is based on affine transformations of bright point features, which are viewed as a means of examining the similarity of luminescence-based pattern images.

4.6.1 Image processing algorithm

Several approaches have been developed to algorithmically authenticate the patterns based on their input characteristics. One such method for conducting similarity assessments involves comparing point patterns across two images – a 'reference image' and a 'test image' – in a manner that remains unaffected by affine transformations.²⁰⁷ Essentially, this authentication algorithm works by comparing the point pattern of the test image against that of the reference image through a series of defined steps, as follows:

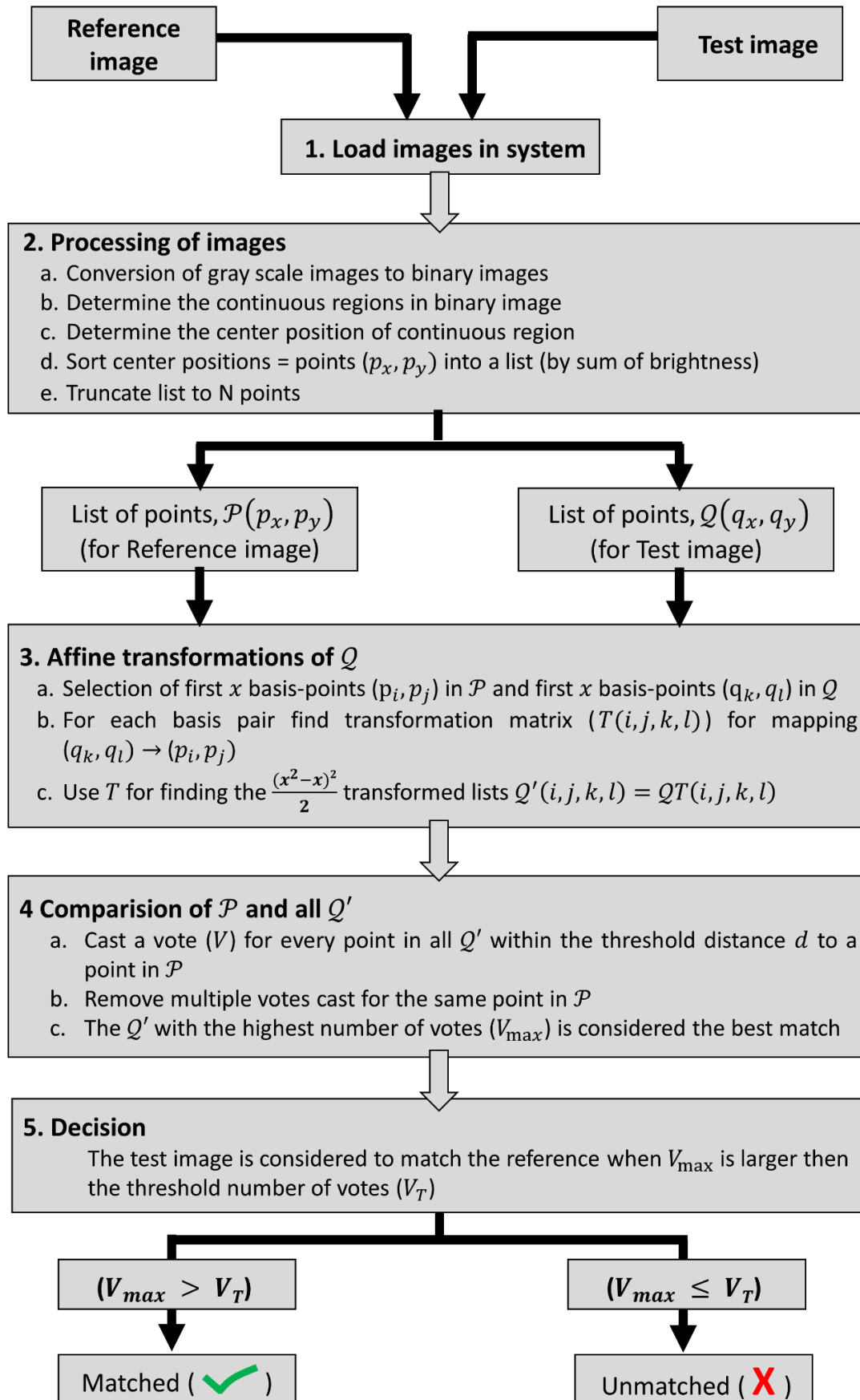


Figure 4.6 Diagram Illustrating the authentication process for Verifying a test pattern from a reference.²

Processing the Image of PL point-pattern into a List of Bright Points

In the preprocessing phase of the authentication algorithm, both reference and test images undergo a series of steps to transform them into a structured list of bright points. This transformation begins with the binarization of the images, an initial step aimed at simplifying the images to a binary format. The procedure begins with an assessment of the ambient noise levels within a designated region external to the ML arrays in the image. This noise measurement serves as a benchmark for distinguishing signal from noise, wherein each pixel intensity surpassing a threshold – set at thrice the measured noise level – is converted to a binary value of '1'. Conversely, pixels falling below this threshold are relegated to a binary state of zero. This binary representation facilitates the identification and listing of contiguous regions of luminescence in the image. Subsequently, the analysis progresses to pinpointing the (x, y) coordinates of the pixel that lies at the centroid of each illuminated region, thereby mapping the geometric centre of every bright spot. The following phase leverages the binary image as a mask over the original captured image. This masking action allows for the isolation and quantitative assessment of each bright region, following the calculation of an integrated value for each spot by summing up the pixel values contained within the masked area. This process yields an ordered array of points (P), meticulously arranged from the brightest spot (P_1), indicative of the highest intensity region within the image, down to the least luminous (P_p), marking the region of lowest brightness.

Test Image vs Reference Image Comparison

In the comparative analysis stage of the algorithm, the focus shifts to the evaluation of the point lists – ' P ', derived from the reference image, and ' Q ' obtained from the test image. The underlying argument is that, should P and Q emanate from the identical label under identical illumination conditions, they should affiliate under the influence of a suitable affine transformation, essentially satisfying the condition $P = Q$. To identify such an affine transformation, the methodology references the framework proposed by Wolfson *et. al.*, aiming to discern a transformation that aligns Q with P , indicative of the test image's authenticity.²⁰⁷ This identification process involves exploring number of affine transformations applied to the test image's point list Q . The objective is to discover a specific transformation under which Q aligns with P , thereby validating the test image's authenticity. For each transformation applied to Q , a voting mechanism is

employed wherein each point in P accrues a vote for every corresponding point in the transformed Q that falls within a predefined proximity. The transformation that results in the highest aggregate of votes is deemed the most congruent, from the similarity standpoint, effectively signifying the transformation that best merges Q with P . The core of this authentication process resides on the vote count: a test and reference image pair are classified as 'matching' if the accumulated votes surpass a predetermined threshold. This decision criterion quantifies the concept of image matching, securing the authentication procedure in a numerical evaluation.²⁰⁷

To validate the patterns, affine transformations are determined as follows: ' x ' number of brightest points are considered in both points lists P and Q , for reference and test images respectively. For each of the $(x(x - 1))$ permutations of the ordered choice of two points from ' x ' brightest points in P , an affine transformation can be found that maps the location of those two points, (p_i, p_j) , onto the positions of each of the $(x(x - 1))$ possible permutations of the brightest points in Q . By doing so, $(x^2 - x)^2$ affine transformations can be derived, which can be applied to the reference point list P before comparing it to the test point list Q . Since the transformation (p_i, p_j) to (q_i, q_j) is the same as the transformation (p_i, p_j) to (q_j, q_i) , therefore only half of the affine transformations are unique and must be taken into consideration. It is, therefore, necessary to compare the two lists using $\frac{(x^2 - x)^2}{2}$ to determine which of them matches more closely, in a manner invariant to affine transformations between the two point-lists of the reference and test image. The results proved to be reliable for finding matching basis pairs when $x = 5$ is used, while at the same time limiting the computational cost that is necessary for making adequate comparisons (to 200).

4.6.2 Steps for generating a threshold number of votes

In the previous section of this chapter, the process for using an algorithm to generate a list of bright points from a test and reference image was described. Additionally, a concept of affine transformation is also discussed that utilizes the list of bright points (of test and reference image) for making the similarity comparison of the test-reference patterns. Briefly, when a co-ordinate based transformed list of bright points of a reference image overlap with an individual transformed point list of a test image, a vote (V) number is generated. A list of vote numbers is generated upon comparing different

affine-transformed point lists of a reference image (Q') with a point list of a test image (Q). From many such comparisons, a transformed point list (Q') of the reference image results in the maximum number of the vote (V_{max}) is considered the best match. However, a minimum limit on the vote number, called as 'threshold vote number' (V_T) must be established to determine the matching and non-matching comparison of a test image with a reference. This section presents the procedure that is used to generate a threshold vote (V_T). The threshold vote is obtained by comparing 100 different reference images with 100 different test images based on the prototype design of the UC labels.

A dataset comprising 100 reference images is generated by subjecting four distinct labels to illumination at 25 different AOIs, which varied from -12° to 12° in increments of 1° . It is critical to note that despite the variation in AOIs, all four labels are constructed using an identical ML arrays design with a focal length of $1900\mu\text{m}$ and are embedded with a phosphor doped PDMS layer containing the same UC particles. Given the design parameters of the UC based PULs, a 1° alteration in the AOI causes a focal shift of approximately $33\mu\text{m}$. This shift scale is significantly larger than the $10\mu\text{m}$ diameter of the UC particles, leading to the expectation that each image's point pattern would be unique and uncorrelated with others. To further validate the authentication protocol, the same four labels are carefully removed from the setup and then precisely reposition within the sample holder to be imaged once more under identical illumination conditions. This procedure is aimed at generating another set of 100 test images. This approach not only underscores the reproducibility of the imaging technique but also sets the stage for a rigorous validation of the uncorrelated nature of the point pattern images across varying AOIs, which is elaborated upon in the subsequent analysis. There are 10,000 unique comparisons that this dataset allows to be made from these 100 references and 100 test images. However, only 100 of these comparisons are likely to be authentic (Concerning the reference and test images that are recorded from the same label under the same AOI).

The next step involves applying the affine transformation-based algorithm to determine how many votes are cast for each test image when compared to the reference image.²⁰⁷ The following conditions are used in the algorithm to generate the results:

The first step is to truncate the points list in each image to the brightest 32 points from each of the two lists P and Q . Authentication is found to be robust when using this

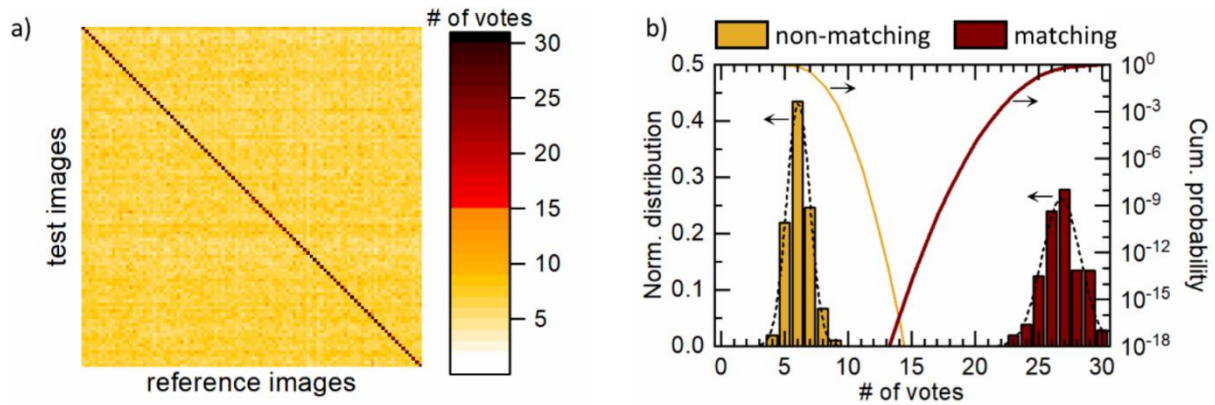


Figure 4.7 Quantitative Analysis of label verification using an affine transformation-based algorithm. A detailed comparison between 100 reference and 100 test images is shown in Figure a) illustrating the vote counts achieved for each paired reference and test image. Figure b) displays the normalized vote count distributions for pairs categorized as 'identical' (same label and AOI) versus 'distinct' (different labels or AOI), with Gaussian fits represented by dashed lines and the corresponding cumulative distribution functions (CDFs) depicted by solid lines. Reproduced with permission from Kumar *et al.*²

number while decreasing the cost of computation at the same time. As a second step, the five brightest points in P and Q are taken as basis points for determining possible affine transformations. As a result, the number of possible affine transformations can be restricted to 200, which provides and allows robust authentication. The third step involves determining the threshold distance for casting a vote. This threshold was found to be 15 pixels, which is half the spacing between ML in the images.

In Figure 4.7 a), the authentication algorithm's ability is depicted through the visualization of vote counts from comparing each pair of reference and test images. The matrix's diagonal, representing instances where test and reference images align for authentication, shows a vote range of 24 to 30 votes, indicating strong matches. In contrast, the non-diagonal elements, which reflect comparisons between non-matching pairs, exhibit significantly fewer votes, ranging from 4 to 9, underscoring the algorithm's ability to discern between matching and non-matching image pairs. Expanding on this analysis, Figure 4.7 b) quantitatively demonstrates the distribution of votes across 9900 comparisons deemed non-authentic and 100 comparisons considered authentic. Through statistical normalization, the count of occurrences within each group is proportionately adjusted to their total count – normalizing non-matching comparisons to 9900 and matching comparisons to 100. This normalization ensures that the sum of probabilities across each distribution equals one, effectively making the area under each distribution curve equivalent to one. This normalization is important for comparing the relative frequencies of vote counts across vastly different sample sizes. High vote

counts are predominantly observed in comparisons involving images from the same label and identical AOI, highlighting the algorithm's precision in confirming matches.

A decisive task is to establish an optimal vote threshold that would categorize a test image as authentic, while also assessing the expected rate of false positive or false negative at or below this threshold. To facilitate this, normalized Gaussian distributions are employed to model the statistical distributions of vote counts for both matching and non-matching image comparisons. These Gaussian fits, depicted as dashed lines in Figure 4.7 b), serve as analytical tools to parameterize the vote distributions, thereby enabling us to predict the likelihood of erroneous authentication outcomes based on selected vote thresholds.²⁰⁹ Utilizing these Gaussian models, the cumulative distribution functions (CDFs) are calculated for two scenarios: one where non-matching images exceed a certain vote count, and another where matching images fall below a certain vote count. These CDFs are represented by two solid lines in Figure 4.7 b). The CDF for non-matching comparisons (yellow line) helps us determine the probability that non-matching images will mistakenly accumulate votes above a specified threshold, which in turn allows us to estimate the false-positive rate for any given threshold.²¹⁰ Conversely, the CDF for matching comparisons (red line) aids in assessing the likelihood of matching images not reaching a predetermined vote threshold, thereby enabling the estimation of false-negative rates. By setting the vote threshold for authentication at 10, the yellow CDF shows a very small chance – only 1 in a million (10^{-6}) – that non-matching images will incorrectly accumulate enough votes to be deemed authentic, indicating a low risk of false positives. Increasing this threshold to 14 votes decreases the false positive rate even further, to a virtually negligible chance of 1 in 1 quadrillion (10^{-15}). On the other hand, examining the red CDF reveals that the likelihood of a false negative, where two matching images fail to reach the vote threshold, is similarly low (1 in a million) when the threshold is set at 20 votes. Reducing the threshold to 14 votes dramatically lowers the chance of false negatives to an extremely rare occurrence of 1 in 1 quadrillion (10^{-15}).

Selecting the optimal threshold for the number of votes in the authentication algorithm is crucial for minimizing the combined risk of false positives (incorrectly authenticating non-matching images) and false negatives (failing to authenticate matching images).²¹⁰ The strategic choice of this threshold is guided by identifying the intersection point of the CDF curves for non-matching and matching image comparisons.²¹⁰ This

intersection represents a balance point where the likelihood of both types of errors is minimized. In the analysis, illustrated in Figure 4.7 b), this balance is achieved at a threshold of 14 votes. At this critical vote number, the statistical analysis indicates that the chance of erroneously authenticating a non-matching pair (false positives) or incorrectly rejecting a matching pair (false negatives) is remarkably low, on the order of 10^{-15} . This remarkably low probability highlights the ability of the proposed method for label authentication, demonstrating its potential for highly reliable and secure verification processes.

4.7 Label authentication as a function of AOI

As discussed earlier, the luminescence-based point patterns generated by the PUL change with AOI. As the AOI changes, the foci position generated by each ML shifts in the phosphor layer. This results in random overlapping of foci with different sub-sets of microparticles, resulting in the generation of unique patterns. The design parameters, which control the rate of change of pattern with AOI, are the focal length of the ML and the size of the microparticles used. A longer focal length ML results in a narrow foci

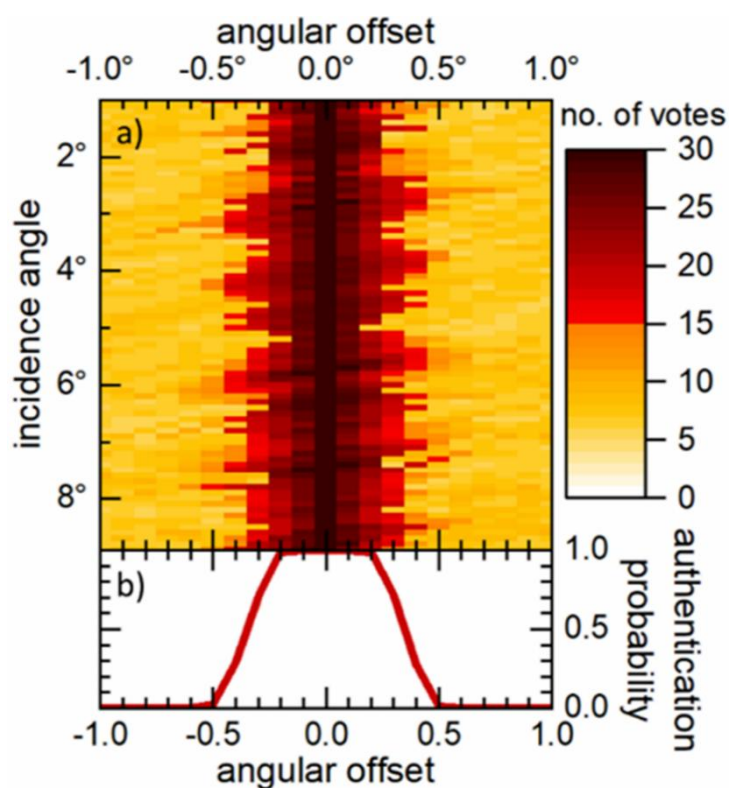


Figure 4.8 a) Results from the authentication algorithm showcasing the number of votes for each comparison between a reference image and test images captured at AOI deviations within $\pm 1^\circ$. b) Graph describing the authentication probability with the angular offset from the reference to test images, utilizing a vote threshold of 14 for authentication evaluation. Reproduced with permission from Kumar *et al.*²

volume, and if the particle is smaller than the foci volume, the patterns change quickly with the illumination angle. A detailed discussion on the role of particle size and a relatively small focal length ML arrays ($f = 550\mu\text{m}$) implemented in the PUL for investigating the AOI tolerance of authentication will be discussed in the following chapter.

This section examines the rate of change of the point patterns for the prototype UC label to determine the AOI tolerances to generate a similar pattern, and thus evaluate their ease of use in anti-counterfeiting. In comprehensive analysis, the prototype UC label's tolerance to angular variations is examined by evaluating the authentication performance across a series of PL-based pattern images. A total of 100 images are captured from the label, spanning angular orientations from 0° to 10° in increments of 0.1° . These images are subjected to a careful comparison using the previously discussed affine-transformation-based authentication algorithm to assess the similarity across varying AOIs. For this purpose, an image captured at a specific AOI serve as the benchmark reference, against which 21 proximal images – spanning a range of $\pm 1^\circ$ from the reference image in steps of 0.1° are evaluated as test cases. The experimental outcomes of this procedure are depicted in Figure 4.8 a), illustrating the volume of votes garnered while comparing a single reference image against its 21 adjacent AOI counterparts. Leveraging the established authentication threshold of 14 votes, a quantitative analysis was then conducted to determine the probability of authentication relative to changes in AOI. This is achieved by calculating the 'authentication probability' for each test-reference image pair, defined as the fraction of the observed vote count over the predetermined threshold, referred as:

$$\text{Authentication Probability} = \frac{\text{Gained number of votes}}{\text{Threshold vote number}} \quad (4.1)$$

Figure 4.8 b) shows the authentication probability plot against the AOI angular offset for the UC-based prototype label. The plot provides an understanding of the label's authentication robustness in terms of AOI deviations, thereby offering valuable insights into its operational tolerances and potential application scope. As can be seen in Figure 4.8 b), the probability of authentication is '1.0' for angular offset within $\pm 0.2^\circ$, but it drops down to 0.9 at AOI offset $\pm 0.3^\circ$ or even lesser as the AOI offset increases. This means that reproducible authentication can only be achieved when the AOI offset is less than 0.2° . The sensitivity of the authentication mechanism to minute AOI variations serves

a dual purpose; on one hand, it enhances security by generating highly specific and unique patterns for slight AOI tuning. Conversely, it necessitates rigorous control over the AOI precision in practical applications, posing a significant challenge in achieving the requisite angular alignment accuracy of less than 0.2° for reliable label verification. This sensitivity to AOI shifts can be attributed to the substantial difference between the ML array's focal length ($f = 1900\mu\text{m}$) and the diminutive size of the particles involved (under $10\mu\text{m}$), which results in pronounced shifts in the focal point location – approximately $7\mu\text{m}$ – for even minimal changes in the AOI. The findings from the prototype UC label examined herein highlight the balance between achieving high-security authentication and the operational challenges of maintaining exacting AOI control.

Qualitative assessments have highlighted that variations in the pattern due to changes in the AOI can enhance the security features of the label. Nonetheless, an excessively high sensitivity to angular changes is not advantageous, as it necessitates extremely precise alignment of the label relative to the excitation source to ensure the AOI is maintained within a very narrow range. This level of precision is required to consistently reproduce a reference pattern from the label for authentication purposes, emphasizing the challenge in balancing security enhancements with practical limitations in the label and source positioning accuracy.

4.8 Design assessment of the unclonable label

4.8.1 Figure of merits

The ML array glass substrate when sandwiched with a phosphor doped PDMS layer generates unique and unclonable point patterns under excitation illumination. The luminescence-based patterns are based on micro-scale randomness resulting from the random overlapping of ML foci with the phosphor particles. The AOI dependence of the label to generate many unique patterns from a single label provides unclonable and unpredictable security. With the changes in AOI, there is a shift in the foci underneath the ML, altering the emitted PL pattern. This capability enables a single label to present diverse pattern at distinct AOIs, enhancing its security. For robust authentication, it is essential to employ numerous distinct patterns obtained at different AOIs, which leverage macroscopic feature detection. For instance, while duplicating a single emission pattern might be straightforward using luminescent ink and low-resolution

pattern printing – bypassing the need for a ML arrays – accurately replicating the complex emission patterns seen at varying angles would necessitate exact replication of the random microparticle positions relative to the ML, with a precision under 100 μm . This precision requirement presents a significant challenge from a technical perspective, making large-scale counterfeiting impractical due to the associated costs and time constraints. Additionally, the micro-scale point patterns, which are a hallmark of these unclonable labels, can be observed with macroscopic simplicity using basic, low-cost detection setups, such as a CMOS camera or a smartphone. The investigations with the prototype UC labels demonstrate that authentication relies solely on the security provided by AOI, independent of detector positioning, thereby mitigating limitations of field-based authentication technologies.⁵⁴

4.8.2 Challenges

Phosphor material and authentication setup challenges

The prototype unclonable label incorporates the lanthanide-based UC phosphor ($\text{Gd}_2\text{O}_2\text{S: Yb}^{3+}/\text{Er}^{3+}$) particles, that are randomly dispersed in a PDMS matrix. The phosphor exhibits visible light emission (major emission peaks at 550nm and 675nm) under a 980nm excitation light. An IR laser ($\lambda_{\text{ex}} = 980\text{nm}$) is implemented to illuminate the label, for generating the AOI-dependent patterns. Moreover, an excitation rejection filter is inserted before the detector to eliminate the excitation light to see a bright luminescence pattern. From an application perspective, it is not desirable to include an optical filter and an IR laser source as an excitation source. Firstly, the IR laser source is more expensive (and less in practice) than low-cost LEDs. Secondly, the excitation wavelength is not compatible with human eye vision, so the application is unsafe.^{211,212} Utilizing a DS phosphor that can be excitable using a 450nm LED (or smartphone flashlight) can eliminate the requirement for an IR laser source. The label demonstration incorporating DS phosphor and a 450nm LED (or a smartphone flashlight) as an excitation source is discussed in the following chapter.

The prototype label design (with closely spaced ML arrays) and the authentication setup discussed in this chapter include an excitation source that illuminates the label from the front surface (i.e. the ML side), and a detector must be placed behind the label (facing the back surface of the label) to observe the luminescence pattern. It has been found that the closely spaced ML arrays distort and collimates the emission of the

microparticles by propagating them towards the source of excitation in reverse order. As a result, the label cannot be used to validate authenticity if a reflection geometry setup is employed, which refers to the arrangement where the excitation source and detector are put on the same side of the label (e.g. using a smartphone flashlight and camera for authentication). For a label to work in reflection geometry, it must be re-designed. Firstly, increasing the spacing of the ML arrays so that the light emitted from a bright particle hits the substrate surface from a single ML head. Secondly, adding a scattering texture to the front surface of the label between the ML arrays to better out-couple the emission light back to the camera placed on the front side of the label.^{213,214} The detailed geometry of the label and the optical system for the reflection-based authentication system are discussed in the following chapters.

High angular sensitivity

The prototype UC label includes a ML array of ($f = 1900\mu\text{m}$) and small-size phosphor particles (on the order of $10\mu\text{m}$). The two design parameters of the prototype label necessitate the requirement of a complex authentication system (e.g. a motorized stage) for achieving high precision in the AOI ($< 0.2^\circ$) to reproduce a similar pattern. This issue of achieving high-precision positioning of AOI can be addressed in two different ways, to preserve the security created by angular dependence. The first approach involves optimizing the label's design by selecting ML with a shorter focal length and utilizing larger phosphor particles. This modification would broaden the AOI tolerance range within which a phosphor particle remains in focus under a ML, effectively expanding the authentication window and making the system more forgiving of slight deviations in AOI. Alternatively, the second strategy leverages the inherently low probability of false positive authentication results to relax the strict AOI precision requirements in practical settings. This could be achieved by comparing a test image, captured at an approximate but not exactly known AOI, against a library of reference images spanning a wide range of AOIs. For example, if the likelihood of encountering a false positive in any given comparison is as low as 10^{-15} , then when conducting ' n ' such comparisons, the cumulative probability of observing at least one false positive across n comparisons can be calculated as:

$$P = 1 - \left(\frac{(10^{15}-1)}{10^{15}} \right)^n \quad (4.2)$$

In experiments where the number of comparisons is significantly lower than the false positive rate, a proportional increase in the false positive rate is observed as a function of 'n', the number of comparisons. Consequently, the likelihood of a false positive increases marginally to 10^{-14} or 10^{-13} when a single test image is compared against a collection of 10 or 100 reference images, respectively. The computational trial is conducted on a desktop PC equipped with an Intel Core i5-3470 CPU at 3.2GHz, required 2056 seconds to complete 10,000 pairwise comparisons as depicted in Figure 4.7 a), averaging approximately 0.2 seconds per comparison. Thus, assessing a single test image against a suite of 10 or 100 reference images would necessitate 2 or 20 seconds, respectively. Given the AOI sensitivity discussed, reference images captured at every 0.2° increment would permit a relaxation in the required precision for AOI in practical applications to $\pm 1^\circ$ or $\pm 10^\circ$ when comparing with 10 or 100 images, respectively. This balance between the false-positive rate and the operational costs, including AOI precision and computational time, remains viable for the label's authentication process. Moreover, optimizing the authentication algorithm could potentially expedite the authentication process further. Presently, 200 distinct affine transformations are considered for each test-reference comparison, a number that presents considerable room for reduction. This reduction could be achieved by implementing fiducial markers on the label's surface to pre-estimate the label's orientation relative to the imaging device, thereby narrowing down the requisite range of affine transformations to be evaluated.²¹⁵⁻²¹⁸ Such an optimization not only promises to shorten the authentication time but also to moderate the risk of false positives, especially as the array of reference images broadens.

The weak contact assembly of the label

The prototype UC label consists of an ML array (printed on a glass substrate) which is sandwiched on top of a phosphor doped PDMS layer, by applying a light press onto the PDMS layer. Although the ML array glass substrate makes optical contact with the phosphor-doped layer, this form of label assembly presents a weak contact resistance. It has been observed that the point pattern produced by the ML arrays developed on a glass slide, and the underlying phosphor doped polymer layer gradually changes over time due to the slight slip between the glass slide and the phosphor doped polymer layer. The label will then fail to authenticate against the original reference image that is taken. To overcome this challenge, revised label designs is explored in chapter 5

where the ML layer is firmly bonded to the polymer layer. Chapter 6 demonstrates the working principle of a single-layer unclonable PDMS label, which consists of random phosphors dispersed over its bulk volume and has ML arrays surrounded by a scattering surface on its top surface.

4.9 Summary

This chapter presents an in-depth examination of a novel anti-counterfeiting technology using a ML array combined with UC phosphor layer to produce PULs, highlighting their potential to significantly enhance product security. The chapter progresses to detail the design and operational principles of the preliminary label, which utilize the unique interplay of ML arrays and the UC particles to generate distinctive and unclonable luminescence patterns. The study evaluates the robustness of the label's point-patterns through both qualitative and quantitative analyses. It confirms their consistency across various camera placements and demonstrates the effectiveness of an image processing algorithm in authenticating the labels, employing a threshold number of votes for validation. Furthermore, the chapter delves into the detailed role of the AOI in creating multiple secure patterns from a single label, thereby adding an additional layer of security. These preliminary PULs demonstrate the capability to authenticate test images, maintaining the AOI tolerance up to 0.2° relative to the reference image. Despite facing challenges such as the need for precise control over the AOI, it proposes potential solutions to enhance the practical application of these labels. Concluding with a summary, the chapter underscores the label's innovation in creating a secure, unclonable pattern, marking a significant advancement in the fight against counterfeiting and setting a foundation for future research in product authentication technologies.

5 Expanding the AOI tolerance of the unclonable anti-counterfeiting label's design

This chapter deals with the design and engineering aspects of the PUL, focusing on how these features were implemented to facilitate authentication. The design considerations include a) a shorter focal length of the ML arrays and b) large-size DS phosphor particles whose excitation (in the blue region) and emission (in the green region) fall within the visible wavelength region.^{219,220} Moreover, different size of phosphor particles are incorporated into the label design with given ML arrays (of $f = 550\mu\text{m}$) and the AOI tolerance behaviour for regenerating similar patterns is investigated. Furthermore, the architectural design of the label is advanced by attaching the ML array glass substrate directly on the top of a phosphor-doped PDMS layer, therefore providing a more stable label system compared to the UC-doped unclonable label for authentication. A study of the AOI tolerance for generating similar patterns from a given label is conducted using a transmission-based authentication system, wherein the excitation source and camera detector are placed at two sides of the label (facing the front and the back surface of the label respectively). Additionally, a demonstration of the label's point pattern generation in a reflection-based authentication geometry is presented, wherein a single smartphone is used for both excitation (using the smartphone flashlight) and detection (using the smartphone camera). The results discussed herein are based on the following first-author publications:

Kumar, V., Dottermusch, S., Katumo, N., Chauhan, A., Richards, B. S., & Howard, I. A. (2022). Unclonable anti-counterfeiting labels based on microlens arrays and luminescent microparticles. *Advanced Optical Materials*, 2022, 10, 2102402.

Kumar, V., Dottermusch, S., Chauhan, A., Richards, B. S., & Howard, I. A. (2022). Expanding the angle of incidence tolerance of unclonable anticounterfeiting labels based on microlens arrays and luminescent microparticles. *Advanced Photonics Research*, 202100202.

The work is conceived by the first author in close coordination with Dr. Ian Howard and Prof. Bryce Richards. As presented in chapter 4, the AOI tolerance for the UC label is $\pm 0.2^\circ$. By incorporating a short focal length ML array ($f = 550\mu\text{m}$), and large-size phosphor particles (with a diameter of $30 - 35 \mu\text{m}$), an $18\times$ enhancement in the AOI tolerance has been achieved, allowing for a $\pm 3.6^\circ$ to reproduce a similar pattern from a given label. The first author in presence of Dr. Stephan Dottermusch develop the ML arrays (of focal length, $f = 550\mu\text{m}$) using the 2PL based 3D printer. SEM images of the 3D-printed ML arrays and the DS phosphor particles are captured by Dr. Stephan Dottermusch together with the first author. The replication of ML arrays on a glass substrate using the master mold, fabrication of the DS phosphor-doped unclonable labels, and the optical experiments using an excitation–detection–based authentication setup are conducted by the first author. Dr. Dirk Fuchs at the Institute of Quantum Materials and Technologies (IQMT), KIT has provided the facility of PLD of Al_2O_3 on the ML array substrate. Dr. Arndt Last at the IMT has provided the technical support for capturing the experimental setup shown in Figure 5.1 b). All the authors have contribution in interpreting the results.

5.1 Introduction

A PUL has been developed consisting of a ML array laminated on top of a polymer layer. This polymer layer is doped with phosphor particles, that are randomly dispersed in its bulk volume, as illustrated in Figure 5.1. Each of the ML focuses the incident light into a specific focal volume which may or may not contain a phosphor particle (Figure 5.1 a). A phosphor microparticle located at the focus of a ML emit light much brighter than phosphor microparticles that are not located at the ML focus. It is critical to note that due to the random locations of the microparticle phosphor particles in the polymer layer, there is a random subset of phosphor particles that coincide with ML arrays foci, and therefore, the label shows a unique pattern of bright luminescence emission, looking alike stars in the night sky. As shown in Figure 5.1 b), a smartphone camera can easily capture this unique constellation of glowing luminescent point pattern.

In chapter 4, it is established that the positioning of the camera – whether moved or rotated – does not alter the observed pattern from a PUL. Such movement simply captures a varied projection of the emission pattern. Nonetheless, applying an affine transformation to align the test image with the reference image during the authentication process successfully alleviates any adverse impacts arise from the

camera positioning. Contrarywise, the AOI of the light source plays a critical role in altering the focal spots within the ML arrays, thereby creating distinct emission patterns from the same label. By employing a range of AOIs, it is possible to generate unique PL patterns from a single label. For ensuring the security of the proposed system, it is imperative to authenticate the label by comparing multiple distinct emission patterns obtained at varying AOIs. This is crucial because simulating a single bright-point pattern could be relatively straightforward through low-resolution printing of a PL pattern using standard printing technology, bypassing the necessity for a ML arrays. Such an approach could mimic the outcome of using a single AOI. However, replicating the intricate emission patterns that arise from different angles poses a significant challenge. This is because accurately positioning the random microparticles in relation to the ML arrays – with sub-100 μm precision – is a technically demanding task. Achieving this level of accuracy is impractical on a large scale, considering the

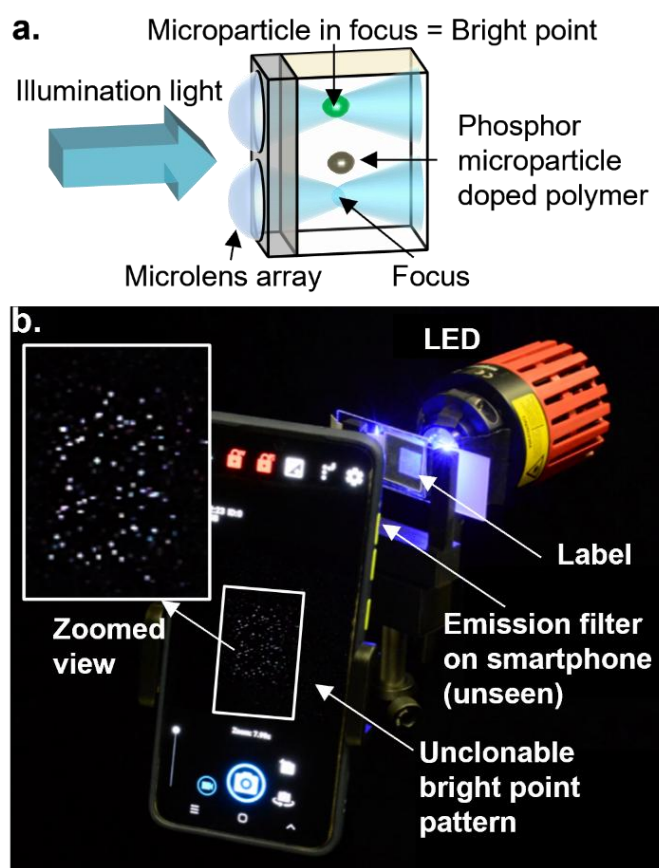


Figure 5.1 Illustration of a secure PUL featuring a ML array affixed to a polymer layer doped with DS particles. a) Each ML focuses incoming light into a specific area in the polymer layer. The DS particles within these focused areas shine more intensely than those outside, creating a distinctive constellation of bright spots on the label. b) Particles situated at the ML foci emit sharply, forming a pattern akin to a starry sky, which can be captured using a smartphone. In the depicted scenario, a 450nm LED illuminates the label, and the PL emission is recorded by a smartphone camera equipped with a 500nm long-pass filter. Reproduced with permission from Kumar *et al.*²

associated costs and time requirements, thus maintaining the integrity of the unclonable label's security mechanism.

5.2 Design and working principle of the unclonable label

The introduction part of this chapter details the process by which a distinct point pattern is generated from a PUL when it is illuminated with a 450nm LED, and how this pattern is captured using a smartphone camera. Within the framework of this label configuration, two critical factors emerge as essential for evaluating the label's sensitivity to variations in the AOI concerning the generation of a consistent pattern: (1) the ML focal length, and (2) the diameter of the phosphor microparticles. A tolerance to the AOI is characterized as the maximal allowable angular deviation between the reference and test images, wherein the test image remains verifiable. The ML focal length controls the degree of lateral displacement of the focal area with changes in the AOI. This concept is graphically represented in Figure 5.2, which considers three distinct labels with phosphor particles of varying sizes, designated as label S, Label M, and Label L. The formula $\frac{dx}{d\theta} = f \sec^2 \theta$, where ' dx ' is the lateral shift of the focus due to an AOI change ' $d\theta$ ' and ' f ' represents the focal length of the ML, mathematically describes this lateral displacement. At AOIs nearing perpendicular, $\sec^2 \theta$ is approximately equal to 1, simplifying the formula to $dx = f d\theta$. In the preliminary design of the UC-based PUL, a ML array with a focal length, ' f ', of 1900 μm is employed, resulting in a calculated dx of 38 μm per degree.² Initially, the use of a shorter focal length is inhibited by the substantial thickness of the ML substrate (1000 μm). However,

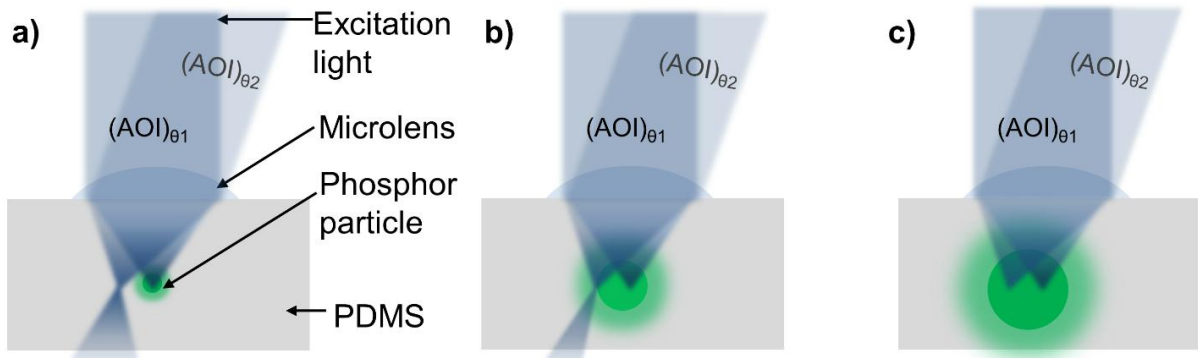


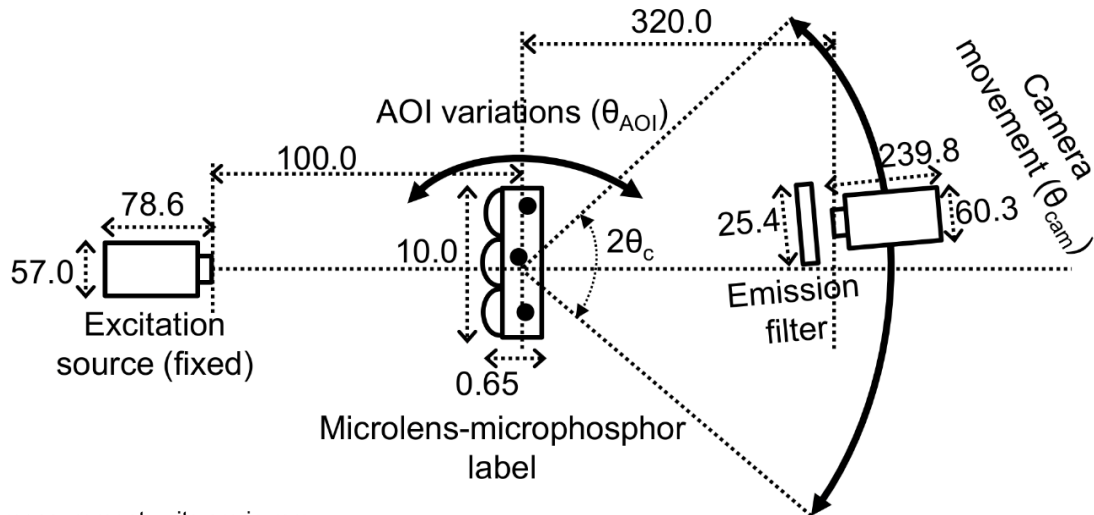
Figure 5.2 Impact of phosphor particle dimensions on the tolerance of PL point patterns to variations in the AOI. With smaller phosphor particles (a) in Label S, minor shifts in AOI can displace the focal volume from the particle, altering the PL pattern and necessitating precise AOI alignment for the test image to align with the reference image. For larger particles (b,c) in Labels M and L, the PL pattern is expected to be more consistent across a range of slightly different AOIs, allowing for a broader tolerance in authentication processes regarding the AOI discrepancies. Figure is Adapted with permission from Kumar *et al.*³

modifications in the manufacturing process now permit the use of a thinner substrate ($400\mu\text{m}$), enabling the application of a ML array with a reduced focal length ($f = 550\mu\text{m}$). This adjustment significantly decreases ' dx ' by a factor of 3.4 to an estimated $10\mu\text{m}$, thereby enhancing the label's tolerance to generate a single pattern against the AOI deviations.

It is also important to note that particle size has an impact on the AOI tolerance, as when a particle is larger, the focal volume resulting from a large lateral shift will remain within the particle. A comparison is conducted on the three commercially sourced DS phosphors, each of varying sizes, to assess how particle size impacts the pattern's tolerance to changes in angular positioning. Figure 5.2 illustrates a schematic drawing describing how an increase in particle size affects the formation of point patterns across the three labels when viewed at different AOIs. It is postulated that there exists a direct relationship between the tolerance to variations in AOI and the dimensions of the DS phosphor particles. Consequently, by integrating larger phosphor particles with ML of shorter focal length ($f = 550\mu\text{m}$) in the fabrication of unclonable labels, it is anticipated that the system's AOI tolerance exceeds 0.2° , a benchmark previously established for UC-based preliminary PULs.

5.3 Experiment using an LED excitation and CMOS-based camera detector

Figure 5.3 illustrates the overhead schematic layout of the setup for verifying the authenticity of the PUL. Central to this setup is the illumination source, a 450nm excitation LED, which is positioned to maintain a constant location throughout the experiment. This source directly illuminates the unclonable label, which itself is securely mounted on the motorized stage, ensuring both stability and the capability for precise angular adjustments. The detection apparatus consists of the s-CMOS camera, which is equipped with the zoom lens, and a 500nm long-pass emission filter to selectively capture the emitted light from the label post-excitation. The geometric configuration between the elements of this setup is defined as follows: the excitation source and the label are separated by 10cm , ensuring optimal illumination. Meanwhile, the label and the camera are positioned approximately 32cm apart, a distance calculated to provide a clear, undistorted view of the label through the camera lens. A critical aspect of this experimental design is the AOI value (denoted as θ_{AOI}) at which the excitation light strikes the label. This is achieved by rotating the motorized stage, a feature that allows for the exploration of how varying angles impact the visibility and



* All measurement units are in mm

Figure 5.3 Experimental Setup Schematic (Top View): This diagram illustrates the arrangement of key components involved in the experiment, including the excitation source, the PUL, an emission filter, and a camera detector. The excitation source remains stationary, while the label is adjustable within the x-y plane to explore variations in the angle of incidence (θ_{AOI}). Positioned behind the label, the camera is equipped with an emission filter and can be adjusted within designated critical angle boundaries (θ_{cam}) to capture the specific point pattern generated by the label. Figure is adapted with permission from Kumar *et al.*²

characteristics of the point-patterns generated by the label. The camera's viewing angle (θ_{cam}), defined relative to the optic axis of the label, is another variable in this experiment. It is crucial that this angle remains within predefined critical limits (expressed as $-\theta_c < \theta_{cam} < +\theta_c$) to ensure the point-patterns are within the camera's FOV and can be captured effectively.^{221,222} The schematic illustrates that the camera's position and consequently the viewing angle θ_{cam} can be adjusted to various locations behind the label, provided these adjustments respect the critical angle boundaries. This flexibility in camera positioning is essential for thoroughly analysing the label's point-patterns under different viewing angles.

5.4 Qualitative analysis: AOI tolerance of PUL against phosphor particle size

The experimental setup shown in Figure 5.3 facilitates a qualitative analysis of the likeness of PL point patterns produced under varying AOIs by the three distinct labels, each embedded with S, M, and L sized particles. Point-patterns are obtained from each label utilizing an illumination from the 450nm LED, across three distinct AOIs. These patterns from PULs are captured by the s-CMOS camera, attached with a zoom lens. To isolate the luminescence from the excitation light, a 500nm long-pass filter is placed in front of the camera. The three labels are sequentially positioned on a motorized

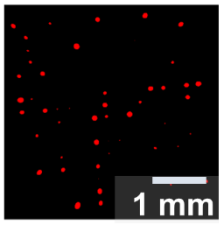
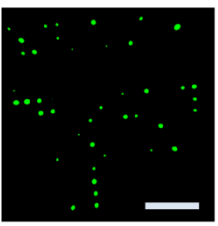
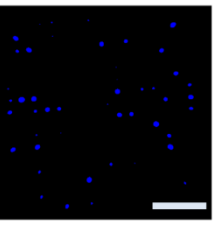
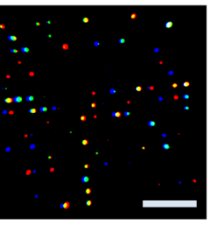
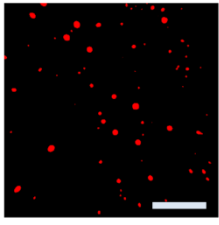
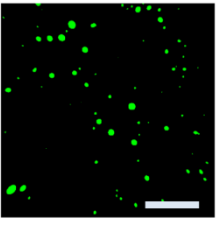
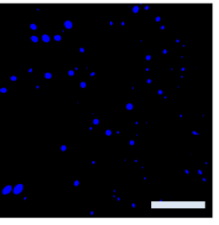
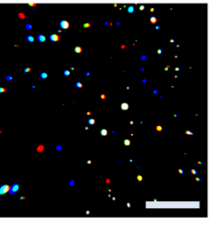
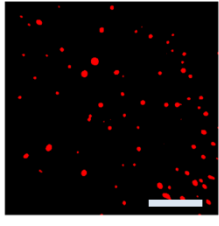
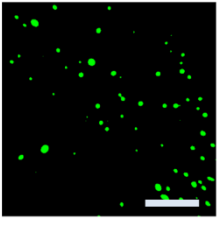
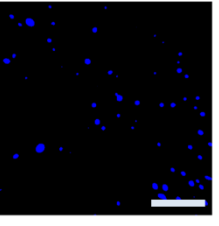
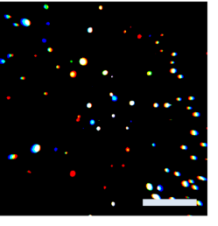
Particle Diameter (ϕ , D50)	Angle (θ , in deg)			Combined image
	0°	2°	4°	Angles
Label S ($\phi = 8 - 10 \mu\text{m}$)				
Label M ($\phi = 19.5 - 21.5 \mu\text{m}$)				
Label L ($\phi = 30.5 - 34.5 \mu\text{m}$)				

Figure 5.4 Qualitative comparison of PL-based point patterns from labels S, M, and L, each embedded with DS phosphors of varying sizes. The patterns captured at AOIs of 0°, 2°, and 4° are represented in R, G and B respectively, for each label. The composite image, merging the R, G, and B captures into one (RGB), reveals the spatial alignment of luminescence across the three different AOIs. White (W) dots signify areas where point-patterns from all three AOIs coincides, yellow dots indicate regions of point-pattern shared between R and G images, and cyan dots emerge where G and B images overlap. Reproduced with permission from Kumar *et al.*³

rotating stage for the experiment. Image of the PL-based point patterns are then captured at three different AOIs, specifically by rotating the label to 0°, 2° and 4°.

Figure 5.4 shows the colour-coded images of the PL-based point patterns from the three labels. Firstly, the noise level in the grayscale image is determined by computing the integrated pixel regions outside the ML arrays. Next, a value of '1' is assigned to pixels that have three times higher pixel value than the noise level. The rest of all pixel regions valued less than three times the noise level is assigned to '0'. From this transformed image, continuous regions of '1' (that consists of bright points in the image) are determined and listed. The image processing steps, and listing the continuous region of bright spots in the point pattern are presented previously in details in chapter 4 and is followed herein the same manner.²⁰⁷

In doing the qualitative analysis, images captured from each label at AOIs of 0° , 2° , and 4° are colour-coded as R, G and B respectively. This colour transformation process is mainly implemented to visually distinguishing the point-patterns obtained at different AOIs. Subsequently, these colour-coded images are merged into a composite RGB frame. This methodology facilitates a direct visual comparison of the positional consistency of point-patterns across varying AOIs, enabling a qualitative assessment of pattern stability. In the composite image, the appearance of yellow points is attributed to the overlap of bright points visible in the R (0° AOI) and G (2° AOI) images, without a corresponding overlap in the B (4° AOI) image.²⁰⁸ Cyan points emerge where bright point in the G (2° AOI) and B (4° AOI) images coincide, indicating a positional match at these AOIs without a corresponding match in the red (0° AOI) image.²⁰⁸ White points denote luminescent spots that align across all three AOIs, showcasing spots that remain unchanged in position irrespective of AOI shifts.²⁰⁸

For label S, the composite image predominantly features yellow and cyan points, with a mere distribution of white points. This indicates that while many bright points align between adjacent AOIs (0° and 2° or 2° and 4°), few maintain consistent positioning across all three AOIs. This suggests a greater positional variance in the three point-patterns as the AOI changes. Contrastingly, label M's composite image displays a higher occurrence of white points alongside yellow and cyan points.²⁰⁸ This suggests an enhanced stability of bright point's positions across the range of three AOIs compared to label S, indicating that more bright points remain unchanged in position from 0° to 4° AOI. In the case of label L, the composite image reveals an even greater proportion of white points, indicating that the largest fraction of bright points maintains consistent positioning across all the three AOIs. This implies that the PL-based bright points within label L exhibit the highest positional stability with AOI variations, attributed to the largest particle size used in this label.

This preliminary qualitative analysis elucidates that larger particles facilitate the observation of consistent luminescent patterns across a larger AOI variations. In contrast, smaller particles exhibit a more restricted range of AOI within which similar patterns are discernible, highlighting the significant impact of particle size on the system's angular tolerance. By incorporating the largest particles into label L, it is possible to show similar patterns regardless of changes in AOI of several degrees.

5.5 Statistical interpretation of the randomness of the point-patterns

For the label technology to be unclonable, it is crucial that the positions of the phosphor microparticles in the polymer film are random (or unpredictable) relative to the ML arrays. From a manufacturing perspective of the label, the procedure of mixing a low concentration of particles into the PDMS component and then casting this mixture leads to random particle positions. Moreover, this section presents a statistical interpretation confirming the randomness and uniqueness of each pattern experimentally derived from different labels of label S. Figure 5.5 illustrates the degree of correlation between two variables using the Pearson correlation coefficient (r). The red and orange regions represent low and moderate correlations, respectively. Whereas the green regions indicate strong correlation, with the left side showing a high negative correlation and the right side showing a high positive correlation between the two variables.

The method for demonstrating the randomness of the patterns produced by different labels is as follows: Four different labels of type S were considered. Point-pattern images from each of the four labels were captured at AOI = 0° under 450nm LED excitation. The luminescence-based point patterns obtained from four different labels are shown in Figure 5.6. Next, the brightest 32 points in each binary image are selected and a list of bright points is created in order of brightness (wherein each bright point accounts for an integrated sum of the pixel values through a continuous region). The two (x, y) positions of the two brightest points in each pattern are identified, and a virtual line is drawn joining these two points. The midpoint of this line is determined and considered as the reference point 'O'.

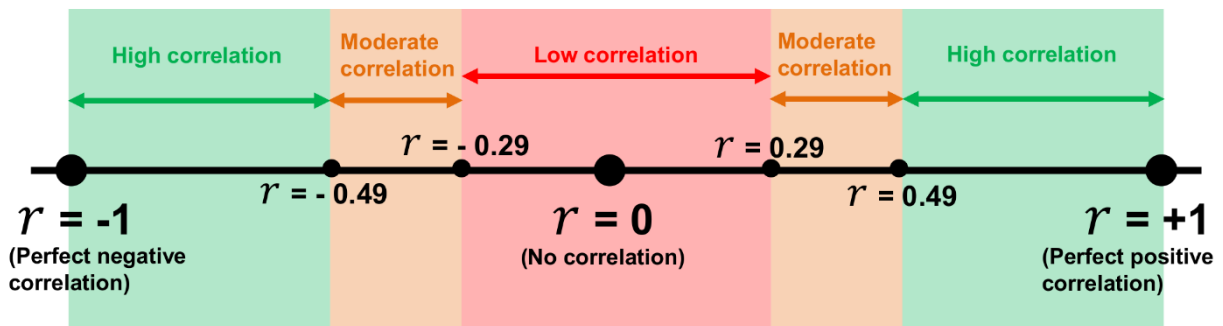


Figure 5.5 Degree of correlation between two variables based on the Pearson correlation coefficient (r). Low and moderate correlations are indicated by the red and orange regions respectively. Whereas the green coloured regions are characterized by a high level of negative correlation (green, left) and positive correlation (green, right) between two different variables. Reproduced with permission from Kumar *et al.*³

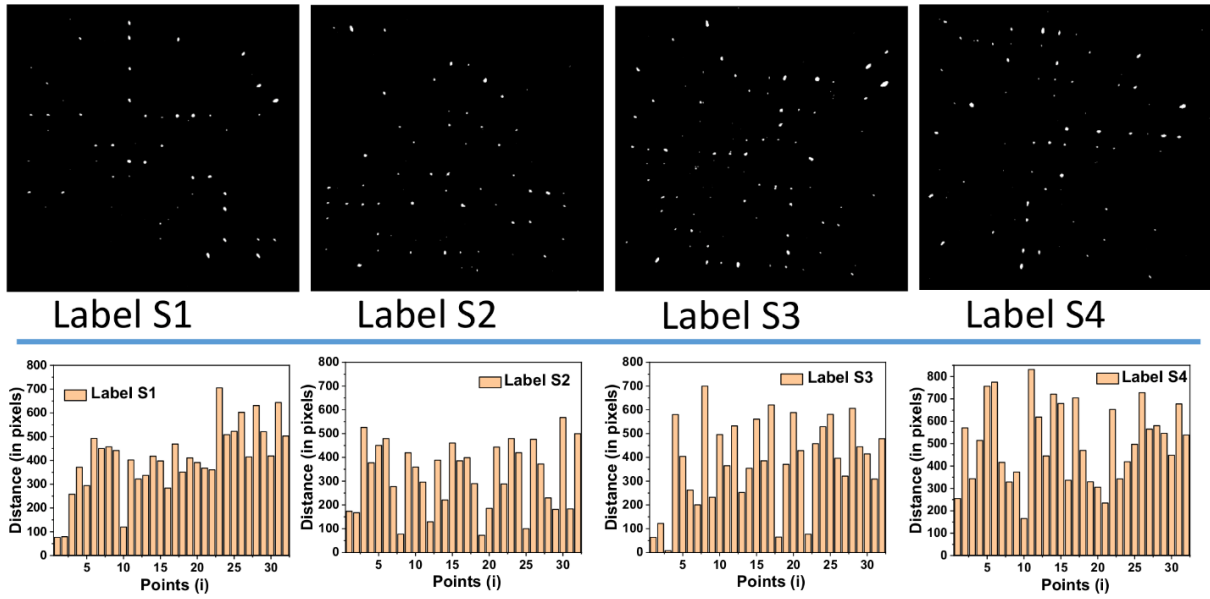


Figure 5.6 Statistical analysis of randomness of phosphor particles dispersion (that result in a point pattern) using four different labels. a) Bright point patterns at AOI = 0° under 450nm LED excitation; b) Histogram of the distance of the 32 brightest points for each label (in order of decreasing brightness) from the reference point. The distance lists are rotation and translation invariant and are used to determine pattern randomness via analysing the similarity correlation. Reproduced with permission from Kumar *et al.*³

The distance between each of the 32 bright points from the reference point ‘O’ is evaluated for each image. This process results in a list of 32 distances sorted by decreasing order of the brightness of the points, for each image. This logic of the algorithm makes sure that the list of distances remains invariant with rotation or translation changes. The distance lists obtained from different labels are compared to determine the degree of similarity between them. Pearson's correlation coefficients, r are calculated for each pair of labels based on the distance lists^{223,224}:

$$r = \frac{\sum (x_i - x_m) (y_i - y_m)}{\sqrt{\sum (x_i - x_m)^2 \sum (y_i - y_m)^2}} \quad (5.1)$$

In expression 5.1, x_i represents the value of the first label, x_m represents the mean of all the values on this label, y_i represents a value on the second label, and y_m represents the mean of all the values on the third label.^{223,224} The Pearson correlation coefficient has a range of -1 to +1, with -1 being a perfectly negative correlation and 1 being a perfectly positive correlation. In Figure 5.6, the standard interpretation of the correlation between the compared variables is illustrated.

Figure 5.7 shows a tabular comparison of distance lists of four different labels using Pearson's correlation coefficient theory. The correlation between most label pairs is

	Label S1	Label S2	Label S3	Label S4
Label S1	1	0.09	0.41	0.31
Label S2	0.09	1	-0.09	0.07
Label S3	0.41	-0.09	1	0.03
Label S4	0.31	0.07	0.03	1

Figure 5.7 Pearson coefficient of correlation for the pairwise comparison of distance lists, derived from the four different labels. Reproduced with permission from Kumar *et al.*³

found to be low, while a moderate correlation occasionally occurs. Thus, the statistical interpretation obtained using Pearson correlation theory indicates in a very simple way that the bright point patterns created by different labels are random, with no correlation between the bright points produced by the different labels.^{223,224} It is noted that other evidence for this randomness is the low number of votes cast for non-matching images (resulting from different labels) in the authentication algorithm, which will be discussed in the quantitative analysis of the labels in the following section.

5.6 Quantitative analysis of the labels with different size phosphor particles

In chapter 4, the image-processing algorithm and authentication procedure for verifying the point patterns generated by the labels were discussed. Briefly, a comparison is made between one image, referred to as the ‘reference image’ and another image, called the ‘test image’, using the affine transformation-based algorithm.²⁰⁷ The comparison of a reference–test image pair may result in matching or non-matching, depending on the label or AOI conditions. A test image generated from a single label under different trials at similar AOI placement conditions leads to a matching result when compared with the corresponding reference image. Whereas a test image generated from a different label or different AOI conditions results in a non-matching result.

5.6.1 Generating a threshold number of votes for label authentication

The algorithm employed for image authentication operates on the principle of vote counting, necessitating the establishment of a predetermined threshold to ascertain the match between test and reference images. Through comprehensive analysis of an extensive dataset comprising pairs of test and reference images, it becomes feasible to identify an optimal vote count threshold. This threshold is critical for accurately

classifying the images as either matching, where the test image sufficiently corresponds to the reference, or non-matching, indicating a significant deviation

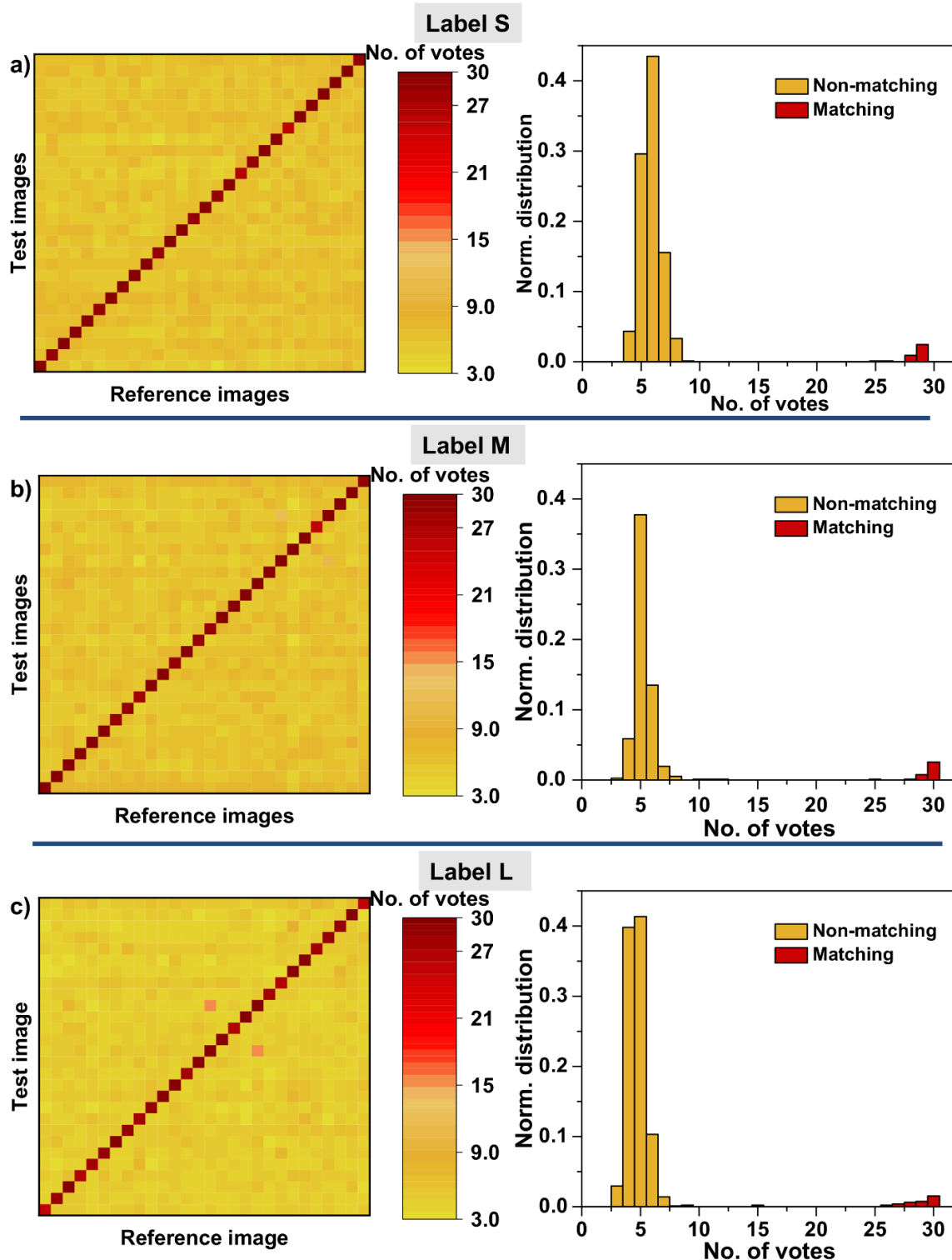


Figure 5.8 Matrix and histogram representations of vote distributions from pairwise comparisons between test images and their corresponding reference images for labels a) S, b) M, and c) L. The matching votes are from the same pattern image (shown in red), which is generated from the same label and at the same AOI. While the non-matching votes are the results from comparison of different images (different label or different AOI), shown in orange. Reproduced with permission from Kumar *et al.*³

between the two. The threshold vote for the three labels S, M, and L is determined as follows: Each of the three labels is inserted into the sample mount, fixed on a rotating stage, and seven point-pattern images are taken using an angle of illumination (AOI) of -24° to $+24^{\circ}$ in steps of 8° . The AOI step size here is selected to be far enough (in terms of the rotation degree) not to reproduce the same point pattern from a given label. Afterward, the label is removed from the sample stage and then reinserted onto the stage for getting the second trial. For each phosphor S, M, and L, this measurement procedure is repeated for two different labels (label 1 and label 2) under different AOIs. In this way, for each label S, M, and L, a total of 28 images are generated: (7 AOI images) \times (2 trials) \times (2 labels) = 28 total images, referred to Figure 5.8. The image comparison algorithm is used to compare 28 test images with 28 reference images for a matching/non-matching decision.

To compare the test image with the reference image, the algorithm considers 200 affine transformations of 32 bright point patterns, as well as the five brightest points used as basis-pair points in the test image. In this way, the comparison of many affine transformed lists of bright points (of a test image) with a reference image generates a list of 'vote numbers'. The transformed list of points that yields the maximum number of a vote (due to the merging of points of a test image with a reference image) is considered the most accurate matching. A detailed description of the algorithm used for label authentication as well as the source code is provided in the following GitHub repository (Project name of the repository file – 'Algorithm_label_authentication_design_optimized', Repository Project ID: 26705, https://git.scc.kit.edu/zi3429/algorithm_label_authentication_design_optimized).

In Figure 5.8, the vote comparisons and their normalized histogram distributions from 28×28 test–reference comparisons for each of the three labels S, M, and L have been presented. According to the histogram that is generated from the comparison of the 784 images of the three label designs (label S, M, and L), there is a distinguishable difference in the centre of the histogram for the number of votes cast for matching and non-matching images. Based on the comparison of 28 test images with 28 reference images, with the same label at the same AOI, 28 similarity votes are generated. This process results in a total of 25-30 matching votes out of a total of 32 votes, which are highlighted in red along the diagonal elements of the matrix. While a total of 756 different votes have been obtained by comparing different test images produced by

either different labels or with the same label but at different AOIs. Comparing different image patterns generates 3-15 non-matching votes, highlighted in orange in the off-diagonal matrix elements, shown in Figure 5.8. Therefore, a minimum of 16 match-points is considered the threshold for approving the authentication of a test image with a reference.

5.6.2 Quantitative analysis of the AOI tolerance with phosphor particle size

To determine how the three labels performed against the AOI tolerances, each label is placed on the sample stage and 101 images are taken from AOI = 0° to 20° in step rotation of 0.2°. Among the 101 images, 41 images that are taken between the AOI of 6° and 14°, are used as reference images (y-axis at AOI offset 0°, Figure 5.9 a). A comparison of each reference image with 61 adjacent images is then performed with the offset of each of the adjacent images varying between - 6° and + 6° in relation to the AOI for the reference image (x-axis, Figure 5.9 a). When the test images are compared with different reference images, the z-axis (colour scale) shows the number of votes cast for every test image compared to every reference image. It is estimated that 30 votes are cast for each label (referred to as the dark red regions) under small

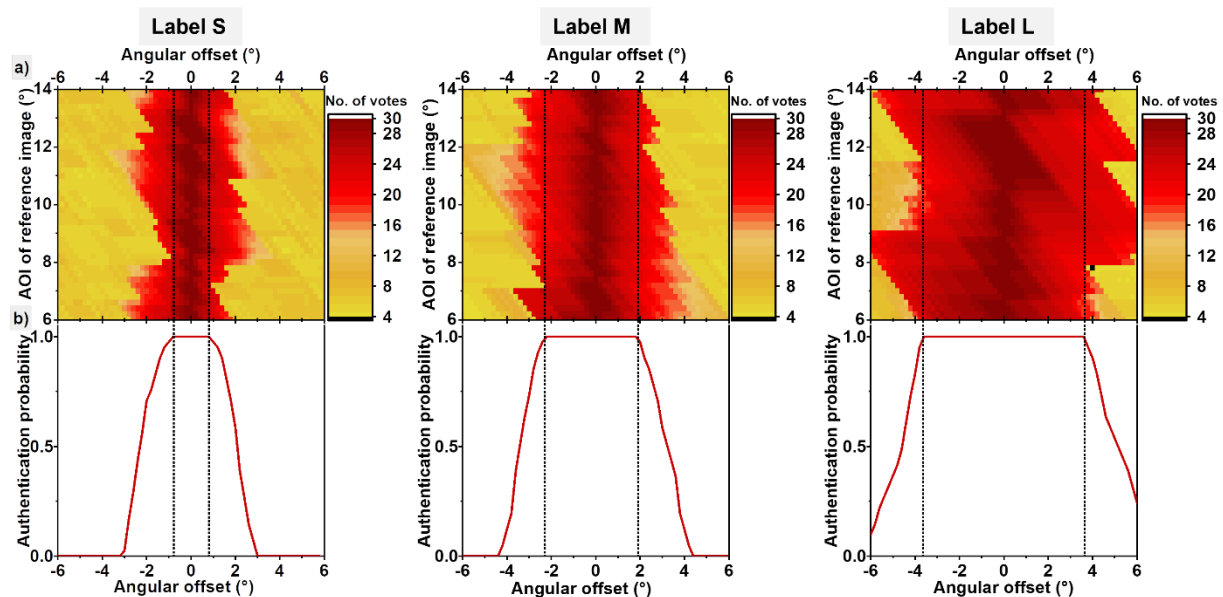


Figure 5.9 a) Results from the authentication process, displaying the number of votes achieved by comparing a single reference image against 61 distinct test images across the noted AOI offsets. To broaden the scope of analysis, 41 reference images from different initial AOIs are utilized. b) The relationship between authentication probability against the AOI offset for the three separate PULs, using a minimum criterion of 16 votes for authentication. The dashed lines represent the bounds of AOI tolerance, describing the maximum permissible AOI variance that maintains an authentication success rate above 99%. Reproduced with permission from Kumar *et al.*³

angular offsets from the original label. However, it has been noted that when the AOI offset reaches a specific edge in relation to the reference image, there is a rapid decline in the number of votes during the comparison between a test image and its reference. This observation indicates a significant reduction in the similarity or alignment between the test images and the reference image as the AOI deviation increases beyond a certain point.

It is important to recall that for positive authentication to work, 16 or more votes (in the red colour zone, on the colour scale) must be cast. Using the 41 AOIs from the reference image for each AOI offset, a fraction of test images leading to more than 16 votes is tabulated. By comparing the tabulated votes (along the y-axis) to the threshold vote number, the probability of authentication is determined. In Figure 5.9 b), a probability metric is presented for each of the labels, quantifying the likelihood of achieving successful authentication at various angular offsets between the reference and test images. Additionally, the concept of AOI tolerance is introduced as the critical angular deviation from the reference image within which a test image can be authenticated with a probability exceeding 99% when compared to the reference image. The experimental evidence provided in Figure 5.9 b) supports the adoption of this definition for AOI tolerance, illustrating a pronounced decline in authentication probability from nearly perfect to significantly lower values beyond this critical angular offset.

5.7 Understanding the particle size range for validating a linear relation of AOI tolerance

In Figure 5.10 a), the authentication probability curves for each label are merged into a single graph, summarizing the findings depicted in Figure 5.9. While Figure 5.10 b) elucidates the correlation between AOI tolerance and particle size utilized in fabricating the labels. The data shown in Figure 5.10 a) reveals a progressive expansion in the AOI tolerance, which increases from 0.8° to 2.0° in another (label S), and peaks at 3.6° for label L. This trend suggests a direct, possibly linear, relationship between the size of the particles used in the labels and the extent of AOI tolerance. This linear trend between particle size and AOI tolerance is evident across the spectrum of particle sizes and AOIs examined in this research. The linearity between particle size and AOI tolerance is predicated on a couple of key assumptions: firstly, that the particles are of

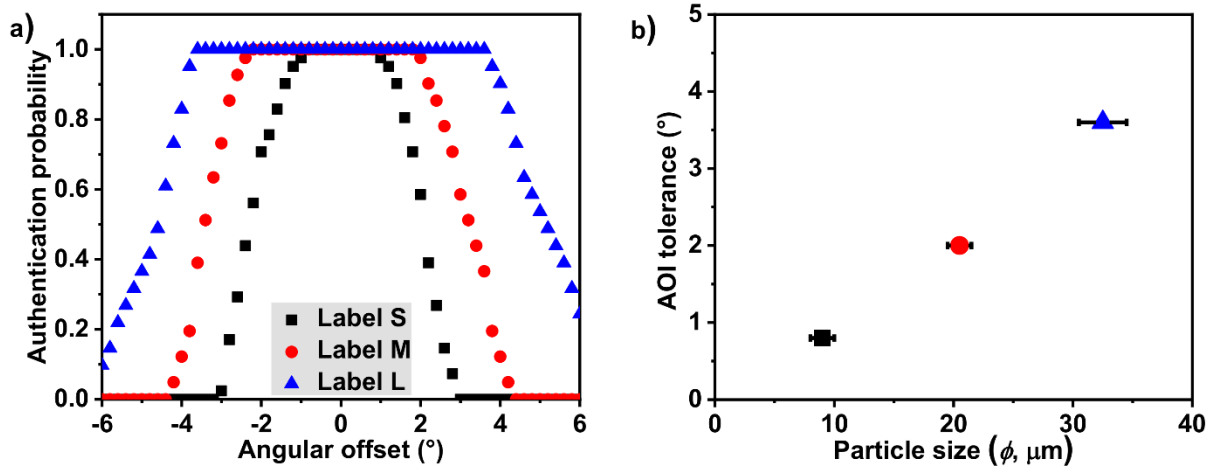


Figure 5.10 a) Authentication probability in relation to angular offset between reference and test images, with a range from 10μm (label S) to 30μm (label L) of particle size incorporated in the three different labels, label S (black colour), label M (red colour) and label L (blue colour) respectively. B) AOI tolerance based on three different particle sizes in the three labels S, M and L (where authentication probability remains greater than 0.99). Reproduced with permission from Kumar *et al.*³

a magnitude large enough for the illumination's focal spot diameter to be considered small in comparison to the diameter of the particle; and secondly, that the particles are sufficiently small to validate the approximation that $\sec^2 \theta \approx 1$, especially at AOIs where the focal spot surpasses the particle's boundary. To further understand this phenomenon within the realm of wave optics, a theoretical analysis is conducted to approximate the diameter of the focal spot as it pertains to the specific label design.

It is important to note that the particle size above which the AOI tolerance starts to become linear with the particle radius depends on the radius of the focus spot. If the excitation focal spot generated by the ML is much smaller than the radius of the phosphor particle, and the approximation $\sec^2 \theta \approx 1$ remains valid for the maximum AOI for which the excitation is still within the phosphor particles, the AOI tolerance varies linearly with the particle radius. To illustrate this, an example of a point-size phosphor particle that is infinitely small is used. The AOI tolerance in this case would be given by the range of angles at which the point particle is still contained within the finite focal volume of the excitation light. It can be approximated that the diameter of the focus of the excitation light can be determined by the distance between the first minima of the airy disc (under the assumption of wave optics).^{114,225,226} This is expressed by:

$$d = 2.44 * \frac{\lambda F}{nD} \quad (5.2)$$

Where λ is the wavelength of the illumination light, F is the focal length of the ML, n is the refractive index of the lens material, and D is the base diameter of the ML.^{114,226} Using the label design parameters, i.e. $\lambda = 450\text{nm}$, $f = 550\mu\text{m}$, $n = 1.5$, and $D = 250\mu\text{m}$, the above expression of focal spot results in a diameter (d) of $1.6\mu\text{m}$ in the focus of the ML. Therefore, the linear relationship of the AOI tolerance should be justified for particles an order of magnitude larger in diameter, if the excitation focus is relatively small compared to the particle size. When one considers the AOI tolerance for the smallest particles in the study, the presence of a finite-size focal point is likely to have a slight influence (increase) on the AOI tolerance.

In examining the AOI tolerance study for label S, which have particles diameter of $9\mu\text{m}$ – significantly larger than the $1.6\mu\text{m}$ diameter of the focal spot – it becomes evident that the assumption treating the focal spot generated by a ML as a point of infinitesimal size is marginally valid. This approximation, however, begins to lose its validity when considering particles smaller than those in label S, since the physical dimensions of the excitation radius at the focal spot cannot be ignored. As the relationship between particle size and AOI tolerance is explored further, it becomes apparent that for particles significantly larger than the focal spot diameter, a linear relationship between particle size and AOI tolerance holds. Nonetheless, this linear correlation is expected to weaken when the particle size decreases to the point where the size of the focal spot's excitation radius must be accounted for. Delving deeper into the analysis, it is identified that the upper limit of particle size, which maintains a linear relationship with AOI tolerance, is determined by the angular deviation at which the approximation error for $\sec^2 \theta \approx 1$ becomes 10%. This specific deviation occurs at an AOI of 18° , corresponding to a lateral displacement of the focus spot by $180\mu\text{m}$ for such an AOI. This observation implies that particles with diameters up to $180\mu\text{m}$ are likely to fall within the linear regime of AOI tolerance in relation to particle size. Beyond this point, the linear model may not adequately describe the relationship, underscoring the interplay between particle size and AOI tolerance in the design of these labels.

These findings signify that employing ML with reduced focal lengths, combined with larger phosphor particles in the construction of the PULs, enhances their tolerance to change in the AOI between the reference and test images. This adjustment in design parameters means that even when a test image is captured at a significantly divergent AOI from the reference image, it is still likely to be authenticated successfully. It's

important to note, however, that the likelihood of incorrect authentication – mistakenly identifying different labels as the same – remains unaffected by these modifications. The following section will briefly discuss the implications and future directions for the development of this label technology to evaluate its potential for practical implementation in real applications.

5.8 Label demonstration using an LED and smartphone camera

Verifying a security label using a low-cost authentication system is a key requirement when considering the end-user application. In this context, the operation of the unclonable label is demonstrated using a simplified setup that includes an LED source (providing an excitation lightening to the label) and a smartphone camera (recording the luminescence-based patterns).

A schematic representation of the setup used to capture the DS emission-based pattern from a label is shown in Figure 5.11. The label includes a 2mm thick PDMS layer doped with the DS particles (doping concentration 0.5 wt. %) attached under an ML array glass substrate of $f = 1900\text{mm}$. A 3D-printed sample holder is used to mount the label, and a 450nm LED at an AOI = 0° is used to illuminate the label. The emission-based pattern from the label is recorded simultaneously by the s-CMOS camera (placed at 32cm from the back of the label, $\theta_1 = 10^\circ$ off the optical axis), and by a smartphone (Samsung Galaxy A71, 10cm from the back of the label, $\theta_2 = -10^\circ$ off the

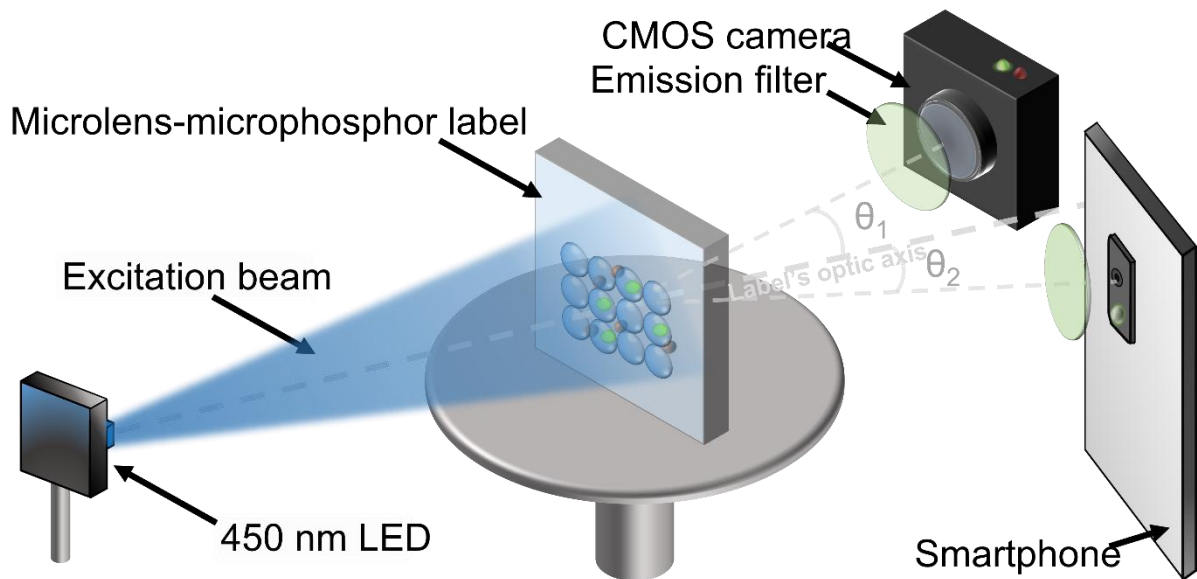


Figure 5.11 Authentication setup consisting of a 450nm LED as an excitation source for the unclonable label. An excitation-filtered smartphone and a scientific camera serve as detectors behind the label. Figure is reproduced with permission from Kumar *et al.*²

optical axis). The excitation intensity from the 450nm LED is maintained at 10mWcm^{-2} to the label position. To filter out the excitation light to the detectors, a 500nm long-pass filter is inserted before the smartphone and scientific camera. For the reader to visualize how the two detectors are positioned at an angle of detection of -10° and 10° (concerning the label's optic axis), dotted lines are used in Figure 5.11.

Figure 5.12 a) and b) present the colour-coded image of a point pattern of the specified label when illuminated with a 450nm LED light source at normal incidence. The two images are captured using two different imaging devices: the s-CMOS camera and a smartphone camera. Both devices are positioned behind the label to capture the PL-based pattern. To resolve the differing camera perspectives, an affine transformation technique is employed, ensuring the images from both devices are aligned and comparable. A critical observation from this experiment is the obvious variation in emission intensity of the DS particles located within a focus volume of ML compared to those outside it. This variance results in a distinct bright point pattern within the image, facilitating easy identification of the microparticles' distribution. Remarkably, both the 8-bit colour image captured by the smartphone and the 16-bit grayscale image from the s-CMOS camera successfully recognize this bright point pattern, highlighting the pattern's clarity and the sensitivity of both imaging devices. Furthermore, it is noted

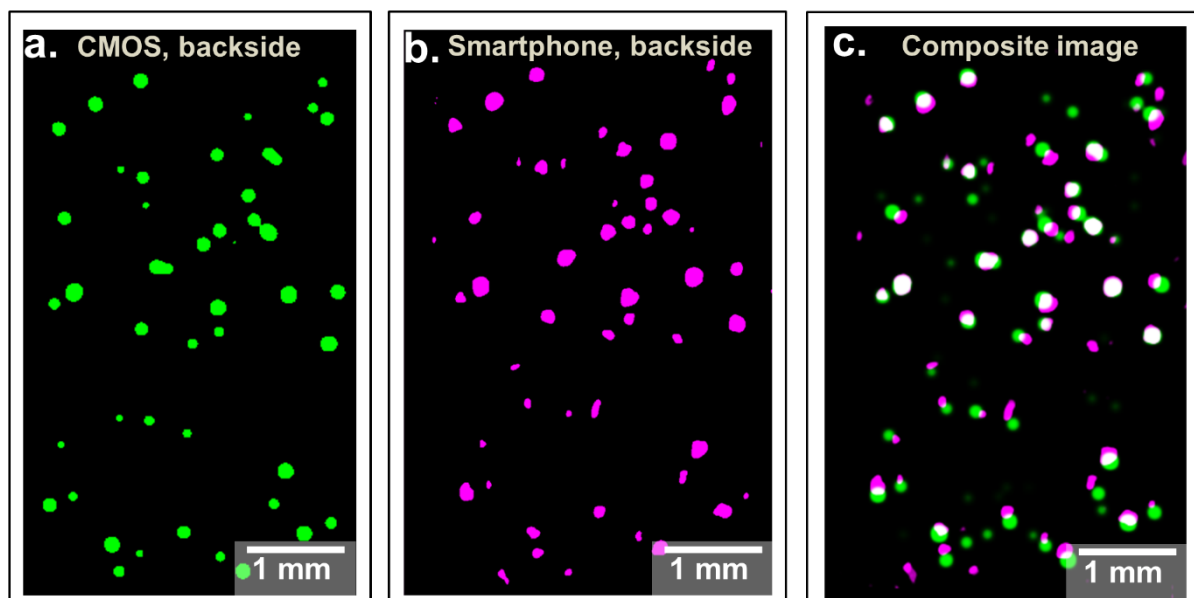


Figure 5.12 Demonstrating a luminescence-based pattern from the DS phosphor-based PUL under a 450nm LED excitation and filter-equipped camera detectors. a) A colour-coded DS pattern (green) observed by the s-CMOS camera. b) A colour-coded DS pattern (magenta) observed by the smartphone camera. c) A composite image of a CMOS (reference) image and a smartphone-captured image after an affine transformation. Reproduced with permission from Kumar *et al.*²

that the smartphone camera does not require supplementary lenses to observe the bright point pattern. Nevertheless, the application of an emission filter is necessary to mitigate the interference of excitation light in the smartphone's captures. This observation underscores the potential for using readily available smartphones in this label's imaging, provided appropriate filtering techniques are employed.

A quantitative comparison of the two patterns shown in Figure 5.12 a) and b) is made using the image authentication algorithm. The analysis reveals that 27 out of 32 votes are cast based on an affine-transformed similarity analysis. This vote count significantly surpasses the algorithm's predefined similarity threshold of 14 votes, leading to the conclusion that the images from the two different cameras are indeed matching. To further interpret the degree of similarity between the two images, the specific affine transformation that collected the majority of votes is applied to both Figure 5.12 a) and b). This step facilitates the creation of a composite false-colour image, designated as shown in Figure 5.12 c). In this composite visualization, the image acquired by the CMOS camera is assigned a green colour, while the smartphone image, post-transformation, is assigned in magenta. The strategic overlay of these two images leads to white points in the composite Figure. This phenomenon serves as a clear visual indicator of the alignment and matching of bright point patterns between the two images, thus confirming the analytical results derived from the image authentication algorithm's assessment of similarity.

5.9 Labels with widely spaced ML arrays and scattering surface

The findings from the previous analysis indicate the practicality of using DS phosphor based PULs for security purposes, with the capability of capturing their distinct bright point patterns using a smartphone under a 450nm LED illumination. It is particularly noteworthy that the emission spectrum of standard smartphone flashlights also centres around 450nm, suggesting the potential for a smartphone to serve dual roles in both exciting and detecting these unique labels.²²⁷ This hypothesis suggests a potential and simplified approach of validating such PULs using a only smartphone. However, for this dual-functionality approach to be viable, a critical design consideration must be addressed: both the excitation of the phosphors and the subsequent detection of their emission must occur from the same side of the label. This necessitates a redesign of the label, as the current configuration featuring closely packed ML alters (either by collimating or focusing) the emitted light from the microparticles when it travels back

towards the light source. This optical behaviour complicates the direct backscattering detection necessary for the proposed single-device operation.

To enable the label to function effectively in a 'reflection-based authentication' system, where both the illumination source and the detector are positioned on the same side of the label, specific design modifications are essential. These modifications include: first, the inclusion of spacing between ML in the array, ensuring that the light emitted from any DS particle is predominantly directed through a single ML located directly above it. Second, the integration of a scattering texture on the label's surface, situated among the ML, aims to enhance the coupling of emitted light into the detection apparatus. This texture serves to mitigate the losses due to total internal reflection (TIR) by scattering the light, thus improving its capture by the camera.²²² Figure 5.13 provides a schematic depiction of the redesigned label. This illustration highlights the label's composition, featuring ML each surrounded by a micro-textured scattering

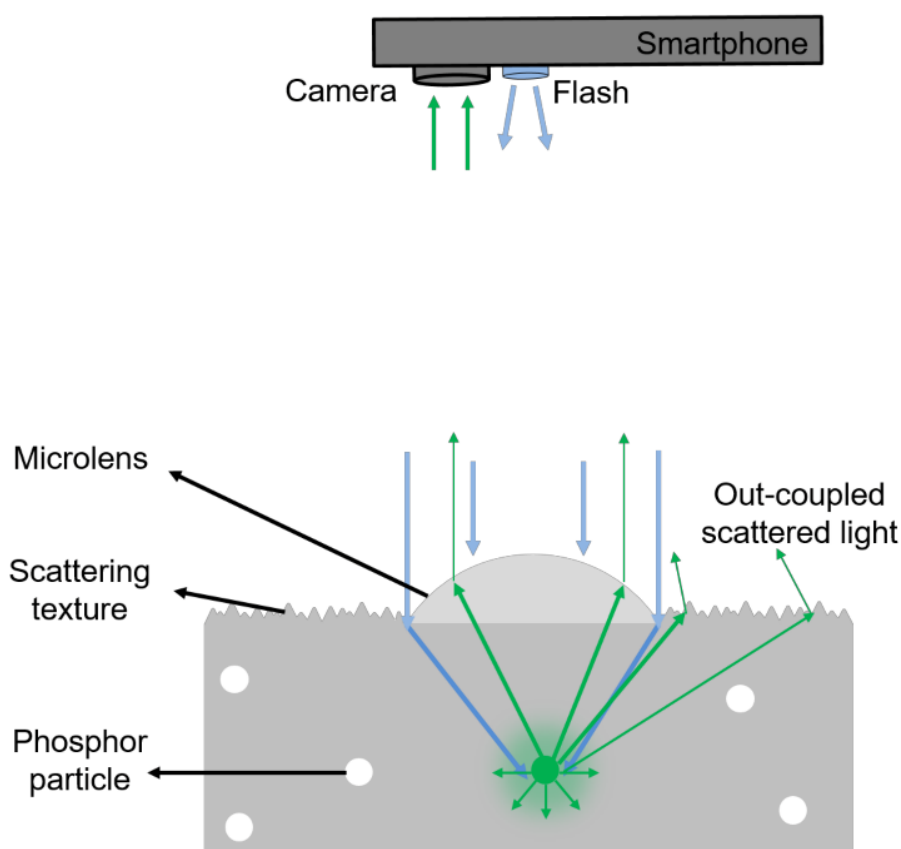


Figure 5.13 Label design incorporating a scattering textured surface around a ML. The excitation light from a smartphone flash (blue rays) illuminates the label, and a bright emission (green rays) from a phosphor particle within the focal volume appears underneath a ML. The bright particles emission is collimated by the ML and scattered from the micro-textured surface, leading to two different emissions captured by the camera above. (from the micro-textured surface).

surface. Embedded within the label's substrate is a random dispersion of DS phosphor particles. In this configuration, each ML is responsible for concentrating the excitation light onto a phosphor particle situated directly underneath it, resulting in a bright emission. This emitted light is then collimated and directed outwards from the ML surface above the particle, facilitating a direct path towards the detection device, such as a smartphone camera. Concurrently, the micro-textured surface surrounding the ML plays a crucial role in scattering the emitted light, effectively reducing the impact of TIR and thus enhancing the light's out-coupling towards the detector.^{221,222} This design ensures efficient light capture and contributes to the effectiveness of the reflection-based authentication process.

Figure 5.14 (a-c) presents optical images of this novel ML arrays design, which is developed on a silicon textured surface. The fabrication procedure of the two-layer unclonable label including the ML arrays and scattering textured surface (developed on a glass substrate), is explained in the methodology chapter. In brief terms, the fabrication can be summarized as follows: first, the ML arrays and the scattering textures are replicated on the glass substrate, and then this glass substrate is laminated onto a phosphor doped PDMS layer. In this label design, the PDMS layer is doped with 0.5 wt.% of the DS phosphor. As shown in Figure 5.14, the label includes a 14×14 ML arrays with $f = 550 \mu\text{m}$, featuring a ROC of $200 \mu\text{m}$ and a base diameter of $250 \mu\text{m}$. These ML are arranged in a square-packing configuration, with a centre-to-centre distance of $750 \mu\text{m}$.

Firstly, a demonstration of this silicon textured PUL is evaluated from both a qualitative and quantitative perspective, using the optical authentication setup referred in Figure

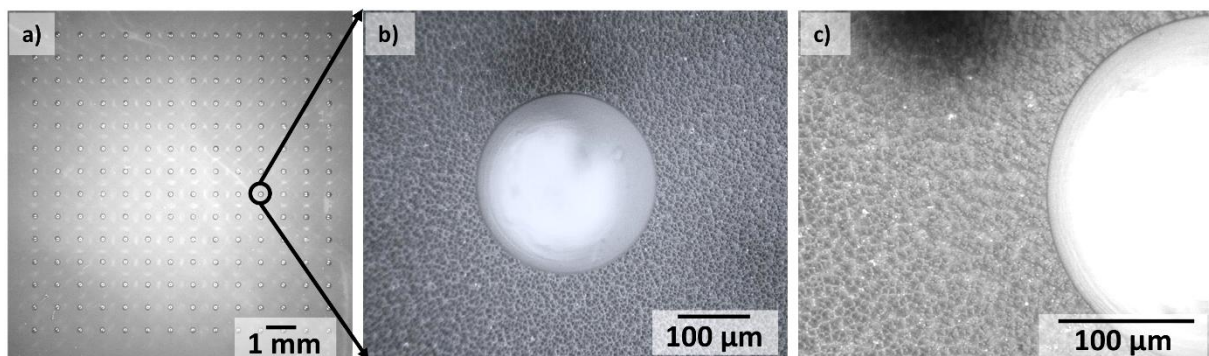


Figure 5.14 Optical images of the label incorporating a 14×14 ML array and the silicon micro-textured surface, developed on a $400 \mu\text{m}$ thick glass substrate (images are taken with a Keyence VH-Z500R optical microscope). Figure is reproduced with permission from Kumar *et al.*²

5.11. Following the novel operation of the label (in the transmission-based authentication system), the label operation in a reflection-based authentication model is then conducted, wherein an authentication device (e.g. a smartphone) can be used to excite the label (with the smartphone flashlight) and simultaneously record the luminescence-based bright point pattern from the PUL (with the same smartphone camera).

5.9.1 Qualitative analysis of labels including widely spaced ML arrays and scattering surface

The silicon textured PUL is demonstrated qualitatively by illuminating the front side with a 450nm LED and recording a luminescence pattern from the back side with a CMOS

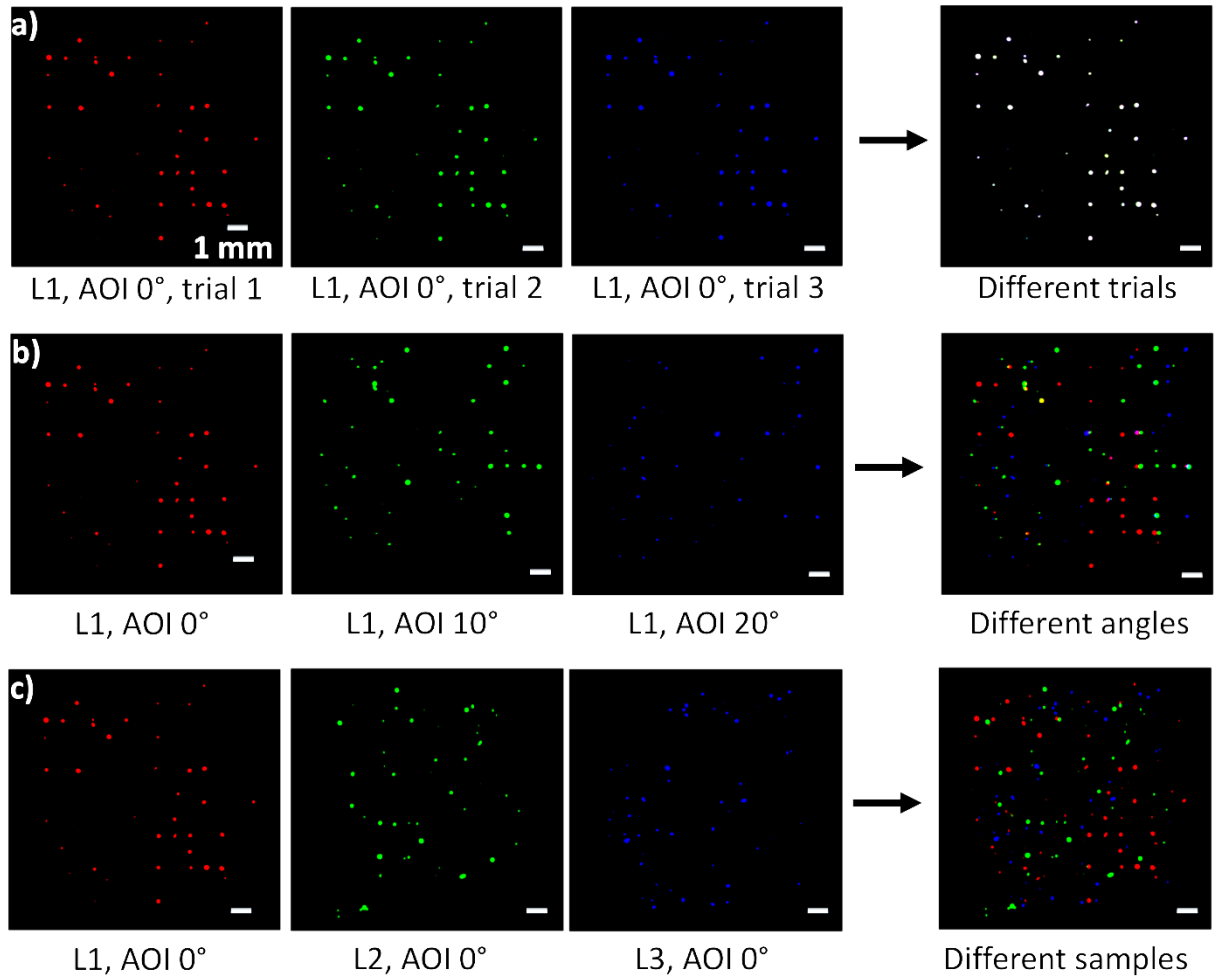


Figure 5.15 Qualitative comparison of point patterns for the novel label design based on the DS phosphor doping. False-colour R, G and B images illustrate the individual point patterns. The final comparison includes a pixel-wise summed-up composite image showing the overlap of the three images in a single frame. a) Three different trials of the same label (L1) taken under the same AOI result in matching patterns (White); b) Point patterns observed at three different AOIs = 0°, 10°, and 20° for a single label (label L1) results in non-matching patterns; c) Point patterns from three different labels L1, L2, and L3 taken at same AOI (at AOI = 0°) produce different point patterns. Reproduced with permission from Kumar *et al.*²

camera. Figure 5.15 illustrates a qualitative analysis of the silicon textured PUL, analysed in a similar way as shown for the DS-based labels. As shown in panel a), for three trials of the same label (removing and re-inserting the label between different trials), the point patterns are always similar. In all three trials, the label position with respect to the light source is maintained in such a way that the AOI for each measurement is maintained at 0° . Images of different trials are presented in three false colours - R, G and B. A composite image created by combining all three images of different trials in a single frame leads to overlapping points that produce a white point pattern ($R+G+B = W$). Figure 5.15 b) shows a false-colour representation of three different point patterns recorded at three AOIs of 0° , 10° , and 20° using the same label (label L1). An overlay image of a single frame shows that the patterns, as can be seen from the individual colour appearances, differ from one another.²⁰⁸ In a similar manner, the three point-patterns associated with three different labels (L1, L2 and L3) are presented in Figure 5.15 c) and are also clearly distinct.

5.9.2 Quantitative analysis of labels including widely spaced ML arrays and scattering surface

A quantitative analysis of the patterns generated by the silicon textured PUL is carried out, following the same procedure as that used for the UC-based prototype labels. The

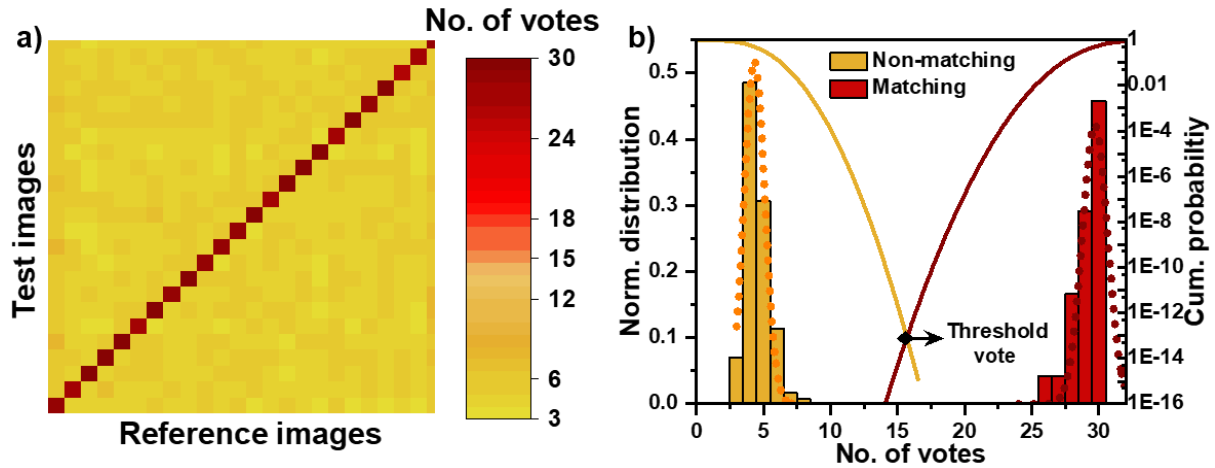


Figure 5.16 a) Number of votes obtained from the comparison of 24 by 24 reference-test images for the silicon-textured PULs. The diagonal elements indicate that 24 matching images (that are recorded at the same AOI and with the same label) are identified, resulting in a high number of votes (26 to 30). The off-diagonal elements are the results of non-matching comparisons (from different labels or AOIs) that contain a low number of votes (3 to 8). b) Normalized distribution of the number of votes obtained from the matching (red) and non-matching (yellow) comparisons. Solid curves represent the CDF curve for each distribution, enumerated using Gaussian fits (dashed curves). A threshold of 16 votes is set for making the authentication decision, based on the intersection of the two CDF curves. Reproduced with permission from Kumar *et al.*²

label is illuminated from the front side using a 450nm LED, and the luminescence-based patterns are recorded using a camera, facing the back side of the label. Transmission-based multiple patterns are generated from a single label by varying the AOI from -25° to $\text{AOI} = +25^\circ$, in step rotations of 10° . The label is observed to generate entirely different patterns for each 10° change in AOI. The experiment is performed using four different labels, which resulted in the creation of 24 reference images (4 samples, 6 angles per sample). A new set of 24 'test' images is then captured with the same labels (by removal and re-insertion into the sample stage at the same AOIs). The experiment yielded the number of votes cast for the 24 reference-test pairs that are expected to match (diagonal) and the remaining 552 reference-test pairs that are expected not to match (Off-diagonal). This is shown in Figure 5.16 a).

Figure 5.16 b) shows the normalized distribution of the vote numbers resulting from the 24×24 comparisons of the reference-test images, derived from Figure 5.16 a). A comparison of non-matching images (from different labels and AOIs) results in a small number of votes (3 to 8), on the other hand, a comparison of matching images (from the same AOI and same label) results in a high number of votes (26 to 30). A Gaussian distribution function is fitted to the distribution of votes, and then a CDF curve is plotted to estimate the probability of matching/non-matching for a test-reference comparison based on the selected number of votes.^{209,210} The intersection point between the two CDF curves provides the threshold vote, which has the lowest likelihood of false-positive and false-negative authentication for a given test-reference comparison. As can be seen in Figure 5.16 b), the threshold vote for the silicon textured PUL is calculated as '16' for making an authentication decision.

The AOI tolerance experiment is conducted with the silicon textured PUL to quantitatively analyse the degree of AOI precision required to generate a similar pattern. The label is carefully positioned on the sample stage, and a series of 100 images is captured. This process involves rotating the label from an AOI of 0° to 20° , employing a precise step-rotation increment of 0.2° . Throughout this imaging sequence, the label is illuminated using the 450nm LED. Comparisons of test-reference images are performed using the same authentication algorithm as implemented for validating the UC and DS-doped labels. A minimum of 16 matching votes are considered for each pair of test-reference image comparisons. A total of

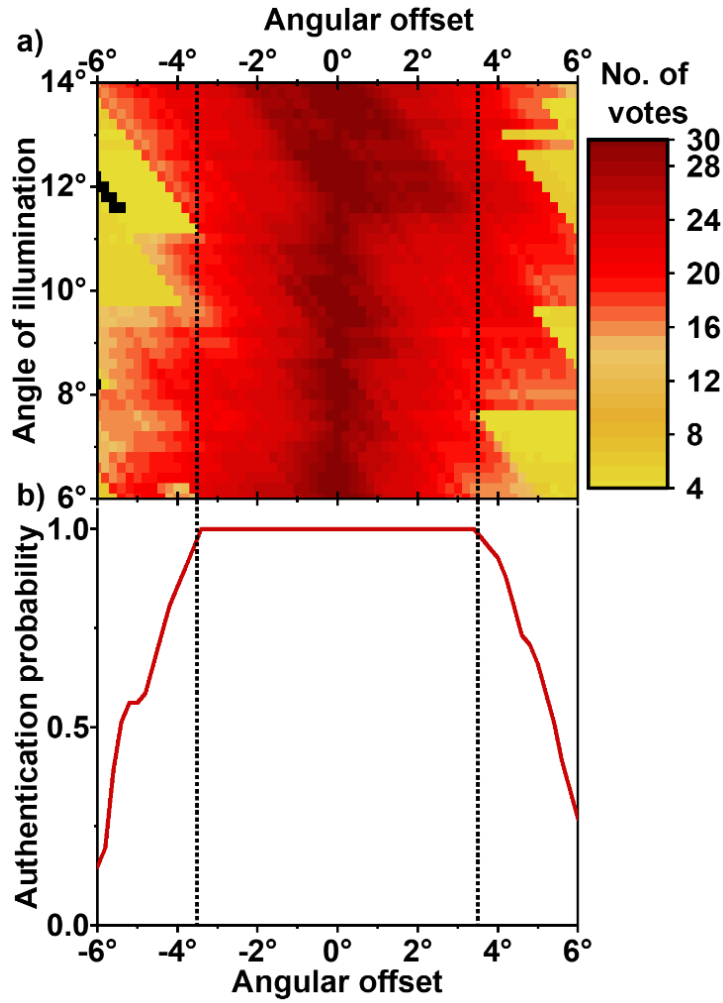


Figure 5.17 Quantitative study of the AOI reposition accuracy of the silicone textured PUL. a) Number of votes obtained from 41 reference image comparisons for AOI = 6° to AOI = 14° (along y-axis), with 61 test images having angular offset of 0° to $\pm 6^\circ$ along x-axis. b) Authentication probability over angular offset. The area between the two dotted lines (in red colour) exhibits a 100% authentication probability which translates into an AOI repositioning accuracy of 7° for achieving a similar pattern. Reproduced with permission from Kumar *et al.*²

(61×41 = 2501) test-reference images are compared with each other using the authentication algorithm, shown in Figure 5.17 a).

In this study, it is observed that with a short focal length ML array (having $f = 550\mu\text{m}$) and the large-size DS phosphor particles (D50 diameter $\approx 30 - 35 \mu\text{m}$), the angular repositioning accuracy increases to 7.0°. This improvement provides nearly a 20-fold improvement in AOI tolerance compared to the UC-doped unclonable label for achieving a similar pattern. As a result of this increased angular reposition accuracy, the subsequent section demonstrates that this label technology can replace complex authentication setups (e.g., motorized stage, laser setup) with a smartphone, which can function both as an excitation device and a detector for validating such unclonable labels.

5.9.3 Label authentication using a single smartphone

In the schematic shown in Figure 5.18, an experiment is designed to validate the scattering based PULs composed of ML arrays (on top) and the DS particles (within its bulk volume). This label is positioned on a designated sample holder, ensuring optimal orientation and position stability. The experimental setup incorporates a smartphone, specifically a Samsung Galaxy S20, positioned at an AOI of 10° . This placement facilitates the dual role of the smartphone: it illuminates the label from the front, targeting the ML surface, and concurrently, its built-in camera serves to capture the PL-based point pattern generated by the label. To enhance the fidelity of the captured image and eliminate any interference from the excitation light, a 500nm long-pass filter is positioned in front of the smartphone's camera. An s-CMOS camera is employed, facing the back surface of the label. This camera is equipped with a zoom lens and a 500nm long-pass emission filter. This arrangement of s-CMOS camera is used to capture the transmission-based PL point pattern of the label, offering a complementary perspective to the smartphone-captured imagery. To ensure the integrity and comparability of the data captured from these two distinct imaging modalities, steps involving mirror adjustments and affine transformations is applied in the authentication

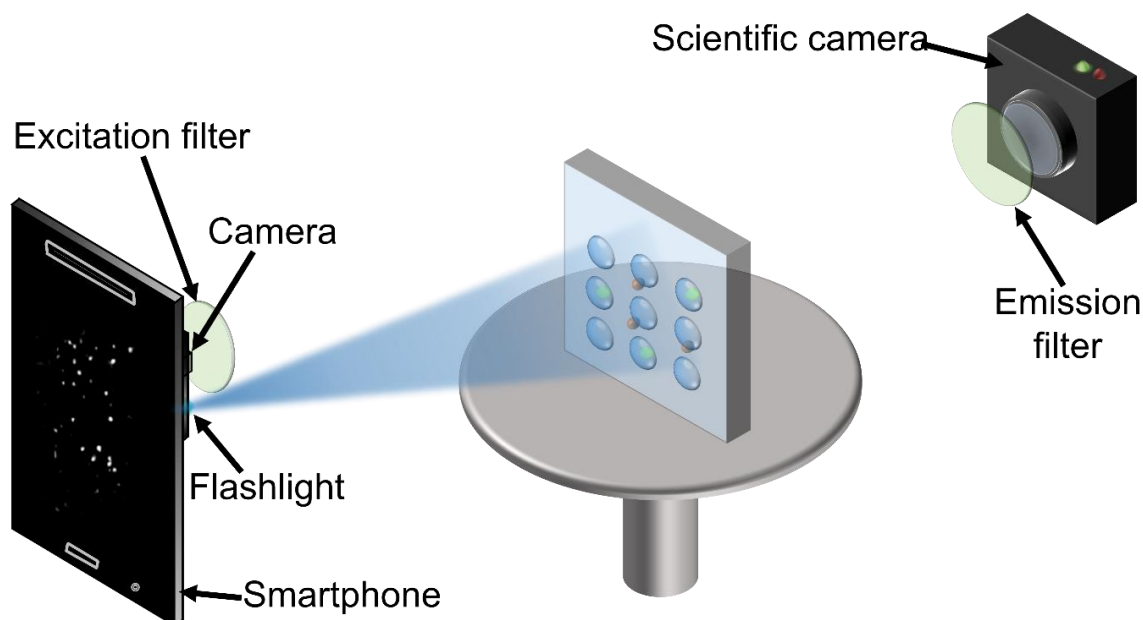


Figure 5.18 Authentication setup with a smartphone serving as both excitation and detection device. The flashlight of the smartphone illuminates the label, and the smartphone camera records filtered emission. An emission filter equipped CMOS camera is placed behind the label, recording the transmitted PL pattern. Figure is reproduced with permission from Kumar *et al.*²

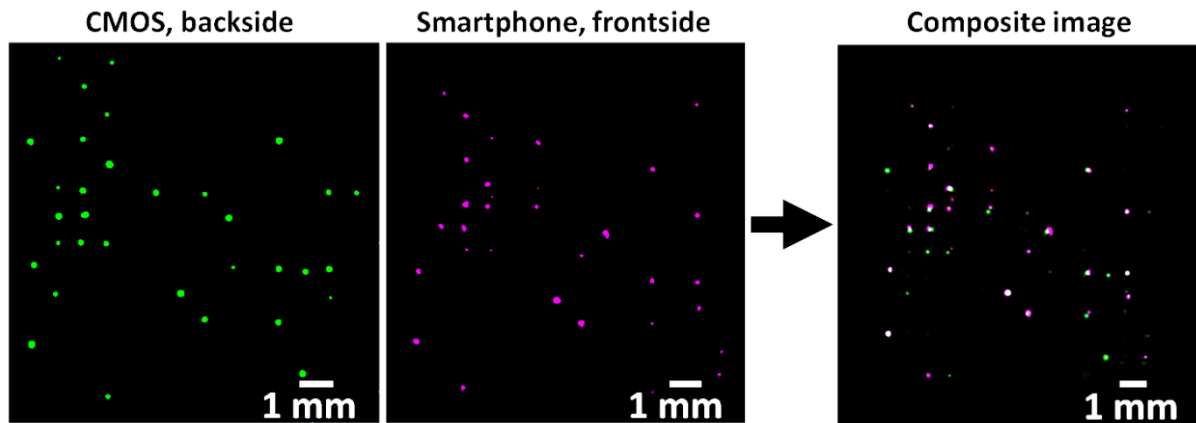


Figure 5.19 Qualitative analysis of the DS pattern seen from the silicon-textured unclonable label. A comparison is made between image captured by the CMOS camera, represented in green, and image taken with a smartphone camera, depicted in magenta, under illumination from the smartphone's flashlight positioned at the front. A qualitative similarity analysis is presented by pixel-wise summation of the two images, resulting in generating white points in the composite image where the two patterns match. From a quantitative perspective, the authentication process validates the similarity comparison by awarding 21 votes for the two images, surpassing the predetermined threshold of 16 votes. Reproduced with permission from Kumar *et al.*²

algorithm to compare the similarity of the two recorded patterns. This process is critical for aligning and correlating the point patterns recorded, enabling a robust and reliable authentication of the scattering label.

In Figure 5.19, the process of analysing images of the point patterns captured by two distinct imaging devices: the s-CMOS camera and a smartphone camera, is presented. The captured images showcase the point patterns with the CMOS camera images highlighted in green and those from the smartphone camera in magenta.²⁰⁸ A critical step in these comparative analysis involves adjusting the orientation of the smartphone camera image to align with the perspective from which the CMOS camera image is captured. This adjustment results in mirroring the smartphone image to ensure both sets of images reflected the same orientation relative to the label. To align the orientations of the two images, an affine transformation is employed for a more detailed comparison.²⁰⁷ This transformation is based on identifying and utilizing three corresponding points within each image, thereby enabling a precise overlay and comparison of the captured patterns. The result of this process, illustrated in Figure 5.19, is a composite image that demonstrates a high degree of similarity between the patterns captured by the two detectors, affirming the effectiveness of the affine transformation in aligning and comparing the images. To supplement the visual comparison with quantitative analysis, a similarity correlation metric is employed with a predefined threshold of 16 votes. In this context, 'votes' refer to points of correlation

between the two images. Upon comparison, the analysis yields 21 votes, indicating a significant level of similarity that surpasses the established threshold. This high level of correlation provides strong evidence supporting the feasibility of using a single smartphone as a means for authentication. By leveraging the smartphone's flashlight for front side excitation and its camera for detection, this study demonstrates a novel approach to employing the silicon textured PULs for authentication purposes.

5.10 Merits of the label design

5.10.1 High AOI tolerance for label authentication

It has been demonstrated that the AOI tolerance can be controlled by tuning the design parameters of the label. In this regard, large-size phosphor particles (D50 diameter 30 – 35 μm) have been utilized along with a relatively shorter focal length ML array ($f = 550\mu\text{m}$). This label design has demonstrated that it is possible to relax the AOI tolerance by 20 times (3.6°) for authenticating such labels, which represents a substantial improvement over the use of UC-based labels in terms of ease of authentication when considering the orientation of the label in relation to the excitation source. This enhancement in AOI tolerance is achieved without compromising the label security, as multiple random-based point patterns can still be generated by varying the AOIs.

5.10.2 Low-cost authentication setup

Regardless of whether a transmission-based or reflection-based authentication setup, a 450nm LED excitation (or a smartphone flashlight) has been utilized to generate patterns from the DS-doped unclonable label. This excitation approach is a low-cost and relatively eye-safer for verifying the DS-doped labels (compared to the UC-based labels that necessitate a laser excitation). Additionally, it has been demonstrated that low-cost detectors, such as smartphone camera, can effectively record the bright patterns produced by these labels. Hence, this novel technology, along with an increased AOI tolerance for pattern authentication from the label, eliminates the need for complex and expensive hardware devices (e.g. an s-CMOS camera, zoom lens, lasers, motorized stage for sample alignment, etc.) in the authentication setup.

5.10.3 Application in anti-counterfeiting

In this section, a practical approach of the novel PUL is discussed through an example scenario: authenticating a medication contained within a blister pack. To understand the implications of the AOI tolerance on the authentication device design, Figure 5.20 is referenced, which depicts a schematic design of an authentication setup tailored for blister packs. Within this setup, the insertion of the blister pack is meticulously guided by elements shown in brown, which ensure the blister pack is positioned accurately both in terms of angle and depth. This positioning places the pack on a support surface, illustrated in white, at a precise distance of approximately 10cm from a linear arrangement of three LED sources. These LEDs are strategically positioned and oriented to cast light onto the blister pack's transparent sections – specifically those areas not covered by the aluminium sealing foil – at three distinct AOIs: -10° , 0° , and $+10^\circ$. As the LEDs sequentially illuminate the label from these varied angles, a camera unit, represented in the schematic as a black box with orange stripes and situated atop the device, captures the resultant bright point patterns originating from the label. These

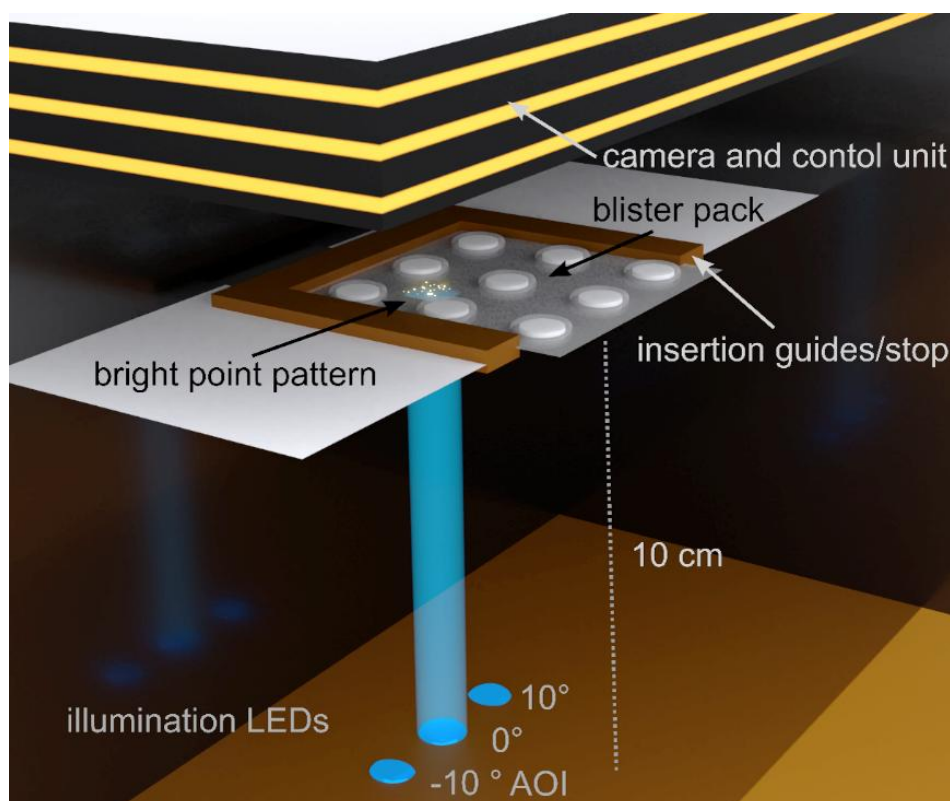


Figure 5.20 An example of how the unclonable label could be used in blister packed medication. On one side of a 400 μ m thick polymer substrate of the blister package, a ML array can be applied. The lidding seal on the other side of the patch is removed, for inserting the labelled product. Three fixed LEDs provide illumination at -10° , 0° and $+10^\circ$ AOIs in this simple apparatus shown above. If the LEDs are 10 cm apart, then a 3.6° AOI tolerance would allow for a deviation in the positioning of the label of less than 6 mm. Adapted with permission from Kumar *et al.*³

captured patterns, each corresponding to a different AOI, are then relayed to an integrated computer system. This system undertakes the task of comparing the observed patterns against a pre-established database containing known bright point patterns associated with authentic products. The envisioned authentication system demonstrates a versatile approach that could be adapted for products beyond blister-packed medications, including those with transparent plastic packaging. The label design achieves an AOI tolerance up to 3.6° , equating to a permissible lateral displacement of up to 6mm between the label and the LED array. Through the incorporation of the mechanical guides, as depicted in the schematic, it becomes feasible to ensure the precision placement required to maintain within this tolerance, thereby enabling reliable authentication based on the unclonable label technology.

5.10.4 Smartphone-based authentication

It has been demonstrated that a single smartphone can serve as an authentication device for verifying patterns from a silicon textured PUL label. The spacing between the ML arrays ensures that emission from a bright particle out-couple from overhead ML (not from the neighbouring ML). Through the scattering textures surrounding the ML arrays, the emission light is outcoupled beyond the critical angle limits towards the front side. In this way, simultaneous operation of the smartphone flashlight (as an excitation source) and the smartphone camera (for recording the emission-based bright point pattern) is possible with this novel label design for its authentication.

5.11 Challenges of the label design

5.11.1 Application-oriented challenge

The unclonable label presented in this chapter includes a ML array (printed on a microscopic standard glass substrate) and Ce^{3+} -based DS particles doped PDMS layer. Since the glass substrate has a flat surface, implementing such labels on a curved surface presents a challenging aspect. As unclonable labels are capable of being applied to a wide range of anti-counterfeit goods (including those with curved surfaces), the ability to label such goods is of paramount importance.^{46,90,228} The ML arrays described in this study are developed on a glass substrate, making these preliminary PULs less optimal for direct application purposes. To enhance the practicality and applicability of this concept, a significant advancement would be to

develop the labels using a single layer of flexible polymer. Within this polymer, microparticles could be embedded, and a ML array could be directly imprinted onto its surface. This approach would not only streamline the label's application process but also make it possible to affix the entire label onto a product in a unified form, thereby realizing a more direct and practical solution for integrating these labels onto various products.

It is essential to understand that when collimated light is directed onto a curved surface, the angle at which this light interacts the surface – referred to as the AOI – will change in relation to the surface's curvature. This variation can be quantitatively described by the formula: $\theta = \frac{180x}{\pi R}$. In this context, 'x' denotes the ROC of the object being marked, while 'R' stands for the distance from the point on the label closest to the light source to the specific ML undergoing marking. To illustrate this concept with a practical example, consider a perfume bottle with a curvature radius of 3 cm, and a label that spans a length of 2cm. For ML located at the central part of the label, the AOI would be 0°, indicating that the light strikes these lenses perpendicularly. However, for ML positioned at the label's outer edges, the AOI shifts. Applying the given formula, the AOI for these peripheral ML calculates to $\theta = \frac{180}{3\pi}$, which approximates to $\pm 20^\circ$. This demonstrates how the AOI adjusts based on the curvature of the product and the position of the ML on the label, highlighting the importance of considering these factors in the design and application of ML-based marking systems on curved surfaces. A label from this concept should work on surfaces that are curved as long as the ROC remains constant (under a strain condition), and as long as the reference images that are captured from the label are retrieved as a test image from the product that is being used. The marking of goods that are on a flexible substrate will require careful consideration to validate the label concept. Recognizing the significance of the AOI and its variation with the object's ROC is crucial. Thus, when an object, especially one marked on a flexible substrate, undergoes in validation process, it is imperative to ensure that it is positioned in an identical configuration (for instance, laid flat) for capturing the test image as is maintained during the capture of the reference image. As near-market-ready applications have not been developed yet (e.g. label deformation due to scratches or ML deformation), these initial results can serve to stimulate further research to meet these challenges.

Labels discussed in this chapter incorporate DS phosphor particles that are excitable using a 450nm wavelength peak excitation source. The emission response from the particles lies in the visible region (with green and red emission peaks). To prevent the excitation light from reaching the detector, optical filters are necessary. This is accomplished by using a 500nm short pass filter in front of the excitation source and a 500nm long pass filter in front of the camera detector to observe a point pattern. From an application perspective, it is not desirable to include any addition of optical components in the authentication setup, either to the excitation source or to the detector. According to the design considerations for the unclonable label, it is hypothesized that scattering particles (in visible wavelengths) or persistent phosphor-doped layers could be utilized to eliminate the need for optical filters.⁴ Post-excitation of such an unclonable label, either scattering or afterglow emission can be recorded as a bright pattern without implementing any optical filters.

5.11.2 Authentication oriented challenges

To validate the label, it is preferable to use a smartphone, either manually held or mounted on a basic mechanical setup, as the authentication instrument. To facilitate reliable authentication under such conditions, it's essential to aim for further improvements in the precision of the AOI positioning. From the perspective of optimizing label design, transitioning towards ML arrays with shorter focal length and incorporating larger particles emerges as a promising strategy. Additionally, the application of fiducial markers on the label's front surface could significantly enhance the estimation of the label's spatial orientation relative to the smartphone, thereby contributing to the refinement of AOI accuracy. Alternatively, the authentication process could involve comparing a single captured test image against a broader array of reference images, possibly ranging from 10 to 100, which are recorded across a spectrum of AOIs, to accommodate variations in positioning.

To achieve maximum tolerance for the AOI when designing the label, it is recommended to optimize the two design parameters (focal length and particle size) of the label. As far as ML arrays are concerned, by laminating or embossing them directly onto or into a microparticle-containing layer, it is also possible to reduce their focal length even further. Currently, the 400µm thick glass substrate on which the ML are developed limits their focal length. However, if the ML arrays are made directly onto

a PDMS layer, this constraint can be eliminated. By decreasing the focal length (f) of the ML arrays, it is estimate that a corresponding increase in AOI tolerance of roughly a factor of $2\times$ can be achieved with this approach.

Furthermore, adapting this technology for use on polymer banknotes presents a unique challenge due to their considerably thinner substrates compared to those of blister packs. It's crucial that the addition of a security feature does not significantly increase the thickness of the banknote to avoid complications with stacking and processing in automated currency handling systems. Typically, the plastic substrates used in blister packs have a thickness of around $400\mu\text{m}$, whereas polymer banknotes maintain a thickness of less than $100\mu\text{m}$.²²⁹ Advancing this technology for application on such slender substrates necessitates additional investigation into the design of the labels, ensuring they meet the stringent requirements of banknote security without compromising their physical and mechanical properties.²³⁰

5.11.3 Label stability with aging

To investigate label long-term stability for generating a similar pattern, an optical experiment is conducted using the same transmission-based authentication setup. Two different images from a single label are recorded over a 12-month period after label fabrication. It is noted that, when capturing the pattern from the label in the authentication set-up, both the AOI and the label position in regard to the excitation source are similar over the two periods. Figure 5.21 a) and b) shows the binary image

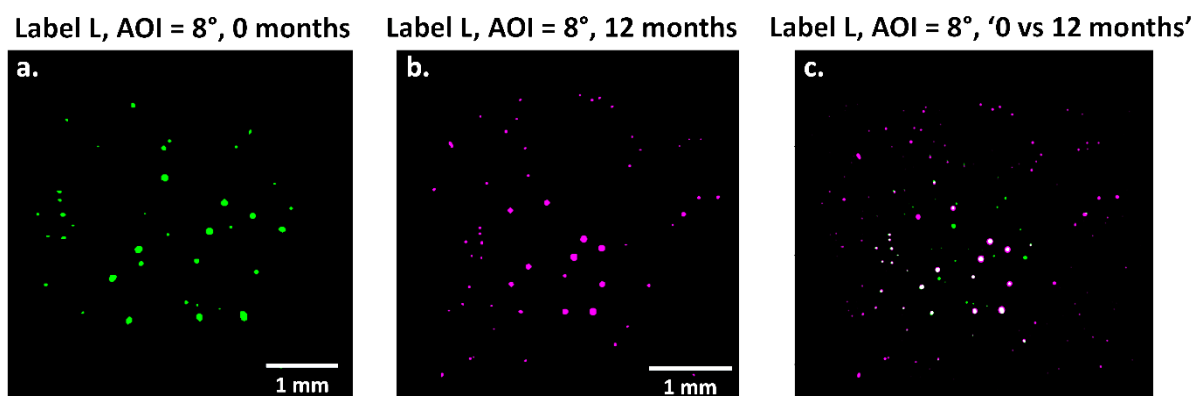


Figure 5.21 An investigation of the stability of a label (label L) showing the binary images of the two point-patterns observables immediately after fabrication (0 months, green colour) and 12 months (magenta colour) later. Despite some similarities in the central brightest points (see composite image), the patterns have substantially changed. Slip occurring in the lamination layer between the ML array and the phosphor layer is hypothesized to cause the observed effect in this prototype design of the label. Reproduced with permission from Kumar *et al.*³

of the two patterns from a single label (L1), captured at the time of manufacture, i.e. at 0 months (green colour) and after a 12-month interval (magenta colour) respectively.²⁰⁸ False colour representations of the two patterns are originally recorded at the same AOI, i.e. at AOI = 8°. It is to be highlighted that there are no concerns regarding the photostability of the phosphors that are incorporated into the label. In fact, there has been no noticeable change in the brightness of the points generated by the DS phosphor over a time interval of twelve months. Also, since the label concept is intended to work with a wide variety of phosphor particles and polymer layers, guidance from the lighting community (e.g., phosphor-converted LEDs will be helpful in selecting phosphor that are highly photostable in conjunction with polymers).^{231,232}

A major challenge in reproducible long-term authentication in the current prototype design is the shift in the PDMS layer loading with phosphor particles and the ML array glass substrate that occurs with aging. In Figure 5.21 c), a qualitative comparison of the two patterns is presented, including a composite image that overlaps the two patterns in a single frame, following the feature-based affine transformation. The overlapping of similar bright points in the two patterns results in generating white bright points. As a result, it qualitatively represents a similar pattern over two different time intervals from a given label. A quantitative analysis of these two patterns results in 19 votes in the authentication algorithm, which is also above the threshold vote number '16'. It was observed that while the pattern at this AOI (at AOI = 8°) authenticates, patterns recorded at other AOIs from the same label do not match with corresponding references recorded at 0-month. It is hypothesized that pressing glass and PDMS layers together (through the curing process) in these prototype designs does not create a lamination that will last over a long period of time duration. As the ML arrays are fabricated on a glass slide that is gradually slipping away from the phosphor-doped polymer layer underneath it as time passes. This results in progressively changing point patterns from the given label over time, ultimately resulting in the label ceasing to authenticate with the original reference images. In chapter 6, a revised label design will be examined to overcome these stability challenges. The discussion will focus on a redesigned unclonable label in which either the ML array substrate is optically bonded to the phosphor-doped polymer layer, or the ML is directly embossed onto the polymer layer.

5.12 Summary

This chapter explores the advancement in anti-counterfeiting technology through the development of unique PULs that employ a ML array and commercially available DS phosphors with varying median diameters (D50) on the micron scale. The study reveals a positive correlation between the D50 particle diameter and the AOI tolerance, indicating that larger particle sizes result in increased AOI tolerance. Specifically, particle diameters of $(9.0 \pm 1) \mu\text{m}$, $(20.5 \pm 1) \mu\text{m}$, and $(32.5 \pm 2) \mu\text{m}$ yielded AOI tolerances of 0.8° , 2.0° , and 3.6° , respectively. This finding marks a significant enhancement in label design, achieving an AOI tolerance nearly twenty times greater than previous iterations using longer focal length ML and UC particles. The potential application of this technology is highlighted for blister pack marking, where its compatibility with transparent polymer substrates offers a promising avenue for integrating the ML arrays and particle-doped layer. The chapter also discusses the prospects of adapting this technology for use on thinner substrates, which could broaden its applicability to areas such as currency authentication. Additionally, the introduction of a silicon textured PUL is examined, showcasing the feasibility of authentication using a single smartphone with optical filters. Practical demonstrations using LED or smartphone flashlight as light sources and smartphone cameras emphasized the label's accessibility and feasibility, highlighting its significant merits such as high AOI tolerance, cost-effectiveness, and ease of use for anti-counterfeiting purposes. Despite these advantages, the challenges associated with the label's application, authentication, and long-term stability are critically examined, acknowledging the necessity for ongoing refinement. In summary, this chapter presented a comprehensive overview of the PUL's potential as an innovative solution to counterfeiting, balancing its promising benefits against the practical challenges it faces for widespread adoption.

6 Designing an unclonable label for authentication using a smartphone

In recent times, efforts have focused on developing unclonable labels that can be easily verified using ubiquitous and cost-effective technology like smartphones.^{65,72} The simplicity of hardware requirements for validation enhances accessibility and commercial relevance. In this context, my Ph.D. work discussed in chapter 4 and 5 has introduced unclonable labels based on micron-scale randomness, which initially required sophisticated imaging setups for authentication.^{2,3} Notably, these labels are designed to function in transmission mode, involving illumination and detection on opposite sides. The ML arrays and phosphor-doped polymer layer form the basis of these labels. However, the need for additional optical elements and the complexity of imaging setups limited the accessibility of the authentication process.

6.1 Introduction

Building upon this foundation, recent advancements have explored the feasibility of utilizing smartphones for both illumination and detection on the same side, thereby simplifying the authentication process. The concept of redesigning the PUL was conceived by the first author in collaboration with Dr. Stephan Dottermusch, Dr. Ian A. Howard and Prof. Bryce S. Richards. The first author redesigned the labels, introducing larger inter-lens spacing surrounding a scattering surface. A refined authentication algorithm is developed by first author in collaboration with Fabrizio Gota and Dr. Ian Howard, demonstrating the potential for single smartphone-based authentication. The redesigned labels utilize a ML array and DS phosphor particles to create distinct bright point patterns, enabling smartphone-based authentication with optical filters to control illumination and observation wavelengths. Additionally, the first author introduced single-layered PDMS labels loaded with DS phosphor, offering flexibility and qualitative characterization for practical applications. These labels generate macroscopic, high-contrast images that are easy to capture and analyse using a smartphone, while relying on precise micron-scale random overlapping of incident focused light onto random particles to ensure unclonability. This combination guarantees that the labels are not

only secure but also user-friendly, meeting the criteria for an ideal authentication system. The first author conducted the qualitative and quantitative analyses of the label's performance together with Dr. Ian Howard and Prof. Bryce Richards, including assessment of AOI tolerance, threshold number generation and smartphone placement tolerance. The first author also performed a statistical interpretation of the randomness of patterns generated by the novel PUL design. Furthermore, the first author tested the labels under constant solar illumination at elevated temperature to ensure its optical performance and demonstrated that the labels can be conformally applied to curved surfaces. These findings, validated through rigorous environmental testing, confirm the label's suitability for practical anti-counterfeiting applications. The results presented in this chapter are based on the following first-author publications:

Kumar, V., Dottermusch, S., Katumo, N., Chauhan, A., Richards, B. S., & Howard, I. A. (2022). Unclonable anti-counterfeiting labels based on microlens arrays and luminescent microparticles. *Advanced Optical Materials*, 2022, 10, 2102402.

Kumar, V., Gota, F., Neyret, J., Katumo, N., Chauhan, A., Dottermusch, S., Richards, B.S., Howard, I. A. (2023). Smartphone authentication of unclonable anticounterfeiting labels based on a microlens array atop a microphosphor-doped layer. *Advanced Materials Technologies*, 2023, 2201311.

6.2 Label design and working principle

A sparsely distributed ML array surrounded by scattering surface is developed on a glass-substrate and overlaid on a phosphor-doped layer of PDMS layer. A detailed description of the label manufacturing process is provided in the methodology chapter. This section offers a concise overview of the process. Initially, a master mold of the ML arrays is developed by TPL technique on a silicon substrate. The design of the ML arrays incorporates an aspherical lens structure with a focal length measuring 550 μm and a base diameter of 250 μm , organized in a grid pattern of 14 \times 14 with an inter-lens spacing of 750 μm . Following this, a negative replica is created using PDMS. This replica is then used to develop a positive ML arrays and scattering layer of UV-reactive adhesive (NOA-88) onto a 400 μm thick glass base. Subsequently, the phosphor-doped PDMS layer is then drop-casted underneath the glass substrate. This involves incorporating an RTV-B curing agent and commercial phosphor powder at a predetermined concentration into a silicone elastomer RTV-A base. DS phosphor-

doped solution is carefully poured onto a glass slide before being pressed against the ML arrays. The whole design is then relieved on a hotplate, bringing about the development of the two-layer unclonable label.

An integration of ML arrays around the micro-cone scattering surface is of paramount importance for redirecting light that is not going through the ML, potentially leading to enhanced front-side recognition capabilities of the point-pattern.²¹³ The fabrication of this two-layer unclonable label, despite its simplicity and limitations, paves the way for smartphone-based authentication. The smartphone's ability to both illuminate and identify on the same side of the label presents a significant advancement, streamlining the authentication process and enhancing its accessibility.²³³ The phosphor doped PDMS layer of the label is crucial to the creation of individual patterns from the unclonable label. The label concept presented in this chapter has two key advantages that contribute to its effectiveness as an anti-counterfeiting measure: 1) the ability to magnify and visualize micron-scale features on macroscale, generating high-contrast images that are readily interpretable, and 2) the introduction of a ML arrays that enhances security by introducing a further layer of complexity. By selectively illuminating and interpreting a subset of the micron-scale positions with each illumination angle, the ML arrays deter counterfeiters by making it extremely difficult to replicate the label's unique pattern. This added layer of security, coupled with the ability to generate high-contrast images for easy analysis, makes the label concept a formidable tool in the fight against counterfeiting.

6.2.1 Experiment using a smartphone

Figure 6.1 a) presents a composite image capturing a smartphone projecting light onto a bottle adorned with one of the anti-counterfeiting labels (e.g. a medicine box). The photograph merges multiple shots taken at varying exposure times, culminating in a high dynamic range (HDR) image that highlights contrasts in regions with distinct lighting levels. The smartphone, a Samsung Galaxy S20 5G, utilizes its flashlight, filtered through a 500nm short pass filter, to illuminate the label ($1 \times 1 \text{ cm}^2$). This results in a distinctive blueish hue, deviating from the bottle's white appearance under standard lighting. The smartphone camera, equipped with a 500nm long pass filter, captures the PL-based point pattern from the label. The digitally zoomed view of the

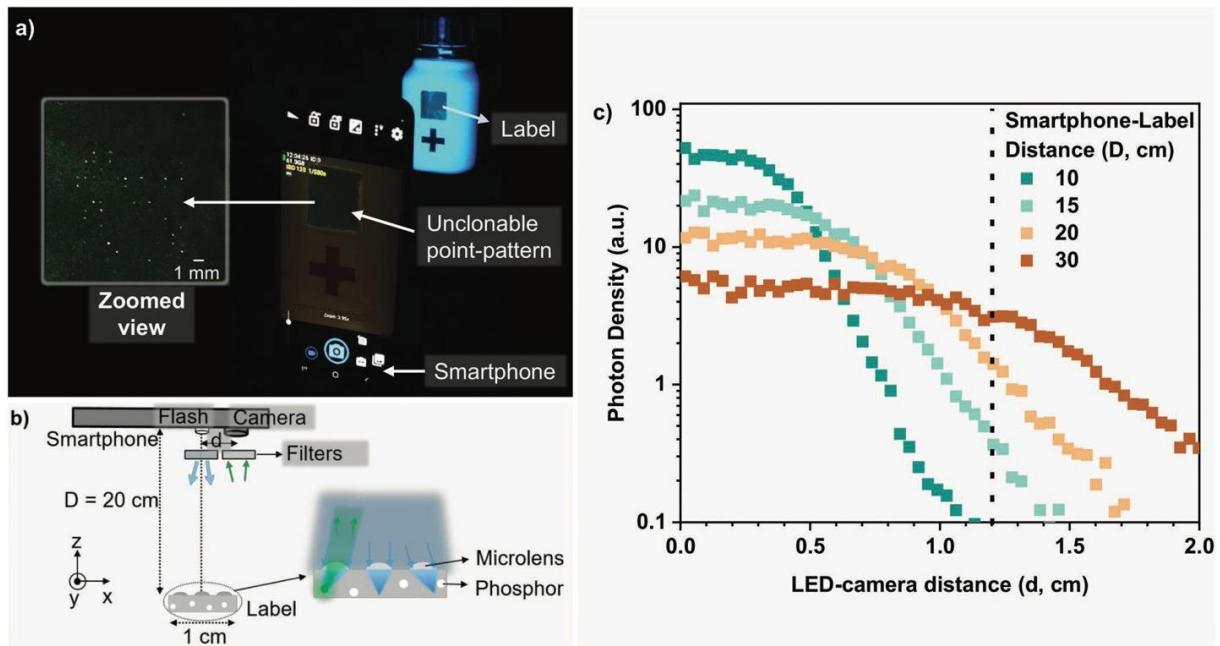


Figure 6.1 Schematic setup of label–smartphone setup to record a luminescence-based bright point pattern of a label. The smartphone is fixed in its position, whereas the label is placed on a translational stage that varies the label-smartphone distance (D). b) Qualitative analysis of three different patterns of the label that are captured at $D = 20$ cm, 18 cm, and 22 cm, and shown in red, green, and blue false colour respectively. A composite RGB image shows overlapping of the same bright points in the three images. c) Quantitative analysis of the luminescence-based images obtained from a single label. 11 different test images are recorded (by varying D from 15 cm to 25 cm, in steps 1 cm) and compared with the reference image ($D = 20$ cm). Reproduced with permission from Kumar *et al.*⁸

recorded pattern from the label (under smartphone flash illumination and camera detection) is elucidated in the inset of Figure 6.1 b).

In Figure 6.1 b), the arrangement of excitation (from a smartphone flashlight) and emission response (from the label) is illustrated. Here, the term 'origin' refers to the point directly under the smartphone's flashlight, which is centrally positioned over the ML arrays. The experimental design allows for the smartphone to be moved along the 'y' axis relative to the label, enabling adjustments in its position. This movement is key as it alters the AOI on each individual ML on the label. The AOI varies across the label due to two primary factors:

- **Point-source-like angular illumination of the smartphone flashlight:** The smartphone flashlight emits light in a point-source-like manner, meaning that the light rays emanate from a single point. This results in a variation in AOI across the label, as the rays from the flashlight strike the different ML at different angles.
- **Different angles from the flashlight to each ML in the array:** The angle between the flashlight and each ML on the label is not uniform. This is because

the ML are arranged in a regular array, and the flashlight is not directly aligned with the centre of the array. As a result, the AOI varies across the label, with some ML receiving more direct illumination than others.

As depicted in Figure 6.1 b), the emitted light from a bright particle must pass through the individual overhead ML element to reach the detector (smartphone camera). This interaction between the emitted light and the ML leads to a phenomenon known as partial collimation, where the light rays, initially spreading out from the ML, are partially confined into a narrow beam. The extent of partial collimation that reaches to the detector depends on the characteristics of the ML (e.g. focal length, base diameter of the ML) and the detector position. If the distance between the ML arrays and the smartphone camera is relatively small (along the z-direction in Figure 6.1 b), then the partially collimated light beam will be sufficiently focused to be captured by the camera, resulting in a bright, identifiable spot on the camera image. However, as the distance between the ML arrays and the smartphone camera increases (along z-direction), the beam expands due to the non-perfect collimation of the light. In this case, the camera may no longer be within the confines of the light beam (along the x-direction in Figure 6.1 b), leading to a diminished or even non-existent spot on the camera image. This phenomenon of beam expansion with increasing distance between the label and camera is a crucial factor in determining the effective range of the unclonable label system.

To ensure reliable detection of the label's unique pattern, the distance between the ML arrays and camera should be maintained within an optimal range, typically around 20cm, as employed in the experiments. The simulated model of the label and camera detector, as shown in Figure 6.1 c), indicates that at a distance of 20cm between the smartphone and the label, more than 10% of the maximum intensity of the light emitted from the smartphone flashlight is captured by the smartphone camera. This amount of light is sufficient light to effectively excite the phosphors in the label and generate the unique pattern required for authentication. However, increasing the distance between the smartphone and the label to 30cm results in a significant decrease in the amount of light captured by the camera. This is because the light emitted from the smartphone flashlight becomes more diffuse and spread out as it travels further away from the flashlight. As a result, there is not enough light to effectively excite the phosphors, and the unique pattern of the label cannot be generated. Therefore, a distance of 20cm between the smartphone and the label was chosen for the experiments. This distance

provides a balance between capturing enough light to effectively excite the phosphors and maintaining a reasonable distance for practical use. Additionally, the distance (d) between the flashlight and the smartphone camera is 1.2cm, which is the standard configuration for the smartphone model used. These distance parameters (D & d) are well within the range of a normal smartphone operation, ensuring that the label can be effectively illuminated and imaged by mostly available smartphones at current.

6.2.2 Simulation theory for the 2D distribution of emission profile from a bright particle over a ML

PVtrace, a ray-tracing simulation environment, enables users to construct virtual worlds composed of geometries and light sources.^{234,235} These geometries exhibit diverse attributes, including defined shapes, index of refraction, scattering properties, PL capabilities, and mirror-like surfaces.²³⁴ Light sources emit rays that can be tracked individually as they interact with the various geometries within the simulated world.^{234,235}

To approximate whether a smartphone camera, positioned at a certain distance from the smartphone's flashlight, can effectively capture the bright light outcoupled from a ML at a specific distance between the label and the smartphone, ray-tracing simulations is conducted using PVtrace software. This approach provides a preliminary estimation, crucial for understanding the interaction between the flashlight, an underlying ML, and the emission light reaching to smartphone camera in the

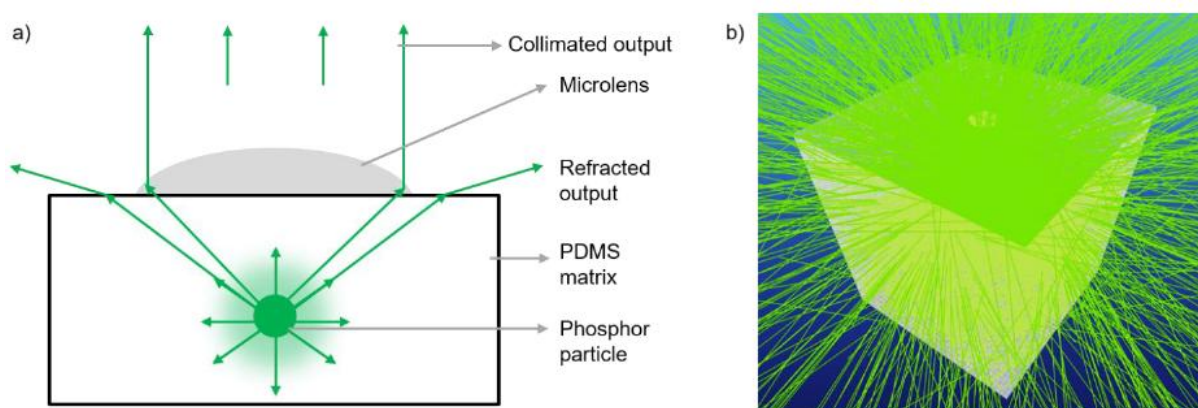


Figure 6.2 a) Schematic 2D-illustration of an isotropic emission from a bright particle (as a source). The light rays reaching to the ML out-couple in a collimated form, whereas light rays reaching to the PDMS surface (below the critical angle limits) out-couple through refraction. b) Simulated view of an isotropic emission by a bright particle source (unseen in the picture) in the PDMS matrix. The analysis is made on the PVtrace simulation software. Figure is adapted with permission from Kumar *et al.*⁸

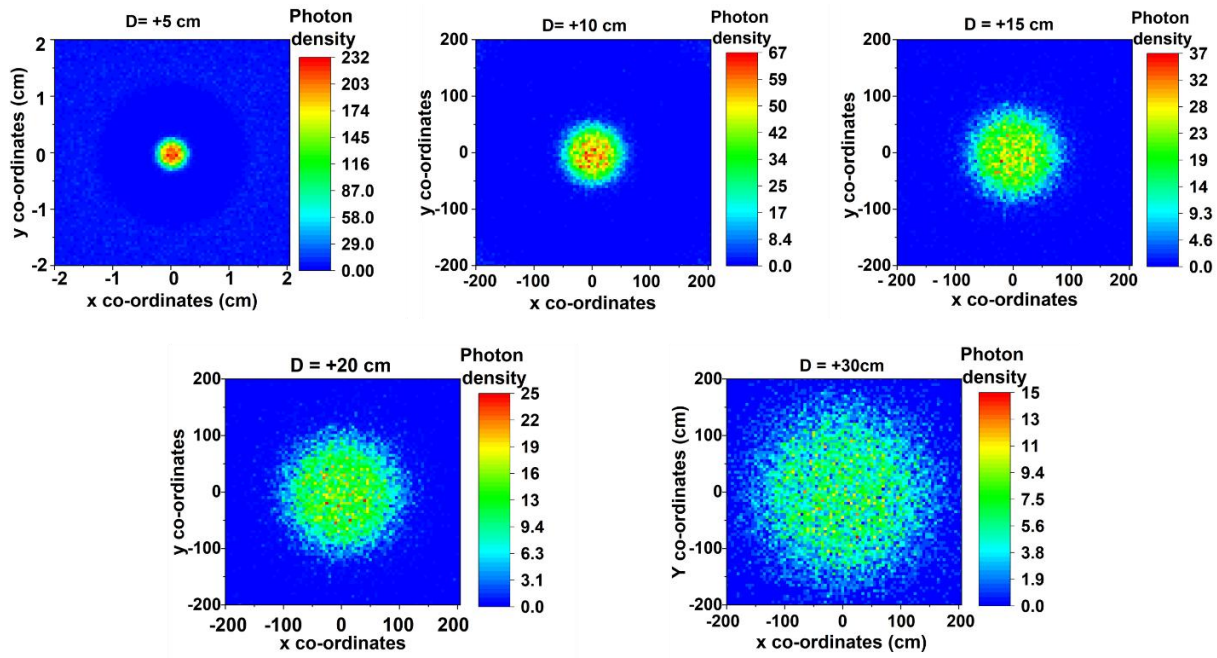


Figure 6.3 2D profile depicting the distribution of light intensity emitted by a bright particle as it exits through the lens and reaches virtual detectors. The detectors are positioned at distances (D) of +5cm, +10cm, +15cm, +20cm, and +30cm from the top of the label. The expansion of the emitted light 'cone' becomes evident as the distance increases, facilitating the capture of the bright point-pattern by a camera offset from the excitation LED. Reproduced with permission from Kumar *et al.*⁸

experimental setup. In this study, a geometric structure is created using the 3D graphics software Blender and subsequently implemented in the PVTrace world, as shown in Figure 6.2 b). The geometry consists of a box with dimensions of 2mm, featuring a modified half-sphere with a base diameter of 250 μ m and a ROC of 200 μ m positioned on top. A spherical isotropic light source with a radius of 15 μ m is placed inside the box at a height of 15cm, precisely at the centre of the horizontal plane. Rays emitted by the light source interact with geometry, and some escape through the top plane. To capture and analyse these interactions, detector planes are strategically positioned at +5cm, +10cm, +15cm, +20cm, and +30cm from the source. The positions of the escaping rays are recorded, generating 2D histograms at each detector plane, shown in Figure 6.3. The 2D histograms, based on the positional data from the simulated rays (106 rays in total), provide insights into the distribution of escaped rays at different distances from the source.

In summary, this simulation approach using PVTrace and Blender allows for a detailed examination of how light interacts with a specific geometric structure, providing valuable insights into the spatial distribution of escaped rays at various detector positions. The results contribute to a comprehensive understanding of the optical

behaviour within the defined world, offering applications in fields such as optics, photonics, and light modelling.

6.3 Label authentication algorithm

In the prior work on point-pattern validation from unclonable labels, an algorithm was employed to extract and compare the 2D coordinates of bright points in captured images.^{2,3} However, with the closely packed ML arrays design presented in chapter 4 and 5, accurately associating a single bright emission point with a specific lens is challenging.

This limitation is effectively addressed in the present approach, where a more sparsely spaced ML arrays enables the unambiguous assignment of each bright spot to its corresponding lens. This association forms the basis for generating a simple binary code. The code's length corresponds to the number of ML in the array, with '1' denoting a bright emission under the focus of the respective ML, while '0' indicates the absence of emission. To ensure consistent orientation, a fiducial mark is employed. This

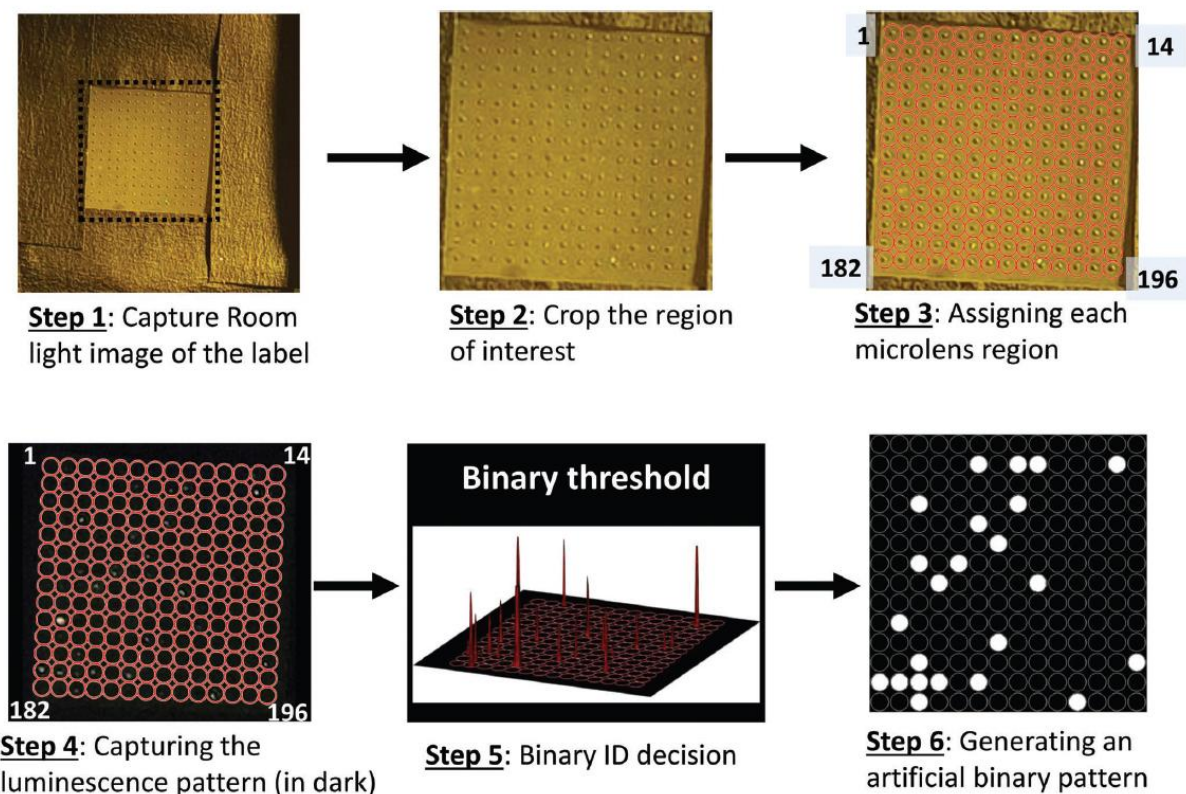


Figure 6.4 Illustration of the algorithm that generates a binary string representing each ML as either bright (1) or dark (0). The process involves capturing a label's image with background lighting to locate the ML via a fiducial mark. A ML is classified as 'bright' if at least three pixels within its region exceed 1.5 times the average pixel values. Reproduced with permission from Kumar *et al.*⁸

straightforward approach simplifies comparison of reference and test strings based on shared bright point locations. The algorithm cycle starts by fixing the label and cell phone in the ideal position, utilizing a laser-cut holder for exact arrangement. An underlying picture of the label is caught with background lighting, uncovering the ML positions, shown in step 1, Figure 6.4. Each ML is centred in a square array of touching circles that are manually identified four ML centres in a sequential way, as shown in step 3. When it comes to associating pixels with each ML, this number association with the ML arrays serves as a reference. In step 4, The smartphone flashlight is turned on, the background light is turned off, and an image of the point pattern from the label is taken. Utilizing the Open camera application (version 1.48.1, code: 77), the image capture settings are standardized by fixing the ISO at 450 and exposure time at 1/50 second, with the white balance consistently set to 7000K. These specific conditions are selected to produce images predominantly dark in nature, interspersed with distinct bright points.

6.3.1 Transforming the bright pattern into an artificial binary pattern

For each ML region, defined by a circular ring, the average pixel value is calculated. This average is then multiplied by 1.5 and subtracted from the entire image, effectively isolating the bright pixel as 'spikes', as shown in step 5 of Figure 6.4. To determine whether a lens region is considered 'bright', the sum of pixel values in the modified image for each lens is computed. A sum exceeding a threshold value of 10 within any lens area is indicative of a bright point. The original images of the label, corresponding point pattern and the source code of the algorithm utilized for creating the artificial point pattern image (as shown in Figure 6.4) are available in the GitHub repository (<https://git.scc.kit.edu/zl3429/label-authentication-algorithm-for-smartphone-application>).

6.3.2 Logic for the similarity comparison of a test-reference image pair

To conduct a quantitative analysis on the similarity between two distinct point patterns, the approach is centred on measuring the proportion of bright spots that are consistently present in two images, captured under the same illumination conditions. The first phase of the analysis entails registering the total count of bright spots identified within each of the two images. This step is facilitated through the analysis of

binary representations of each image, where the presence of a bright spot is denoted by a '1'. By calculating the sum of '1's in each binary string, the total count of bright spots (denoted as TB) for both the reference image and the image under examination is ascertained. Following this, a bitwise summation of the binary strings corresponding to the reference and the test images is performed.^{236,237} In this process, a position that holds a '1' in both strings contributes a '2' to the resultant sum at that specific position. The occurrence of '2's in this combined binary string directly corresponds to the number of bright spots that are identically located in both the reference and the test images. By tallying these occurrences, the count of shared bright spots (denoted as SB) is derived, effectively quantifying the positional concordance of bright spots across the two images under study.

To assess the degree of similarity between the two images, a quantitative metric, denoted as F is introduced. This metric represents the proportion of overlapping bright points relative to the total number of bright points observed across both images. The computation of F is executed through a simple formula: $(F = 2*SB/TB)$. Here, 'SB' stands for the sum of bright points that occupy matching positions in both images, while 'TB' signifies the aggregate count of bright points when considering both images collectively. The resultant value of F can vary on a scale from 0 to 1, where a value of 0 indicates an absence of any positional concordance among bright points – thereby reflecting completely different patterns. Conversely, a value of 1 is indicative of a complete positional alignment of bright points across the images, thereby denoting identical patterns. The analysis demonstrated that this metric, F , serves as a robust quantitative tool for comparing the degree of match between given test and reference strings. It is particularly noted that, compared to the Hamming distance, F exhibits less variability in cases of non-matching strings. This attribute of F makes it a more effective metric for classification decisions, providing a clearer distinction between matching and non-matching cases. It's noteworthy that the reduced variability in F enhances the reliability of the pattern matching assessment in practical applications.

To delve into a detailed examination of the potential diversity of unique codes that can be generated by such a label, the current scenario considers a label with a 14×14 grids of sparsely distributed ML arrays. This configuration enables the generation of a binary string with a length of 196 bits. In this string, each '1' represents a bright point and can be randomly distributed across the array. Given the current doping concentration 0.5

wt.% of the DS phosphor, approximately 25 bright points are typically observed on average. This observation suggests a theoretical possibility of approximately 10^{31} unique codes. Consequently, when this physical arrangement is converted into a binary string ID, the system retains a substantial amount of information. This high information content is crucial for the creation of a multitude of unique labels, thereby ensuring the probability of generating two identical labels extremely low. This aspect is essential for maintaining the authenticity and security of such labels in practical application in anti-counterfeiting.

6.4 Qualitative Analysis: AOI Tolerance of the labels

A comprehensive qualitative examination has been undertaken on the patterns of the label, with a detailed focus on its reproducibility, unclonability, and uniqueness. These attributes are paramount for an effective anti-counterfeiting strategy. This examination is incorporated into the binary ID-based authentication algorithm that converts luminescence-based point patterns into binary string ID. The following section presents a qualitative comparison of patterns for two-layered and single-layer all PDMS labels, shown in Figure 6.5.

6.4.1 Two layered PUL

Reproducibility: Multiple trials on a single label are carried out so that the reproducibility of the point patterns could be evaluated. The label is given a notation L1, and luminescence-based patterns are captured with a filter-equipped smartphone camera. For each trial, the label is removed, reinserted, and translated to various random positions before being returned to its home position. During each trial, both the luminescence-based pattern and corresponding image are captured in room light from Label L1. As demonstrated in Figure 6.5 a), three separate trials are conducted for a single label, L1. For a straightforward visual comparison, the binary strings resulting from these trials are depicted, aligning with three primary colours: R, G and B. Additionally, a composite image combining all three trials into a single frame, is created. Despite some minor variations, the majority of the bright points in the images from different trials overlap, leading to the creation of white (W) colour dots ($R + G + B \rightarrow W$) in the composite image, thus verifying the reproducibility of the patterns associated with the label.

Unclonability: To establish that a single label can produce a variety of unique and unclonable patterns, label L1 is positioned on the sample holder and move the smartphone along the y-axis (referred in Figure 6.5 b) at increments of 0, 2.5, and 5.0 cm. This movement alters the relative positioning between the smartphone and the label, leading to shifts in the AOI and consequently changing the focal volume beneath each ML. The new bright point patterns obtained at these varied distances are then encoded into strings, and are displayed in R, G and B colours respectively, as shown in Figure 6.5 b). By overlapping the three coloured images into a single composite frame, distinct variations corresponding to each smartphone movement are observed. This concludes the label's unclonability and affirming the robustness as an anti-counterfeiting label.

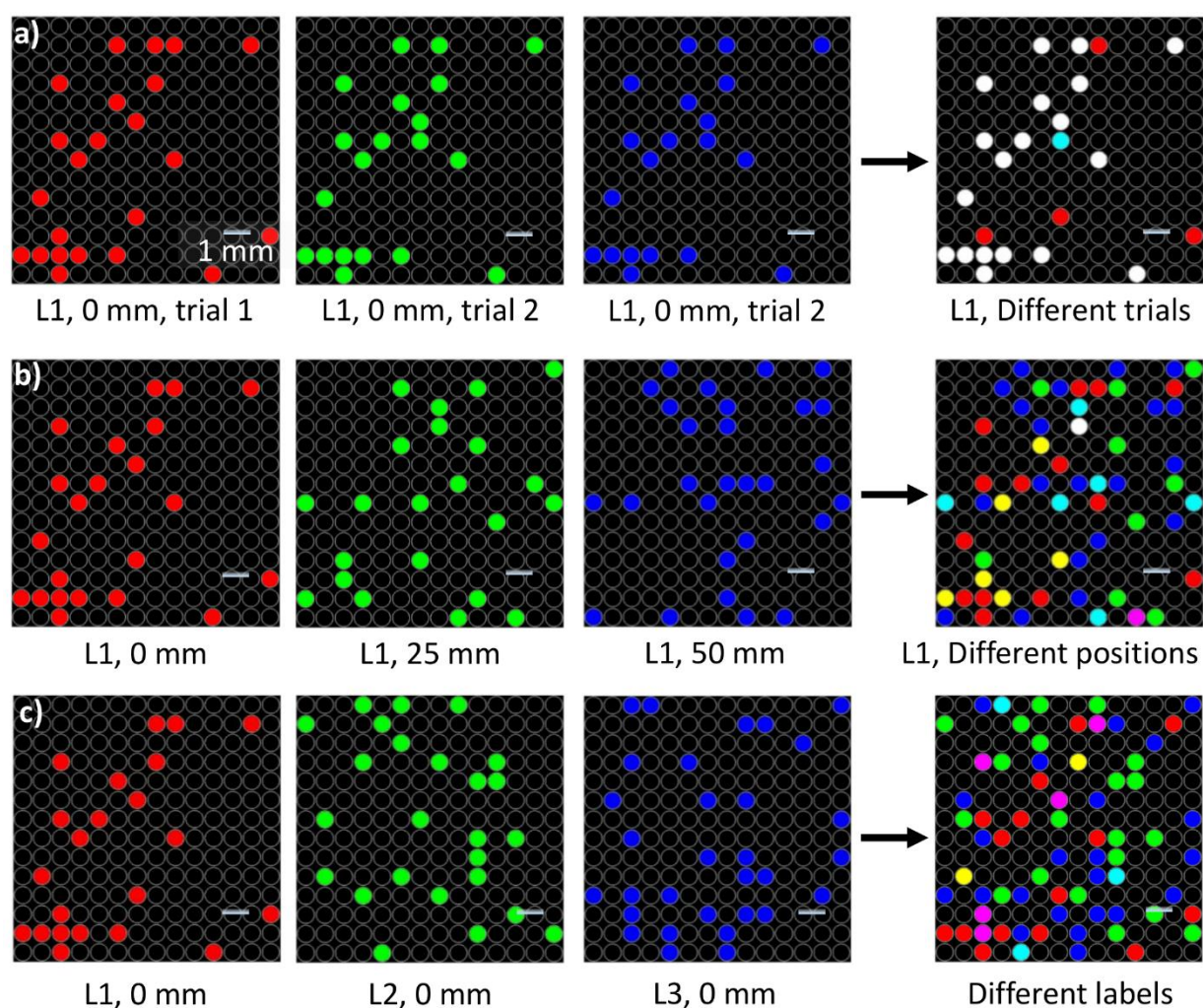


Figure 6.5 Qualitative analysis of patterns that are transformed into binary string ID from a) repeated trials of the same label L1, in a fixed position for reproducibility analysis; b) the same label, L1, at various positions to illustrate pattern changes and unclonability with smartphone movement; and c) different labels L1, L2 and L3 to demonstrate uniqueness. Individual and composite images in each row highlight the similarities and differences among different binary ID strings. Reproduced with permission from Kumar *et al.*⁸

Uniqueness: Three distinct labels are examined, each with the same phosphor doping concentration, to demonstrate the uniqueness of manufactured labels. Figure 6.5 c) shows the R, G and B colours of the ID strings that are generated for three different labels that are taken while the smartphone is in the home position. The composite picture supports that each label has a unique point-pattern because of the irregular distribution of microparticles in the doped film. A statistical evaluation of random distribution of particles in different labels will be presented in the following section in this chapter, that is accomplished by the Pearson correlation co-efficient.^{223,238}

6.4.2 Single layered all PDMS PUL

By utilizing a single layer of PDMS, the label maintains the algorithm for verifying unclonable and unique luminescence-based point patterns. Figure 6.6 shows a qualitative comparison of the point patterns generated by single-layered all PDMS

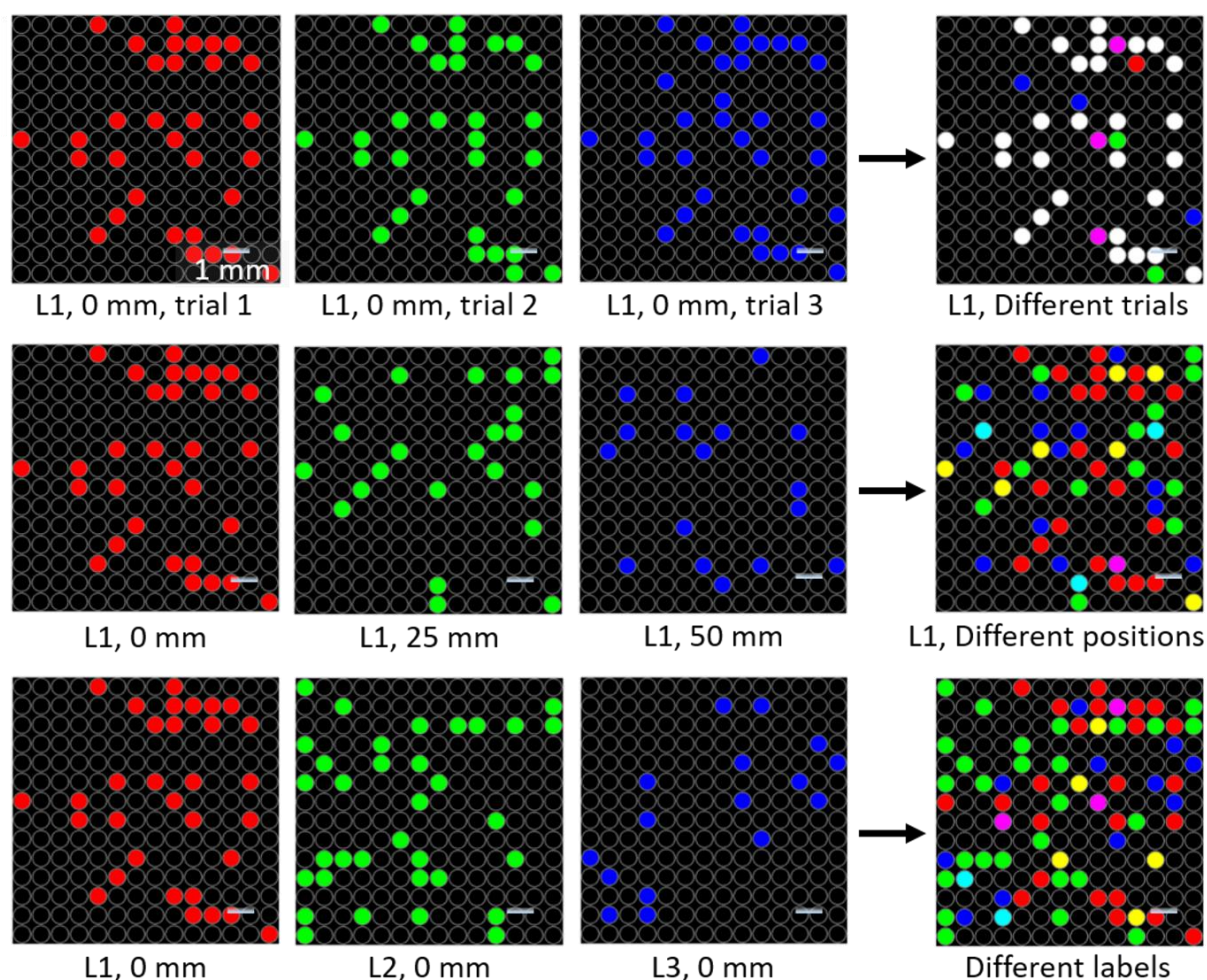


Figure 6.6 A qualitative assessment comparing the performance of single-layer all PDMS label, showing their equivalence in functionality as that of the two-layered PDMS-glass unclonable label. Reproduced with permission from Kumar *et al.*⁸

labels, affirming their equivalence to the PDMS-glass two-layered labels previously discussed. This comparison is critical in evaluating the reproducibility and uniqueness of the label's patterns, two key factors in their potential application for anti-counterfeiting. Moreover, a statistical approach is employed to quantify these characteristics, using an F value as a metric for analysis. In the trials, where reproducibility is tested by capturing images of the same label under identical conditions, the F value consistently exceeded 0.9. This high value indicates an exceptional level of reproducibility, as it suggests that the luminescence patterns produced by a label in repeated trials are almost identical. This is a vital feature for ensuring reliability in any anti-counterfeiting system, as it assures that each label can be dependably recognized and verified across multiple scans or readings.

On the other hand, when evaluating the uniqueness of the patterns – a measure of how distinctly a label can be identified – the F value dropped below 0.3 in scenarios where either the smartphone's position is altered during image capture or when different labels are used. This significant decrease in the F value reflects the unique luminescence patterns generated under varying conditions or from different labels, highlighting the labels' potential to act as individualized markers. This uniqueness is imperative for anti-counterfeiting measures, as it ensures that each label is distinct and cannot be easily replicated or confused with another, thus providing a robust mechanism against counterfeiting efforts.

6.5 Statistical interpretation of randomness of the labels

The Pearson correlation coefficient between patterns x and y can be computed using the formula²³⁸:

$$r_{xy} = \frac{\sum(x_i - x_m)(y_i - y_m)}{\sqrt{\sum(x_i - x_m)^2 \sum(y_i - y_m)^2}} \quad (6.1)$$

Where x_i and y_i are the individual i -th sample points in Binary string ID x and y . The value of the i -th element can be either 1 or 0, corresponding to whether the lens results in a bright point or a dark point, respectively. x_m and y_m represents the average values of patterns x and y , calculated as the total number of bright points divided by the total sum of ML.²³⁸

In the context of Pearson correlation coefficient analysis, a coefficient value approaching either 1 or -1 signifies a robust correlation or anticorrelation,

	Label 1	Label 2	Label 3	Label 4	Label 5
Label 1	1	-0.02	0.13	-0.09	0.18
Label 2	-0.02	1	0.01	-0.01	0.05
Label 3	0.13	0.01	1	-0.04	0.06
Label 4	-0.09	-0.01	-0.04	1	-0.01
Label 5	0.18	0.05	0.06	-0.01	1

Figure 6.7 Pairwise comparisons of patterns from five distinct labels using Pearson correlation coefficients. Reproduced with permission from Kumar *et al.*⁸

correspondingly. On the other hand, a coefficient value hovering around 0 is indicative of a lack of correlation between the patterns. This means that the variations in one pattern do not systematically align with changes in the other, pointing to their independent or unrelated behaviors.²³⁸ In this specific case as shown in Figure 6.7, where the observed correlation coefficients are consistently less than 0.2 in magnitude, it implies that the point-patterns generated by individual label instances are distinct and uncorrelated. This low degree of correlation suggests that each label instance produces a unique luminescent pattern, which is not predictably similar or related to the patterns produced by other label instances. Such uniqueness and lack of correlation in the emission patterns are pivotal for the integrity and reliability of the authentication system, as they ensure that each label provides a distinct, non-reproducible signature that can be used for secure identification purposes.

6.6 Quantitative comparison of the labels

To conduct a quantitative analysis of the label's performance, it is imperative to establish a substantial dataset comprising both test and reference images. These images should represent pairs that are expected to authenticate as well as those that are not. To objective this objective, eight distinct labels are fabricated. These labels are then imaged using a smartphone from two specific positions: at ($y = 0\text{cm}$) and slightly offset ($y = 5.0\text{cm}$). This initial set of images serves as a baseline reference. After capturing these reference images, the labels are repositioned. Utilizing the same smartphone, a new series of test images are captured. The aim here is to replicate the initial imaging conditions as closely as possible, returning to the same relative positions. This methodical approach ensures a robust and varied collection of test

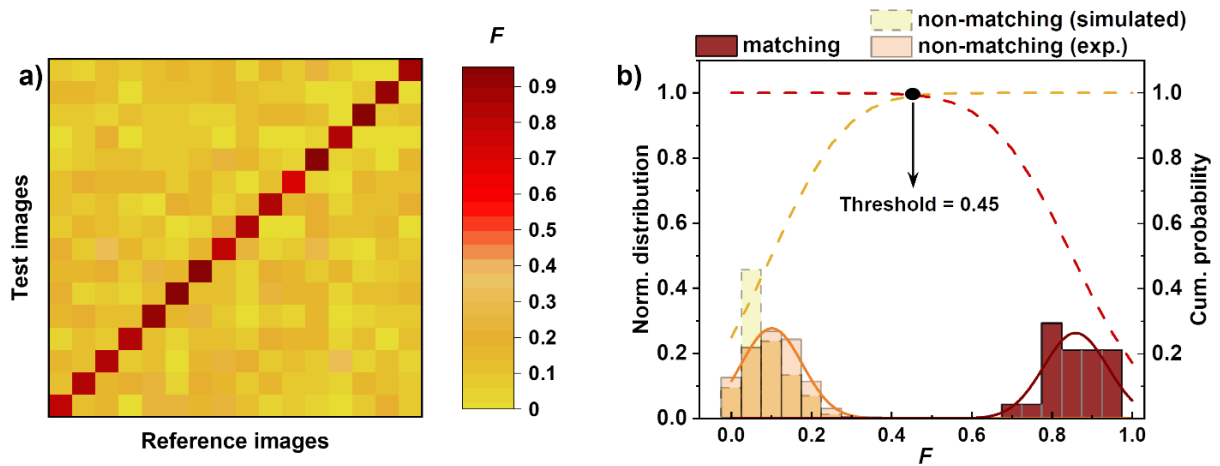


Figure 6.8 (a) Correlation factor F indicating the fraction of bright points at identical locations in reference and test images for matching (diagonal) and non-matching (off-diagonal) populations. (b) Histograms distribution of F for both populations with fitted normal distribution curves (solid lines) and their cumulative density functions (dotted lines), highlighting the crossing point used to determine the F threshold for image matching. Reproduced with permission from Kumar *et al.*⁸

images. These images are critical for rigorously evaluating the authentication performance of the labels under different, yet controlled, conditions. This systematic approach yielded 16 reference and 16 test images, creating 256 potential comparisons of binary strings, shown in Figure 6.8 a). To enhance the statistical robustness of the quantitative comparison of patterns, a strategy is implemented to increase the sample size of the 'matching' reference-test image pairs. This is achieved by capturing additional images of each label at a distinct position, specifically at a smartphone illumination position at ($y = 2.5\text{cm}$). It is imperative to note, however, that these newly acquired images at $y = 2.5\text{cm}$ cannot be reliably utilized to augment the statistics for the "non-matching" image set. The rationale behind this exclusion lies in the partial correlation these images bear with those captured at a proximal distance (specifically, images taken at $y = 0\text{cm}$ compared to those at $y = 2.5\text{cm}$ exhibit a correlation factor, denoted as F , of approximately 0.5). By incorporating these additional images from the 2.5cm position, the "matching" dataset has been expanded by an additional 8 cases.

Consequently, this enhancement brings the total count of the "matching" population to 24 cases. This enlargement of the dataset is anticipated to provide more substantial and reliable statistical insights, thereby strengthening the validity of the authentication system's performance assessment. The comparison of the 256 reference-test image pairs reveals that 16 should authenticate, while the remaining should not. For the nonmatching pairs (off-diagonal binary ID comparisons), the fraction (F) varies between 0 and approximately 0.35, with a mode below 0.1.

Moreover, a methodology is developed to generate a model histogram that simulates the distribution of bright points on labels, analogous to the image comparison analysis. The process begins with the random selection of 30 integers within the range of 0 to 196, where repetitions in selection are permissible. This step is crucial as it mirrors the random emergence of bright points on a label. This procedure is replicated 10^6 times, with each iteration representing a different label, thereby creating a large dataset that simulates the location of bright points across 10^6 distinct labels. Statistically, each label is anticipated to have an average of 28 unique bright points. This estimate is based on the likelihood that, out of the 30 randomly chosen integers, approximately 2 will be repeated selections, thus not contributing to unique bright points. This theoretical average aligns closely with the experimentally observed average number of bright points from the labels. Following this, the correlation factor, denoted as F , is computed for 10^6 pairwise comparisons drawn from the simulated label population. This theoretical computation clarifies the distribution of bright points in non-matching label pairs. The resulting histogram from these computations is then analysed and compared with the distribution obtained from experimental observations. Notably, there is a general similarity between the two distributions, although the experimentally derived distribution exhibits a slightly broader range. This deviation is likely attributable to a greater variation in the number of bright points among the actual labels, as opposed to the more uniform distribution anticipated in the theoretical model calculations. Despite this slight discrepancy, the overall similarity between the theoretical model and experimentally observed distributions allows us to draw a significant conclusion. It validates the hypothesis that the distribution of F values for non-matching label pairs is consistent with the statistical likelihood of bright points coinciding by random chance.

In the analytical approach to understanding the distribution characteristics of the nonmatching label pairs, a Gaussian PDF is fitted to the data representing this population. This statistical model is particularly chosen due to the Gaussian distribution's efficacy in representing data distributions that naturally occur in many scientific phenomena.²⁰⁹ Upon fitting a Gaussian PDF to the nonmatching population data, key parameters describing the distribution are derived. The central position, also known as the mean of the distribution, is found to be 0.16. This value indicates the central tendency around which the data points are clustered. Additionally, the width of the distribution, quantified by the FWHM, is determined to be 0.19. The FWHM is a measure of the spread of the data and is particularly insightful in understanding the

variability or dispersion in the values of the correlation factor F for non-matching pairs.²⁰⁹ Furthermore, to provide a more comprehensive interpretation of the data, the corresponding CDF is also generated. The CDF is depicted as a dashed orange line in Figure 6.8 b). This function cumulatively aggregates the probabilities, offering a visual and analytical means to ascertain the total probability that the correlation factor F will assume a value less than or equal to a specific value for a pair of non-matching labels. The CDF is particularly useful in this context as it allows us to quantitatively assess the likelihood of certain outcomes within the dataset, offering a deeper insight into the statistical behaviour of nonmatching label pairs.²¹⁰

An in-depth analysis of the histogram representing the matching population is illustrated through rosewood columns in Figure 6.8 b). This population pertains to the instances where the reference and test images are expected to match. A noteworthy observation from this analysis is the noticeable large separation between the distributions of the correlation factor F for the nonmatching and matching populations. This separation is a crucial aspect as it highlights the potential effectiveness of using F as a discriminative metric for classification purposes. The matching population exhibits a notably tight distribution in terms of the values of F . By fitting a Gaussian PDF to this distribution, the central position or mean of the distribution is identified as 0.15. Additionally, the width of the distribution, quantified using the FWHM, is calculated to be 0.18. These parameters indicate the consistency and the narrow spread of the F values within the matching population, reflecting a high degree of similarity among the pairs of images that are supposed to match. Complementing the PDF analysis, the CDF for the matching population is presented as a dashed rosewood line in Figure 6.8 b). The CDF is particularly insightful as it provides a cumulative probability measure, indicating the total likelihood that the correlation factor F will exceed a certain threshold value in the context of comparing images within the matching population. This dual approach of analysing both the PDF and CDF for the matching population is instrumental in this study. It not only facilitates a detailed understanding of the distribution characteristics of F within this population but also reinforces the feasibility of employing F as a reliable statistical tool for differentiating between matching and nonmatching image pairs. Such differentiation is critical for the purpose of accurately determining whether a given pair of reference and test images should authenticate or not, enhancing the robustness and reliability of the image authentication methodology.

In the authentication system, a pivotal aspect is the establishment of an appropriate threshold value for the correlation factor F , which is used to discern between matching and nonmatching image patterns. The determination of this threshold is critical, as it directly influences the authentication decision-making process. A value of F above the threshold would lead to authentication (indicating a match), while a value below would be deemed non-matching. The analysis as shown in Figure 6.8 b) reveals a commendable separation between the distributions of F for the matching and nonmatching populations, which is a promising indicator for the effectiveness of F as a discriminatory metric.

To optimally position the threshold within the observed gap between these distributions, the focus is on the intersection point of the CDFs of both populations. This intersection represents a balance between the probabilities of false positives (where non-matching images are incorrectly authenticated) and false negatives (where matching images fail to authenticate). The CDFs of the matching and nonmatching populations intersect at an F value of 0.45, with the crossing point yielding a probability exceeding 0.99. Setting the threshold at $F = 0.45$, therefore, implies that the likelihood of encountering either a false positive or a false negative is less than 1%. This threshold value is particularly significant given the computational efficiency with which F can be calculated. The calculation of F is not only straightforward but also remarkably rapid. In the experiments, a single test-reference comparison (using MATLAB) on an Intel Core i5-3740 3.2 GHz processor is completed in a mere 100 microseconds. This computational efficiency is advantageous, especially when considering scenarios where multiple test images need to be compared against a large database of reference images. Therefore, approaches that entail comparing a small number of test images with a vast array of reference images are straightforward to execute and could effectively bypass certain challenges associated with hand-held authentication systems, e.g. use of a smartphone.

6.7 Classifying the tolerance of point-pattern robustness against smartphone position

In the preceding section of this chapter, it was successfully established that employing a single smartphone positioned at the front side of the label is effective in accurately distinguishing between matching and non-matching pairs of reference and test images, provided that these images are captured from the same camera angle and position.

However, a crucial aspect of practical applicability in real-world scenarios is the system's ability to tolerate minor variations in the smartphone's positioning during image capture.^{239,240} Specifically, it is advantageous for the system to still recognize images as matching when the position of the smartphone varies slightly, for instance, within a 1cm range, between the capturing of reference and test images. This level of positional tolerance is not only desirable but also practically feasible to achieve with relatively simple hardware solutions, such as a basic holder where the smartphone and label can be manually aligned. Such a setup ensures that the minor positional adjustments required for accurate image matching are easily attainable without necessitating overly complex or precise equipment. On the other hand, it is imperative for the security and unclonability of the system that significant changes in the smartphone's position, such as a displacement of around 5cm, result in a complete lack of correlation in the patterns of bright points. This characteristic is vital to prevent unauthorized duplication of the labels.

In the ensuing part of this study, an in-depth analysis is conducted to demonstrate that the label design meets the specified criteria. The aim is to show the label can accommodate a positional tolerance of up to 1cm for smartphone placement while maintaining the integrity and unclonability of the authentication process in the presence of more substantial positional changes of smartphone. This analysis is pivotal in ensuring that the system is both user-friendly and secure, catering to the practical demands of real-world authentication scenarios while upholding robust security standards. To investigate the degree of positional tolerance in the correct classification of reference and test images, an experiment is conducted focusing on the impact of varying the position of the smartphone along a single axis (y-axis). The smartphone is systematically moved from a starting position at $y = 0\text{mm}$, progressing incrementally to $y = 40\text{mm}$, with each step being precisely 1mm. Throughout this process, a consistent vertical distance of 20cm between the smartphone and the label is maintained to ensure uniformity in the experimental setup.

The methodology involves selecting a subset of 11 images from the central range of the movement to serve as reference images. For each reference image, a series of test images is generated. These test images are characterized by their relative positional offsets to the corresponding reference image, varying within a range of $\pm 15\text{mm}$ at 1mm intervals. Consequently, for each reference image, there existed a pool

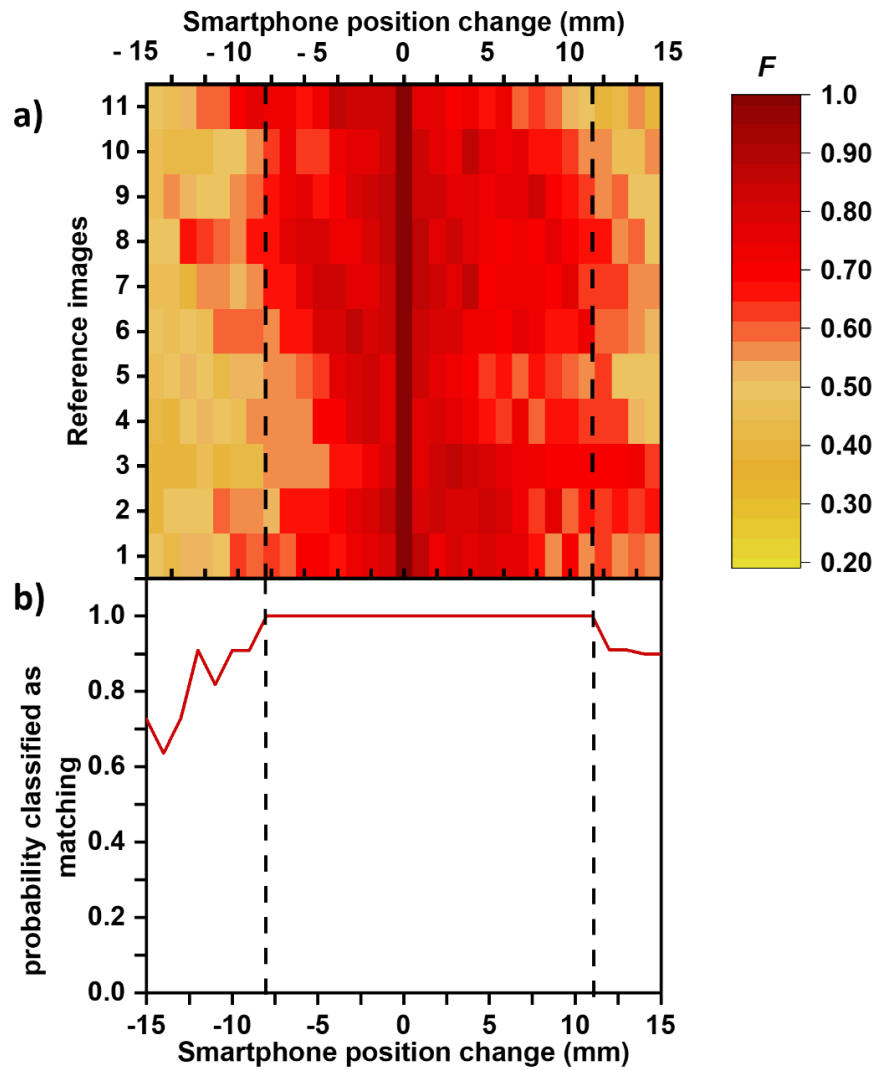


Figure 6.9 a) Correlation of bright points in reference-test image pairs with varying smartphone positions, analysing 11 reference images and their corresponding 30 test images at different offsets. b) Probability of successful authentication relative to the smartphone's positional offset, indicating label authentication for offsets under 0.95cm. Reproduced with permission from Kumar *et al.*⁸

of 31 test images, with positional offsets extending from -15mm to +15mm. Notably, the test image with a zero offset is identical to its reference image, invariably resulting in a perfect correlation factor (F) of 1. In Figure 6.9 a), the correlation factor F for each pair of reference and test images is presented, with the test images spanning the specified offset range. Referring to Figure 6.8, where the critical threshold for F is set at 0.45, a colour-coded system is used in Figure 6.9 a) to denote the pairs of reference-test images that are classified as matches (highlighting regions in red). The results indicate that test images within an offset range of -8mm to +12mm from the reference images are consistently classified as matches. This finding is further substantiated in Figure 5b, which illustrates the probability of a pair being classified as a match. This probability is determined by the proportion of the 11 reference images that successfully

authenticate with a test image at each specific offset. Intriguingly, the analysis reveals that the 'certainty' window for classification as a match – where all 11 trials result in successful authentication – spans a width of 2cm. This implies that if the smartphone's position is altered by no more than 1cm from its original location during the capture of the reference image, the system still retains its ability to correctly classify the images. This finding is critical as it emphasizes the practicality and robustness of these label authentication system, demonstrating its capacity to accommodate minor positional variances without compromising the accuracy of authentication.

The observed asymmetry in the tolerance window, as depicted in Figure 6.9 b), can be primarily attributed to the specific geometric characteristics inherent in the experimental setup. Specifically, the AOI on the ML arrays exhibits a more pronounced change in response to the smartphone's movement when it deviates from its central or 'home' position atop the ML arrays. This phenomenon can be understood in terms of the relative sensitivity of the focal point positions to the smartphone's displacement: a mere 1mm shift from the home position induces a significantly more noticeable alteration in focal points compared to the same 1mm movement when the smartphone is already situated 1.5cm away from the home position. When the smartphone subsequently moves back towards the home position, it traverses through a region where the shift in the focal volume is most pronounced. This dynamic explains why the smallest tolerance margins are observed for reference images corresponding to minimal initial movements away from the home position.

To sum up, the findings presented in Figure 6.9 confirms that the current label design successfully achieves a tolerance margin of 1cm with respect to the smartphone's movement between the validation of reference and test images. This is a significant outcome, affirming that the manual positioning of the smartphone and label, aided by basic markers, is sufficiently accurate to replicate the original geometrical setup within the established tolerance threshold. The asymmetry noted in Figure 6.9 a) and b) further emphasizes that the shift in the focal volume is more abrupt and pronounced when the smartphone is in proximity to its home position. From a practical standpoint, this insight implies that for real-world applications, it might be advantageous to intentionally capture test images with a greater offset from the home position. Such a strategy would potentially offer a slightly larger margin for error in the positioning of the

smartphone relative to its reference position, thus enhancing the practicality and robustness of the authentication process under varying real-life conditions.

6.8 Classifying the tolerance behavior of pattern robustness under variable LED – camera distance

In research presented so far, all experimental results have been derived using a particular smartphone model, Samsung Galaxy S20. However, a critical factor in broadening the applicability of the findings is the variability in the spatial arrangement of the camera and LED flashlight across different smartphone models. It is essential to investigate how variations in the distance between the LED and the camera affect the accuracy of classifying test images, particularly in the context of frontside detection. Previous studies of the PULs presented in chapter 4 and chapter 5 have established that for backside detection, the precise positioning of the camera is generally not a significant factor in influencing detection outcomes.^{2,3} However, this assumption does not necessarily hold true for frontside detection scenarios. Theoretical models, as illustrated in Figure 6.1 c), indicate that when employing a perfect lens system without any scattering structures, only a subset of the LED – camera distance configurations permit the successful observation of a bright point's emission.

The underlying principle here is related to the phenomenon of partial collimation of light emitted from the bright points. This collimation effect implies that the emitted light from a bright point is only observable within certain angles relative to the lens, thus making its detection conditional on the LED – camera distance. As this distance increases, the probability that the camera will capture the emission from a bright point correspondingly decreases. Therefore, it becomes imperative to systematically assess the influence of varying LED – camera distances across different smartphone models on the fidelity of frontside detection. This assessment is crucial for ensuring the robustness and generalizability of pattern detection methodology, especially considering the wide range of smartphone configurations in use. Understanding and quantifying this aspect will not only enhance the accuracy of the detection system but also provide valuable insights into the optimal configurations necessary for effective frontside detection across diverse smartphone models.

In the experimental design, illustrated in Figure 6.10 a), a controlled illumination and detection set up is employed using an external LED and smartphone camera. The illumination source utilizes the white LED positioned at a fixed distance of 1cm laterally

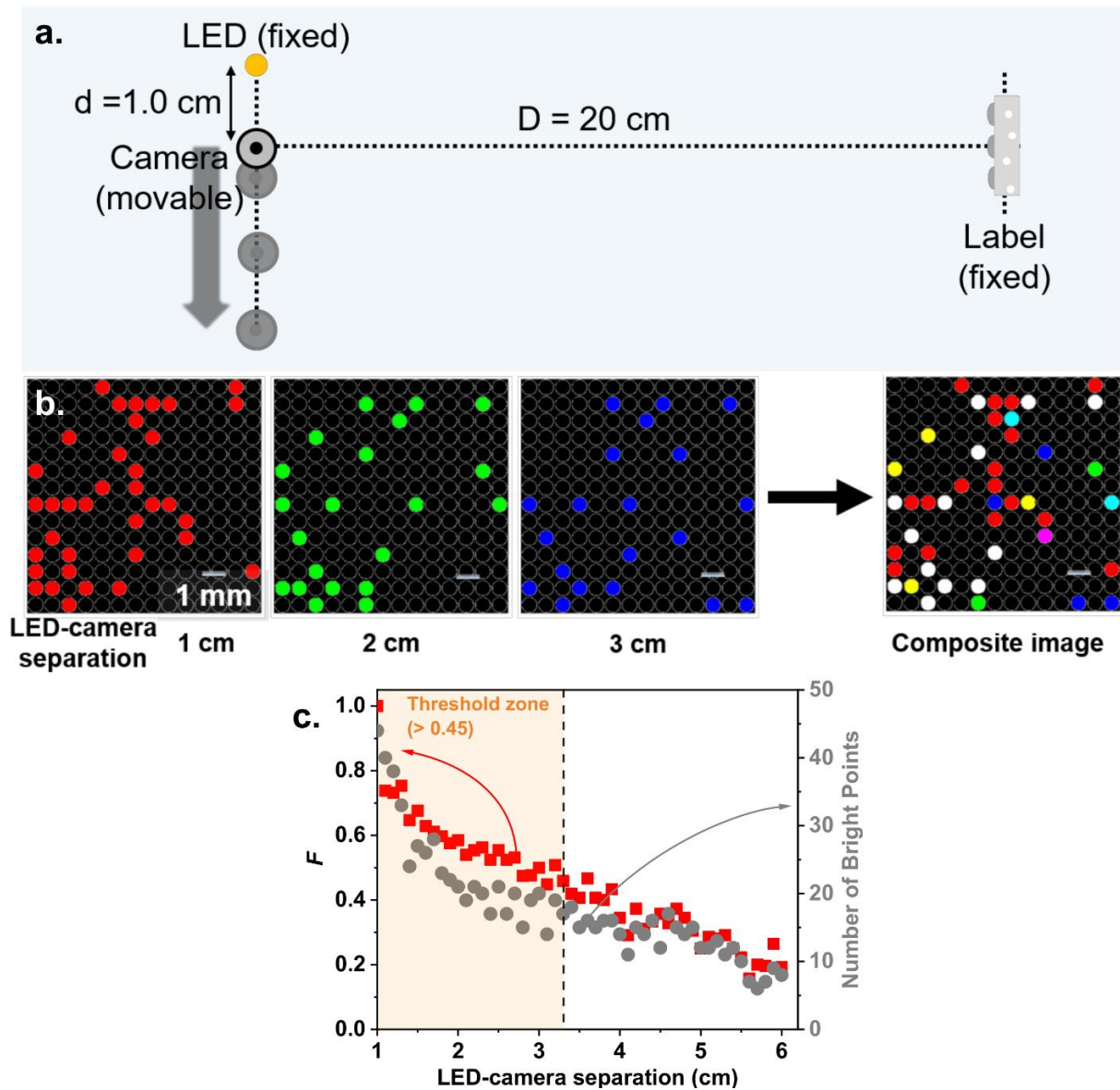


Figure 6.10 a) A schematic illustrating the setup for varying the LED-camera distances to record different patterns from a given label. b) Qualitative comparison of bright point patterns at LED-camera separations of 1, 2, and 3 cm. Comparison is shown in false-colour notation in R, G and B for the three positions respectively c) Graph showing the fraction of consistent bright points (F) when comparing test images at different LED-camera distances with a reference image at a 1.0 cm separation, along with the count of bright points in each test image. Reproduced with permission from Kumar *et al.*⁸

from the pre-defined 'home' position. This arrangement ensures consistent and directed illumination to the label for capturing different experimental trials. A crucial component of the experimental apparatus is a smartphone, selected for its ubiquity and advanced camera capabilities.^{86,199} The smartphone is mounted on a precision-scale linear translation stage, enabling controlled and measurable variation in the distance between smartphone's camera and the external LED. The lateral distance (denoted as 'd') between the smartphone camera and the LED is systematically varied,

starting from a minimum offset of 1cm and increasing incrementally up to a maximum offset of 6cm. The translational stage allows fine adjustment with a precision of 1mm increments. At each incremental position, point pattern images of the label are captured using the smartphone camera. In this way, the experiment results in capturing 50 different patterns while moving the smartphone position from start position (from offset 1cm) to end position (offset 6cm).

In the experimental observations presented in Figure 6.10 b), the spatial distribution of bright points is analysed under different LED – camera offsets, specifically at 1cm, 2cm, and 3cm separations. These distributions are represented through different colour-coded strings: R for 1cm, G for 2cm, and B for 3cm offsets. Visually, it is evident that the density of bright points diminishes as the distance between the LED and the camera increases. Quantitative analysis, as depicted in Figure 6.10 c), reinforces this observation. Figure 6.10 c) illustrates a clear inverse relationship between the LED – camera separation and the number of detectable bright points. Specifically, the number of bright points decreases from approximately 40 at a 1cm separation to a mere 10 points at a 6cm separation. Interestingly, despite the reduction in the number of bright points with increasing LED – camera distance, the spatial integrity of the remaining points is maintained. This is evident in the composite image in Figure 6.10 b). Out of the bright points, 13 white points consistently appear across all images, indicating their robust visibility. In contrast, 4 additional yellow points, which are visible at a 2cm offset, become undetectable at a 3cm offset. To conduct a more rigorous analysis, the bright point patterns at 2cm and 3cm offsets are considered as test strings, with the 1cm pattern serving as a reference. This approach allows for the calculation of the fraction of total bright point positions that match across these patterns, denoted as F . The matching fractions are 0.6 and 0.5 for the 2cm and 3cm offsets, respectively. These values are notably above the threshold value of 0.45, which has been established for determining the adequacy of pattern matching. Consequently, this implies that even with increasing LED – camera distances, accurate classification is feasible when using reference images captured at a closer LED – camera distance of 1cm. This finding is significant as it demonstrates the robustness of the system in maintaining pattern recognition accuracy despite variations in the LED – camera spatial configuration.

In a more detailed quantitative analysis, the fraction of matching bright point positions, F is evaluated as a function of increasing LED – camera separation. This is achieved

by comparing test images, captured at each 1mm increment, with a reference image taken at a 1.0cm separation, as shown in Figure 6.10 c). Notably, F demonstrates a gradual decline as the LED – camera distance increases. However, it remains above the critical threshold of 0.45 for separations up to 3.3cm. These findings suggest that a single reference image, captured at a 1cm LED – camera distance, is sufficient for accurate authentication across various smartphone models, as long as the LED – camera distance does not exceed 3cm. Given that the LED – camera distances in contemporary smartphones do not typically surpass 3cm, this method appears universally applicable for authentication purposes with current smartphone technology.

6.9 Analyzing the vertical placement tolerance of a single smartphone for authentication of a given label

This section examines the impact of varying distances between the smartphone and the label (denoted as D) on the probability of classifying test and reference images as matching. Figure 6.11 a) presents a schematic of the label-smartphone arrangement used to record bright point-patterns, with the smartphone's distance shifting from the label from 15cm to 25cm, in 1cm increments. The analysis indicates a high tolerance for deviations in the smartphone's position, particularly in height, with discrepancies up to 3cm resulting in only minor effects on the fraction of consistent bright points (F).

A qualitative analysis of point-patterns from the label at varying distances (D) of 20cm, 18cm and 22cm is shown in Figure 6.11 b). It includes a composite image where non-overlapping bright points at different D positions are shown in distinct colours, while overlapping bright points, resulting from the combination of R, G, and B appear white ($R+G+B \rightarrow W$). The predominance of white points over coloured points in this composite image suggests that the fraction of matching bright points (F) is likely to exceed 0.45, indicating that these images would be classified as matching under the image validation criteria.

In a quantitative analysis, the label's bright point-pattern is evaluated at distances (D) ranging from 15cm to 25cm, in 1cm increments, resulting in a total of 11 different distances. The label's pattern image obtained at $D = 20$ cm is designated as a reference image. Subsequently, this reference image is used for comparison with all 11 test images, each corresponding to a different smartphone-label distance within the 15cm to 25cm range. The results of this comparative analysis are shown in Figure 6.11 c), where the fraction of bright points remaining in consistent locations across the test and

reference images, (denoted as F), is plotted against the varying smartphone-label distances. The findings reveal that for the range of $D = 15\text{cm}$ to $D = 23\text{cm}$, the F -value remains > 0.45 , above the established threshold for matching. This indicates that the test images captured within this distance range are successfully classified as matching when compared to the reference image at 20cm . The only exception is the image at

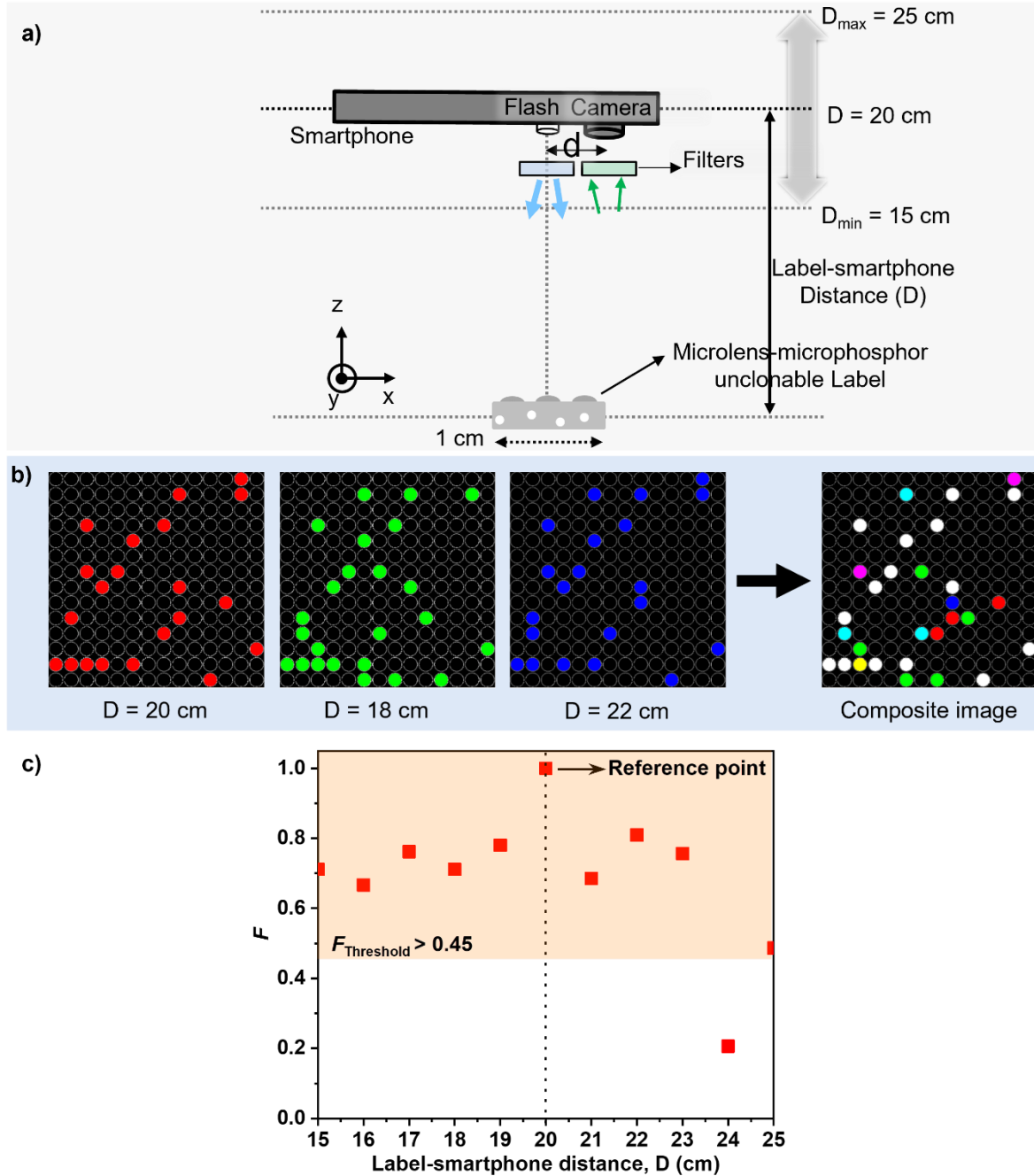


Figure 6.11 a) Schematic representation of the experimental setup with the smartphone fixed in position and the label on a translational stage to vary label-smartphone distance (D). b) Qualitative comparison of label patterns at $D = 20\text{cm}$, 18cm , and 22cm , depicted in R, G, and B, respectively, with a composite RGB image illustrating the overlap of identical bright points. c) Quantitative analysis of 11 test images, captured at D distances ranging from 15 cm to 25 cm in 1cm increments, compared to a reference image at $D = 20\text{cm}$. Reproduced with permission from Kumar *et al.*⁸

24cm, potentially an outlier. This analysis provides a critical insight into the system's tolerance for movements of the smartphone in the direction perpendicular to the plane of the label. It is observed that even with a deviation of up to 3cm from the optimal distance, the system retains its accuracy in pattern recognition. This level of tolerance to positional variance is particularly significant as it suggests that the system can function effectively even without the need for highly sophisticated or precise hardware setups. This finding underscores the practical viability of the authentication system in real-world applications, where maintaining exact distances may not always be feasible or convenient.

The variation in the count of bright points across different patterns, resulting from changes in the label – smartphone distance, remains relatively insignificant. This consistency can be attributed to the ML consistently scanning the same bright points during the smartphone translation process. Consequently, such uniformity in the bright point count ensures that the fraction of bright points in the same locations (*F*-value) does not undergo drastic changes within the permissible range of distance offset for pattern authentication.

6.10 Label's optical performance analysis under constant solar illumination at elevated temperature

In the investigation of label stability against aging, label L1 underwent an extended exposure within an environmental test chamber (Angelantoni test technologies, ATT) designed for solar cell testing. This controlled environment simulated one sun illumination under standard conditions, with a light intensity of 1000Wcm^{-2} , coupled with an elevated temperature maintained at 80°C inside the chamber. The point-patterns recorded by label L1 are consistently recorded using the same smartphone-based setup for illumination and detection at intervals of 0, 12, 24, 36, 100, and 124 hours.

Qualitative analysis, depicted in Figure 6.12 a) and b), reveals composite white image from R, G and B images, that are recorded over different time of exposure. The analysis confirms that there is no discernible alteration in the observed pattern over the specified time intervals. Despite the prolonged exposure to heightened light intensity and elevated temperature, the visual examination suggests remarkable stability in the label's luminescent pattern.

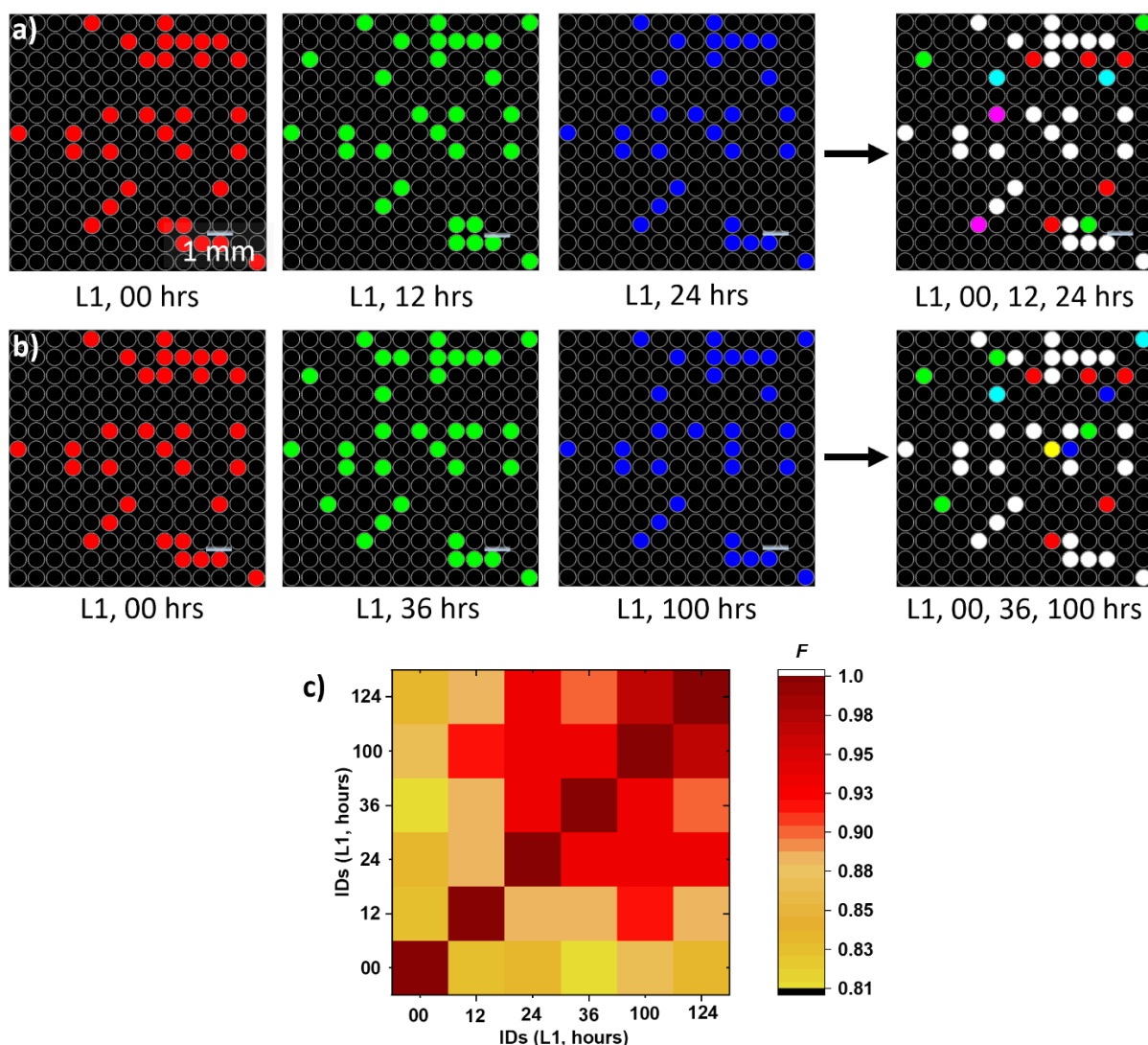


Figure 6.12 Assessment of PDMS label stability under accelerated aging. Labels are subjected to a constant 80° C temperature and 1 standardized sun (1000W/m²) illumination. a) Visual comparison of patterns at initial, 12, and 24-hour intervals. b) Qualitative comparison of binary strings derived from images at 36 and 100 hours against the initial string. c) Calculation of F for 6 different time points, showing values consistently >0.8, indicative of stable authentication performance similar to unaged labels. No significant impact from accelerated heat and light exposure observed. Reproduced with permission from Kumar *et al.*⁸

In Figure 6.12 c), a quantitative analysis is conducted using a binary string-based authentication algorithm to compare patterns associated with the same labels across different exposure of time intervals. This method involves generating binary strings from the images captured at different times and then conducting pairwise comparisons between these strings. A key observation from this analysis is that when a reference image is compared with itself, the fraction of matching bright point positions (F) naturally reaches the maximum value of 1.0, indicating a perfect match. When comparing different pairs of images from the same label under identical illumination and detection condition, it is observed that the F -value fluctuates within a range of 0.8

to 1.0. This variability in F suggests a high degree of consistency, albeit with minor variations, in the pattern recognition over time. The similarity in outcomes between aged labels (subjected to prolonged light exposure and heat) and non-aged labels is particularly noteworthy. It underscores that the aging process, under the specified conditions of extended light and heat exposure, does not adversely impact the efficacy of the label authentication system. This resilience of the label patterns to aging factors enhances the reliability of authentication approach, ensuring that even under varying environmental conditions, the labels retain their unique identifying characteristics necessary for accurate authentication.

6.11 Conformal application of flexible label to curved surface

Figure 6.13 showcases the versatility of label application on a curved surface, specifically a bottle, placed on a rotating stage. The experimental setup involves fixing the smartphone in place while the bottle undergoes various rotations on the stage. To ensure consistent positioning and rotation across different trials, a mark is made as a reference point on both the bottle and the stage. This method facilitates the capture of the luminescent bright point pattern under different rotational orientations of the bottle. By maintaining precise alignment through the marked reference points, the trials enable a comprehensive examination of how the point-pattern varies with the rotation

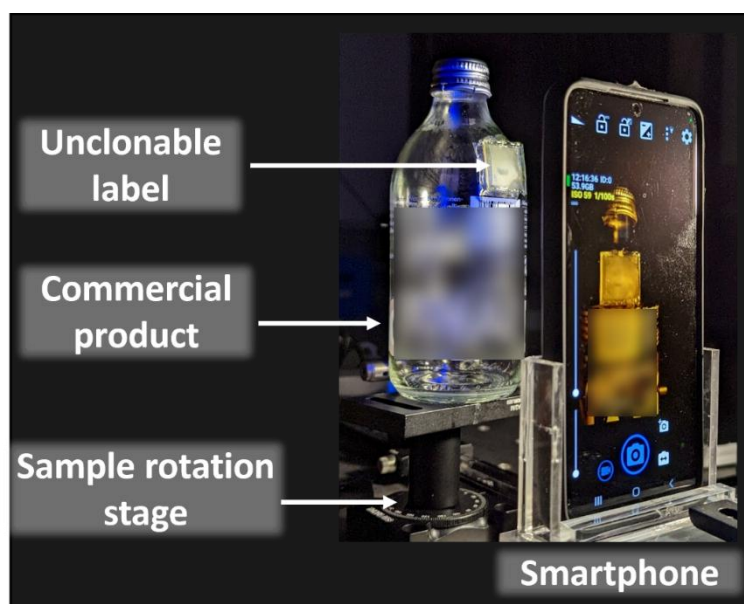


Figure 6.13 Demonstration of Authenticating a PDMS-based PUL on a Commercial Product. The Figure shows a smartphone with excitation rejection filters (not visible) used for authentication. Labelled commercial product is placed on a rotating platform. This arrangement allows systematic variation in the label's orientation relative to the smartphone's camera, making it easier to study how label positioning affects authentication accuracy. Adapted with permission from Kumar *et al.*⁸

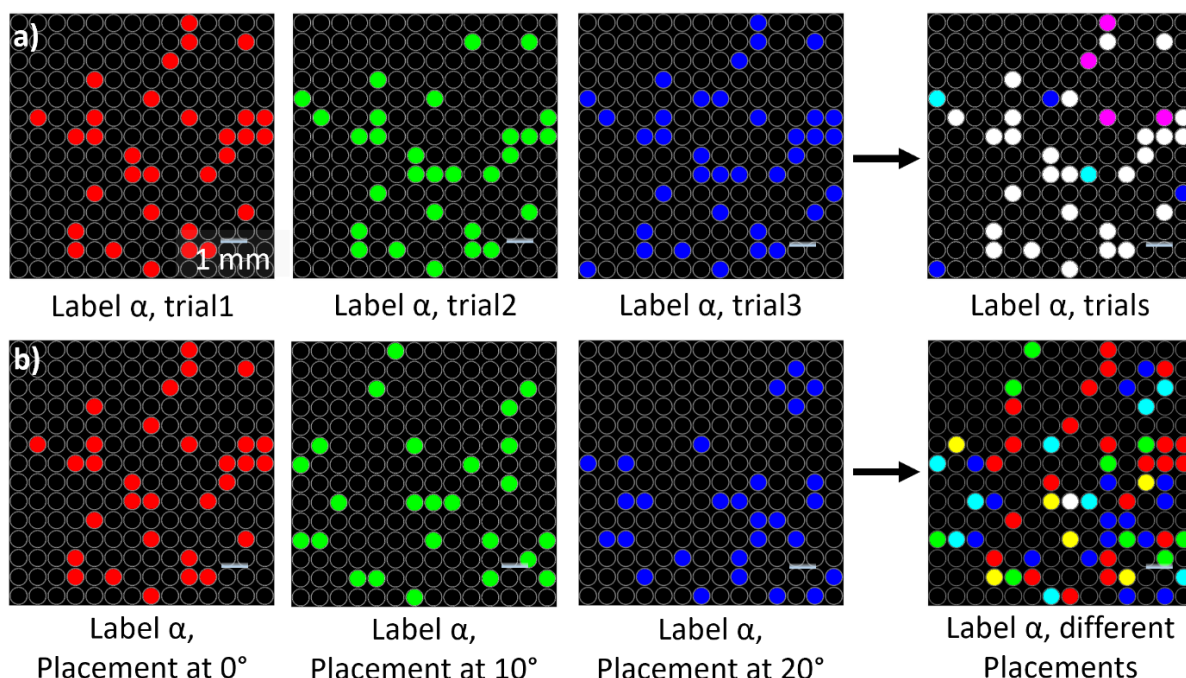


Figure 6.14 Authentication Analysis of a Conformal Label on a Bottle (as depicted in Figure S5). a) Repeatedly positioning the bottle manually at a fixed location and angle, showcasing consistent pattern generation. b) Demonstrating pattern changes with the bottle rotated to specified degrees, highlighting the sensitivity of the label to orientation changes. Reproduced with permission from Kumar *et al.*⁸

of the curved surface. This experimental design not only highlights the label's adaptability to non-planar surfaces but also allows for a systematic analysis of the luminescent patterns under dynamic conditions, reinforcing the label's potential for authentication applications on objects with curved or irregular geometries.

Figure 6.14 demonstrates a qualitative evaluation of the authentication process for a setup outlined in Figure 6.13. In Figure 6.14 a), it is demonstrated that identical luminescent patterns are consistently obtained when a bottle, bearing the label, is manually removed, and then repositioned at the same location and orientation. Contrastingly, Figure 6.14 b) illustrates the effect of bottle rotation by 10° and 20°, leading to significant changes in the incidence angles on the label and, consequently, the generation of completely distinct patterns. This highlights the capability of the label to function effectively on curved surfaces, albeit with the caution that the surface curvature must be consistent between the acquisition of the reference image and the subsequent test images in practical applications.

6.12 Summary

This chapter introduces a novel label design and authentication algorithm based on labels, incorporating a ML arrays, scattering surface and smartphone excitable DS

phosphor particles. The label is developed as an anti-counterfeiting tag for enhanced security that can be authenticated simply using a smartphone. The label's unique optical response under controlled smartphone-based illumination allows for reliable authentication even under varying angles of incidence, smartphone positions, and LED-camera distances. A qualitative and quantitative assessment of the label's pattern are conducted using a binary-ID string algorithm, establishing the robustness, uniqueness and unclonable features of patterns. The chapter also presents experimental results demonstrating the label's robustness against environmental conditions such as elevated temperature and constant solar illumination. Finally, the conformal application of the flexible label to curved surfaces is discussed.

7 Conclusion

The research presented in my thesis introduced a novel approach to anti-counterfeiting PULs by integrating ML arrays with UC and DS phosphor particles. These labels exploited the interplay between ML optics and luminescence to generate visually intricate and inherently unique patterns that also change with excitation and observation geometry, enhancing robustness in verification. This section summarizes the key findings derived from the progression of the prototype PUL design to the advanced PUL configuration, highlighting the significant results and offering insights into potential future developments in anti-counterfeiting technology.

7.1 Prototype design of PULs using ML arrays and a UC phosphor doped PDMS layer

The prototype design of PULs introduced a novel approach to anti-counterfeiting by combining a ML array with a PDMS layer embedded with GOSYE UC phosphor particles. This design leveraged micron-scale randomness inherent in the particle distribution to create unique PL patterns that varied with AOI. By selectively focusing incoming light onto the randomly dispersed phosphor particles, the PUL generated constellation of bright emission points, captured using a standard digital camera that are equipped with excitation rejection filter.

The robustness of the label's point patterns was thoroughly evaluated through both qualitative and quantitative analyses, demonstrating their consistency across different camera placements. Additionally, an image processing algorithm was developed to authenticate the labels by validating point patterns using a threshold voting mechanism. The study further explored how the AOI influences the creation of multiple secure patterns from a single label, adding an extra layer of security for authentication and enhancing the label's resistance to counterfeiting. A rigorous evaluation of 100 test images compared against 100 different reference images (10^3 comparisons) yielded a false positive probability as low as 10^{-15} , highlighting the reliability and robustness of this proof-of-concept system.

While the two-layer prototype labels demonstrated exceptional reliability, it also faced challenges, particularly a narrow angular tolerance ($\text{AOI} \leq 0.2^\circ$) and the requirement for precise alignment of the excitation source with the ML arrays. These limitations

presented barriers to practical, large-scale implementation. Nonetheless, the concept successfully demonstrated that micron-scale randomness could be harnessed to create unclonable labels visible on the macroscale, offering a significant advantage over designs reliant on magnification in authentication hardware. This innovative approach paves the way for further development to meet the increasing demand for secure and unique product identification.

7.2 Optimizing the PUL design for enhanced AOI tolerance

To address the limitations of the prototype PUL design, my successive research advanced the PUL concept by incorporating ML arrays with a shorter focal length ($f \approx 500 \mu\text{m}$) and larger DS phosphor particles with varying D50 diameters on the micron scale. These refinements addressed critical challenges associated with practical implementation, particularly the strict alignment requirements of the excitation source, by significantly enhancing the AOI tolerance of the labels.

The AOI tolerance between the reference and test images for successful authentication, was systematically improved by varying the D50 particle diameters. For particle sizes of $9.0 \pm 1 \mu\text{m}$, $20.5 \pm 1 \mu\text{m}$, and $32.5 \pm 2 \mu\text{m}$, the AOI tolerances achieved were 0.8° , 2.0° , and 3.6° , respectively. This increase in the acceptable AOI range to 3.6° represents an 18 \times enhancement over the prototype PUL design. This broaden tolerance marked a critical step towards making the labels viable for practical applications, where precise AOI control is often impractical. The integration of larger DS phosphor particles also contributed to brighter and more distinguishable PL patterns, enhancing the robustness of the PULs and enabling their use with an LED excitation (e.g. a 450 nm LED or smartphone flash) and standard digital camera (e.g. a smartphone camera). This innovation reduced reliance on specialized laboratory equipment and broadened the potential applications of the labels.

The enhanced understanding of AOI tolerance gained from this study provided a solid foundation for developing robust PUL design for smartphone-based authentication. However, the two-layered PUL design revealed a significant challenge related to mechanical stability over time. Aging or exposure to mechanical stress, such as transportation or physical agitation, caused the two layers to slip relative to one another. This misalignment between the ML arrays and the phosphor layer adversely affected the authentication process, undermining the reliability of the label.

Consequently, addressing the mechanical stability of the two-layer structure is essential to ensure consistent authentication performance over time, particularly under demanding handling or environmental conditions. Furthermore, achieving a PUL design where a single smartphone serves as both the excitation source (via its flashlight) and the detection system (via its camera) would render these labels highly accessible and practical for widespread anti-counterfeiting applications.

7.3 Advanced PUL design for smartphone-compatible authentication

Building on the advanced PUL designs developed in this research, the feasibility of authenticating PULs using a smartphone was successfully demonstrated. For this implementation, PULs were developed by integrating larger DS particles and optimized focal length ML arrays into both a two-layer structure and an all-PDMS single-layer design. The single-layer architecture was specifically engineered to enhance robustness and practicality, offering greater compatibility for anti-counterfeiting applications. This design integrated a ML array and scattering micro-textures directly into a phosphor doped PDMS layer. This streamlined structure demonstrated seamless compatibility with smartphones as authentication devices, paving the way for practical and cost-effective authentication solutions.

The smartphone-based authentication system utilized the smartphone flashlight as the excitation source and the camera for detection, with optical filters applied to block scattered light. Captured luminescence-based point patterns were translated into a 196-bit binary string, where each bit corresponded to whether a given microlens created a bright emission point. The authentication process matched the binary strings of reference and test images, achieving a classification confidence exceeding 99%. This approach enabled rapid and computationally efficient determination of authenticity. Moreover, these labels demonstrated high resilience under environmental stressors, such as temperature variations and extended storage, ensuring their long-term usability. Their conformal application to curved surfaces, such as blister packs, demonstrated the versatility of the technology for diverse anti-counterfeiting applications. The key findings demonstrated a smartphone position tolerance of up to 1 cm when capturing test images, consistent with simple hardware setups that ensured relative alignment between the smartphone and the label. Furthermore, the labels maintained their authentication reliability across varying LED-camera separations,

provided the distance remained within 3 cm – a requirement fulfilled by all known smartphone models. These attributes underscored the practicality of the label design, offering robust and cost-effective authentication using readily available consumer devices.

7.4 Outlook

Although the design concept of the label technology is unique and unclonable, there remains considerable scope for further improvements to enhance the efficiency and practicality of anti-counterfeiting labels. Future advancements in the PUL technology could include the incorporation of two or more distinct types of phosphor particles, along with scattering particles, to generate different point patterns under varied excitation sources. The inclusion of scattering particles would eliminate the need for wavelength-selective filters, as it would enable detection of scattering-based patterns instead of relying solely on luminescence from the label. This approach would enhance security by offering multiple authentication signatures based on different excitation conditions, while also simplifying the detection process.

Moreover, implementing on-the-fly algorithms for smartphone positioning and pattern classification could further enhance the user experience and operational efficiency. Such innovations would facilitate seamless, real-time authentication using handheld smartphones, enabling users to perform quick and reliable verifications on-the-spot. This would not only improve accessibility but also preserve the security advantages of the labels, which are derived from the inherent randomness of the luminescent point patterns. By continuing to refine these technologies, we bring the vision of practical, smartphone-based anti-counterfeiting solutions closer to reality, combining both high security and ease of use for everyday consumers.

The application of fiducial markers to the label geometry can enable quick and robust authentication of the patterns from the label.^{215,218} In this approach, uniquely designed markers (which are non-symmetric under image rotation or flip cases) would be printed on the label. The relative position of the fiducial markers should be fixed in relation to the ML arrays for each label designed. By doing so, the fiducial markers can serve as a reference point to validate patterns using a simple algorithm. Moreover, This approach would allow the comparison of a single test image with multiple reference images concerning the fiducial markers; resulting in low computational cost, ease of

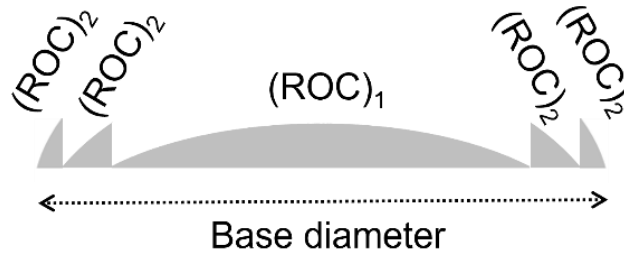


Figure 7.1 Schematic of a Fresnel alike ML geometry, incorporating a centre lens of focal length f_1 (from ROC_1) and two ring lens of focal length f_2 (from ROC_2). The proposal design has $f_1 < f_2$ (i.e. $ROC_1 < ROC_2$).

use in authentication devices and high-speed results without compromising the label's unclonable security. One must give a careful consideration to the ML array's resistance to scratches and dirt to ensure their endurance. On the contrary, existing practical deployments of ML arrays on currencies for the purpose of including security measures demonstrate that this design can achieve an overall longevity of several years.^{143,241}

Designing the ML arrays in a manner similar to a Fresnel ring lens architecture is one potential approach to enhance the performance of the unclonable label. In the case of a single-layered all PDMS label, validating the pattern under off-axis illumination can be challenging. This is because the emission light guided out from a bright particle underneath the ML surface is not intense enough to be detected by the same smartphone camera. Figure 7.1 shows a design proposal for a Fresnel- ring lens like microlens, which includes a central lens with focal length f_1 (originated from ROC_1), and two ring lenses of focal length f_2 (originated from ROC_2), positioned around the central lens. It is recommended that the focal length of the ring lenses be greater than

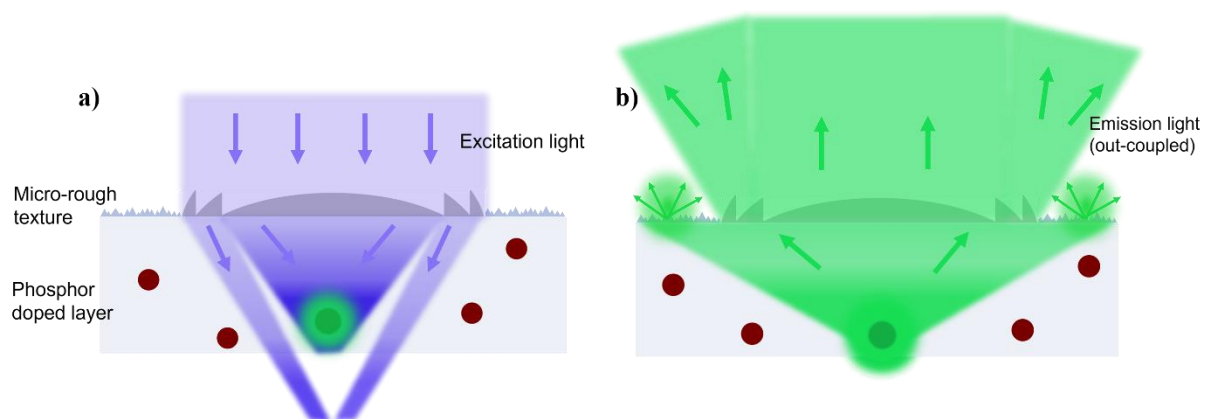


Figure 7.2. Schematic illustration of illumination and out-coupling response from a Fresnel-like ML. a) A bright particle results only from the focal volume generated by the central lens, whereas focal volume generated by ring lens exceeded the phosphor layer thickness. b) The central lens outcouples the emission light from a bright particle in a collimation form, whereas the ring lens guides the out-coupled emission light in a diverging manner as the emission light towards the detector.

that of the central lens, i.e. $f_1 < f_2$ (or $ROC_1 < ROC_2$). The concept behind this design is to exclude the focal volume generated by the ring lenses from the particles doped layer, Figure 7.2 a). In this way, only the focal volume from the central lens will interact with the particles doped layer. A bright particle positioned underneath the central lens will outcouple the emission light in a collimation manner from the overhead central lens. Whereas the ring lenses will outcouple the emission from the bright particle in a non-collimated diverging fashion (Figure 7.2 b). This design allows the emission response from a bright particle to be detected even at non-normal positions of the authentication device, such as a smartphone that simultaneously illuminate and records the pattern through its camera. In this scenario, the emission response from the ring lens will appear as a bright circular ring in the smartphone camera's view.

This research has established a strong foundation for developing and implementing PULs based on ML arrays and PL particles as anti-counterfeiting labels. The demonstrated security, practicality, label stability and scalability of this technology offer significant potential for safeguarding consumer interests, maintaining product integrity, and combating counterfeiting across a wide range of applications.

8 References

- 1 Gu, Y. *et al.* Gap-enhanced Raman tags for physically unclonable anticounterfeiting labels. *Nature communications* **11**, 516 (2020).
- 2 Kumar, V. *et al.* Unclonable Anti-Counterfeiting Labels Based on Microlens Arrays and Luminescent Microparticles. *Advanced Optical Materials* **10**, 2102402 (2022).
- 3 Kumar, V., Dottermusch, S., Chauhan, A., Richards, B. S. & Howard, I. A. Expanding the angle of incidence tolerance of unclonable anticounterfeiting labels based on microlens arrays and luminescent microparticles. *Advanced Photonics Research* **3**, 2100202 (2022).
- 4 Katumo, N. *Persistent Phosphors for Smartphone-Based Luminescence Thermometry and Anti-Counterfeiting Applications*, Karlsruher Institut für Technologie (KIT), (2022).
- 5 Fischer, J. & Wegener, M. Three-dimensional optical laser lithography beyond the diffraction limit. *Laser & Photonics Reviews* **7**, 22-44 (2013).
- 6 Kirm, M., Lushchik, A., Lushchik, C. & Zimmerer, G. in *ECS Proc.* 113-122.
- 7 Dong, H., Sun, L.-D. & Yan, C.-H. Energy transfer in lanthanide upconversion studies for extended optical applications. *Chemical Society Reviews* **44**, 1608-1634 (2015).
- 8 Kumar, V. *et al.* Smartphone Authentication of Unclonable Anticounterfeiting Labels based on a Microlens Array atop a Microphosphor-Doped Layer. *Advanced Materials Technologies* **8**, 2201311 (2023).
- 9 Zhang, M. & Bermak, A. CMOS image sensor with on-chip image compression: A review and performance analysis. *Journal of Sensors* **2010** (2010).
- 10 Fink, C., Maskus, K. E. & Qian, Y. The Economic Effects of Counterfeiting and Piracy: A Review and Implications for Developing Countries. *The World Bank Research Observer* **31**, 1-28 (2015). <https://doi.org/10.1093/wbro/lkv010>
- 11 OECD & Office, E. U. I. P. *Dangerous Fakes*. (2022).
- 12 Chen, C.-L. *et al.* An anti-counterfeit and traceable management system for brand clothing with hyperledger fabric framework. *Symmetry* **13**, 2048 (2021).
- 13 Meng, X. *et al.* in *2023 IEEE 10th International Conference on Cyber Security and Cloud Computing (CSCloud)/2023 IEEE 9th International Conference on Edge Computing and Scalable Cloud (EdgeCom)*. 120-125 (IEEE).
- 14 Blakeney, M. *Counterfeit Goods and Organised Crime*. (Edward Elgar Publishing, 2023).
- 15 Amaral, N. B. What can be done to address luxury counterfeiting? An integrative review of tactics and strategies. *Journal of Brand Management* **27**, 691-709 (2020).
- 16 Wu, T., Wang, C., Kao, H., Su, P. & Ma, J. in *Optics Frontier Online 2020: Optics Imaging and Display*. 136-142 (SPIE).
- 17 Xun, Y. *et al.* in *Advances in Graphic Communication, Printing and Packaging: Proceedings of 2018 9th China Academic Conference on Printing and Packaging*. 187-196 (Springer).
- 18 Khalil, G., Doss, R. & Chowdhury, M. A comparison survey study on RFID based anti-counterfeiting systems. *Journal of Sensor and Actuator Networks* **8**, 37 (2019).
- 19 Ambadiyil, S., Sreelekshmi, R., Pillai, V. M. & Prabhu, R. in *Optics and Photonics for Counterterrorism, Crime Fighting, and Defence XII*. 13-19 (SPIE).
- 20 Kumar, P., Dwivedi, J. & Gupta, B. K. Highly luminescent dual mode rare-earth nanorod assisted multi-stage excitable security ink for anti-counterfeiting applications. *Journal of Materials Chemistry C* **2**, 10468-10475 (2014).

- 21 Yoon, B. *et al.* Recent functional material based approaches to prevent and detect counterfeiting. *Journal of Materials Chemistry C* **1**, 2388-2403 (2013).
- 22 Queiroz, M. M., Telles, R. & Bonilla, S. H. Blockchain and supply chain management integration: a systematic review of the literature. *Supply chain management: An international journal* **25**, 241-254 (2020).
- 23 Ibrahim, A. A. A., Nisar, K., Hzhou, Y. K. & Welch, I. in *2019 IEEE 13th international conference on application of information and communication technologies (AICT)*. 1-4 (IEEE).
- 24 Coskun, V., Ozdenizci, B. & Ok, K. The survey on near field communication. *Sensors* **15**, 13348-13405 (2015).
- 25 Mohanta, B. K., Jena, D., Satapathy, U. & Patnaik, S. Survey on IoT security: Challenges and solution using machine learning, artificial intelligence and blockchain technology. *Internet of Things* **11**, 100227 (2020).
- 26 Wu, J. *et al.* A High-Security mutual authentication system based on structural color-based physical unclonable functions labels. *Chemical Engineering Journal* **439**, 135601 (2022).
- 27 Maes, R. & Verbauwhede, I. Physically unclonable functions: A study on the state of the art and future research directions. *Towards Hardware-Intrinsic Security: Foundations and Practice*, 3-37 (2010).
- 28 Li, Q. *et al.* Intrinsic random optical features of the electronic packages as physical unclonable functions for internet of things security. *Advanced Photonics Research* **3**, 2100207 (2022).
- 29 Dias, L. M. *et al.* Smart optical sensors for Internet of things: Integration of temperature monitoring and customized security physical unclonable functions. *IEEE Access* **10**, 24433-24443 (2022).
- 30 Leem, J. W. *et al.* Edible unclonable functions. *Nature Communications* **11**, 328 (2020).
- 31 Bolotnyy, L. & Robins, G. in *Fifth Annual IEEE International Conference on Pervasive Computing and Communications (PerCom'07)*. 211-220 (IEEE).
- 32 Wang, Y.-M., Tian, X.-T., Zhang, H., Yang, Z.-R. & Yin, X.-B. Anticounterfeiting quick response code with emission color of invisible metal–organic frameworks as encoding information. *ACS applied materials & interfaces* **10**, 22445-22452 (2018).
- 33 Kalytchuk, S., Wang, Y., Poláková, K. i. & Zboril, R. Carbon dot fluorescence-lifetime-encoded anti-counterfeiting. *ACS applied materials & interfaces* **10**, 29902-29908 (2018).
- 34 Ren, W., Lin, G., Clarke, C., Zhou, J. & Jin, D. Optical nanomaterials and enabling technologies for high-security-level anticounterfeiting. *Advanced Materials* **32**, 1901430 (2020).
- 35 Liu, Y. *et al.* Unclonable Perovskite Fluorescent Dots with Fingerprint Pattern for Multilevel Anticounterfeiting. *ACS Applied Materials & Interfaces* **12**, 39649-39656 (2020). <https://doi.org:10.1021/acsami.0c11103>
- 36 Li, Q. *et al.* Physical Unclonable Anticounterfeiting Electrodes Enabled by Spontaneously Formed Plasmonic Core–Shell Nanoparticles for Traceable Electronics. *Advanced Functional Materials* **31**, 2010537 (2021). <https://doi.org:https://doi.org/10.1002/adfm.202010537>
- 37 Ru, Y. *et al.* Recent advances in chiral carbonized polymer dots: from synthesis and properties to applications. *Nano Today* **34**, 100953 (2020).
- 38 Lin, Y. *et al.* Unclonable Micro-Texture with Clonable Micro-Shape towards Rapid, Convenient, and Low-Cost Fluorescent Anti-Counterfeiting Labels. *Small* **17**, 2100244 (2021). <https://doi.org:https://doi.org/10.1002/sml.202100244>
- 39 Khalid, M. & Rahman, S. U. Word ofmouth, perceived risk and emotions, explaining consumer's counterfeit products purchase intention in a developing country:

- Implications for local and international original brands. *Advances in business-related scientific research journal* **6**, 145-160 (2015).
- 40 Ziavrou, K. S., Noguera, S. & Boumba, V. A. Trends in counterfeit drugs and pharmaceuticals before and during COVID-19 pandemic. *Forensic Science International* **338**, 111382 (2022).
- 41 Hashemi, L. M., Meo, S. & Shelley, L. Transnational crime during a pandemic: how criminals are capitalizing on the chaos caused by COVID-19. *A World Emerging from Pandemic: implications for intelligence and National Security*. National Intelligence University, Washington, DC, 161-188 (2022).
- 42 Staake, T., Thiesse, F. & Fleisch, E. The emergence of counterfeit trade: a literature review. *European Journal of Marketing* **43**, 320-349 (2009).
- 43 Sharypov, A., Brusnikin, V., Koval, S., Glukhov, G. & Gubanov, O. Aircraft components life cycle monitoring as a tool for identifying inauthentic aviation equipment items. *International Journal of Mechanical Engineering and Technology (IJMET)* **9**, 612-620 (2018).
- 44 Kim, M. S. *et al.* Revisiting silk: a lens-free optical physical unclonable function. *Nature Communications* **13**, 247 (2022).
- 45 Maes, R. Physically Unclonable Functions: Constructions, Properties and Applications (Fysisch onkloonbare functies: constructies, eigenschappen en toepassingen). (2012).
- 46 Arppe, R. & Sørensen, T. J. Physical unclonable functions generated through chemical methods for anti-counterfeiting. *Nature Reviews Chemistry* **1**, 0031 (2017).
- 47 Shaik, C. Preventing counterfeit products using cryptography, qr code and webservice. *Computer Science & Engineering: An International Journal (CSEIJ)* **11** (2021).
- 48 Gebali, F. & Mamun, M. Review of Physically Unclonable Functions (PUFs): Structures, Models, and Algorithms. *Frontiers in Sensors* **2** (2022). <https://doi.org/10.3389/fsens.2021.751748>
- 49 Suh, G. E. & Devadas, S. in *Proceedings of the 44th annual Design Automation Conference* 9–14 (Association for Computing Machinery, San Diego, California, 2007).
- 50 Yoon, S., Kim, B. & Kang, Y. in *2021 International Conference on Information and Communication Technology Convergence (ICTC)*. 1198-1200.
- 51 Dey, K., Kule, M. & Rahaman, H. in *2021 International Symposium on Devices, Circuits and Systems (ISDCS)*. 1-6.
- 52 Gope, P. & Sikdar, B. A Comparative Study of Design Paradigms for PUF-Based Security Protocols for IoT Devices: Current Progress, Challenges, and Future Expectation. *Computer* **54**, 36-46 (2021). <https://doi.org/10.1109/MC.2021.3067462>
- 53 Shariati, S., Koeune, F. & Standaert, F.-X. 26-38 (Springer Berlin Heidelberg).
- 54 Pappu, R., Recht, B., Taylor, J. & Gershenfeld, N. Physical One-Way Functions. *Science* **297**, 2026-2030 (2002). <https://doi.org/doi:10.1126/science.1074376>
- 55 Babu, H. U., Stork, W. & Rauhe, H. in *Advances in Optoelectronics and Micro/nano-optics*. 1-5.
- 56 Kou, Y. *et al.* Electrostatic Self-Assembly of Ag-NPs Mediated by Eu³⁺ Complexes for Physically Unclonable Function Labels. *Aggregate*, e701 (2024).
- 57 Park, J. *et al.* Disordered Heteronanostructures of MoS₂ and TiO₂ for Unclonable Cryptographic Primitives. *ACS Applied Nano Materials* **4**, 2076-2085 (2021). <https://doi.org/10.1021/acsanm.0c03367>
- 58 Im, H. *et al.* Chaotic Organic Crystal Phosphorescent Patterns for Physical Unclonable Functions. *Advanced Materials* **33**, 2102542 (2021). <https://doi.org/https://doi.org/10.1002/adma.202102542>

- 59 Zhang, T. *et al.* Random Nanofracture-Enabled Physical Unclonable Function. *Advanced Materials Technologies* **6**, 2001073 (2021). <https://doi.org/10.1002/admt.202001073>
- 60 Wan, Y. *et al.* Bionic optical physical unclonable functions for authentication and encryption. *Journal of Materials Chemistry C* **9**, 13200-13208 (2021). <https://doi.org/10.1039/D1TC02883A>
- 61 Mesaritakis, C. *et al.* Physical Unclonable Function based on a Multi-Mode Optical Waveguide. *Scientific Reports* **8**, 9653 (2018). <https://doi.org/10.1038/s41598-018-28008-6>
- 62 Chen, F. *et al.* Unclonable fluorescence behaviors of perovskite quantum dots/chaotic metasurfaces hybrid nanostructures for versatile security primitive. *Chemical Engineering Journal* **411**, 128350 (2021). <https://doi.org/10.1016/j.cej.2020.128350>
- 63 Im, H. *et al.* Four-Dimensional Physical Unclonable Functions and Cryptographic Applications Based on Time-Varying Chaotic Phosphorescent Patterns. *ACS nano* **18**, 11703-11716 (2024).
- 64 Meruga, J. M. *et al.* Security printing of covert quick response codes using upconverting nanoparticle inks. *Nanotechnology* **23**, 395201 (2012). <https://doi.org/10.1088/0957-4484/23/39/395201>
- 65 Carro-Temboury, M. R., Arppe, R., Vosch, T. & Sørensen, T. J. An optical authentication system based on imaging of excitation-selected lanthanide luminescence. *Science advances* **4**, e1701384 (2018).
- 66 Leem, J. W. *et al.* Edible Matrix Code with Photogenic Silk Proteins. *ACS Central Science* **8**, 513-526 (2022).
- 67 Wang, C. *et al.* Multicolor Light Mixing in Optofluidic Concave Interfaces for Anticounterfeiting with Deep Learning Authentication. *ACS Applied Materials & Interfaces* **14**, 10927-10935 (2022).
- 68 Buchanan, J. D. *et al.* 'Fingerprinting' documents and packaging. *Nature* **436**, 475-475 (2005).
- 69 Bae, H. J. *et al.* Biomimetic microfingerprints for anti-counterfeiting strategies. *Advanced Materials* **27**, 2083-2089 (2015).
- 70 Torun, N., Torun, I., Sakir, M., Kalay, M. & Onses, M. S. Physically unclonable surfaces via dewetting of polymer thin films. *ACS applied materials & interfaces* **13**, 11247-11259 (2021).
- 71 Deb, D., Ross, A., Jain, A. K., Prakah-Asante, K. & Prasad, K. V. in *2019 international conference on biometrics (ICB)*. 1-8 (IEEE).
- 72 Esidir, A., Kiremitler, N. B., Kalay, M., Basturk, A. & Onses, M. S. Unclonable Features via Electrospraying of Bulk Polymers. *ACS Applied Polymer Materials* **4**, 5952-5964 (2022).
- 73 Moglianetti, M. *et al.* Nanocatalyst-Enabled Physically Unclonable Functions as Smart Anticounterfeiting Tags with AI-Aided Smartphone Authentication. *ACS Applied Materials & Interfaces* **14**, 25898-25906 (2022).
- 74 Melumad, S. & Pham, M. T. The smartphone as a pacifying technology. *Journal of Consumer Research* **47**, 237-255 (2020).
- 75 Chen, W. *et al.* Application of smartphone-based spectroscopy to biosample analysis: A review. *Biosensors and Bioelectronics* **172**, 112788 (2021).
- 76 Banik, S. *et al.* Recent trends in smartphone-based detection for biomedical applications: a review. *Analytical and Bioanalytical Chemistry* **413**, 2389-2406 (2021).
- 77 Hsiao, K. L. Android smartphone adoption and intention to pay for mobile internet: Perspectives from software, hardware, design, and value. *Library Hi Tech* **31**, 216-235 (2013).

- 78 Biswas, S. K. *et al.* Smartphone-enabled paper-based hemoglobin sensor for extreme point-of-care diagnostics. *ACS sensors* **6**, 1077-1085 (2021).
- 79 Böck, F. C., Helfer, G. A., da Costa, A. B., Dessuy, M. B. & Ferrão, M. F. PhotoMetrix and colorimetric image analysis using smartphones. *Journal of Chemometrics* **34**, e3251 (2020).
- 80 Kanazawa, T. *et al.* Use of smartphone attached mobile thermography assessing subclinical inflammation: a pilot study. *Journal of wound care* **25**, 177-182 (2016).
- 81 Kustov, P. *et al.* Mie-Resonant Silicon Nanoparticles for Physically Unclonable Anti-Counterfeiting Labels. *ACS Applied Nano Materials* **5**, 10548-10559 (2022).
- 82 Onorato, P., Rosi, T., Tufino, E., Caprara, C. & Malgieri, M. Quantitative experiments in a distance lab: Studying blackbody radiation with a smartphone. *European Journal of Physics* **42**, 045103 (2021).
- 83 Larkou, G., Mintzis, M., Andreou, P. G., Konstantinidis, A. & Zeinalipour-Yazti, D. Managing big data experiments on smartphones. *Distributed and Parallel Databases* **34**, 33-64 (2016).
- 84 Merazzo, K. J., Totoricaguena-Gorriño, J., Fernández-Martín, E., Del Campo, F. J. & Baldrich, E. Smartphone-enabled personalized diagnostics: current status and future prospects. *Diagnostics* **11**, 1067 (2021).
- 85 Johnston, W. *et al.* Recommendations for determining the validity of consumer wearable and smartphone step count: expert statement and checklist of the INTERLIVE network. *British journal of sports medicine* (2020).
- 86 Blahnik, V. & Schindelbeck, O. Smartphone imaging technology and its applications. *Advanced Optical Technologies* **10**, 145-232 (2021).
- 87 Hunt, B., Ruiz, A. J. & Pogue, B. W. Smartphone-based imaging systems for medical applications: a critical review. *Journal of Biomedical Optics* **26**, 040902-040902 (2021).
- 88 Iqbal, U. Smartphone fundus photography: a narrative review. *International Journal of Retina and Vitreous* **7**, 44 (2021).
- 89 Sischka, N. Design Considerations for New High Resolution and Frame Rate CMOS Sensors. *Quality*, 10-13 (2020).
- 90 Arppe-Tabbara, R., Tabbara, M. & Sørensen, T. J. Versatile and validated optical authentication system based on physical unclonable functions. *ACS applied materials & interfaces* **11**, 6475-6482 (2019).
- 91 Wu, B.-H. *et al.* Grain boundaries of self-assembled porous polymer films for unclonable anti-counterfeiting. *ACS Applied Polymer Materials* **1**, 47-53 (2018).
- 92 Fernández-Benito, A., Hoyos, M., López-Manchado, M. A. & Sørensen, T. J. A Physical Unclonable Function Based on Recyclable Polymer Nanoparticles to Enable the Circular Economy. *ACS Applied Nano Materials* **5**, 13752-13760 (2022).
- 93 Wang, Z., Wang, H., Wang, P. & Shao, Y. Robust Optical Physical Unclonable Function Based on Total Internal Reflection for Portable Authentication. *ACS Applied Materials & Interfaces* (2024).
- 94 Sun, N. *et al.* Random fractal-enabled physical unclonable functions with dynamic AI authentication. *Nature Communications* **14**, 2185 (2023).
- 95 Yu, X., Zhang, H. & Yu, J. Luminescence anti-counterfeiting: from elementary to advanced. *Aggregate* **2**, 20-34 (2021).
- 96 Kumar, P., Singh, S. & Gupta, B. K. Future prospects of luminescent nanomaterial based security inks: from synthesis to anti-counterfeiting applications. *Nanoscale* **8**, 14297-14340 (2016).
- 97 Resch-Genger, U., Grabolle, M., Cavaliere-Jaricot, S., Nitschke, R. & Nann, T. Quantum dots versus organic dyes as fluorescent labels. *Nature methods* **5**, 763-775 (2008).

- 98 Abdollahi, A., Roghani-Mamaqani, H., Razavi, B. & Salami-Kalajahi, M. Photoluminescent and chromic nanomaterials for anticounterfeiting technologies: recent advances and future challenges. *ACS nano* **14**, 14417-14492 (2020).
- 99 Li, X. & Hu, Y. Luminescent films functionalized with cellulose nanofibrils/CdTe quantum dots for anti-counterfeiting applications. *Carbohydrate polymers* **203**, 167-175 (2019).
- 100 Jiang, K. *et al.* Triple-mode emission of carbon dots: applications for advanced anti-counterfeiting. *Angewandte Chemie International Edition* **55**, 7231-7235 (2016).
- 101 Xu, L. *et al.* Double-protected all-inorganic perovskite nanocrystals by crystalline matrix and silica for triple-modal anti-counterfeiting codes. *ACS applied materials & interfaces* **9**, 26556-26564 (2017).
- 102 Binnemans, K. Lanthanide-based luminescent hybrid materials. *Chemical reviews* **109**, 4283-4374 (2009).
- 103 Bünzli, J.-C. G., Comby, S., Chauvin, A.-S. & Vandevyver, C. D. B. New Opportunities for Lanthanide Luminescence. *Journal of Rare Earths* **25**, 257-274 (2007).
[https://doi.org/10.1016/S1002-0721\(07\)60420-7](https://doi.org/10.1016/S1002-0721(07)60420-7)
- 104 Bünzli, J.-C. G. & Eliseeva, S. V. Basics of lanthanide photophysics. *Lanthanide luminescence: photophysical, analytical and biological aspects*, 1-45 (2011).
- 105 Donohue, T. Lanthanide photochemistry initiated in f-f transitions. *Journal of the American Chemical Society* **100**, 7411-7413 (1978).
- 106 Suo, H. *et al.* High-security anti-counterfeiting through upconversion luminescence. *Materials Today Physics* **21**, 100520 (2021).
- 107 Gorris, H. H. & Wolfbeis, O. S. Photon-upconverting nanoparticles for optical encoding and multiplexing of cells, biomolecules, and microspheres. *Angewandte Chemie International Edition* **52**, 3584-3600 (2013).
- 108 Katumo, N., Li, K., Richards, B. S. & Howard, I. A. Dual-color dynamic anti-counterfeiting labels with persistent emission after visible excitation allowing smartphone authentication. *Scientific Reports* **12**, 2100 (2022).
- 109 Ma, X. *et al.* Enhancement of Cerenkov luminescence imaging by dual excitation of Er³⁺, Yb³⁺-doped rare-earth microparticles. *PLOS one* **8**, e77926 (2013).
- 110 Bünzli, J.-C. G. Benefiting from the unique properties of lanthanide ions. *Accounts of chemical research* **39**, 53-61 (2006).
- 111 Ropp, R. C. *Luminescence and the solid state*. (elsevier, 2013).
- 112 Eliseeva, S. V. & Bünzli, J.-C. G. Lanthanide luminescence for functional materials and bio-sciences. *Chemical Society Reviews* **39**, 189-227 (2010).
- 113 Höppe, H. A. Recent developments in the field of inorganic phosphors. *Angewandte Chemie International Edition* **48**, 3572-3582 (2009).
- 114 Richards, B. S., Hudry, D., Busko, D., Turshatov, A. & Howard, I. A. Photon upconversion for photovoltaics and photocatalysis: a critical review: focus review. *Chemical Reviews* **121**, 9165-9195 (2021).
- 115 Sun, G., Xie, Y., Sun, L. & Zhang, H. Lanthanide upconversion and downshifting luminescence for biomolecules detection. *Nanoscale Horizons* **6**, 766-780 (2021).
- 116 Goldschmidt, J. C. & Fischer, S. Upconversion for photovoltaics—a review of materials, devices and concepts for performance enhancement. *Advanced Optical Materials* **3**, 510-535 (2015).
- 117 Duan, Q., Qin, F., Zhang, Z. & Cao, W. Quantum cutting mechanism in NaYF₄: Tb³⁺, Yb³⁺. *Opt. Lett.* **37**, 521-523 (2012).
- 118 Richards, B. S. Luminescent layers for enhanced silicon solar cell performance: Down-conversion. *Solar energy materials and solar cells* **90**, 1189-1207 (2006).
- 119 Nadort, A., Zhao, J. & Goldys, E. M. Lanthanide upconversion luminescence at the nanoscale: fundamentals and optical properties. *Nanoscale* **8**, 13099-13130 (2016).

- 120 Pollnau, M., Gamelin, D. R., Lüthi, S., Güdel, H. & Hehlen, M. P. Power dependence of upconversion luminescence in lanthanide and transition-metal-ion systems. *Physical Review B* **61**, 3337 (2000).
- 121 Pokhrel, M., Kumar, G. & Sardar, D. Highly efficient NIR to NIR and VIS upconversion in Er³⁺ and Yb³⁺ doped in M₂O₂S (M= Gd, La, Y). *Journal of Materials Chemistry A* **1**, 11595-11606 (2013).
- 122 Song, Y. *et al.* Gd₂O₂S: Yb, Er submicrospheres with multicolor upconversion fluorescence. *RSC advances* **2**, 4777-4781 (2012).
- 123 Fischer, S., Fröhlich, B., Krämer, K. W. & Goldschmidt, J. C. Relation between excitation power density and Er³⁺ doping yielding the highest absolute upconversion quantum yield. *The Journal of Physical Chemistry C* **118**, 30106-30114 (2014).
- 124 Mahata, M. K., Hofsäuss, H. C. & Vetter, U. Photon-upconverting materials: advances and prospects for various emerging applications. *Luminescence—An Outlook on the Phenomena and Their Applications*, 109-131 (2016).
- 125 Suyver, J. *et al.* Novel materials doped with trivalent lanthanides and transition metal ions showing near-infrared to visible photon upconversion. *Optical materials* **27**, 1111-1130 (2005).
- 126 Alonso-Álvarez, D. *et al.* Luminescent down-shifting experiment and modelling with multiple photovoltaic technologies. *Progress in Photovoltaics: Research and Applications* **23**, 479-497 (2015).
- 127 McIntosh, K. R. *et al.* Increase in external quantum efficiency of encapsulated silicon solar cells from a luminescent down-shifting layer. *Progress in Photovoltaics: Research and Applications* **17**, 191-197 (2009).
- 128 Solodovnyk, A. *et al.* Highly transmissive luminescent down-shifting layers filled with phosphor particles for photovoltaics. *Optical Materials Express* **5**, 1296-1305 (2015).
- 129 Wang, C., Xuan, T., Liu, J., Li, H. & Sun, Z. Long Afterglow SrAl₂O₄: Eu²⁺, Dy³⁺ phosphors as luminescent down-shifting layer for crystalline silicon solar cells. *International Journal of Applied Ceramic Technology* **12**, 722-727 (2015).
- 130 Richards, B. & McIntosh, K. Overcoming the poor short wavelength spectral response of CdS/CdTe photovoltaic modules via luminescence down-shifting: ray-tracing simulations. *Progress in Photovoltaics: Research and Applications* **15**, 27-34 (2007).
- 131 Klampaftis, E., Ross, D., Seyrling, S., Tiwari, A. N. & Richards, B. S. Increase in short-wavelength response of encapsulated CIGS devices by doping the encapsulation layer with luminescent material. *Solar Energy Materials and Solar Cells* **101**, 62-67 (2012).
- 132 Richards, B. Enhancing the performance of silicon solar cells via the application of passive luminescence conversion layers. *Solar energy materials and solar cells* **90**, 2329-2337 (2006).
- 133 Zhao, M., Zhang, Q. & Xia, Z. Narrow-band emitters in LED backlights for liquid-crystal displays. *Materials Today* **40**, 246-265 (2020).
- 134 Bispo-Jr, A. G., Saraiva, L. F., Lima, S. A., Pires, A. M. & Davolos, M. R. Recent prospects on phosphor-converted LEDs for lighting, displays, phototherapy, and indoor farming. *Journal of Luminescence* **237**, 118167 (2021).
- 135 Zhong, Y. *et al.* Boosting the down-shifting luminescence of rare-earth nanocrystals for biological imaging beyond 1500 nm. *Nature communications* **8**, 737 (2017).
- 136 Pei, P. *et al.* An advanced tunable multimodal luminescent La₄GeO₈: Eu²⁺, Er³⁺ phosphor for multicolor anticounterfeiting. *Advanced Functional Materials* **31**, 2102479 (2021).
- 137 Jiang, X., Guo, Y., Wang, L. & Zhang, Q. Self-reduction induced CaAl₁₂O₁₉: Eu^{2+/3+}: A phosphor with dynamic photoluminescence and photochromism for advanced anti-counterfeiting and encryption. *Ceramics International* (2023).

- 138 Silva, C. L., Bispo-Jr, A., Lima, S. & Pires, A. Eu³⁺ complex/polymer films for light-emitting diode applications. *Optical Materials* **96**, 109323 (2019).
- 139 Wang, C. *et al.* A spatial/temporal dual-mode optical thermometry platform based on synergetic luminescence of Ti⁴⁺-Eu³⁺ embedded flexible 3D micro-rod arrays: High-sensitive temperature sensing and multi-dimensional high-level secure anti-counterfeiting. *Chemical Engineering Journal* **374**, 992-1004 (2019).
- 140 Ji, T. *et al.* Ce³⁺-doped yttrium aluminum garnet transparent ceramics for high-resolution X-ray imaging. *Advanced Optical Materials* **10**, 2102056 (2022).
- 141 Aizenberg, J. & Hendler, G. Designing efficient microlens arrays: lessons from Nature. *Journal of materials chemistry* **14**, 2066-2072 (2004).
- 142 Arai, J., Kawai, H. & Okano, F. Microlens arrays for integral imaging system. *Applied optics* **45**, 9066-9078 (2006).
- 143 Yuan, W., Li, L.-H., Lee, W.-B. & Chan, C.-Y. Fabrication of microlens array and its application: a review. *Chinese Journal of Mechanical Engineering* **31**, 1-9 (2018).
- 144 Lee, D., Allington-Smith, J. R., Content, R. & Haynes, R. in *Optical Astronomical Instrumentation*. 810-820 (SPIE).
- 145 Wu, D. *et al.* High numerical aperture microlens arrays of close packing. *Applied Physics Letters* **97** (2010).
- 146 Zhou, S. & Jiang, L. Modern description of Rayleigh's criterion. *Physical Review A* **99**, 013808 (2019).
- 147 Forshaw, M., Haskell, A., Miller, P., Stanley, D. & Townshend, J. Spatial resolution of remotely sensed imagery A review paper. *International Journal of Remote Sensing* **4**, 497-520 (1983).
- 148 Lauterbach, M. A. Finding, defining and breaking the diffraction barrier in microscopy—a historical perspective. *Optical nanoscopy* **1**, 1-8 (2012).
- 149 Heintzmann, R. & Ficz, G. Breaking the resolution limit in light microscopy. *Methods in cell biology* **81**, 561-580 (2007).
- 150 Masters, B. R. & Masters, B. R. Abbe's theory of image formation in the microscope. *Superresolution optical microscopy: The quest for enhanced resolution and contrast*, 65-108 (2020).
- 151 Walton, A. J. The Abbe theory of imaging: an alternative derivation of the resolution limit. *European Journal of Physics* **7**, 62 (1986).
- 152 Li, L. & Allen, Y. Y. Design and fabrication of a freeform microlens array for a compact large-field-of-view compound-eye camera. *Applied optics* **51**, 1843-1852 (2012).
- 153 Kundu, R. *et al.* in *Digital Optical Technologies 2019*. 162-177 (SPIE).
- 154 Ippolito, S., Goldberg, B. & Ünlü, M. Theoretical analysis of numerical aperture increasing lens microscopy. *Journal of Applied Physics* **97** (2005).
- 155 Liu, H., Yan, Y., Yi, D. & Jin, G. Theories for the design of a hybrid refractive-diffractive superresolution lens with high numerical aperture. *JOSA A* **20**, 913-924 (2003).
- 156 Peer, A., Biswas, R., Park, J.-M., Shinar, R. & Shinar, J. Light management in perovskite solar cells and organic LEDs with microlens arrays. *Optics express* **25**, 10704-10709 (2017).
- 157 Zhou, X. *et al.* Fabrication of large-scale microlens arrays based on screen printing for integral imaging 3D display. *ACS Applied Materials & Interfaces* **8**, 24248-24255 (2016).
- 158 Zhang, Q., Schambach, M., Jin, Q., Heizmann, M. & Lemmer, U. Compact multispectral light field camera based on an inkjet-printed microlens array and color filter array. *Optics Express* **32**, 23510-23523 (2024).

- 159 Nam, H. J., Jung, D.-Y., Yi, G.-R. & Choi, H. Close-packed hemispherical microlens array from two-dimensional ordered polymeric microspheres. *Langmuir* **22**, 7358-7363 (2006).
- 160 Shen, S., Zhou, F., Pu, D., Wei, G. & Zhou, Y. in *2012 International Conference on Manipulation, Manufacturing and Measurement on the Nanoscale (3M-NANO)*. 165-168 (IEEE).
- 161 Lee, K. S., Yang, D. Y., Park, S. H. & Kim, R. H. Recent developments in the use of two-photon polymerization in precise 2D and 3D microfabrications. *Polymers for advanced technologies* **17**, 72-82 (2006).
- 162 Malinauskas, M. *et al.* A femtosecond laser-induced two-photon photopolymerization technique for structuring microlenses. *Journal of optics* **12**, 035204 (2010).
- 163 Dumond, J. J. & Yee Low, H. Recent developments and design challenges in continuous roller micro- and nanoimprinting. *Journal of Vacuum Science & Technology B* **30** (2012).
- 164 Dutta, R. K., Van Kan, J., Bettiol, A. & Watt, F. Polymer microlens replication by Nanoimprint Lithography using proton beam fabricated Ni stamp. *Nuclear Instruments and Methods in Physics Research Section B: Beam Interactions with Materials and Atoms* **260**, 464-467 (2007).
- 165 Kirchner, R. & Schiff, H. Thermal reflow of polymers for innovative and smart 3D structures: A review. *Materials Science in Semiconductor Processing* **92**, 58-72 (2019).
- 166 Qiu, J., Li, M., Ye, H., Zhu, J. & Ji, C. Fabrication of high fill-factor microlens array using spatially constrained thermal reflow. *Sensors and Actuators A: Physical* **279**, 17-26 (2018).
- 167 Ding, H. *et al.* Controlled microstructural architectures based on smart fabrication strategies. *Advanced Functional Materials* **30**, 1901760 (2020).
- 168 Lim, C., Hong, M., Kumar, A. S., Rahman, M. & Liu, X. Fabrication of concave microlens array using laser patterning and isotropic etching. *International Journal of Machine Tools and Manufacture* **46**, 552-558 (2006).
- 169 Lee, K.-S., Kim, R. H., Yang, D.-Y. & Park, S. H. Advances in 3D nano/microfabrication using two-photon initiated polymerization. *Progress in Polymer Science* **33**, 631-681 (2008).
- 170 Harinarayana, V. & Shin, Y. Two-photon lithography for three-dimensional fabrication in micro/nanoscale regime: A comprehensive review. *Optics & Laser Technology* **142**, 107180 (2021).
- 171 Carlotti, M. & Mattoli, V. Functional materials for two-photon polymerization in microfabrication. *Small* **15**, 1902687 (2019).
- 172 Wang, H. *et al.* Two-Photon Polymerization Lithography for Optics and Photonics: Fundamentals, Materials, Technologies, and Applications. *Advanced Functional Materials*, 2214211 (2023).
- 173 Pryor, R. W. *Multiphysics modeling using COMSOL®: a first principles approach*. (Jones & Bartlett Publishers, 2009).
- 174 Mayboudi, L. S. *Geometry creation and import with comsol multiphysics*. (Mercury Learning and Information, 2019).
- 175 Dickinson, E. J., Ekström, H. & Fontes, E. COMSOL Multiphysics®: Finite element software for electrochemical analysis. A mini-review. *Electrochemistry communications* **40**, 71-74 (2014).
- 176 Kou, X. & Tan, S. T. Heterogeneous object modeling: A review. *Computer-Aided Design* **39**, 284-301 (2007).
- 177 Piston, D. W. Choosing objective lenses: the importance of numerical aperture and magnification in digital optical microscopy. *The Biological Bulletin* **195**, 1-4 (1998).

- 178 Chang, R., Chen, Z., Yu, C. & Song, J. An experimental study on stretchy and tough
PDMS/fabric composites. *Journal of Applied Mechanics* **86**, 011012 (2019).
- 179 Liu, M., Sun, J. & Chen, Q. Influences of heating temperature on mechanical properties
of polydimethylsiloxane. *Sensors and Actuators A: Physical* **151**, 42-45 (2009).
- 180 Cibert, C. *et al.* Properties of aluminum oxide thin films deposited by pulsed laser
deposition and plasma enhanced chemical vapor deposition. *Thin Solid Films* **516**,
1290-1296 (2008).
- 181 Boidin, R., Halenkovič, T., Nazabal, V., Beneš, L. & Němec, P. Pulsed laser deposited
alumina thin films. *Ceramics International* **42**, 1177-1182 (2016).
- 182 Langenhorst, M. *Cloaked contact grids for perovskite-silicon tandem solar modules*,
Dissertation, Karlsruhe, Karlsruher Institut für Technologie (KIT), 2019, (2020).
- 183 Abu Jarad, N., Imran, H., Imani, S. M., Didar, T. F. & Soleymani, L. Fabrication of
superamphiphobic surfaces via spray coating; a review. *Advanced Materials
Technologies* **7**, 2101702 (2022).
- 184 Katumo, N. *et al.* Anticounterfeiting labels with smartphone-readable dynamic
luminescent patterns based on tailored persistent lifetimes in Gd₂O₂S: Eu³⁺/Ti⁴⁺.
Advanced Materials Technologies **6**, 2100047 (2021).
- 185 Zhou, W., Apkarian, R., Wang, Z. L. & Joy, D. Fundamentals of scanning electron
microscopy (SEM). *Scanning Microscopy for Nanotechnology: Techniques and
Applications*, 1-40 (2007).
- 186 Gee, G. W. & Bauder, J. W. Particle-size analysis. *Methods of soil analysis: Part 1
Physical and mineralogical methods* **5**, 383-411 (1986).
- 187 Fandrich, R., Gu, Y., Burrows, D. & Moeller, K. Modern SEM-based mineral liberation
analysis. *International Journal of Mineral Processing* **84**, 310-320 (2007).
- 188 Lopez, T., Sanchez, E., Bosch, P., Meas, Y. & Gomez, R. FTIR and UV-Vis (diffuse
reflectance) spectroscopic characterization of TiO₂ sol-gel. *Materials chemistry and
physics* **32**, 141-152 (1992).
- 189 Myrick, M. L. *et al.* The Kubelka-Munk diffuse reflectance formula revisited. *Applied
Spectroscopy Reviews* **46**, 140-165 (2011).
- 190 Kortüm, G., Braun, W. & Herzog, G. Principles and techniques of diffuse-reflectance
spectroscopy. *Angewandte Chemie International Edition in English* **2**, 333-341 (1963).
- 191 Tebyetekerwa, M. *et al.* Mechanisms and applications of steady-state
photoluminescence spectroscopy in two-dimensional transition-metal dichalcogenides.
ACS nano **14**, 14579-14604 (2020).
- 192 Lopes, J. M. S., Barbosa Neto, N. M. & Araujo, P. T. in *Springer Handbook of Inorganic
Photochemistry* 131-144 (Springer, 2022).
- 193 Herman, B., Lakowicz, J., Murphy, D., Fellers, T. J. & Davidson, M. W. (2009).
- 194 Meneghini, M., Tazzoli, A., Mura, G., Meneghesso, G. & Zanoni, E. A review on the
physical mechanisms that limit the reliability of GaN-based LEDs. *IEEE Transactions
on Electron Devices* **57**, 108-118 (2009).
- 195 Vu, B. V., Lei, R., Mohan, C., Kourentzi, K. & Willson, R. C. Flash Characterization
of Smartphones Used in Point-of-Care Diagnostics. *Biosensors* **12**, 1060 (2022).
- 196 Peterson, B. *Understanding exposure: how to shoot great photographs with any
camera*. (AmPhoto books, 2016).
- 197 Pollefeys, M. *et al.* Visual modeling with a hand-held camera. *International Journal of
Computer Vision* **59**, 207-232 (2004).
- 198 McHugh, S. T. *Understanding photography: master your digital camera and capture
that perfect photo*. (No starch press, 2018).
- 199 Abdelhamed, A., Lin, S. & Brown, M. S. in *Proceedings of the IEEE conference on
computer vision and pattern recognition*. 1692-1700.

- 200 Malokar, N. K. *et al.* Exploiting the Vulnerabilities of Android Camera API. *IARJSET* **2** (2015).
- 201 Pereira, S. & Pun, T. Robust template matching for affine resistant image watermarks. *IEEE transactions on image Processing* **9**, 1123-1129 (2000).
- 202 Bebis, G., Georgiopoulos, M., da Vitoria Lobo, N. & Shah, M. Learning affine transformations. *Pattern recognition* **32**, 1783-1799 (1999).
- 203 Moons, T., Van Gool, L., Proesmans, M. & Pauwels, E. Affine reconstruction from perspective image pairs with a relative object-camera translation in between. *IEEE Transactions on Pattern Analysis and Machine Intelligence* **18**, 77-83 (1996).
- 204 Mikolajczyk, K. & Schmid, C. in *Computer Vision—ECCV 2002: 7th European Conference on Computer Vision Copenhagen, Denmark, May 28–31, 2002 Proceedings, Part I* 7. 128-142 (Springer).
- 205 Seitz, S. M. & Dyer, C. R. in *Proceedings of the 23rd annual conference on Computer graphics and interactive techniques*. 21-30.
- 206 Shakunaga, T. & Kaneko, H. Perspective angle transform: Principle of shape from angles. *International Journal of Computer Vision* **3**, 239-254 (1989).
- 207 Wolfson, H. J. & Rigoutsos, I. Geometric hashing: An overview. *IEEE computational science and engineering* **4**, 10-21 (1997).
- 208 Ibraheem, N. A., Hasan, M. M., Khan, R. Z. & Mishra, P. K. Understanding color models: a review. *ARPJ Journal of science and technology* **2**, 265-275 (2012).
- 209 Chhikara, R. *The inverse Gaussian distribution: theory: methodology, and applications*. Vol. 95 (CRC Press, 1988).
- 210 Woodroffe, M. Estimating a distribution function with truncated data. *The Annals of Statistics* **13**, 163-177 (1985).
- 211 Wurtman, R. J. The effects of light on the human body. *Scientific american* **233**, 68-79 (1975).
- 212 Griffin, D. R., Hubbard, R. & Wald, G. The sensitivity of the human eye to infra-red radiation. *JOSA* **37**, 546-554 (1947).
- 213 Cheng, Y.-H., Wu, J.-L., Cheng, C.-H., Syao, K.-C. & Lee, M.-C. M. Enhanced light outcoupling in a thin film by texturing meshed surfaces. *Applied Physics Letters* **90** (2007).
- 214 Möller, S. & Forrest, S. Improved light out-coupling in organic light emitting diodes employing ordered microlens arrays. *Journal of Applied Physics* **91**, 3324-3327 (2002).
- 215 Arca, S., Campadelli, P. & Lanzarotti, R. A face recognition system based on automatically determined facial fiducial points. *Pattern recognition* **39**, 432-443 (2006).
- 216 Shen, L. & Bai, L. A review on Gabor wavelets for face recognition. *Pattern analysis and applications* **9**, 273-292 (2006).
- 217 Samal, A. & Iyengar, P. A. Automatic recognition and analysis of human faces and facial expressions: A survey. *Pattern recognition* **25**, 65-77 (1992).
- 218 Agha, H. *et al.* Unclonable human-invisible machine vision markers leveraging the omnidirectional chiral Bragg diffraction of cholesteric spherical reflectors. *Light: Science & Applications* **11**, 309 (2022).
- 219 Berends, A. C., van de Haar, M. A. & Krames, M. R. YAG: Ce³⁺ phosphor: from micron-sized workhorse for general lighting to a bright future on the nanoscale. *Chemical Reviews* **120**, 13461-13479 (2020).
- 220 Zhang, R. *et al.* A new-generation color converter for high-power white LED: transparent Ce³⁺: YAG phosphor-in-glass. *Laser & Photonics Reviews* **8**, 158-164 (2014).
- 221 Lotsch, H. K. Reflection and refraction of a beam of light at a plane interface. *JOSA* **58**, 551-561 (1968).

- 222 Grant, L. Diffuse and specular characteristics of leaf reflectance. *Remote Sensing of Environment* **22**, 309-322 (1987).
- 223 Schober, P., Boer, C. & Schwarte, L. A. Correlation coefficients: appropriate use and interpretation. *Anesthesia & analgesia* **126**, 1763-1768 (2018).
- 224 Armstrong, R. A. Analysis of spatial patterns in histological sections of brain tissue. *Journal of neuroscience methods* **73**, 141-147 (1997).
- 225 Hsieh, H.-T., Lin, V., Hsieh, J.-L. & Su, G.-D. J. Design and fabrication of long focal length microlens arrays. *Optics Communications* **284**, 5225-5230 (2011).
- 226 Camacho P, A. A., Solano, C. E., Cywiak, M., Martinez-Ponce, G. & Baltazar, R. Method for the determination of the focal length of a microlens. *Optical Engineering* **39**, 2149-2152 (2000).
- 227 Di Nonno, S. & Ulber, R. Smartphone-based optical analysis systems. *Analyst* **146**, 2749-2768 (2021).
- 228 Kayaci, N. *et al.* Organic light-emitting physically unclonable functions. *Advanced Functional Materials* **32**, 2108675 (2022).
- 229 Wang, S., Toreini, E. & Hao, F. Anti-counterfeiting for polymer banknotes based on polymer substrate fingerprinting. *IEEE Transactions on Information Forensics and Security* **16**, 2823-2835 (2021).
- 230 Hardwick, B., Jackson, W., Wilson, G. & Mau, A. W. Advanced materials for banknote applications. *Advanced materials* **13**, 980-984 (2001).
- 231 Lin, C. C. & Liu, R.-S. Advances in phosphors for light-emitting diodes. *The journal of physical chemistry letters* **2**, 1268-1277 (2011).
- 232 Yang, Y. *et al.* Luminescent properties of Y3Al5O12: Ce3+ phosphor-in-glass for WLEDs. *Optik* **200**, 163455 (2020).
- 233 Alawsi, T. & Al-Bawi, Z. A review of smartphone point-of-care adapter design. *Engineering Reports* **1**, e12039 (2019).
- 234 Cambie, D., Zhao, F., Hessel, V., Debije, M. G. & Noël, T. Every photon counts: understanding and optimizing photon paths in luminescent solar concentrator-based photomicroreactors (LSC-PMs). *Reaction Chemistry & Engineering* **2**, 561-566 (2017).
- 235 Moraitis, P., Schropp, R. & Van Sark, W. Nanoparticles for luminescent solar concentrators-a review. *Optical Materials* **84**, 636-645 (2018).
- 236 Faro, S. & Lecroq, T. Efficient pattern matching on binary strings. *arXiv preprint arXiv:0810.2390* (2008).
- 237 Navarro, G. & Raffinot, M. in *Annual Symposium on Combinatorial Pattern Matching*. 14-33 (Springer).
- 238 Falk, R. & Konold, C. Making sense of randomness: Implicit encoding as a basis for judgment. *Psychological Review* **104**, 301 (1997).
- 239 Krichen, M. Anomalies detection through smartphone sensors: A review. *IEEE Sensors Journal* **21**, 7207-7217 (2021).
- 240 Yazdi, M. & Bouwmans, T. New trends on moving object detection in video images captured by a moving camera: A survey. *Computer Science Review* **28**, 157-177 (2018).
- 241 Choi, I. S. *et al.* Strain-tunable optical microlens arrays with deformable wrinkles for spatially coordinated image projection on a security substrate. *Microsystems & Nanoengineering* **8**, 98 (2022).